Development of a Time of Flight – Energy spectrometer for applications in Heavy Ion – Elastic Recoil Detection thin film analysis

Mandlenkosi Msimanga

BSc (Hons), MSc.

Thesis Presented for the Degree of

DOCTOR OF PHILOSOPHY

in the Department of Physics

UNIVERSITY OF CAPE TOWN

October 2010

Development of a Time of Flight – Energy spectrometer for applications in Heavy Ion – Elastic Recoil Detection thin film analysis

Mandlenkosi Msimanga
Materials Research Department, iThemba LABS

Abstract

Two principal aims of this work were firstly, to build and characterise a Time of Fight – Energy spectrometer and demonstrate its usability in Heavy Ion – Elastic Recoil Detection thin film materials analysis, and secondly, to measure stopping powers of heavy ions in thin foil compound materials using the newly built spectrometer.

Key to the performance of Time of Flight – Energy spectrometers is the ability to separate detected ions according to mass, facilitating elemental analysis. From system characterisation measurements, the mass resolution was found to range between 0.8 u and 1.7 u in the atomic mass range 12 u to 40 u. The best timing resolution obtained was 0.96 ns for 18 MeV ^{40}Ca recoils ejected from the surface layers of a Calcium Fluoride film on a Silicon substrate, with a resultant depth resolution of 13 ± 1.0 nm.

Thin film depth profiling from elemental energy spectra was implemented using both direct calculation and iterative simulation software codes. Of the latter group, Monte Carlo based simulation using the analysis code CORTEO proved most appropriate for analysis of Heavy Ion – ERDA data, exemplified by the analysis of a Chromium Oxide deposit on a Silicon substrate. The analytical depth achievable was up to 600 nm in a silicon matrix. The lowest detectable atomic concentrations measured in the same matrix were 0.46 at % for carbon and 0.84 at % for oxygen.

Measurements were also carried out to determine stopping powers of ZrO_2 and Mylar foils for ^{12}C, ^{16}O, ^{19}F, ^{24}Mg, ^{27}Al and ^{28}Si ions in the 0.1 – 0.6 MeV/u energy range. Of these, ^{27}Al and ^{24}Mg stopping power data generated in this work are the first such measurements for ZrO_2, and ^{24}Mg and ^{19}F for Mylar.

October 2010

Acknowledgements

For the work presented in this thesis I would like to express my sincere gratitude to the following persons;

- My supervisors, Prof. Craig Comrie and Prof. Carlos Pineda – Vargas, for their help and guidance in experimental work and thesis write up.
- Chris Theron, for introducing me to the field of ion beam techniques.
- Sean Murray for the installation of the data acquisition system.
- Andi Bergmaier of the Universität der Bundeswehr Munchen, Germany, for making available the data analysis program KONZERD.
- Günther Dollinger of the Universität der Bundeswehr Munchen, and Rob Bark (iThemba LABS) for their expert advice on some of the technical details of the experimental set up.
- Rainer Thomae for his unparalleled determination to provide us with optimal beam.
- Lawrence Ashworth, for his expert work on the modification of the target chamber and the ToF flange.
- All members of the Accelerator Group involved in this project in one way or the other.
- The head, Dr Rudzani Nemutudi, and members of the Materials Research Department; staff and students, for their continual encouragement and support.

I would also like to thank my buddies from the 'other world'; Edward, Nkosi, Wilson, Makhosini and Mvalela for seeing in me 'their scientist'.

To my wife Lungi and son Thando and newly arrived daughter Thandeka, thank you so much for bearing with my absence even though I have been around all the time.

Continued support and encouragement from the Msimanga clan at large is greatly appreciated . . . . . *kini bo Thinta Mthangala ngithi eLoNkosi, eMalisa, eKhobongo, eNzimakazi !!*

Lastly I take a bow, give praise and thanks to the Almighty for affording me chance, willpower and the ability to start and see this project through.

Dedication

To my wife Lungile, for believing in me.

Table of Contents

LIST OF FIGURES

LIST OF TABLES

LIST OF ACRONYMS

ADC	Analogue to Digital Converter
ASCII	American Standard Code for Information Interchange
CAB	Cores and Bonds
CFD	Constant Fraction Discriminator
DL	Detection Limit
ERD	Elastic Recoil Detection
ERDA	Elastic Recoil Detection Analysis
FWHM	Full Width at Half Maximum
IBA	Ion Beam Analysis
LABS	Laboratory for Accelerator Based Sciences
MCA	Multichannel Analyser
MCP	Microchannel Plate
MIDAS	Maximum Integrated Data Acquisition System
RBS	Rutherford Backscattering Spectrometry
SBD	Surface Barrier Detector
ToF	Time of Flight
SRIM	Stopping and Range of Ions in Matter
TDC	Time to Digital Converter
TR	Timing Resolution

Chapter 1

Introduction

1.1 An overview

Thin film materials at the micro/nanometre scales permeate many spheres of our technology-oriented world – finding applications in wide ranging industries such as micro/nano electronics, laser technology, solar energy research and development, biomedical industries and so on. This widespread use is driven by the availability of tools and methods to produce and study the structure and composition of these materials and relate these to their material properties. Many advanced thin film materials of technological importance derive their functional properties from compounds containing light elements such as carbides, oxides and nitrides [1].

Elastic Recoil Detection Analysis (ERDA) is now a well-established nuclear analytical technique in the analysis of thin films of technological and medical importance. It is to a large extent the most suitable technique available for simultaneous identification and quantitative depth profiling of light elements in thin films. This is mainly because most of the available surface analysis methods such as X-ray techniques or electron microscopy are relatively insensitive for light element detection [2]. Rutherford Backscattering Spectrometry (RBS) which is quite closely related to ERDA, also suffers from poor sensitivity to light elements. Another, similarly common ion beam technique, Nuclear Reaction Analysis (NRA), is mostly appropriate for the analysis of *one* specific element at a time in a thin film matrix.

ERDA makes use of a medium to heavy ion beam incident on a target surface and consists in the detection of particles recoiled off the target in a forward direction by the beam in a known geometry. A general requirement is that the incident ions be heavier that the

constituent target atoms/ions, and so the commonly used prefix Heavy Ion – ERDA to distinguish it from 'hydrogen' ERDA which refers to hydrogen analysis using alpha particles as the probing incident ions. The quantitative nature of the technique is based on the knowledge of the recoil cross-sections of the projectile – target interactions [3]. Its depth analysis capability depends on the knowledge of energy loss factors of projectiles and recoils as they traverse into and out of target layers.

1.2 Historical development of ERDA

A comprehensive account of the extension of the ERDA method in Ion Beam Analysis laboratories worldwide is given by Tirira J and co-authors [4] in their seminal book of 1996 'Forward Recoil Spectrometry – Applications to Hydrogen Determination in Solids'. Only a brief account of the development of the technique over the last two decades will be attempted here, with a particular emphasis on the recoil detection methods used. Of special interest will be the Time-of-Flight (ToF) variant since this is the detection method developed for use here at iThemba LABS.

The first report of practical implementation of ERDA as a tool in thin film analysis was by L'Ecuyer and co-workers in 1976 [5]. Their method consisted in the bombardment of thin layers containing lithium using a high energy (25-40 MeV) ^{35}Cl ion beam in a transmission geometry set up. Thin (5-7 μm) nickel foils were placed in front of the detector to stop the incoming ^{35}Cl beam and other heavy recoils, but allow the Li atoms through. They obtained a depth resolution of 30 nm FWHM at a depth of 1 μm and further predicted that sensitivity of the order of 10^{14} atoms/cm^2 could be achieved in future experiments.

The main limitation in this conventional set up is that the energy spread of the recoiled particles is broadened while passing through the stopper foil [6, 7]. The depth resolution is as a result degraded. There is also a possibility of getting recoils of different masses emerging from different depths reaching the detector with equal energies leading to what Tirira et al (1996) call *mass-depth* ambiguity. Another problem, which they term *projectile-scattered ion* ambiguity, is that a projectile may be scattered in the same direction as a recoil

atom and end up detected as well, and difficulties arise in trying to distinguish between the two. It is for these reasons that conventional ERDA has largely been restricted to hydrogen analysis [8], where low energy helium ions are used and an absorber foil of sufficient thickness used to stop any helium projectiles scattered in the direction of the detector.

A lot of effort has been expended over the years to extend the applicability of ERDA over a wider target mass range. Various detection techniques have been designed and implemented to overcome the ambiguities mentioned above. These include ΔE-E telescopes [6, 9, 10], magnetic spectrometers [11], elastic recoil coincidence spectroscopy (ERCS) [12] and ToF spectrometers [7, 8, 13-15].

The ΔE-E detection method uses a thin Si transmission detector placed in front of a standard Si surface barrier detector (SBD). In some set-ups the Si transmission detector is replaced by a gas ionisation chamber [3]. The residual energy E is measured using the Si SBD. Measurement of ΔE allows for mass separation between scattered projectiles and recoiled atoms since the relative stopping powers of particles impinging the ΔE detector with the same velocity are determined by their mass differences [6, 9]. The total particle energy is obtained as a sum of the energy loss ΔE and the residual energy E. There is thus an improved depth resolution when compared to the conventional set up where the energy loss through the absorber foil is not accounted for.

The main criteria in the use of a Si transmission detector in the ΔE-E telescope include the thickness and energy resolution of the ΔE detector. For low Z recoils the detector must be sufficiently thick so that signals from different recoils are distinguishable. A thick ΔE detector however leads to a much higher energy loss and this reduces the probing depth obtainable. This is even more so for medium Z atoms where the recoils can be totally stopped in the transmission detector. The alternative for medium to high Z recoils is to use very high energy incident beams which on the other hand is only possible if radiation damage on the target sample is not critical, and if the accelerator in use can produce such high energy beams in the first place. In the end a compromise between transmission detector thickness and energy straggling generally limits the application of this technique to light recoils.

Elastic Recoil Coincidence Spectroscopy and Magnetic Spectrometry are some of the latest improvements in ERDA that to a large extent do solve the *mass-depth* and the *projectile-scattered ion* ambiguities for a wide mass range [4]. The set up for ERCS is the transmission geometry configuration which can only be applied to free standing films since one or both of either the projectile or the recoil atom has to penetrate through the film. By careful choice of the scattering geometry each particle is detected and identified separately. Depth information is obtained by measuring the energies of both the scattered and recoiled atoms in time-coincidence [12], which allows for simultaneous depth profiling of different light elements present in a sample. In magnetic spectrometry the spectrometer is used to separate the recoil particles according to their momentum [11], from which can be derived their energy. They are then identified through measuring their energy in a detection plane using a position-sensitive detector. A depth profile is obtained by measuring the contribution of an element or isotope to the measured energy spectra.

Time of Flight (ToF) detection consists in the measurement of the time of flight of the recoils over a known distance [16] and their energy in a standard Si SBD. The ToF and the energy signals are recorded in coincidence. The technique offers a very high resolving power with respect to mass and energy since the measured ToF can be used to calculate, with the identified mass of the recoil, the corresponding energy [14, 17]. In general the energy spectra are usually deduced from ToF spectra because the ToF detector, unlike the energy detector, which has a non-linear response for medium to heavy ions, has a linear calibration for all ions. Nevertheless it is always prudent to check this for a fact as the ToF detectors, unlike the commercially produced Si detectors, are generally self assembled in most Ion Beam Analysis (IBA) labs.

Several ToF measurement configurations are used [3,4,7] based on the detection of secondary electron emission from thin carbon foils placed in the recoil particle path. The general set up is that two time detectors positioned at a known distance apart are operated in a start-stop mode and a Si SBD measures the energy of the recoils. Each time detector consists of a thin carbon foil placed close to a microchannel plate (MCP) configuration. An MCP consists of millions of very thin separate channels and each channel works as an

independent electron multiplier. An electric field is applied between the foil and a grid to accelerate and guide the electrons to the MCPs where the electron signal is multiplied and detected as a negative output voltage timing signal. Details of the detector system set up in this work are given in chapter 3.

1.3 Ion beam analysis at iThemba LABS

The iThemba Laboratory for Accelerator Based Sciences (LABS) is a multidisciplinary research institution that provides accelerator facilities for research and training in nuclear and accelerator physics, material sciences, radiation biophysics, and for radio nuclide production and radiotherapy. Core activities are centred on a main separated sector cyclotron (SSC) fed, alternately, by two solid-pole injector cyclotrons SPC1 and SPC2. The SPC1 pre-accelerates proton beams for proton therapy and radioisotope production and the SPC2 pre-accelerates polarised protons and light and heavy ion beams for nuclear physics research.

Ion beam materials analysis is based on a fourth accelerator, a 6 MV Van de Graaff accelerator that was commissioned in 1963. The nuclear analytical techniques available at this accelerator are Proton Induced X-ray Emission (PIXE) spectroscopy, Rutherford Backscattering Spectrometry (RBS), Elastic Recoil Detection Analysis (ERDA), Nuclear Reaction Analysis (NRA) and Proton Induced Gamma Ray Emission (PIGE). All the analysis work is done using either helium or proton beams. For that reason current ERD analysis is limited to hydrogen analysis in thin films.

In 2000 a proposal was made by the Materials Research Group (MRG) to the iThemba LABS Physical Sciences Research Program to implement a Heavy Ion-ERDA system as an additional analytical tool using energetic heavy ions from the SPC2 cyclotron. Prof Günther Dollinger of the Technical University of Munich and Dr. Victor Prozesky, the then head of the MRG, were the scientific leaders of the project [2]. Preliminary work on the material design and construction of the ToF detectors was carried out by S. Sepuru for his MSc dissertation in 2001, under the supervision of Prof. Dollinger [18]. Further

progress on the project was hindered by logistical problems pertaining to movement of personnel and the project was subsequently put on hold. Work was resumed in earnest in 2006 by the current author to assemble, characterise and modify, and demonstrate usability of the ToF – E spectrometer in Heavy Ion - ERD applications, culminating in this thesis.

1.4 Aims and objectives

The broad aim of this project was to develop and install a Time of Flight – Energy spectrometer for applications in HI –ERD thin film analysis, to complement the existing nuclear analytical techniques at iThemba LABS. The specific objectives were to;

- Set up and characterise a ToF – Energy spectrometer using radioactive sources and ion beams from the SPC2 cyclotron
- Implement and optimise the data acquisition and analysis system
- Carry out analyses of real samples containing light elements to demonstrate usability of the system
- As an additional application area, use the ToF – Energy spectrometer to measure stopping powers of compound materials for various light ions of interest in HI – ERDA in the 0.1 – 1.0 MeV/u energy range.

1.5 Thesis outline

This introductory chapter gives a general background of the HI – ERDA technique and a brief insight into its historical development. The chapter closes by explaining the development of HI – ERDA within the context of iThemba LABS. Chapter 2 introduces the theoretical basis of the technique, explaining how the underlying ion beam – target interactions extend to actual sample analysis, as well as discussing the limitations encountered therein. The construction of the ToF – Energy spectrometer is described in chapter 3, together with detailed results of preliminary characterisation measurements. Chapter 4 describes the analyses of real samples, aimed at demonstrating the usability of the spectrometer in solving problems specific to the analysis of light elements in thin film

materials. Chapter 5 details measurements carried out to provide stopping power data of various ions ($4 < A < 31$) in the oxide ceramic ZrO_2 and in the polymeric plastic Mylar. Chapter 6 gives a summary of new results obtained in this work and gives concluding remarks on the contribution made by this thesis to the advancement of the fields of ion beam techniques and materials research.

1.6 References

1. Dytlewski N. *Improvement of the reliability and accuracy of heavy ion beam nuclear analytical techniques*, IAEA Coordinated Research Project F11013 (2007).
2. Dollinger G. and Procesky V. (2000) *Research proposal to iThemba LABS: Physical Science Research Programme on Separated Sector Cyclotron Facility*
3. Arnold-Bik W.M and Habraken F.H.P.M *Rep. Prog. Phys.* **56** (1993) 859.
4. Tirira J., Serruys Y and Trocellier P., *Forward Recoil Spectrometry (Applications to hydrogen determination in solids)*, 1996 Plemm Press, New York.
5. L'Ecuyer J. *et al. J. Appl. Phys.* **47** (1976) 381.
6. Prozesky V.M *et al. Nucl. Instr. and Meth.* **B84** (1994) 373.
7. Whitlow H.J., Possnert G and Petersson C.S. *Nucl. Instr. Meth.* **B27** (1987) 448.
8. Thomas J.P., Fallavier M and Ziani A. *Nucl. Instr. and Meth.* **B15** (1986) 443.
9. Petrascu M. *et al. Nucl. Instr. and Meth.* **B4** (1984) 396.
10. Stoquert J.P. *et al. Nucl. Instr. and Meth.* **B44** (1989) 184.
11. Gosset C.R. *Nucl. Instr. and Meth.* **B15** (1986) 481.
12. Hofsäss H.C. *et al. Nucl. Instr. and Meth.* **B58** (1999) 49.
13. Arai E. *et al. Nucl. Instr. and Meth.* **B64** (1992) 296.
14. Bohne W., Röhrich J. and Röschert G. *Nucl. Instr. and Meth.* **B136-138** (1998) 633.
15. Jokinen J. *et al. Nucl. Instr. and Meth.* **B119** (1996) 533.
16. Groleau R., Gujrath S.C and Martin J.P. *Nucl. Instr. and Meth.* **218** (1983) 11.
17. Zhang Y. *et al. Nucl. Instr. and Meth.* **B149** (1999) 477.
18. Sepuru S. *MSc Thesis*, University of North West (2001).

Chapter 2

Theoretical overview

2.1 Introduction

The fundamental theoretical aspects that form the basis of the ERDA technique are thoroughly reviewed and discussed in books by Chu et al [1], Bird and Williams [2] and Tirira et al [3]. This chapter introduces those underlying theoretical concepts that have a direct bearing on the practical realisation of the technique; kinematics, elastic cross-section and stopping power. The last two sections briefly describe the practical limitations to these theoretical formulations and the computer programs developed over the years to aid analysis of ion beam data by taking into account some of these limitations.

2.2 General considerations

2.2.1 Kinematics

The capability of the ERDA technique to perform mass analysis is based on energy transfer in the collisions between projectile ions and target atoms. In a typical ERDA set up the energy of the projectile lies within the 0.1 – 1.0 MeV/u range and the projectile – target interaction can be described in terms of Coulomb repulsion between the two nuclei [4]. The energy transferred from a projectile of mass m_1 to a recoil atom of mass m_2 on the target sample surface can be calculated through conservation of momentum and energy. In the laboratory frame of reference the ratio of the recoil energy E_2 to the projectile energy E_0 is given by

$$\frac{E_2}{E_0} = K_r = \frac{4m_1m_2}{(m_1+m_2)^2}\cos^2\Phi \qquad [2.1],$$

where K_r is called the recoil kinematic factor and Φ is the angle of recoil, measured from the projectile incidence direction [see Fig 2.3]. The projectile is itself scattered through an angle θ with energy E_1 given by

$$\frac{E_1}{E_0} = K_s = \left[\frac{m_1 \cos\theta \pm \sqrt{m_2^2 - m_1^2 \sin^2\theta}}{m_1 + m_2} \right]^2 \qquad [2.2],$$

where K_s is the scattering kinematic factor. An example showing the variation of the kinematic factors with target mass for two different projectile beams and for a fixed recoil or scattering angle of 30° is shown in Fig. 2.1. The chosen angle is the fixed angle between the incident beam direction and the ToF – Energy detector telescope set up in this work. The four curves shown were generated using ORIGIN® graphing and analysis software package. The projectile beams chosen are representative of the two broad categories of light and heavy incident beams encountered in ERDA.

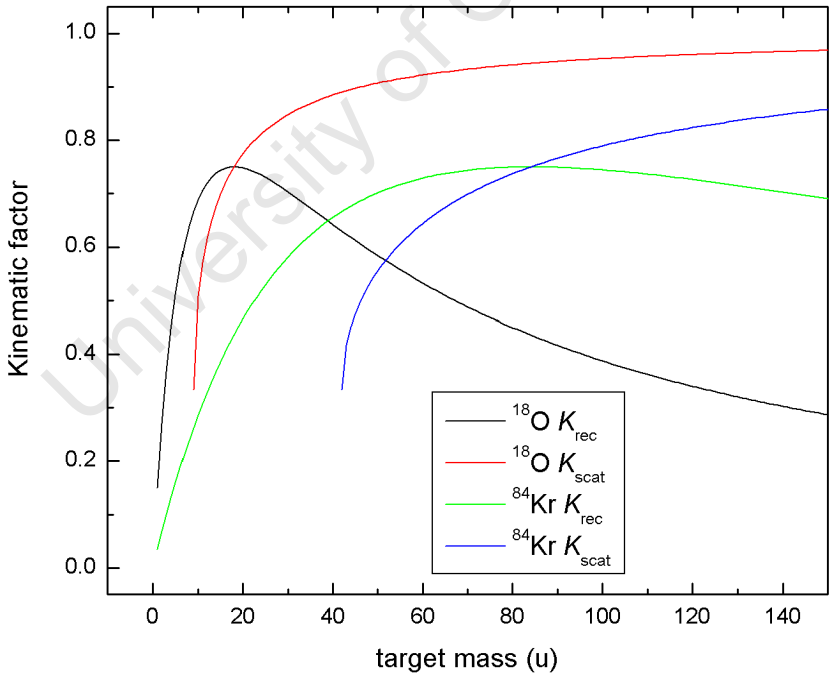

Figure 2.1 Variation of the recoil K_{rec} and scattering K_{scat} kinematic factors of ^{18}O and ^{84}Kr projectiles with target atomic mass at a scattering / recoil angle of 30°.

The main trend observed in Fig. 2.1 is that the fraction of the initial projectile energy transferred to a target recoil atom increases sharply with the target atomic mass up to a maximum, when both the projectile and the target are of the same mass, and thereafter decreases gradually. As the target atom gets heavier, the projectile scatters off with an increasingly higher fraction of the initial energy than a recoil ejected in the same direction. Also, for a fixed recoil/scattering angle, there is a minimum target mass that will scatter the projectile through that angle, and this minimum increases with increasing projectile mass.

The essence of ERDA is that the constituent atoms in a sample material are recoiled by the incident beam in the forward direction towards, and identified by, the detector system. Barring differences in the scattering cross section (see below) and considering just the kinematics, that best happens if the projectile ions are much heavier than the target atoms, because a wider mass range of target atoms can then be detected without interference from forward scattered projectiles as can be inferred from Fig. 2.1. For instance, in the example illustrated above, a krypton projectile can, in principle, recoil any target atom with $1 \leq m_2 \leq 40$ into the solid angle centred on 30^o without itself scattering into the same solid angle, compared to just $1 \leq m_2 \leq 11$ for an oxygen projectile.

On the other hand though, for smaller, low energy accelerators, lighter incident ions e.g 10 MeV ^{35}Cl [5], can still be used, with the advantage that apart from measuring just the light recoils, heavy elements present in a target sample can be quantified using scattered incident beam in the analysis. This can be done in instances where the detector system is mass dispersive, such as ToF – E and ΔE – E spectrometers, where it is possible to obtain separate energy spectra of recoil ions and scattered beam. In addition, effects such as multiple scattering (discussed in section 2.3.3) are smaller for low-Z projectiles when compared to heavier incident ions.

2.2.2 Cross section

The quantitative capability of ERDA is a direct consequence of the physical concept of cross section in projectile – target interactions. The cross section σ describes the probability of a

recoil (or scattering) event occurring in a preferred direction. Alternatively, it is the effective area presented to incoming ions by each interaction centre. The total number Y of target atoms recoiled towards and counted by the detector, assuming 100% detector efficiency, is proportional to the total number of incident projectiles Q, the areal density Nt of the target atoms, where the N is the volume atomic density and t is the sample thickness, and the solid angle $\Delta\Omega$ subtended by the detector [6]

$$Y \propto Q(Nt)\Delta\Omega \qquad [2.3],$$

or

$$Y = Q(Nt)\frac{d\sigma}{d\Omega}\Delta\Omega \qquad [2.4],$$

where the constant of proportionality is the differential cross section. The recoil yield Y is obtained from the number of counts registered by the detector. The solid angle $\Delta\Omega$ and the number of incident particles Q are not so easily measurable accurately. In practice the solid angle is sometimes determined experimentally through the use of standard samples of known composition and the beam dose is estimated by normalisation with the yield of a known major component in a target sample e.g the yield due to a substrate element [7]. Knowledge of the recoil differential cross section of the identified atoms allows for determination of their concentration profiles.

The recoil cross section is determined by the type of interaction potential associated with the collision [3]. For a Coulomb interaction potential, where the collisions are elastic in nature, the elastic recoil cross section, also known as the Rutherford recoil cross section, is given by

$$\left(\frac{d\sigma}{d\Omega}\right)_{recoil} = \left(\frac{Z_1 Z_2 e^2}{2E_o}\right)^2 \left(1+\frac{m_1}{m_2}\right)^2 \frac{1}{\cos^3\Phi} \qquad [2.5],$$

where E_o is given in MeV, $e^2 \approx 1.4398 \times 10^{-13}$ MeV.cm, and $d\sigma/d\Omega$ is in cm^2. Similarly the Rutherford scattering cross section for the incident projectiles is given by

$$\left(\frac{d\sigma}{d\Omega}\right)_{scattered} = \left(\frac{Z_1 Z_2 e^2}{2E_o}\right)^2 \frac{\left(\sqrt{m_2^2 - m_1^2 \sin^2\theta} + m_2 \cos\theta\right)^2}{m_2 \sin^4\theta \sqrt{m_2^2 - m_1^2 \sin^2\theta}} \quad [2.6].$$

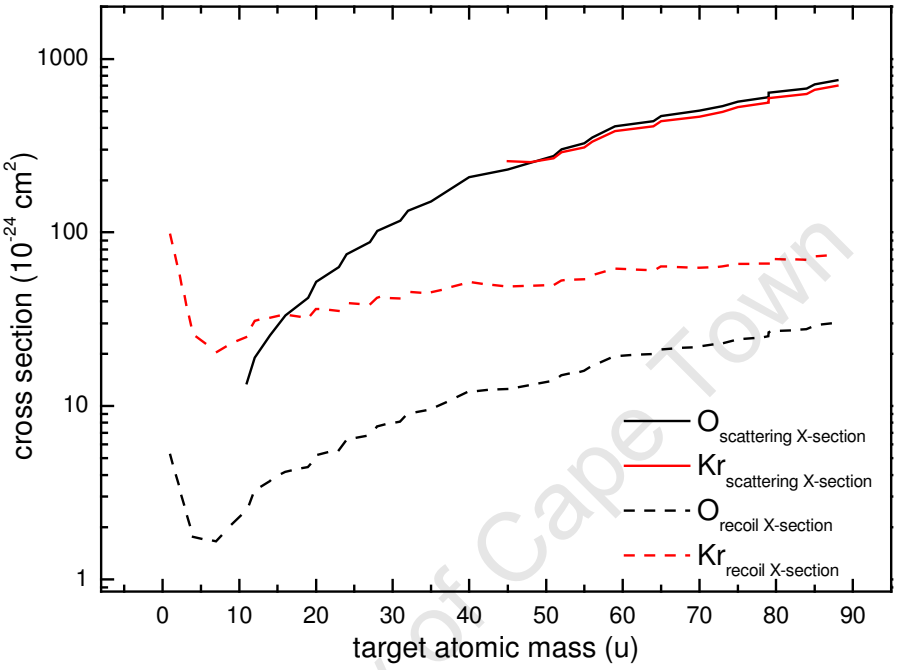

Figure 2.2 Calculated variation of recoil/scattering cross sections with projectile/target mass for ^{18}O and ^{84}Kr incident beams at 0.33 MeV/u incident beam energy.

The plots in Fig. 2.2 show the variation of the recoil cross section and the scattering cross section with target mass, again for each of the ^{18}O and ^{84}Kr projectile beams chosen for the purposes of illustration. The calculations, based on equations 2.5 and 2.6, assume the energy of each incident beam to be 0.33 MeV/u, the typical beam energy of ions from the iThemba LABS SPC2 cyclotron. The scattering/recoil angle is 30°, the fixed angle between the incident beam path and the ToF detector telescope.

It can be seen from Fig. 2.2 that the scattering cross section is generally much higher than the recoil cross section for any given projectile-target ion combination. However careful choice of incident beam for a given geometry and target can limit this apparent setback.

The plots in Fig. 2.2 can help explain the general choice of heavy incident projectiles over lighter ones in HI-ERDA, in instances where possible. Firstly, the recoil cross section is higher for heavier projectiles, and secondly it varies much less with target mass than it does for lighter projectiles. Additionally, as already pointed out, ^{18}O ions as the incident ions would lead to serious interference from the incident beam scattered into the detector system by target atoms of mass $m_2 \geq 11$, whereas for ^{84}Kr projectiles the interference would only become significant for target masses $m_2 \geq 40$.

Deviation from the Rutherford scattering cross section occurs at low incident beam energies when the screening by orbital electrons cannot be neglected and the projectile-target interaction involves the screened potential. Anderson and co-workers [8] reviewed the energies at which this deviation occurs and these are now fairly well known. Deviation also occurs at the high-energy side when the distance of closest approach of the nuclei is within the range of nuclear forces and the interaction potential is no longer a simple Coulomb potential. Bozoian *et al* [9] have determined the energies at which nuclear force field effects become significant.

2.2.3 Energy loss

Depth analysis in ion beam analytical techniques follows directly from the energy lost by the projectile and the target atoms traversing the target sample [10]. In RBS for example, the energy loss of the projectile ion as it enters and exits the target sample gives the location of the scattering atom below the surface, whereas in ERDA it is the total energy lost by the projectile ion as it enters and the recoil atom as it exits the target sample that gives a similar indication. In ERDA the correlation between the measured energy and the depth from which a recoil atom emerges can be inferred from a simplistic *projectile - target* ion collision schematic like in Fig. 2.3 below.

In the figure the incoming projectile enters the sample at a grazing angle to the surface and loses energy as it traverses the sample along path r_{in}. At a depth x it is scattered off at an angle Φ degrees to the incidence direction and imparts energy to the recoil which also loses

part (or all) of that energy as it emerges out of the sample along path r_{out}. The residual energy that the detector measures is given by

$$E_x = K\left[E_0 - \int_0^{x/\sin\beta} S_p(r)dr\right] - \int_0^{x/\sin(\Phi-\beta)} S_{rec}(r)dr \qquad [2.7]$$

where $S_p(r)$ and $S_{rec}(r)$ are the stopping powers for the projectile ion and for the recoil atom, respectively [4]. The first term in parenthesis gives the projectile residual energy just before the collision and the second term gives the energy loss of the recoil as it emerges out of the sample.

The stopping power of matter for ion beams is the key quantity to converting energy into depth information because by definition,

$$\frac{\Delta E}{\Delta x}_{\lim \Delta x \to 0} = \frac{\delta E}{\delta x} = S \qquad [2.8],$$

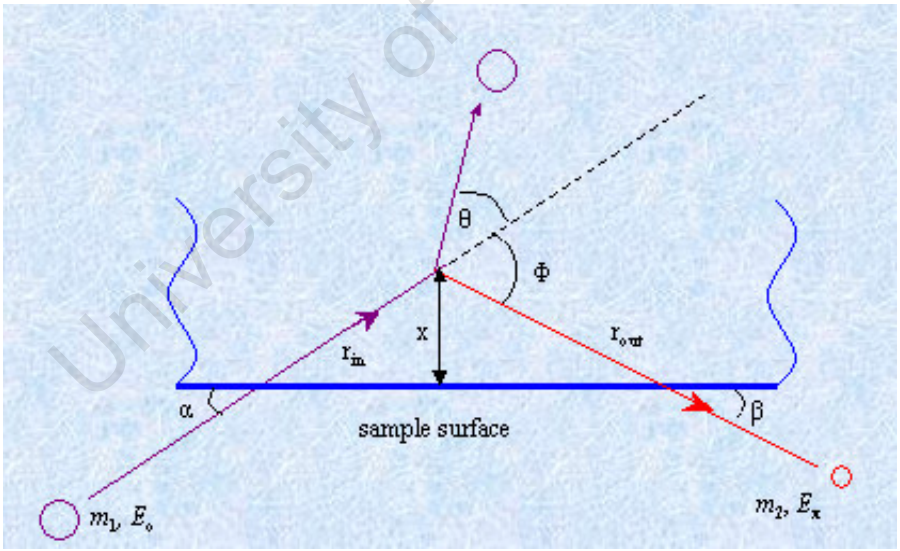

Figure 2.3 A schematic showing the projectile-recoil scattering process. A projectile of mass m_1 and energy E_o collides with a target atom of mass m_2 at a depth x and the latter emerges out of the sample with an energy E_x at an angle Φ to the incidence direction.

where δE is the ion energy loss and δx is the distance traversed. This equation also relates the minimum analysable depth, the depth resolution Δx, to the minimum discernible energy, the energy resolution ΔE.

The stopping power depends on the nature of the interaction between the projectile ions and the target atom nuclei and electrons. This interaction in turn depends on the energy of the incoming ions [11]. Numerous theoretical studies have been carried out over decades to attempt to calculate stopping powers from first principles for any projectile – target combination over a wide energy range. Stopping powers of many elemental targets (and relatively fewer compound targets) for hydrogen and helium ion beams, have been measured in many experimental studies, spanning several decades [12]. Based on available experimental data and theoretical calculations Ziegler *et al* devised a semi empirical parameterisation (ZBL parameterisation) method that can be used to estimate the stopping power for every ion in every material [11]. Their method has become the prime source of stopping power data for many ion beam analysis techniques through the simulation code SRIM [13]. Though largely accurate for hydrogen and helium stopping powers, the inaccuracy of the ZBL parameterisation can be as high as 10 – 20% for heavier ions [14-17]. The experimental determination of the stopping powers of materials for ion beams other than hydrogen and helium is an active and robust field of research [14-17]. Chapter 5 of this thesis details measurements carried out to provide new experimental data in this ongoing field.

2.3 Physical limitations in HI – ERDA

2.3.1 Introduction

The theoretical concepts discussed in the preceding section are not without limitations when it comes to practical implementation. Jeynes and Barradas [in ref 7] describe a whole host of pitfalls in ion beam analysis, and suggest ways of avoiding them or reducing their effects. Problems requiring careful consideration in IBA practice range from issues concerning accurate measurement of the incident beam dose (Q) and solid angle (Ω), to

scattering cross section (σ) evaluation and uncertainties in stopping powers. All of which have an effect on the determination of the concentration depth profiles of atomic species in a sample.

An additional problem for quantification, especially characteristic of HI-ERDA, is the loss of thin film atoms through ballistic effects during measurement [3]. This effect is largely dependent on the combination of beam type, energy and dose, and the nature of the film under analysis. For example Trocellier and co-workers [18] report of degradation in the composition of a Kapton (polymide film) after bombardment with 50 MeV ^{32}S ions to fluences ranging from $2.8x10^{13}$ to $1.3x10^{14}$ ions/cm^2. The degradation is attributed to a redistribution and loss of ^{12}C, ^{14}N and ^{16}O atoms in the polymer due to low binding energies characteristic of polymeric materials. In contrast, Whitlow and co-workers report observing statistically insignificant changes in the stoichiometry of SiO_2/Si sample structures bombarded by 48 MeV ^{81}Br ions up to a fluence of $2x10^{14}$ ions/cm^2 [19]. What these examples simply point out then is that, when analysing polymeric materials for instance, a compromise has to be made between beam dose and getting enough statistical data.

Arguably the source of greatest concern in HI – ERDA (or any ion beam analysis technique), is the accuracy in the measurement of the energy of recoils (scattered beam). The amount of spread in the recoil energy, the total energy resolution, has a direct effect on the accuracy of calculated concentration profiles. An inaccurately measured recoil energy inevitably assumes a wrong collision energy, which affects the recoil cross section used in yield calculation. The depth resolution is also a direct consequence of the energy spread through the energy loss factor. In energy dispersive spectrometry, the degree of mass separation, can be limited by the measured energy spread. It is therefore important that the various factors contributing to the total energy resolution are well understood and accounted for in the analysis of experimental data. These factors, generally categorised as either extrinsic or intrinsic [10] are discussed below.

2.3.2 Extrinsic factors

Extrinsic factors affecting the total energy resolution are those that are due to the experimental set up. These include detector energy resolution, projectile beam energy spread, beam divergence, detection solid angle and, in conventional ERDA, energy spread through the stopper foil.

The energy resolution of the detector system, which in practice is the dominant contributor to the total energy resolution, can be measured using mono-energetic particles from radioactive sources or well-defined beam energies. The beam energy calibration and energy spread can be determined through known narrow resonance reactions. With improvements in accelerator technology the beam energy spread in most of today's accelerators is much less than the detector resolution and so is not a crucial factor in data analysis [7]. The beam optics of the accelerator should be optimised to keep beam divergence as minimal as possible.

With regards to the effect of the solid angle, the finite beam spot size d and the detector aperture w determine what is referred to as geometrical straggling $\Delta\beta$, the spread in the exit angle β of the recoils [5];

$$(\Delta\beta)^2 = \left(\frac{g_d w}{L_D}\right)^2 + \left(\frac{g_b d \sin\beta}{L_D \sin\alpha}\right)^2 \qquad [2.9],$$

which creates an uncertainty in the scattering angle Φ thereby inducing a geometrical contribution ΔE_{geom} to the total energy spread

$$\Delta E_{geom} = E_o \frac{\partial K}{\partial \Phi} \Delta\Phi \qquad [2.10].$$

From the schematic shown in Figure 2.3, $\Phi = \alpha + \beta$, and so $\Delta\Phi = \Delta\beta$ since α is fixed. L_D is the distance between the target and the detector aperture, and the factors g_d and g_b take into account the shape of the beam and the detector aperture. E_o is the incident beam energy and K is the recoil kinematic factor defined in Equation 2.1.

Long target – detector distances and small apertures limit somewhat the degree of geometric (also known as kinematic) energy spread but at a cost of long counting times

which may lead to beam damage. As a result large solid angle specialised position sensitive detectors that allow for kinematic correction have been developed in some IBA labs [20, 21]. In some instances though, the geometrical configuration of the detector system, such as the one adopted in this work [see section 3.3], inherently corrects for kinematic shift without need for position information.

In conventional ERDA, where a stopper foil is employed, an accurate determination of the energy loss through the foil requires that the foil thickness be uniform. Unevenness in the thickness of the foil can be the single most important contributor to energy resolution [22]. Common practice is that Mylar and other polymers are used for stopper foils because of their superior thickness uniformity. In ToF-ERDA employing carbon foil based timing detectors, thick foils and (or) uneven foils foil have an effect of degrading the energy resolution, though generally much smaller than the intrinsic resolution of the detector system.

2.3.3 Intrinsic factors

Intrinsic factors are those due to the nature of the target itself and are not so easily determinable, further complicating spectra analysis. The main target related contributors to total energy spread include energy straggling, multiple and plural scattering and sample roughness [10].

Energy straggling is a consequence of the statistical nature of the collision processes between the projectile and target atoms. The number and frequency of collisions varies for each projectile ion resulting in the energy spread of an initially mono-energetic beam of incident projectiles. Bohr in 1915 used a classical model to derive a simple expression to estimate straggling in thin films [1]. For a layer of thickness Δx, Bohr straggling Ω_B is given by

$$\Omega_B^2 = 4\pi\left(Z_1 e^2\right)^2 N Z_2 \Delta x \qquad [2.11],$$

where Z_1, Z_2 are the projectile and target ion atomic numbers respectively and N is the atomic density of the target material. Bohr's formula assumes that individual energy transfers take place between free stationary electrons and the fully ionised projectile of charge Z_1e. This assumption is only valid in the high-energy limit region where the ion velocity v is much greater than the Bohr velocity ($v>>v_o$). Several improvements, detailed in texts by Chu et al [1] and Tirira et al [3], have been made to this simple model by a number of authors to extend the energy range over which the model is valid to include low- and medium-projectile ion energies. One of these developments is a fitting procedure by Yang et al [23] for experimental straggling data to a model developed by Chu [24]. In Chu's modification of Bohr's formular, energy straggling is not regarded as independent of the projectile ion energy;

$$\Omega^2_{Chu} = H\left\{ E/M_1 , Z_2 \right\}\Omega^2_B \qquad [2.12],$$

where H is a correction factor, which takes into account deviations from Bohr straggling caused by electron binding in the target atoms. Yang's empirical procedure takes into account charge state fluctuations resulting in the following expression for energy straggling;

$$\frac{\Omega^2_{Yang}}{\Omega^2_B} = \gamma^2\left(Z_1, Z_2, v\right)\frac{\Omega^2_{Chu}}{\Omega^2_B} + \frac{\Delta\Omega^2}{\Omega^2_B} \qquad [2.13],$$

where $\gamma(Z_1, Z_2, v)$ is the effective charge factor for ions in matter, v the projectile ion velocity, and $\Delta\Omega^2$ is the additional straggling due to correlation effects.

Multiple scattering refers to the deviation of projectile and recoil ions from straight-line trajectories due to small-angle scattering events resulting from multiple nuclear collisions. The energy of the incident ions changes because of the different path lengths, and the energy of the emitted particle depends on the reaction angle. These effects increase with path length and they are subject to fluctuations. Compared to energy straggling, the contribution of multiple scattering to total energy spread in ERDA is much greater due to angular sensitivity of ERDA kinematics [25]. In addition to small angle scattering events there may also be one or more large angle scattering events before recoil/projectile ions are scattered towards the detector. This is called plural scattering. The combined effects of these types of collisions on energy spectra include broadening and tailing of the low energy

edge and the emergence of a low energy background [26], both of which the analyst should be aware of during data analysis.

Sample roughness is another target related problem that contributes to the energy spread. This is particularly true for ERDA with heavy ions at an oblique scattering geometry. Path differences are increased and as a result recoil energies from a given depth are dispersed. In the elemental energy spectra this shows up as tailing of peaks towards low energies and reduced yield at high energies [27]. In multilayer structures with rough interfaces energy peaks due to deep lying layers are broadened [28]. Both these effects are enhanced if the degree of roughness is comparable to the analytical depth. Fortunately for the ion beam analyst some of the latest ion beam analysis codes, discussed in the next section, have in-built algorithms to describe and account for the effects of roughness in experimental energy spectra.

2.4 Ion beam analysis software

Quite often the object of ion beam analysis is to provide a quantitative depth profile of a sample structure. Using ERD spectrometry as an example, in an idealised experimental situation, an incident ion slows down in a straight line path as it traverses the target and in a collision at a certain depth produces a recoil that moves in a straight line from the point of collision out of the sample surface to the energy detector(s). The depth of collision is a function of the incident and exit energies and the effective stopping power as described by Equation 2.7. From the yield *vs* energy spectrum quantification of atomic concentrations at each given depth requires knowledge of recoil cross sections, which, for pure Coulomb scattering can be calculated analytically according to Equation 2.5. In principle then, for this idealised sequence of events, the sample structure can be calculated from the energy spectra of recoils coming out of the sample. In reality though practical limitations and energy spread effects described in the preceding section lead to a forced departure from this simplified treatment of events.

Computer programs have since been developed over the years to aid ion beam practitioners with the analysis and interpretation of experimental spectra. These can be broadly classified into two categories. The first category encompasses codes that calculate concentration profiles *directly* from experimental energy spectra using modified analytical calculations (e.g screened Rutherford cross sections). The second category (mainstream codes are in this group) includes codes that tackle the problem from an opposite viewpoint; a hypothetical sample structure is assumed and a theoretical energy spectrum calculated either analytically or by Monte Carlo (MC) methods and compared with the experimental one. This sample structure is altered until a best fit is obtained between the simulated and the experimental spectra. The two approaches are now described a bit further using three of the software programs used in this work as examples; starting with KONZERD [29] which typifies direct calculation methods, and then SIMNRA [30] and CORTEO [31] two of the most common analytical and MC-based analysis codes, respectively. The discussion looks at these codes from the viewpoint of analysis of ERDA and RBS data.

2.4.1 Direct profile extraction

Direct conversion methods implemented in programs such as KONZERD [29] are particularly possible where the different elemental contributions to the total spectrum can be separated. A case in point is Heavy Ion - ERDA with a mass dispersive detector system like the one developed in this work. KONZERD employs a method known as slab analysis, where a sample structure is divided into a large number of slabs of equal thickness in which sample composition, stopping power and recoil and scattering cross sections are all assumed to be constant across each slab, but varying from slab to slab.

Starting from the surface an arbitrary elemental composition is assumed in the first slab layer and an energy bin corresponding to the slab thickness calculated for each detected recoil species using a form of Equation 2.7. In the calculation Bragg's additivity rule is used to determine effective stopping powers using the assumed proportions of the different elements present in the slab layer. The experimental yield for each ion species within this calculated energy bin is then used to calculate new values of the elemental concentrations in

the same slab layer using Rutherford cross sections. The new concentrations are then used to re-do the calculation from the beginning. This procedure is repeated until convergence to self-consistent concentration values and then the whole process is repeated for all the subsequent slabs. In this way the concentration profiles are calculated directly.

One advantage of this method is that it is unlikely to generate more information about the sample than the data actually contain, which cannot be said of the simulation-fitting programs. Its main drawback is that the profiles derived are, strictly speaking, not real concentration depth profiles since they still have the energy resolution convoluted and so one has to live with the limited depth resolution given by the experimental and sample conditions [32].

2.4.2 Iterative simulation approach

Spectrum simulation programs use analytical functions to convolute the ideal energy spectrum so as to take into account most of the physical limitations described in section 2.3. The same slab analysis methodology as in direct computation is also used, with the main difference that in this case it is the spectrum shape that is approximated for each slab layer. In SIMNRA for example the simulated spectrum *H(E)* is made up of the superimposed contributions from each element in each sublayer of the target [30],

$$H(E)=\int_0^{\infty} H_o(E')f\left(E',\sigma^2(E')\right)dE' \qquad [2.14],$$

where $H_o(E')$ is the calculated energy spectrum before convolution with a Gaussian function $f\left(E',\sigma^2(E')\right)$, which accounts for energy spread contributions due to the detector resolution and sample related energy spread effects.

SIMNRA is one of the most common and latest analytical simulation codes developed in the 90's placing emphasis on implementing advanced physics and experimental conditions [32]. Energy loss straggling is approximated by any of Bohr, Yang or Chu and Yang's models during spectrum analysis [see Equations 2.11 – 2.13]. Geometrical energy spread is accounted for through Equations 2.9 and 2.10.

Energy spread induced by multiple scattering is modelled by the Szilagi/Amsel theory [33], initially proposed by Sigmund and Winterbon [34]. The latter first derived a formula to calculate multiple scattering angular spread through a classical approach to the single scattering cross section. Their theoretical formulation is however applicable only to single elemental targets, without considering the effect of ion stopping. Szilàgy et al [33] have since extended the original Sigmund theory to multielemental targets and to include ion stopping. In SIMNRA the main approximations made in the calculation of multiple scattering effects is that the energy spread distributions are treated as Gaussian functions and low energy tails are ignored [30].

To account for sample roughness effects the approach in SIMNRA is to approximate the energy spectra of rough films by a superposition of partial spectra from an ensemble of layers with different thicknesses. The layer thickness variation is described by a Gamma function.

MC-based codes such as MCERD [35], CORTEO [31] and FTHIE [36] stand apart from the deterministic simulation codes in the sense that MC methods principally include all the important phenomena involved in ion-target interactions. By following individual ion trajectories complex physical processes such as multiple scattering and the interaction between ions and the detector system are taken into account in a natural way, without the approximations that standard codes involve [37].

A different kind of approximations is made though to describe the nature of interaction between the incident and target ions. Firstly, the binary collision approximation states that the collision between two ions is characterised by the force between those two particles; any other force external to the two ions is negligible. Secondly, the interaction potential between colliding nuclei is assumed to be Coulombic in nature, with allowances for screening corrections (e.g Anderson screening). And, thirdly, the distribution of target ions is assumed to be random, the so called random phase approximation, and can be described by Poisson statistics as opposed to a potentially lengthy deterministic computation of the coordinates of the next collision partner in a crystalline structure [31]. The computations

involved can unfortunately be quite taxing in terms of time required to generate sufficient statistics.

CORTEO is a recently developed MC analysis program designed to improve computation speed by making further approximations. Firstly, the computation follows only those ions that might eventually get detected by deliberately generating recoils from all target depths only within a cone angle towards the detector. Secondly, the idea of a virtual detector several times larger than the real detector improves detection efficiency as trajectories of recoils falling outside the real detector area are corrected to reach the real detector [35]. A third improvement is the presentation of scattering angle components, stopping powers and energy straggling values used in the computation of trajectories, in the form of tabulated functions and indexed using the binary representation of floating point numbers [31]. This facilitates fast access to these values without having to evaluate trigonometric, inverse or transcendental functions, reducing simulation times to generally less than one minute for a modern (>1.6 GHz processor) desktop computer.

In conclusion, the accuracy of ion beam analysis codes is limited by the accuracy of the models applied, the accuracy of the fundamental databases used for cross sections and stopping powers and the accuracy with which the experimental parameters are known [7], all of which must be carefully considered during error analysis. Differences in many of the simulation codes lie mainly in the analytical functions and algorithms implemented to account for energy spread effects. Table A1 [taken from ref 37] in Appendix A lists some of the major simulation codes in use in the IBA community characterised by the fundamental physics handled in the simulations.

2.5 References

1. Chu W. K., Mayer J. W. and Nicolet M. *Backscattering Spectrometry* (1978), *Academic Press, New York.*
2. Bird J. R. and William J. S., *Ion Beams for Materials Analysis* (1989), *Academic Press, San Diego, CA.*
3. Tirira J, Serruys Y and Trocellier P, *Forward Recoil Spectrometry – Applications to hydrogen determination in solids* (1996) *Plenum Press, New York.*
4. Arnold-Bik W.M and Habraken F.H.P.M (1993) *Rep. Prog. Phys.* **56** 859.
5. Kim J. K. et al (1998) *Nucl. Instr. and Meth.* **B140** 380.
6. Rauhala E., Ion backscattering and Elastic Recoil Detection in *Chemical Analysis by Nuclear Methods* (1994) *John Wiley and Sons Ltd.*
7. Jeynes C. and Barradas N. P. (2009), in *Handbook of Modern Ion Beam Materials Analysis*, Editors: Wang Y. and Nastasi M., MRS, Warrendale, Pennsylvania
8. Andersen H. H. *et al* (1980) *Phys. Rev. A21, 1891.*
9. Bozonian M., Hubbard K. M and Nastasi M (1990) *Nucl. Instr. and Meth.* **B50** 291.
10. Szilàgyi E. (2001) *Nucl. Instr. and Meth.* **B183** 25.
11. Ziegler J. F., Biersack J. P and Littmark U. *The Stopping and Range of Ions in Solids* Vol 1 of *The stopping and Ranges of Ions in Matter* (1985), Pergamon Press, New York.
12. Rauhala E. and Ziegler J. F. (2009), in *Handbook of Modern Ion Beam Materials Analysis*, Editors: Wang Y. and Nastasi M., MRS, Warrendale, Pennsylvania
13. J. F. Ziegler, SRIM-2008, http://www.srim.org
14. Harikumar V. *et al* (1997) *Nucl. Instr. and Meth.* **B129** 143.
15. Trzaska W. H. *et al* (2001) *Nucl. Instr. and Meth.* **B183** 203.
16. Zhang Y. and Possnert G (2002) *Appl. Phys. Lett.* **80** 24 p4662.
17. Helmut P. (2007) *Nucl. Instr. and Meth.* **B261** 1176.
18. Trocellier P. *et al* (1991) *Nucl. Instr. and Meth.* **B54** 118.
19. Whitlow H. J., Andersson A. B. and Petersson C. S., (1989) *Nucl. Instr. and Meth.* **B36** 53.

20. Gebauer B., Fink D., Goppelt P., Wilpert M. and Wilpert T., (1990) *Nucl. Instr. and Meth.* **B 50** 159
21. Bohne W., Röhrich J. and Röschert G. (1998) *Nucl. Instr. and Meth.* **B139 219**.
22. Dollinger G. and Bergmaier A. (2009), in *Handbook of Modern Ion Beam Materials Analysis*, Editors: Wang Y. and Nastasi M., MRS, Warrendale, Pennsylvania
23. Yang Q., O`Connor D. J. and Wang Z (1991) *Nucl. Instr. and Meth.* **B61** 149.
24. Chu W. K. (1976) Phys. Rev. **A13** 2057.
25. Wielunski L. S., Szilagyi E. and Harding G. L. (1998) *Nucl. Instr. and Meth.* **B136 – 138** 713.
26. Bauer P., Steinbauer E and Biersack J. P. (1993) *Nucl. Instr. and Meth.***79** 443.
27. Yesil I. M., Assmann W., Huber H. and Löbner K. E. G., *Nucl. Instr. and Meth.* **B 136 - 138** (1998) 623.
28. Sajavaara T. et al (2000), *Nucl. Instr. and Meth.* **B161-163** 235.
29. Bergmaier A., Dollinger G. and Frey C. M., *Nucl. Instr. and Meth.* **B 99** (1995) 488.
30. Mayer M., *SIMNRA User's Guide*, Technical Report IPP9/113, Max – Planck Institut für Plasmaphysik, Garching, Germany, (1997).
31. Schiettekatte F (2008), *Nucl. Instr. and Meth.* **B266** 1880.
32. Rauhala E., Barradas N. P., Fazinic S., Mayer M., Szilágyi E. and Thompson M., *Nucl. Instr. and Meth.* **B 244** (2006) 436.
33. Szilàgyi E., Pàszti F and Amsel G. (1995) *Nucl. Instr. and Meth.* **B100** 103.
34. Sigmund P and Winterbon K. B. (1974) *Nucl. Instr. and Meth.***119** 541.
35. Arstila K., Sajavaara T and Keinonen J. (2001) *Nucl. Instr. and Meth.* **B174** 163.
36. Franich R.D., Johnston P. N., and Bubb I. F. (2004), *Nucl. Instr. and Meth.* **B 219-220** 87.
37. Barradas N. P. and Rauhala E. (2009), in *Handbook of Modern Ion Beam Materials Analysis*, Editors: Wang Y. and Nastasi M., MRS, Warrendale, Pennsylvania.

Chapter 3

Development of the ToF- Energy spectrometer

3.1 Introduction

The design and construction of the Time of Flight – Energy (ToF – E) detector system is an in-house exercise in most HI – ERDA laboratories [1 - 5]. This is in part due to the fragility of some of the components of the timing detectors, described in the following sub sections. Add to that, the developmental process invariably goes through several cycles of trial and error before all the detector components fit in and perform reproducibly together. Chapter 3 begins by describing the HI – ERDA end station where the final version of ToF – E spectrometer used in this work was installed. A description of the spectrometer follows, detailing its construction and the response of its timing detectors to particles from radioactive sources. This is followed by a rundown of the signal processing electronics and the data acquisition system, and immediately thereafter, a preliminary assessment of the timing resolution of the whole system. Finally, the results of more comprehensive characterisation measurements using ion beams from the accelerator are presented and discussed.

Figure 3.1 shows a plan view of a section of the cyclotron complex at iThemba LABS where the HI-ERDA set up was installed. The two solid pole injector cyclotrons SPC1 and SPC2 are shown to the left of the main cyclotron, a separated sector cyclotron SSC, (not shown in the plan for clarity). Beam from the SSC is distributed to three major users, namely radioisotope production, radiation therapy and nuclear physics experiments. The HI – ERDA end station was installed on a beam line, the K-Line, extending from the main beam line coming from the SPC2 cyclotron, where a wide range of ions, from protons to xenon can be produced. The SPC2 pre-accelerates polarised protons and heavy ions from an electron cyclotron resonance (ECR) ion source before they are further accelerated in the SSC to much higher energies (e.g. 6 MeV/u Ne^{4+}) for experiments in nuclear physics. The SPC1 pre-

accelerates protons for radioisotope production and proton therapy after further acceleration in the SSC. For the HI – ERDA set up though, the maximum beam energy that could be attained by ions coming out of the SPC2 is about 0.34 MeV/u, limited by the magnetic field in the cyclotron [6].

3.2 The HI – ERDA end station

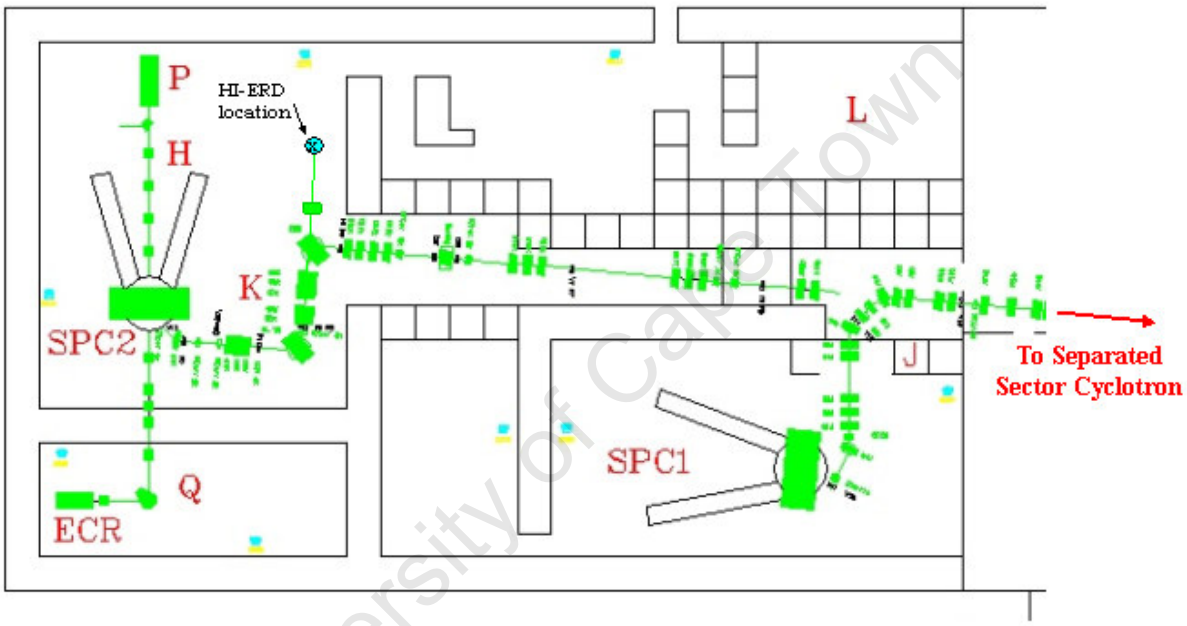

Figure 3.1. A plan view of a section of the iThemba LABS cyclotron complex where the HI-ERDA set up was installed. The location of the HI-ERDA end station is as indicated.

The HI-ERDA chamber was mounted about 3.0 m from a pair of focusing quadruple magnets. A metal rod shaft, onto which a target ladder with samples can be screwed on, was mounted on top of the chamber via a load lock system. The shaft can be moved up and down and can be rotated about the vertical axis. For angular positioning of the target samples with respect to the beam axis, a 0^{o} – 90^{o} calibrated pointer – marker system engraved on the lid at the top of the chamber was used.

The recoil ions(s) flight flange protrudes at an angle of 30° to the incident beam axis. The vacuum system on that section of the beam line where the chamber sits consists of two turbo molecular pumps each backed by a roughing pump. The pressure in the target chamber during measurements was typically in the order of 10^{-7} mbar. A close up of the system set up is pictured in Fig. 3.2, showing a video camera looking into the chamber for target positioning. Figure 3.3 is an engineering drawing showing a broader perspective of the whole set up.

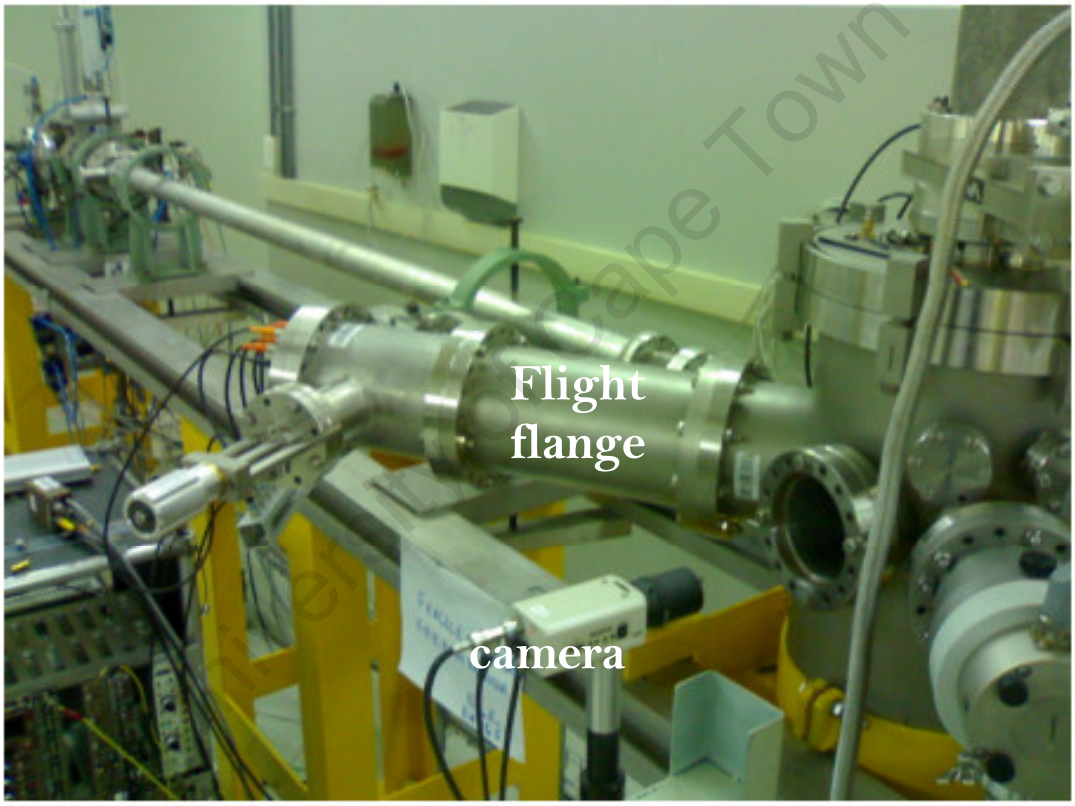

Figure 3.2 The HI-ERDA experimental set up, showing a video camera on the foreground for beam spot viewing and target positioning; and the flight flange protruding at an acute angle to the beam axis.

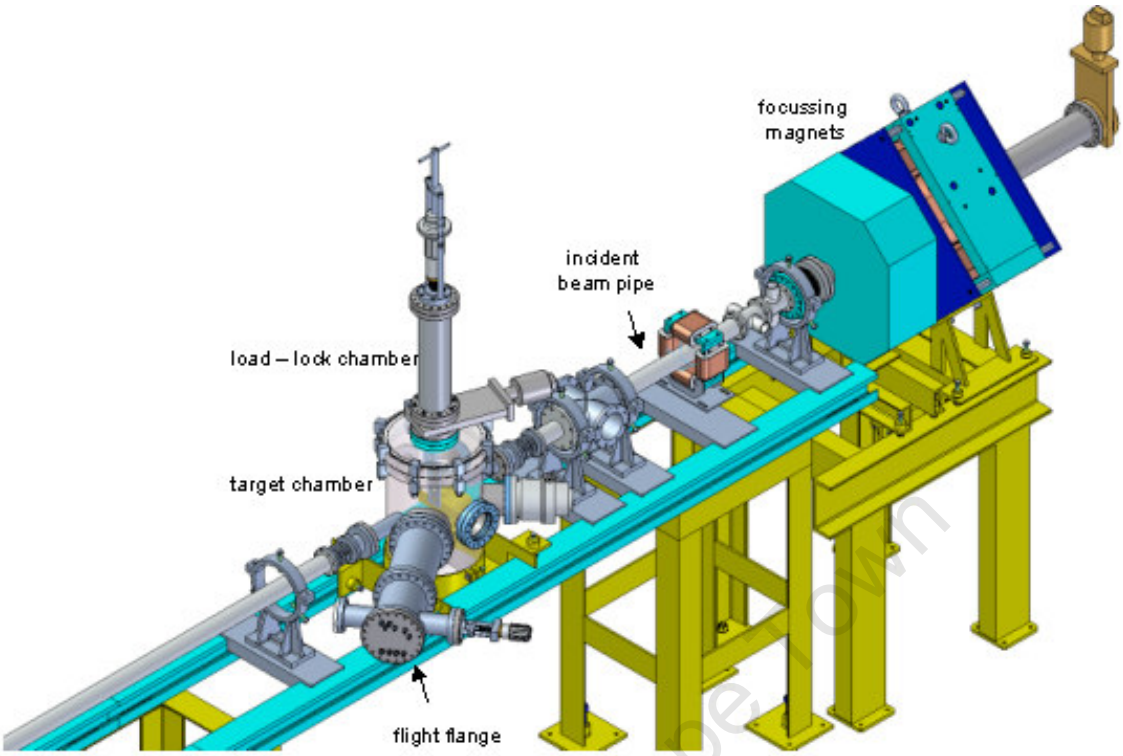

Figure 3.3 An engineering schematic of the HI – ERDA set up

3.2.1 Beam spot

The beam spot could be viewed on a fluorescent wire mesh mounted on the target ladder together with the samples to be analysed. A digital camera connected to a simple monitor was mounted and aimed at the wire mesh through a view port. An estimate of the beam spot size could be obtained by determining the size of the image of the beam spot seen on the monitor screen relative to the size of the image of the wire mesh and then scaling that to the actual wire mesh size. A typical screen image of the beam spot on the mesh is shown in Fig 3.4 below. This is with the viewing lamp turned off.

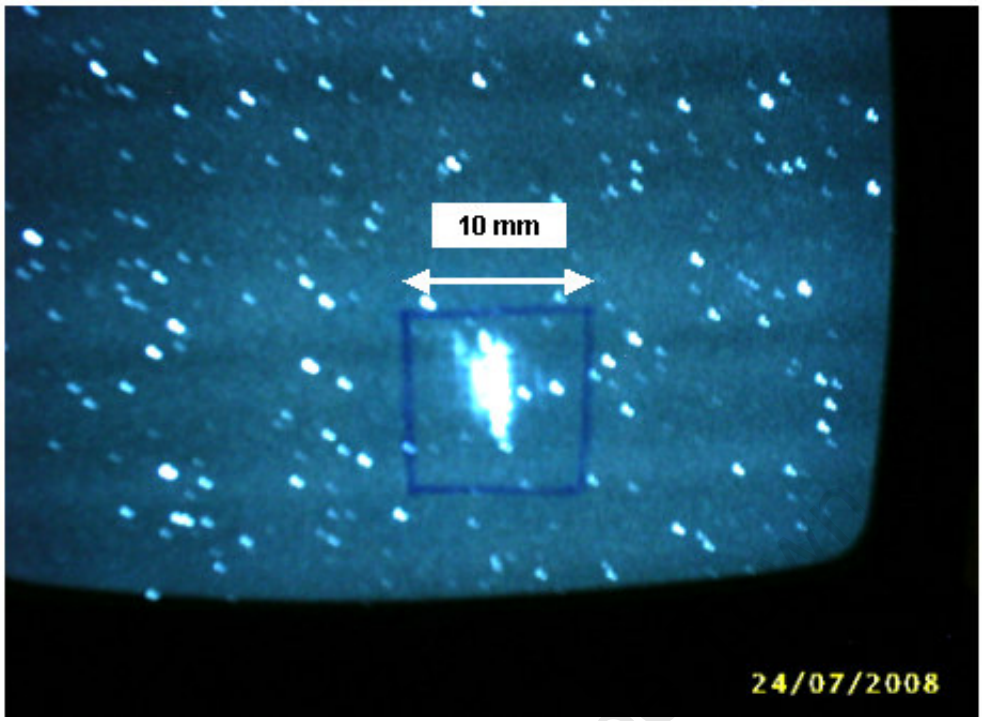

Figure 3.4 The beam spot as seen on a fluorescent wire mesh

The image shown is of a beam spot due to a 27.5 MeV $^{84}Kr^{15+}$ incident beam striking the fluorescent mesh at an angle of 15° to the mesh surface. The best spot obtained in this configuration was rectangular in shape, less than 2.5 mm in the lateral direction. In the vertical though, it could not be cut down to less than 4.0 mm without compromising beam intensity. This however is not expected to affect the kinematics since the scattering angle is mostly affected by the lateral spread of the beam on the target and the solid angle.

3.3 The ToF – Energy spectrometer

The ToF– Energy spectrometer was partly mounted inside the flight flange at an angle of 30° to the incident beam direction. It consists of a ToF detector; built from two tilted timing detectors a flight †distance of 0.584 m apart, and a silicon surface barrier detector (SBD) positioned about 6 cm behind the second time detector for energy measurement (see Figs. 3.5 and 3.6). The first time detector is located inside the target chamber, close to the target, and the second one is towards the end of the flight flange.

† Measurement of the flight distance is described in section 3.6

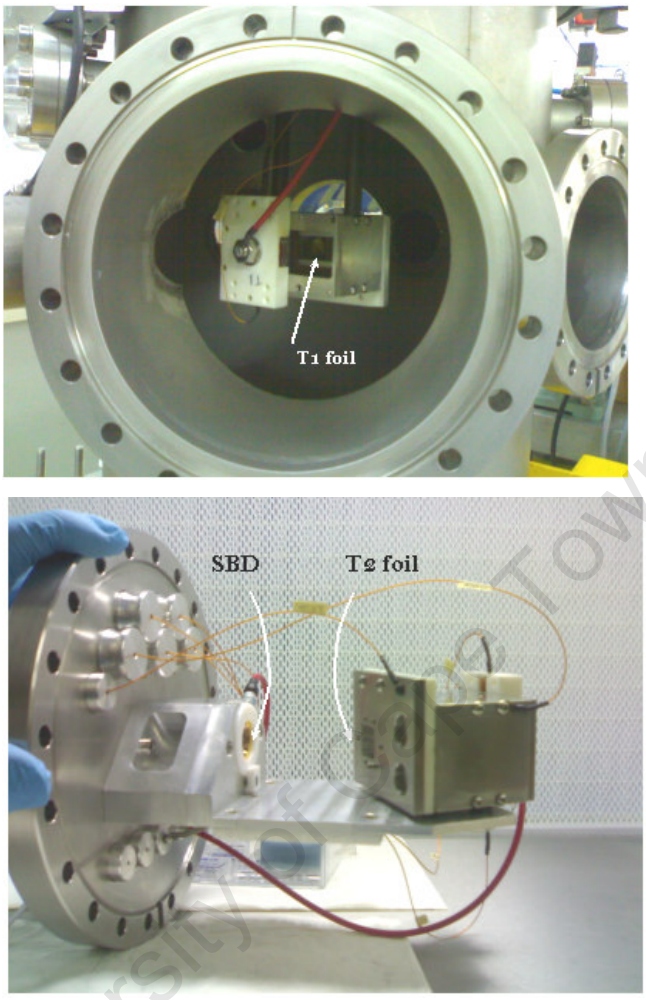

Figure 3.5 Photos of the timing detectors; T1 inside the target chamber (top), and T2 on a flange mounted at the end of the flight tube (bottom).

Each time detector is made up of a ‡9.0 μg cm^{-2} thin carbon foil (T1, T2) mounted 5 cm from a microchannel plate (MCP) chevron assembly. The foils, from ACF® metals, were each mounted on a steel frame with a 96 mm^2 rectangular aperture. The distance between the target and the entrance to T1 is about 0.12 m. A circular collimator of diameter 10 mm that could be routinely inserted halfway between the second time detector and the SB detector limited the solid angle of the detector telescope to about 0.15 msr.

‡ Measurement of the foil thickness is described in chapter 5

Recoil ions passing through each timing detector eject electrons from the foil, and an electric field applied between the carbon foil and a grid structure accelerates and guides the electrons (shown in green in Fig. 3.6) to the MCP assembly, where the electron signal is multiplied to give a timing output signal.

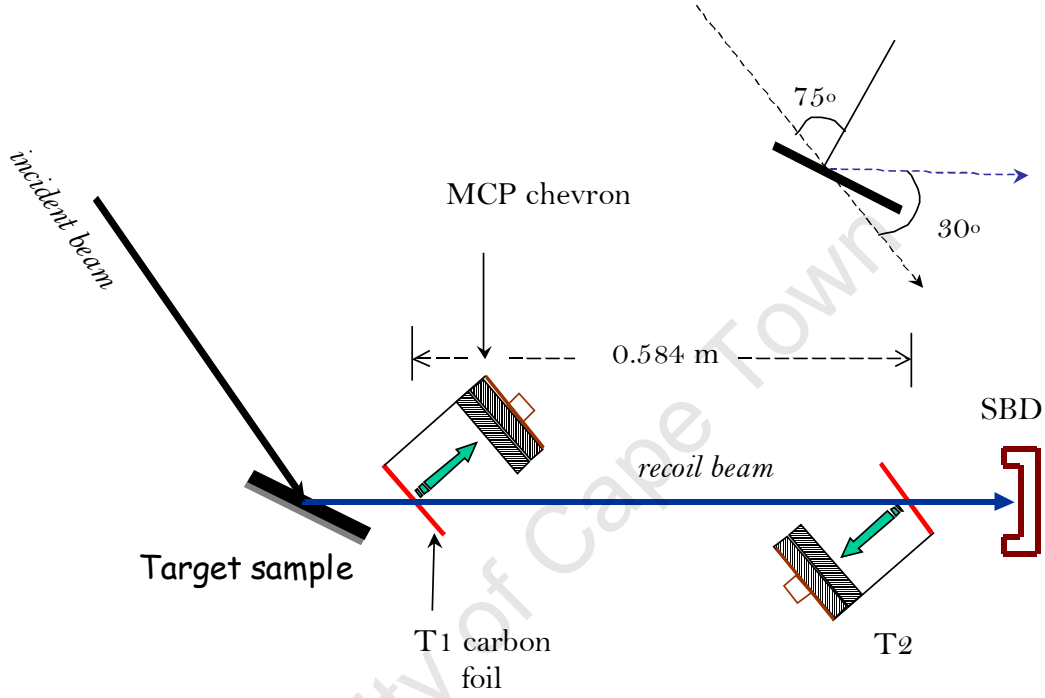

Figure 3.6 A schematic of the ToF – E detector telescope (not to scale), with an inset illustrating the scattering geometry.

A recoil particle passing through the detector system is, depending on the detection efficiency for that particular ion species, detected by the two timing detectors to give the time of flight, and the SBD signal provides both the energy signal and the coincidence trigger between the two timing detectors and the SBD. A more detailed description of the construction of the timing detectors follows in section 3.3.1.

The choice of tilted timing detectors over the other common configuration that employs electrostatic electron mirrors (see Fig 3.7) was informed by two considerations [7]. Firstly, the tilted configuration has only one (and in some cases none [2]) grid structure in the direct path of recoil particles in each timing detector. A grid structure gives rise to non-zero scattering probability of recoils passing through the grid and may limit sensitivity and also

lead to ghost signals due to scattering. Where an electrostatic mirror is used, recoils pass through three grid structures in each timing detector; the double walled mirror and the accelerating grid as illustrated in Fig. 3.7, which makes the scattering probability higher.

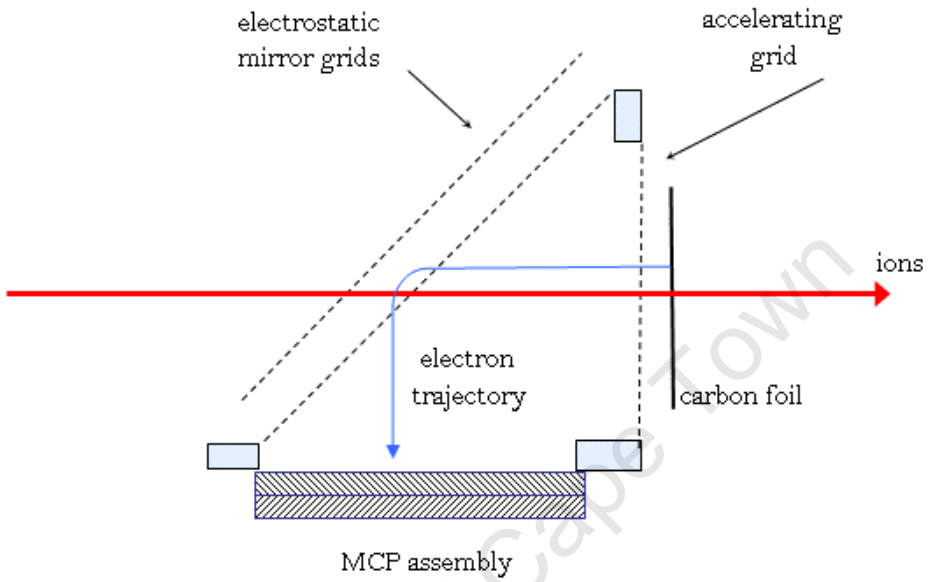

Figure 3.7 A simple schematic of the general configuration of an electrostatic mirror time of flight detector according to Busch *et al* [8].

Secondly, a change $\Delta\Phi$ in the scattering angle due to beam spot size and solid angle leads to a spread in the recoil energy defined in Equation 2.1. This kinematic energy spread in turn leads to a difference in the time of flight of recoils of the same energy, due to differences in flight path lengths. Tilting both time of flight detectors by the scattering angle relative to the recoil beam direction induces a first order kinematic correction [7], in the sense that same energy recoils now travel the same distance between the two timing detectors. This concept is illustrated in the schematic adapted from ref [9] in Fig. 3.8. This intrinsic kinematic correction is absent in other detector configurations and may require specialised detectors in cases where the solid angle is large.

The main drawback of this geometry however is that the effective thickness of the timing foils increases. The effect of this can be minimal though if the thickness of the foils is such

that the effective energy loss straggling of recoils through the foils remains a small fraction (<1%) of the recoil energy.

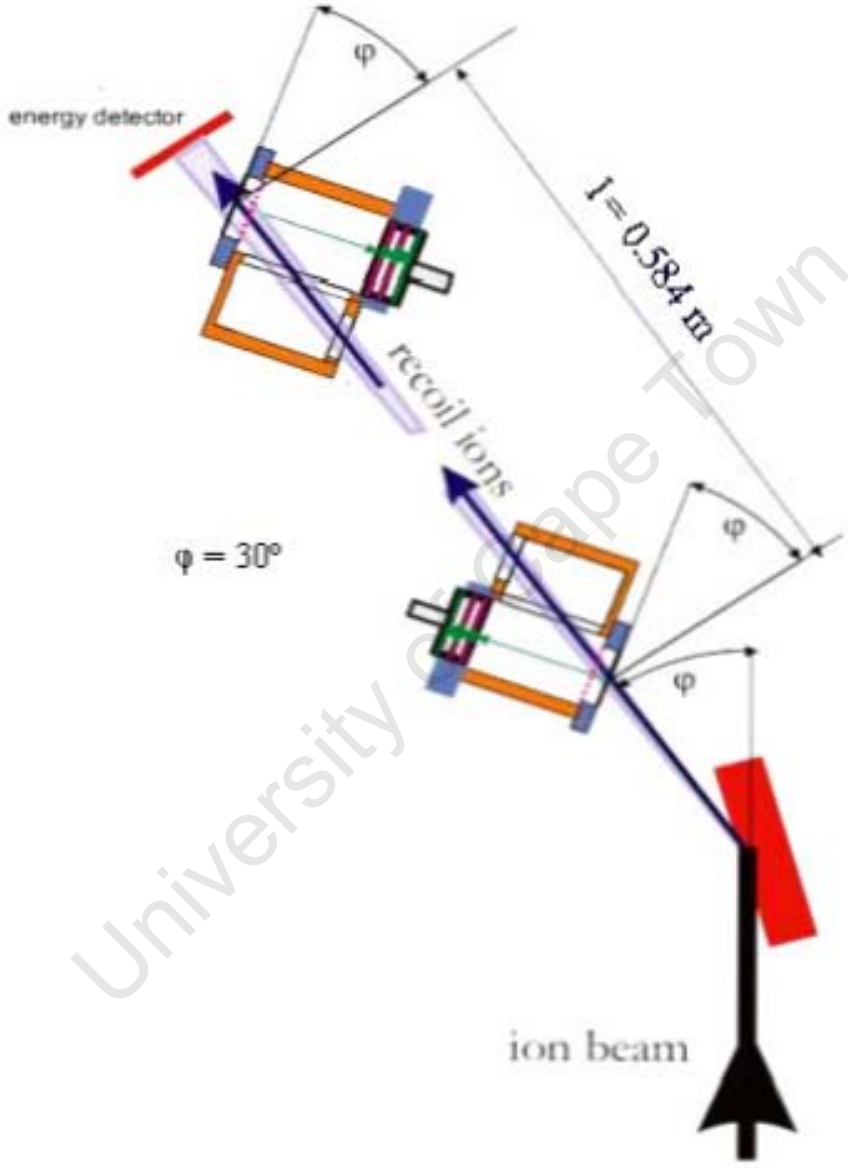

Figure 3.8 Tilted ToF detector configuration designed to correct for kinematic shift to a first order approximation [9].

3.3.1 Timing detector construction

The construction of each detector, whose initial design was by Prof Günther Dollinger [7], is shown in an exploded illustration in Fig. 3.9. A microchannel plate is made up of millions of parallel micro-pores (channels) made of glass, each coated on the inside with an electron rich layer [10]. An electron impinging on the inner walls of a channel creates secondary electrons, which in turn create more electrons, producing an avalanche effect. Drift of the avalanche electrons from one face of the plate to the other is enhanced by a potential difference applied across the plate thickness.

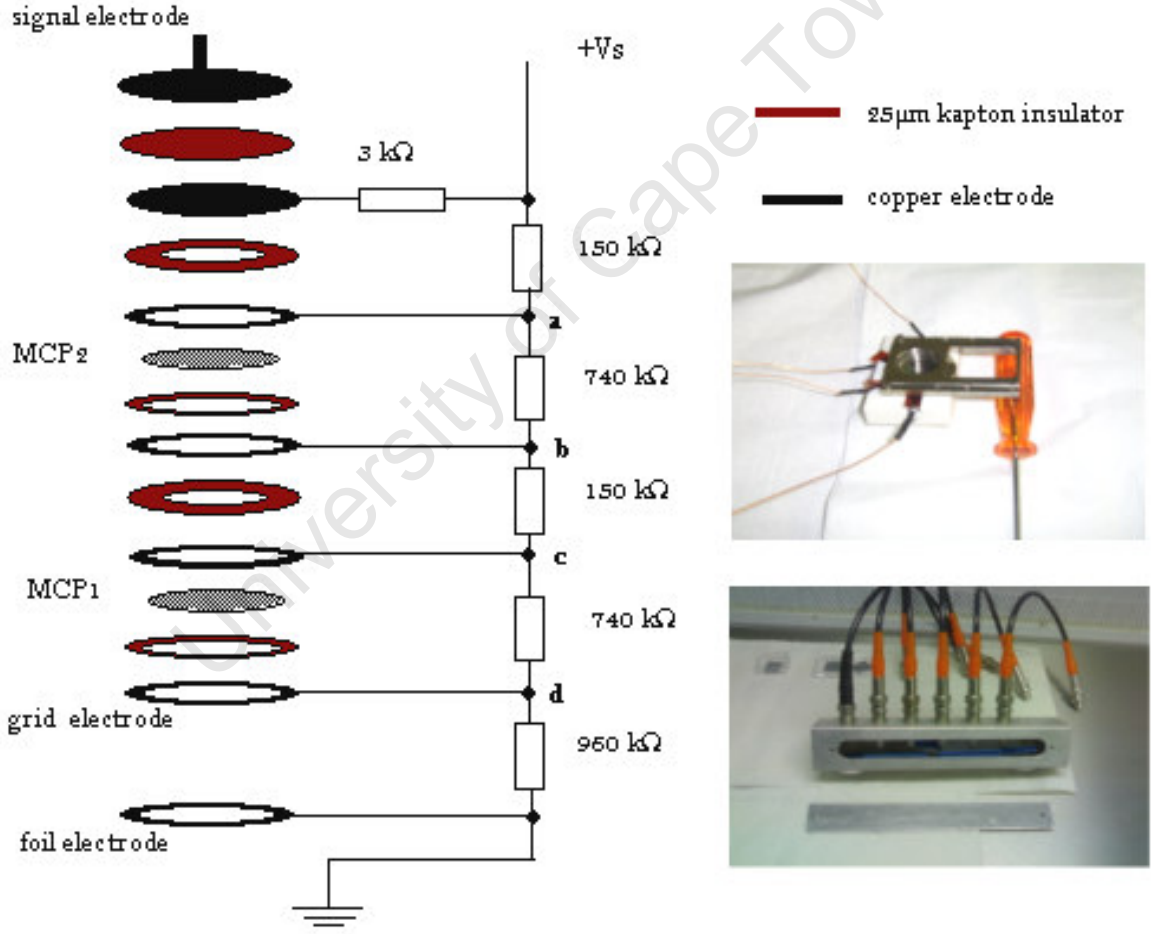

Figure 3.9 An illustrative sketch of the MCP mounting for the timing detectors. The upper picture on the right shows the actual mounting, with vacuum compatible electrode wires that facilitate external connection to a potential divider resistor chain, shown on the bottom picture.

The schematic in Fig 3.9 shows the potential divider network used to apply the bias voltage to a chevron assembly of the two MCPs. The bias electrodes are made of 25 μm thin copper rings that are isolated from each other using 25 μm kapton foil rings. The signal electrode is separated from the bias circuit using a kapton foil disk that serves as the anode capacitor as well.

3.3.2 Bias voltage

The MCP bias voltage for the two timing detectors is from a 0 – 5 kV dual supply unit, with a maximum output current rating of 2 mA. By varying the output voltage from the supply, the voltage drop across the MCPs is also varied. Considering MCP1 in Fig. 3.9, the voltage drop, V_{cd} for a given supply setting V_s, is given by

$$V_{cd} = V_c - V_d = \frac{1700 - 960}{2740} V_s = 0.27 V_s \qquad [3.1],$$

and similarly the voltage drop V_{ab} across MCP2 is given by,

$$V_{ab} = V_a - V_b = \frac{2590 - 1850}{2740} V_s = 0.27 V_s \qquad [3.2].$$

At the maximum supply voltage of 5 kV the bias across each MCP would then be 1350 V with a supply current of 1.82 mA. The current limit of the power supply unit is 2 mA. In the experiments carried out the maximum supply voltage was never reached because the rating of the MCPs used was 1200 V.

In the initial design of the potential divider the MCP bias voltage was limited to 1000 V. While the optimum operating voltage for new MCPs was found to be just below 1000 V, for slightly aged MCPs the best operational voltage was later found to be between 1100 V and 1200 V. This was after changing the resistors in the potential divider chain to the ones shown in Fig. 3.9 to extend the bias voltage range up to beyond 1200 V.

3.3.3 Output timing signals – a shot at simulation

A crude simulation procedure of the expected signals was carried out in an effort to get an idea of the nature of the output signals collected at the signal electrode. An equivalent circuit of the sketch in Fig 3.10 was drawn up to perform transient analysis of the output from the signal electrode. The analysis was done with the aid of PSPICE® circuit analysis program [11].

The equivalent circuit is shown in Fig. 3.10. Each MCP is modelled by a current source I_s1 and I_s2, in parallel with a capacitor C2 and C3, respectively [12], and the resultant electron current arriving at the anode capacitor C1 is modelled by an exponential decay signal. The anode capacitor isolates the anode (which is at high voltage) from the receiving circuit, which operates at ground potential. R10 is the input impedance of the receiving circuit and is generally chosen to be 50 Ω. The values of the resistors in the potential divider are of the initial test set up, and not the eventual choices made in Fig. 3.9. The high voltage supply to the MCP assembly is through SHV cables from the potential divider chain. The cables are connected to kapton electrode wires that are in turn directly in contact with the MCP electrodes. In the analysis circuit the SHV cables and the kapton wires are represented by transmission lines (TL) of different impedances.

The simulation was done in the transient mode; monitoring the output response at TPv1 to an exponential decay current pulse from the MCP chevron assembly over 50 ns. Transient analysis generates an output like that which can be viewed on an oscilloscope over the user specified time interval.

Sample results of the simulations for two different values of the anode capacitance are displayed in Fig. 3.11. From the simulation results the first apparent conclusion to be made is that the expected output signals should be negative with a rise time (typically a few nanoseconds) much shorter than the fall time. It can also be observed that the value of the anode capacitance has an effect on the overshoot or otherwise of the decaying signal. In the practical set up the desired timing signal must not be oscillatory in nature, to avoid false

triggers. The result shown in Fig. 3.11 suggests that an increase in the value of the anode capacitance should prevent any oscillations.

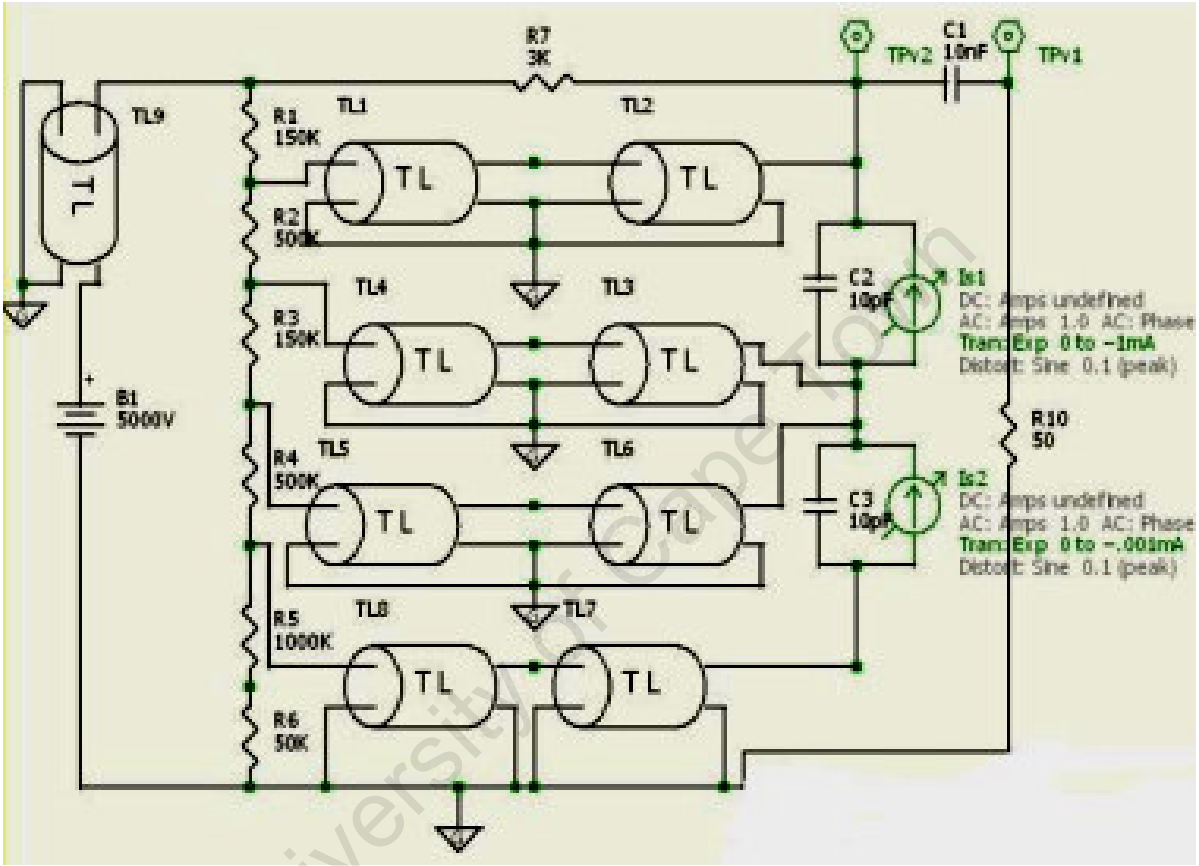

Figure 3.10 Equivalent circuit used in the simulation of MCP output signals.

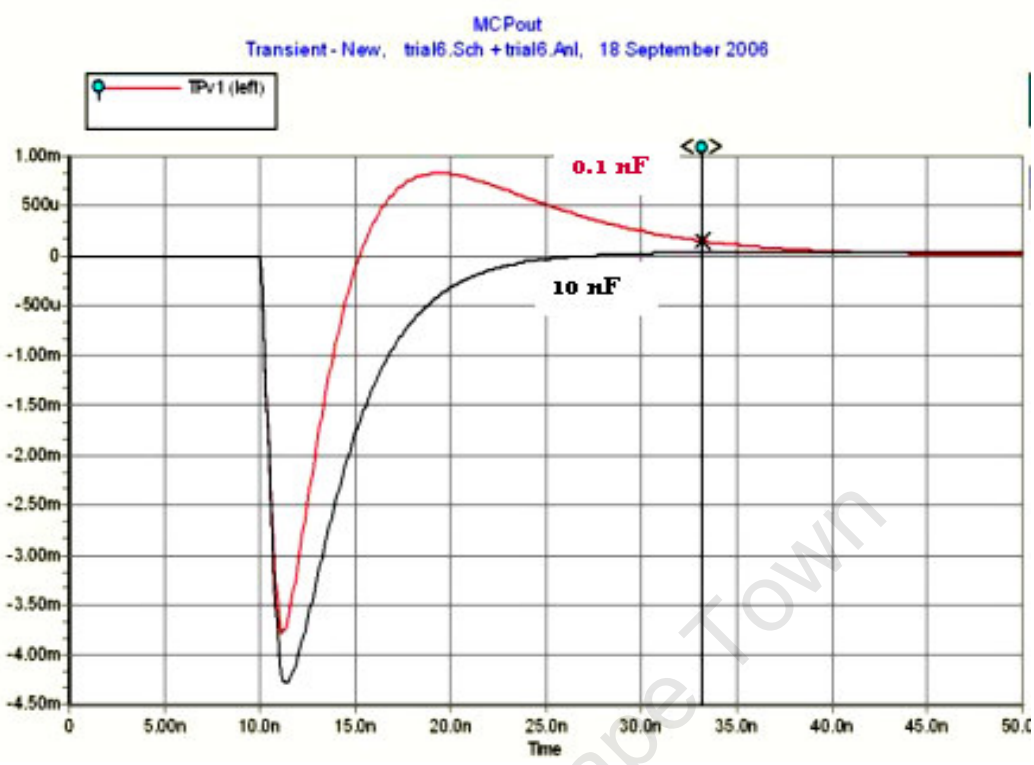

Figure 3.11 Results of the transient response to an exponential decay input current for two different values of the anode capacitance. The response is measured at the signal electrode TPv1 over a period of 50 ns.

3.3.4 Output timing signals – real signals

Preliminary tests on the timing detectors using real signal sources were carried out in vacuum using ^{241}Am and ^{252}Cf radioactive sources, with the pressure in the target chamber ranging between 10^{-6} and 10^{-7} mbar. A simple set up was used to view the output signals of both T1 and T2 directly on a digital oscilloscope of 500 MHz bandwidth. The surface barrier detector (SBD) was also connected so as to use its derived timing signal as the trigger input to the oscilloscope. This arrangement enabled viewing of coincident timing signals between the SBD and either of T1 and T2 or both, from particles passing through and registered by T1 and (or) T2 before being stopped by the SBD. The use of the SBD timing signal as the trigger was based on the premise that the detection efficiency of the SBD is virtually 100 % for alpha particles and the noise level is insignificant [13]. A block diagram of the apparatus set up is shown in Fig 3.12.

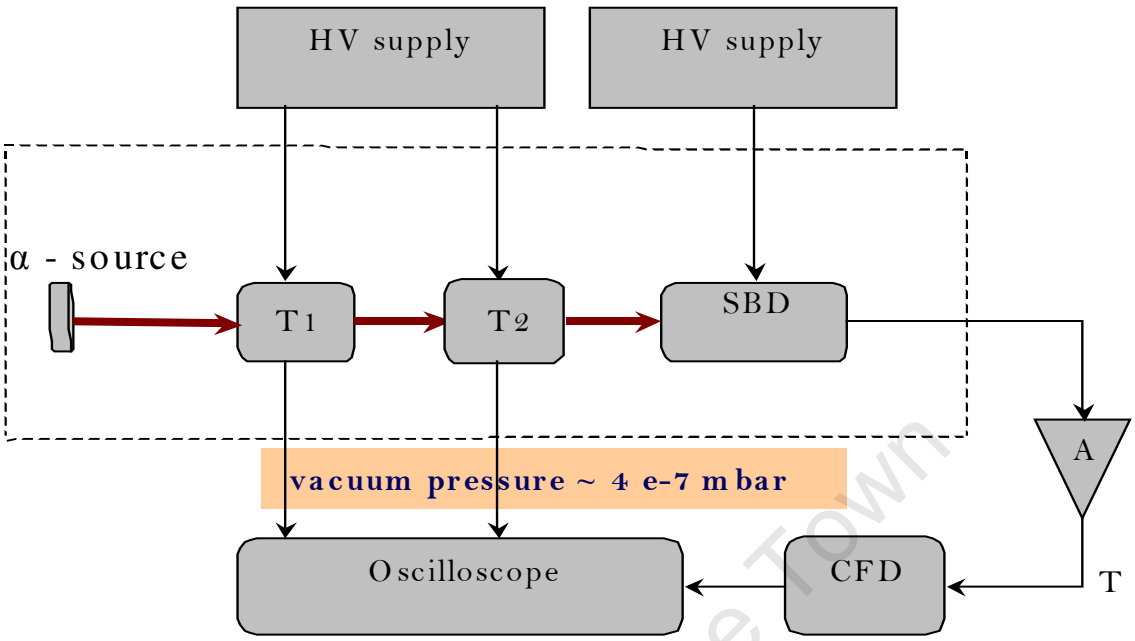

Figure 3.12 Set up of apparatus for testing the MCPs in vacuum using radioactive sources. The SBD trigger signal is first amplified before being fed into a CFD to give out a fast timing output signal.

The output from the SBD is fed into a preamplifier (A) that has both energy and timing signal outputs. The timing output (T) then goes into a Constant Fraction Discriminator (CFD), which gives out a fast negative signal whenever the input exceeds a preset threshold.

The MCP bias voltage was applied in steps of 100 V, over 2 minute intervals to allow the MCPs to reach equilibrium after each voltage increase. For newly installed MCPs, noise signals (also known as dark counts) were observed from about 800 V; their amplitude increasing as the voltage was increased. This threshold bias voltage at which dark counts begin to appear was later seen to increase with usage and as the MCPs aged over time. Another observation made at a later stage was that the output amplitude deteriorated over time most probably due to loss of gain. At every instance though, it was noted that the noise signal count rate gradually decreased a few minutes after each 100 V step increment.

The first tests involved investigating the response of the detectors to alpha particles from the ^{241}Am source of a nominal activity of 5 kBq. Given the small solid angle of the ToF telescope and such a relatively low activity, it was difficult to distinguish between real alpha particle signals and noise counts in both detectors when the oscilloscope was triggering on either of the timing detector signals, presumably because of the very low amplitude of the alpha signals. By triggering on the SBD timing signals though, it was possible to observe coincidences, albeit rare, between either of T1 and T2, and the SBD. The amplitude of the signals from either of the timing detectors was less than 10 mV.

To confirm the observed coincidences (and to further validate the presumption that signals due to alphas are quite small) a source with a higher activity and preferably decay products heavier than alphas was required. This was obtained in the form of ^{252}Cf with an activity of 10 MBq.

The spontaneous fission of ^{252}Cf results in two broad mass groups of heavy and light fission fragments spanning an energy range of 75 – 140 MeV [14]. Alpha particles of 6.12 MeV (85%) and 6.08 MeV (15%) are also emitted. Count rates in the range 1 – 2 per second were registered from this source by the SBD. For every SBD signal there was a coincident small amplitude signal from T2 typically less than 10 mV like the one shown in Fig 3.13**a**. Then there were larger amplitude signals due to fission fragments (see Fig. 3.13**b**) occurring at a rate of about 1 per minute. These observations are in broad agreement with the established [14] decay rate ratio of alphas to fission fragments of 97% to 3% respectively.

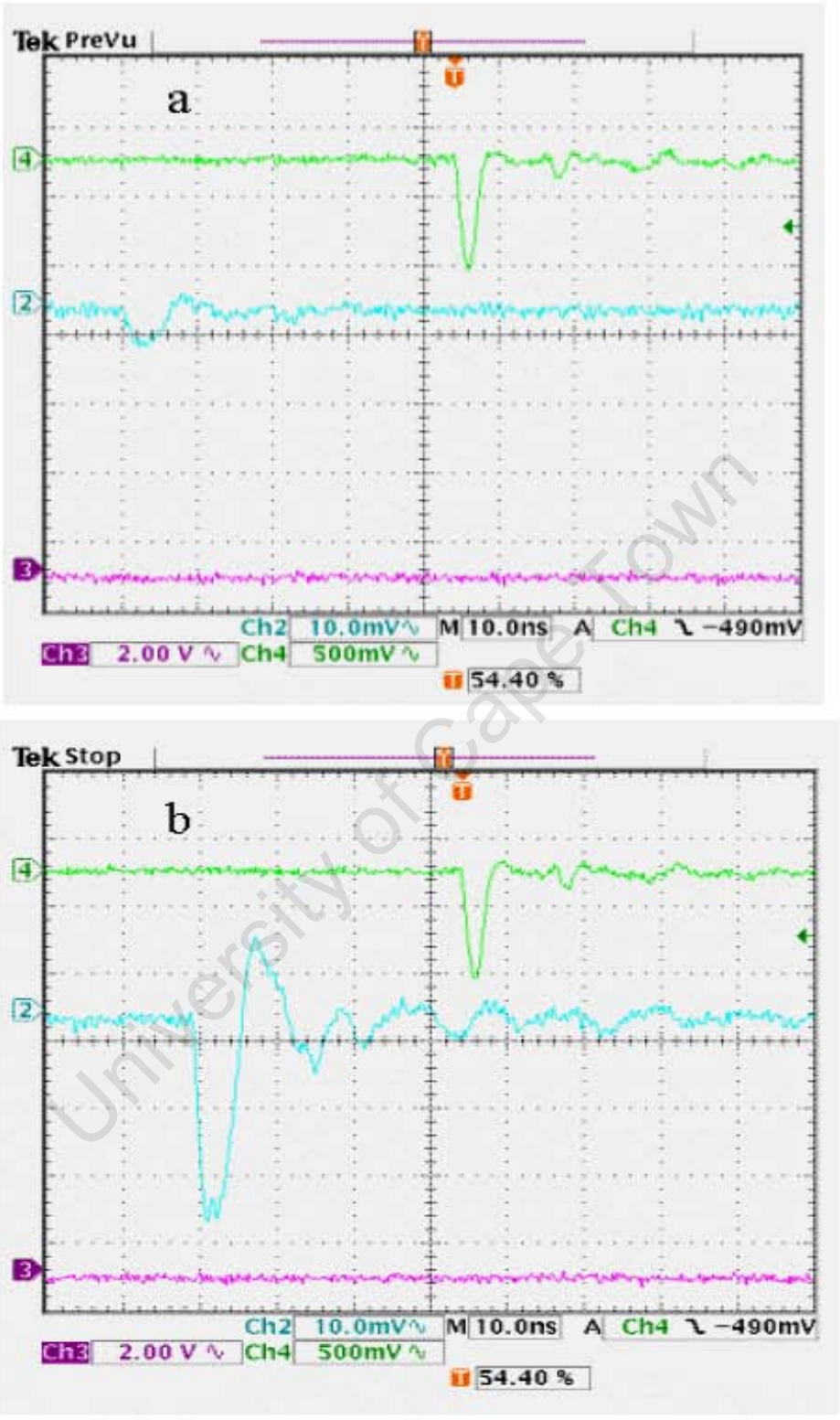

Figure 3.13 Scope traces showing typical MCP output signals from T2 (channel 2) in coincidence with the SBD timing output (channel 4). The signals due to 6 MeV alphas are shown in [a] and those due to >60 MeV fission fragments in [b].

The simulated timing signals are not too far off from the real ones; they are basically of the same shape and the rise time is of the order of a few nano seconds in both cases. The one major difference is the ringing (oscillations) observed in the real signals, thought to be a result of signal reflections at the points of contact between the kapton electrode wires in vacuum and the SHV cables to the potential divider. The reflections are due to differences in the impedances of the wires [13].

The simulation result suggested that increasing the anode capacitance would smoothen the oscillations. An attempt was made to increase the anode capacitance by replacing the anode kapton foil (see Fig. 3.9) with a thin Mylar® foil of the same diameter. The result was a breakdown in the Mylar® insulation as the supply voltage was increased. The breakdown was most probably due to Mylar's lower dielectric field strength. No other suitable material could be obtained immediately to perform further tests. Consequently the original kapton foil was put back. To circumvent the problem of ringing though, the CFDs used to convert the MCP signals into fast timing signals had to be used in their blocking mode [15]. This is further explained in section 3.4 below, which describes the signal processing electronics.

3.4 Electronics

The essence of a ToF - Energy coincidence measurement in ERDA is that from the measured time of flight and energy, recoil ions can be uniquely identified by their mass using the classical kinetic energy – mass relation

$$E = \frac{1}{2}mv^2 \qquad [3.3],$$

where the velocity v is calculated from the time of flight and the length of the flight path. It goes without saying that the contribution of the signal processing electronics to the time and energy resolution should be kept as minimal as possible. As such the choice of the electronics used must attest to that fact.

The expected energy of recoils in this particular HI – ERDA set up, for a 0.34 MeV/u ^{84}Kr incident beam, has an upper energy limit of ~1 MeV/u. The expected minimum time of

flight over a distance of 0.584 m should then be about 42 ns. The rise time of raw MCP signals is typically in the order of 1.0 ns (see Fig 3.13). Apart from the need for good SBD energy resolution, sub nanosecond timing resolution would also be a prerequisite for effective mass separation of different recoils. The electronic modules that are chosen to process such fast signals should do that with minimal distortion of the rise time.

3.4.1 Electronics module set up

The eventual electronics set up for this work is depicted in Fig. 3.14. It is such that, as aforementioned, three timing signals from the detectors are measured in coincidence, and the coincident time of flight and energy are used to uniquely identify any given recoil ion. T1 and T2 are the carbon foil based time detectors. Electrons ejected from the foils by recoil ions passing through the foils are accelerated towards a chevron assembly of microchannel (MCP) plates where the number of electrons is multiplied by a factor of up to 10^7.

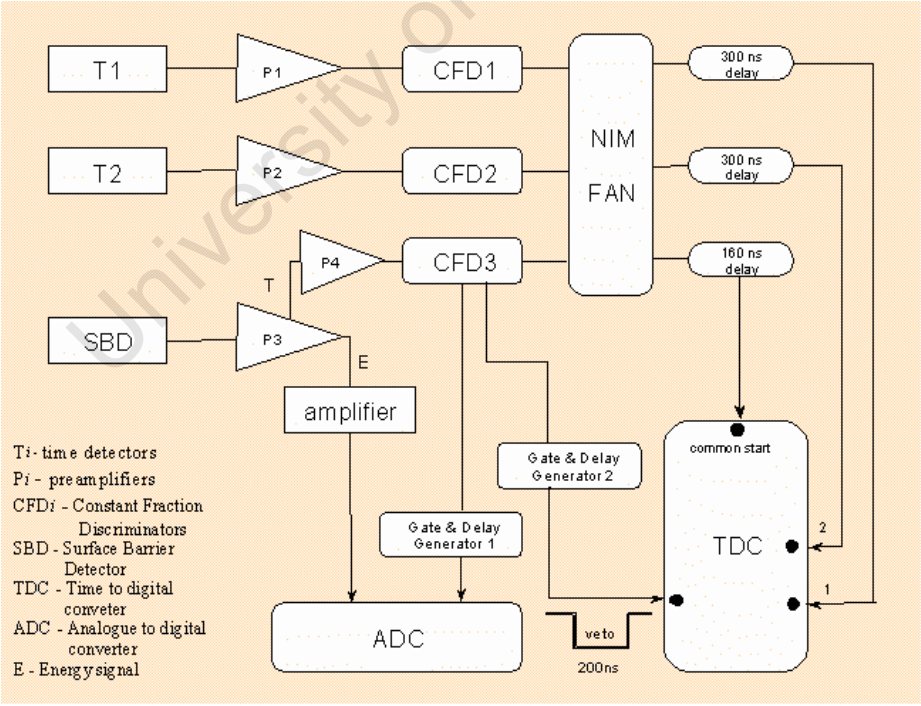

Figure 3.14 The ToF – Energy spectrometer electronics set up. The HV supplies to the time detectors and the SBD are not shown for clarity.

P1, P2 and P4 are ORTEC 474 Timing Filter amplifiers to further amplify the MCP signals and the timing signal from the Si surface barrier detector (SBD). The SBD, from ORTEC, has an active area of 150 mm^2 and a sensitive depth of up to 400 μm. The signal from the SBD is fed into an ORTEC 142A preamplifier P3, which gives out an energy signal E as well as a fast timing signal T. An ORTEC Spectroscopy Amplifier further amplifies the energy signal before it is fed into the Analogue to Digital Converter (ADC).

CFD1, CFD2 and CFD3 are ORTEC 924 constant fraction discriminators that give out fast (< 3 ns rise time) NIM timing signals. The width of the timing output is variable between 0.005 and 1 μs. When used in what is known as the blocking mode, detector pulses arriving within the set timing output width are regarded as a single pulse. From the MCP signal displayed in Fig 3.13**b**, it can be estimated that the oscillations (ringing) completely die out after 80 – 100 ns. The width of the timing output was subsequently set over 200 ns to prevent multiple triggering from the same detector pulse. The problem of pulse pile up [13] does not arise under these conditions, as the recoil count rate at the SBD has never exceeded 1 kHz.

The timing output of preamp P3 for low energy ions can be quite small hence the need for P4. The output from P4 goes into CFD3 to produce a common reference-timing signal; in this instance a common start. Since T1 and T2 signals both occur before the common start signal, the former have to be delayed so as to occur after the common start. This is achieved by using delay line cables in calibrated modules. A fan in-out module drives the timing signals through the delay cables to minimise attenuation. The three signals go into a Time to Digital Converter (TDC) before the digitised times are finally sorted by a multi channel analyser. The TDC triggers on the leading edge of each timing input. The Gate & Delay generators ensure that the ADC and the TDC are triggered within the same coincidence time window. This time window is continuously variable between 0.1 and 1.0 μs.

The trigger for the ADC and the TDC comes from SBD timing signal, chosen under the presumption that recoil ions reaching the SBD *should* have passed through both T1 and T2 detectors. For the preliminary tests using ^{252}Cf, timing signals occurring within 200ns of each other were considered to be coincident. Both the TDC and the ADC are housed in a

VME crate controlled by a 2 GHz Intel Core crate controller. The crate controller assumes the role of the front-end computer of the data acquisition system, as elaborated below.

3.5 Data acquisition and analysis

The data acquisition system is based on the Maximum Integrated Data Acquisition System (MIDAS), a general-purpose system for event based data acquisition for small and medium scale experiments developed at the Paul Scherrer Institute (PSI) in Switzerland and at TRIUMF in Canada [16]. MIDAS consists of a general framework on which users can write code specific to their experimental needs. It is based on a modular networking capability and a central database system. The scale of experiments that can be supported varies from a single PC connected to the hardware for control, data acquisition and analysis, to several front end computers connected to the hardware and linked to back end computers via Ethernet for data storage and analysis. The generic developmental platform is summed up in the schematic in Fig 3.15.

In the local set up a VME based crate controller constitutes the front-end computer that facilitates readout of the stream of data from the hardware. The hardware components in this instance are the ADC and the TDC. Data transfer to the back-end workstation is via Ethernet. The Engineering and Information Technology department of iThemba LABS designed a program [17] to customise the inbuilt MIDAS framework to control the front-end readout on one side and to store and analyse the raw data on the other side. Data analysis is by an external application package ROOT, developed at CERN. The MIDAS – ROOT interface comes in parts each obtainable from PSI, TRIUMF and CERN.

Data polled from the hardware equipment can be analysed both in real time as it comes in and offline after it has been stored. The 2-D ToF – Energy scatter plot, as well as the 1-D ToF and Energy spectra; can be viewed as they build up using the ROOT analyser. The raw data files, stored in a MIDAS format xxx.mid, can be converted into ASCII files for further processing and analysis.

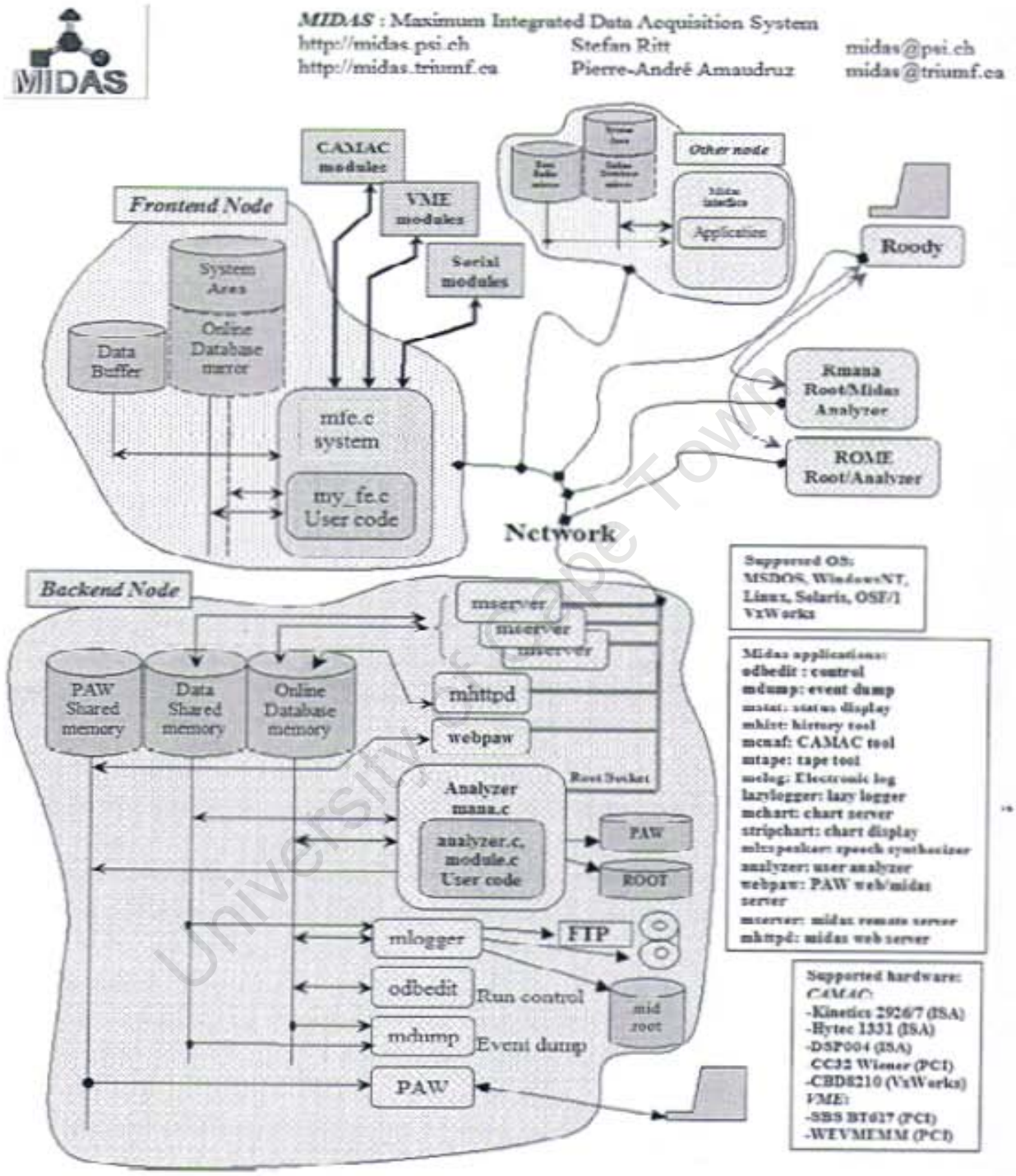

Figure 3.15 The general configuration of the MIDAS development platform [16]. *See text for a general overview.*

3.6 Preliminary tests of the spectrometer

The departure point in the characterisation of the spectrometer as a whole was to assess the timing resolution of the instrument, seeing as the measurement of the time of flight is at the heart of its operation. The procedure adopted here was to start by ascertaining the contribution of the signal processing electronics chain to the total timing resolution, and thereafter the system response to real detector signals from radioactive sources.

3.6.1 Electronics timing resolution

The set up used to determine the overall electronics timing resolution is the same as that in Fig 3.14 save for the timing detectors T1 and T2 and the SBD. A BL-2 Berkley Nucleonics® tail pulse generator was used to simulate signals from the timing detectors and the SBD as shown in Fig 3.16. The output signal was a negative signal with a rise time of 3 ns at a frequency of 100 Hz. A Tee connector was used to split the signal in two, one part going straight into P1 and the other part going through a delay box into P2. The delay box was used to simulate the time of flight; varying the delay settings to get different flight times. To simulate the coincidence trigger from the SBD the test input into P3 was derived from the same signal into P2. The time delay between T2 and the SBD expected in real experiments was ignored in the simulation since the signal from the SBD is there merely to provide the coincidence trigger, and the focus in this case was on the T1 – T2 time delay. The energy aspect was not considered either in the simulation.

With the output frequency from the signal generator set at 100 Hz, five different flight times were simulated and a time of flight spectrum acquired. The delay box calibration settings were confirmed by using the oscilloscope to measure the time difference between T1 and T2 before plugging these into P1 and P2 respectively.

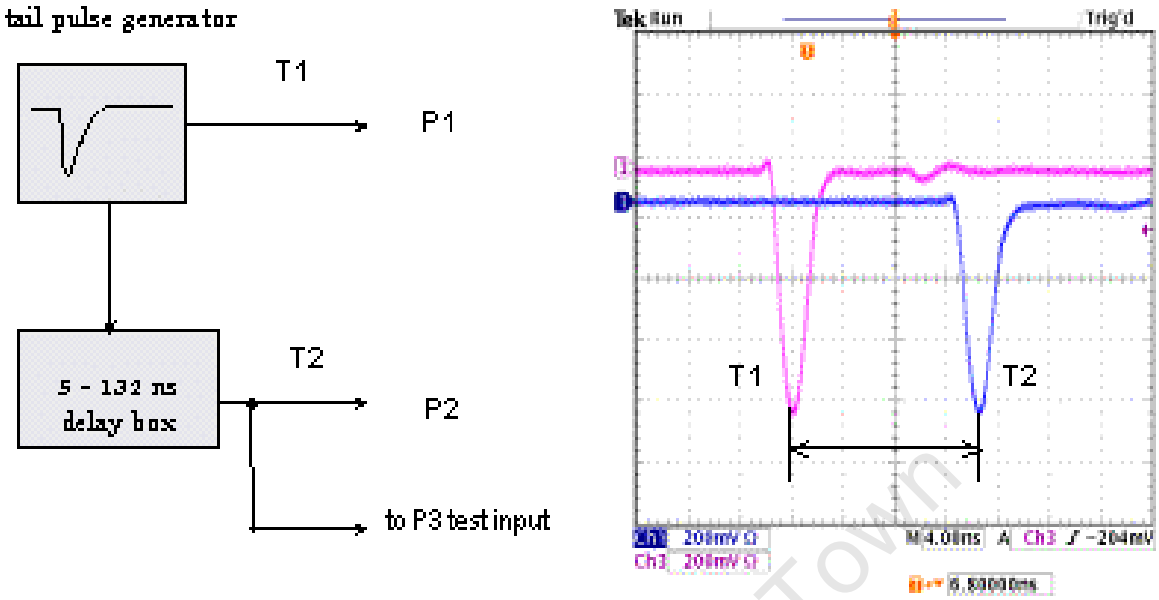

Figure 3.16 Simulation of detector signals using a tail pulse signal generator for measurement of the electronic timing resolution. The oscilloscope screen shot shows a T1 – T2 delay calibration check, with the time base set at 4 ns/division.

Figure 3.17a shows the TDC calibration curve of raw† data from the Multichannel Analyser (MCA) and 3.17b shows a Gaussian fit to one of the peaks to determine the timing resolution of the electronics set up.

The electronic timing resolution was determined from the full width of the Gaussian fit at half the maximum height (FWHM). From Fig. 3.17b this was found to be 0.11 ns at 44.07 ns, or 0.25 %. Compared to later evaluations of the timing resolution of the whole detector system for real signals, the electronic component measured here was found to be a rather small contribution. In addition, the TDC calibration curve shows near ideal linearity over the expected time range of recoils with energy within the range 0.1 – 1.0 MeV/amu. Overall therefore, uncertainties due to the signal processing electronics are negligible.

† Subsequent analyses entail converting x-y projections of the raw data into ASCII format for further processing in ORIGIN®, compacting both the horizontal and vertical the channel ranges to 512.

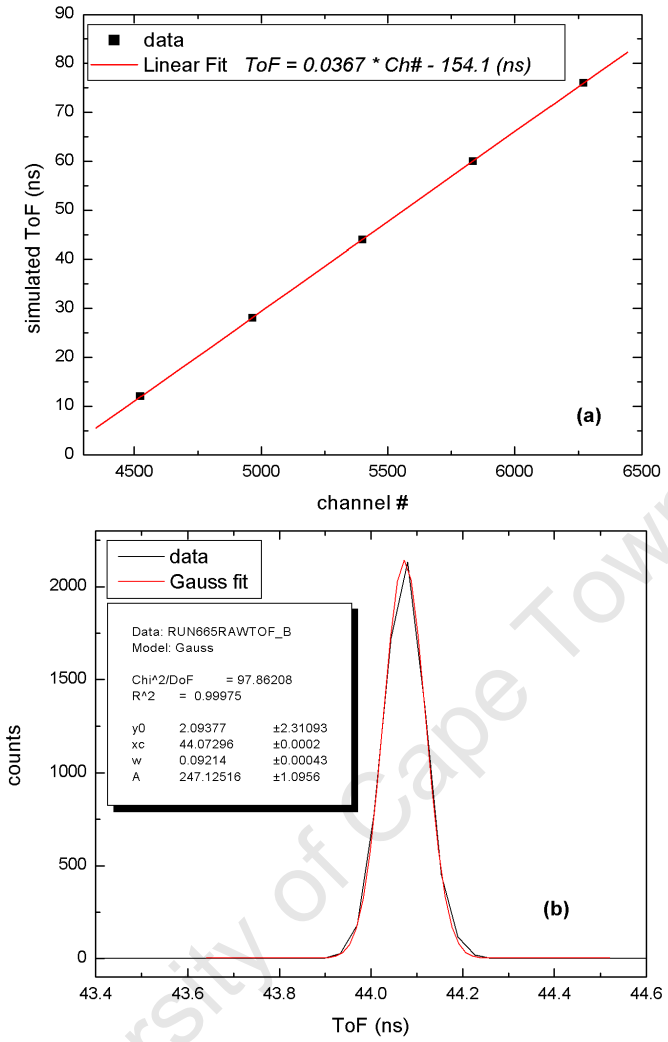

Figure 3.17 Results of the ToF simulation measurements showing the (a) the TDC calibration curve and (b), a Gaussian fit to one of the peaks to determine the electronics timing resolution.

3.6.2 Timing resolution for Cf-252 decay products

Preliminary tests of the timing resolution of the whole detector system for real signals were done using the ^{252}Cf source. The incidental advantage of using this source was that the range of energies of alphas and the fission fragments from this source, 0.5 – 1.5 MeV/amu is within the range of energies of recoil ions of 0.1 – 2.0 MeV/amu in a typical ToF – ERDA set up [1 - 5]. The particle mass range from this source is also quite broad (4 ~ 140 amu), eclipsing the expected range of recoil masses in a routine set up. The one major

setback though was that of very long times (>24 hours in some instances) needed to get meaningful spectra due to the low source activity and the small solid angle.

In a ToF – E coincidence measurement set up such as the one developed here the raw data can be presented in a 2-D scatter plot where each point in the 2-D plane represents a coincidence event. Figure 3.18 shows one such plot generated from ToF – E coincidences of decay products from the ^{252}Cf source. The decay products are broadly separated according to their mass and energy; the 1.53 MeV/u alpha particles showing up at the very low end of the energy scale and the fission fragments at the high-energy end. The fission fragments, though overlapping in energy, are split into the well known [14] heavy and light mass groups according to their time of flight. There is an expected overlap in the time of flight between alpha particles and the most energetic (at E ~1.5 MeV/u) of the light fission fragments since $ToF \propto (A/E)^{1/2}$, where A is the atomic mass.

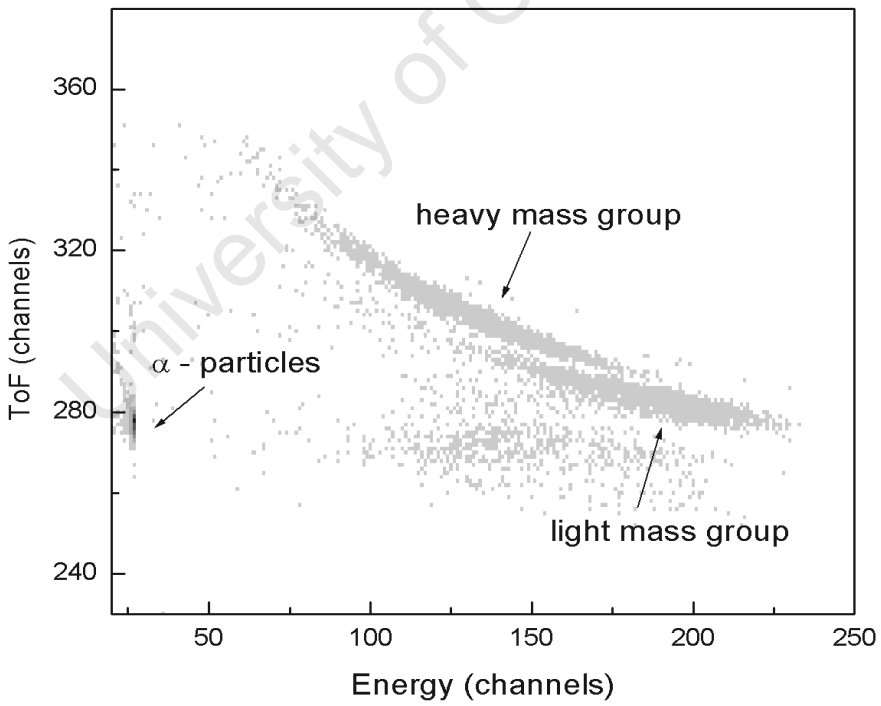

Figure 3.18 A 2-D ToF – Energy scatter plot of decay products from a ^{252}Cf source.

The timing resolution for the alpha particles was determined by selecting from the 2-D scatter plot the alpha particle contour region and projecting it onto the ToF axis and subsequently performing a Gaussian fit to the projection. For the light fission fragments however, comprising atomic species of various mass and energy (and therefore various times of flight), the observed overlap between the time of flight of the (monoenergetic) alphas and that of the most energetic of the fragments allows one to get an approximate value of the timing resolution for the fragment group using the calculated time of flight of alphas. One possible way of doing this would be to perform an *edge* fit to the short time (high energy) edge of the projected fission fragment time of flight spectrum, as opposed to a Gaussian fit, since this spectrum results from certainly non-monoenergetic particles.

The Boltzmann sigmoidal fit function [18] can be used for this purpose. In its functional form it is given by

$$y = \frac{A_1 - A_2}{1 + e^{(x - x_o)/dx}} + A_2 \qquad [3.4],$$

where the fit parameters A_1, A_2, x_o and dx are respectively, the starting point, the end point, the centroid value of the edge and the slope of the edge.

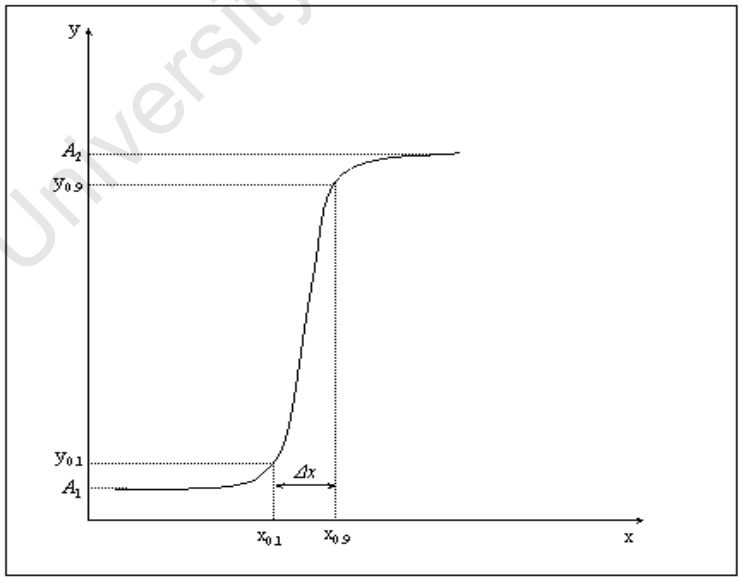

Figure 3.19 An illustrative example of a Boltzmann sigmoid showing the start and end points A_1 and A_2, respectively, the width of the edge Δx and the x-y coordinate pairs at 10% and 90% of the height of the edge.

The resolution Δx is generally defined as the width ($x_{0.9}$ - $x_{0.1}$) of the edge between 10% ($y_{0.1}$) and 90% ($y_{0.9}$) of the height (A_2 - A_1) of the edge as illustrated in Fig. 3.19. To evaluate Δx one has to first obtain $x_{0.1}$ and $x_{0.9}$ from Equation 3.4. The value of y at 10% maximum height is given by

$$y_{0.1} = A_1 + 0.1 \cdot (A_2 - A_1) = \frac{A_1 - A_2}{1 + e^{(x_{0.1} - x_o)/dx}} + A_2 \qquad [3.5],$$

which simplifies to

$$0.9 \cdot (A_1 - A_2) = \frac{A_1 - A_2}{1 + e^{(x_{0.1} - x_o)/dx}} \qquad [3.6],$$

giving

$$x_{0.1} = \ln\left(\frac{1}{9}\right) \cdot dx + x_o \qquad [3.7].$$

Similarly for $x_{0.9}$ one obtains

$$x_{0.9} = \ln(9) \cdot dx + x_o \qquad [3.8].$$

And from Equations 3.7 and 3.8 one finally gets

$$\Delta x = 4.395 \cdot dx \qquad [3.9].$$

The results of the fits are displayed in Figs 3.20 for the alpha particles and Fig 3.21 for the light fission fragment group.

The TDC setting of 0.0367 ns/channel at the 0 – 8192 channel range used when the 2D ToF – Energy scatter plot of the decay products of ^{252}Cf was acquired translates to 0.59 ns/channel when the raw data is converted into ASCII format and the time axis channel range now 0 – 512. The Gaussian fit to the alpha ToF spectrum in Fig 3.20 gives the FWHM as 4.59 x 1.17 channels. This gives an overall timing resolution of 3.2 ns for alpha particles, for a time of flight of about 27 ns, estimated from a flight distance of 0.46† m [7] for an energy of 6.12 MeV. For the light fission fragments the slope dx of the short time edge in Fig 3.21 is 1.017 channels, and using Equation 3.9, translates to a timing resolution of 2.6 ns for the same time of flight of 27 ns. These two values, though different themselves, confirm the earlier finding that the 0.11 ns contribution of the signal processing electronics to the total timing resolution is rather small.

† This was the distance between time detectors T1 and T2 in the preliminary design.

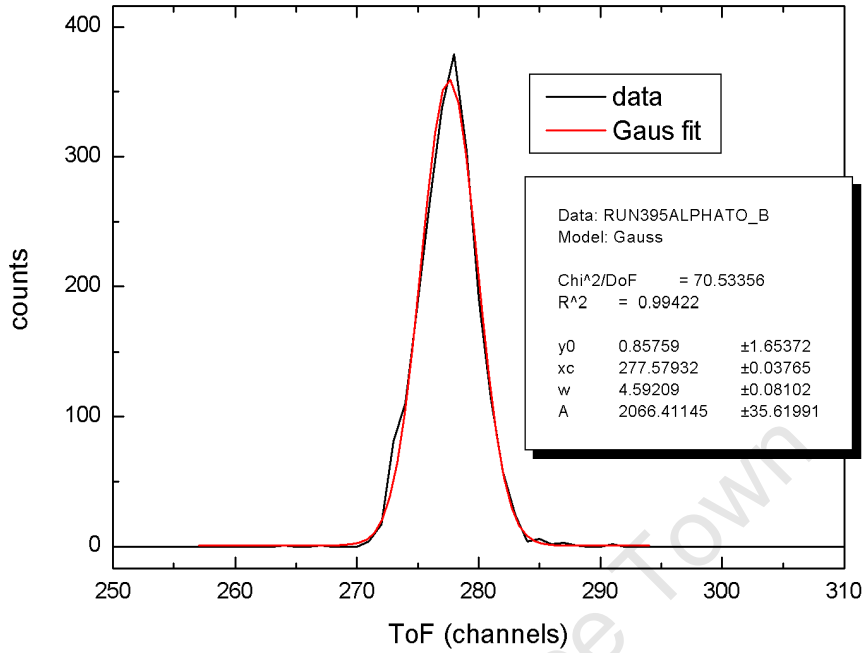

Figure 3.20 Plot showing a Gaussian fit to the ToF spectrum of 6.12 MeV alphas, to determine the timing resolution of the whole detector system for alphas.

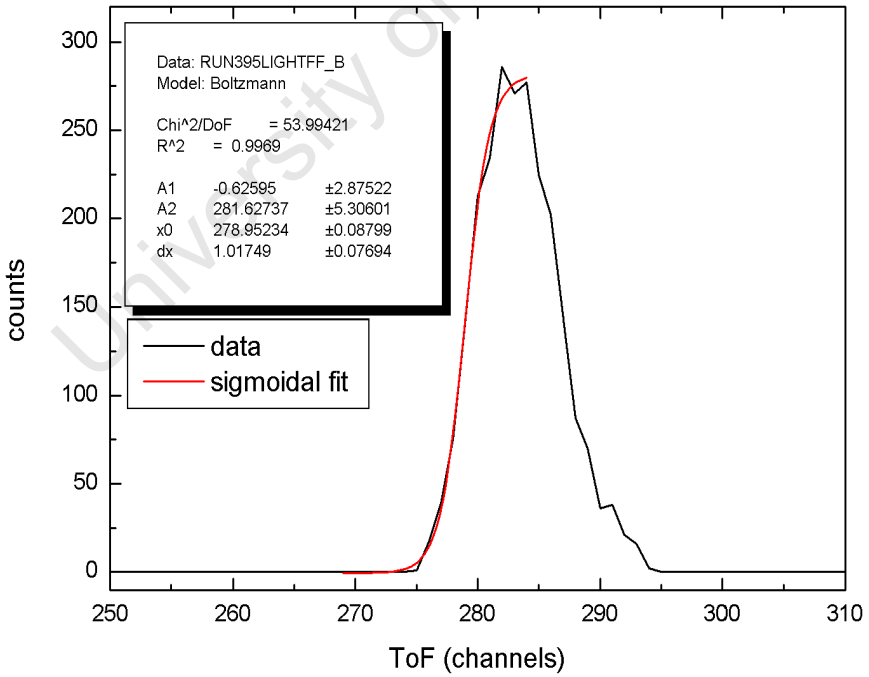

Figure 3.21 Plot showing a sigmoidal (Boltzman) fit to the short time (high energy) edge of the light fission fragment mass group ToF spectrum, to determine the system timing resolution for 1.5 MeV/u fission fragments.

3.7 Characterisation of the spectrometer using recoil ion beams

The initial tests carried out using the ^{252}Cf source provided a means of performing preliminary checks to effect changes and improvements on the set up as it was being assembled. [One of the changes made was to increase the time of flight by increasing the fight distance to roughly 0.60 m with the aim of improving the relative timing resolution]. To fully characterise the system however, under normal operational conditions, further tests had to be carried out using ion beams. Ion beams were obtained in the form of recoils from known target samples bombarded by a 27.5 MeV Kr^{15+} beam. The main parameters under investigation were timing resolution, energy and depth resolution. For a time of flight detector, the latter two are directly affected by the timing resolution. These parameters are key to quantitative depth profiling of thin layers [19, 20]. This sub section describes the target samples and the measurements performed to evaluate the parameters in question. Prior to that though is a description of the measurement of the new flight length.

3.7.1 Measurement of flight length *l*

The new flight length was determined by measuring the time of flight of a 3.33 MeV He^{2+} beam scattered off a thin layer of gold on a silicon substrate. This required re-calibrating the TDC for this specific task and thereafter acquiring a time of flight – energy spectrum of the scattered beam. The re-calibration procedure yielded the following TDC calibration equation

$$ToF = 0.0367 * Channel\# - 151.3\ (ns) \qquad [3.10].$$

The slight difference in the offset between this and the previous TDC calibration in Fig 3.17**a** could be due to differences in the signal propagation delays in the different signal cables used. Figure 3.22**a** shows the raw ToF spectrum of the He^{2+} beam scattered off the Au/Si target sample and Fig 3.22**b** is a close-up of the same spectrum showing a sigmoidal fit to determine the time of flight of those beam ions scattered off the uppermost surface layers of the target.

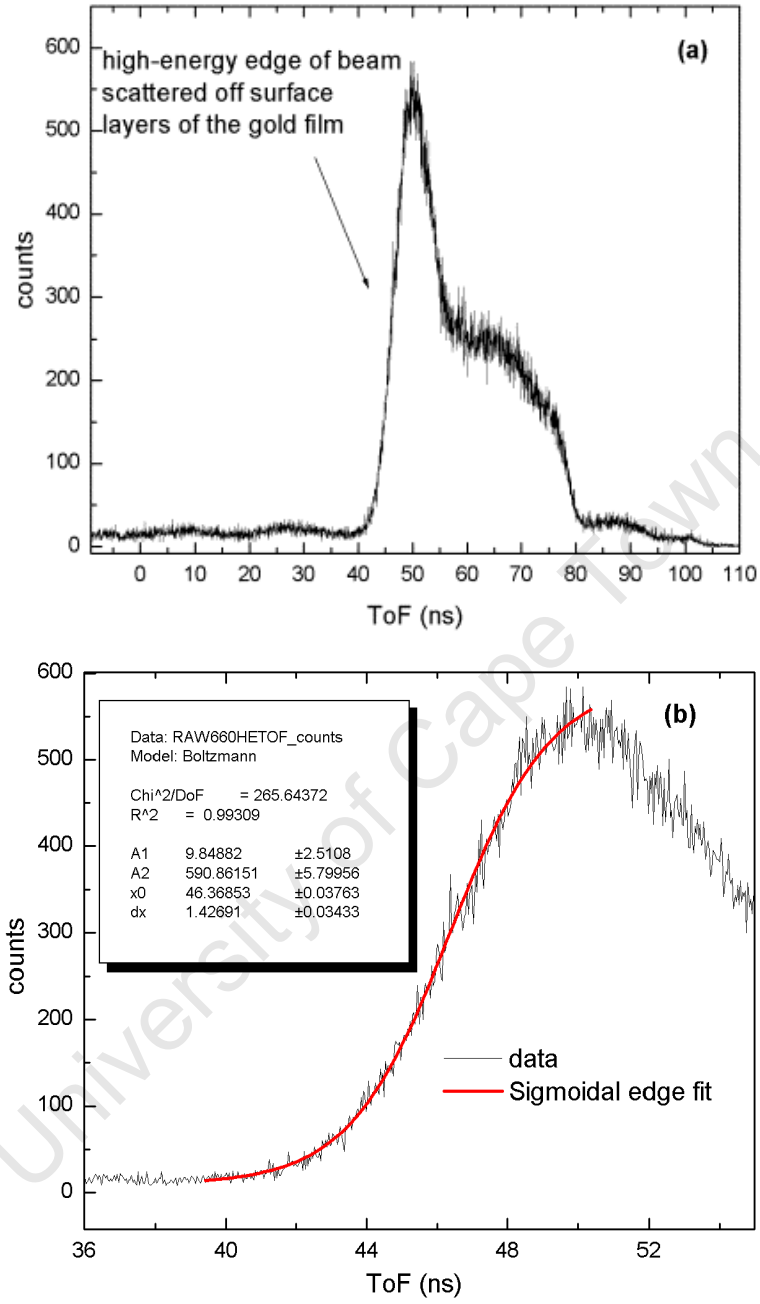

Figure 3.22 Time of flight spectrum of a He^{2+} ion beam scattered off a Au/Si target (**a**), and a close up of the same spectrum to show the high-energy (short time) edge fit of the beam ions scattered off the surface layers (**b**).

From the high-energy edge fit in Fig 3.22**b** the time of flight of the most energetic scattered ions was found to be 46.4 ns. The 'flight' energy E_F of these ions was determined from the relation

$$E_F = E_1 - \Delta E_{T1} = K_s E_0 - \Delta E_{T1} \qquad [3.11]$$

where K_sE_0, introduced in Equation 2.2, is the energy of the incident ion just after scattering and ΔE_{T1} is the energy loss of the scattered ion through the carbon foil of the first time detector.

For this particular instance E_0 = 3.33 MeV and K_s = 0.995. The energy loss ΔE_{T1} was calculated using SRIM2008 [21] code to be 9.58 keV (0.00958 MeV), resulting in E_F = 3.30 MeV. The length l of the flight path was then calculated from

$$l = \sqrt{\frac{2E_F}{m}}\, t \qquad [3.12],$$

where E_F is in joules and m, the mass of the scattered ion, is in kg, giving l = 0.584 m, with an error term of 1.7 % (or 0.01 m) arising mainly from an uncertainty of 3.4 % associated with the calculated energy E_F, discussed in section 5.4.2.1. The error in t, from the edge fitting procedure is 0.08% and is neglected in the analysis. This value of l measured in this way compares favourably with the l = 0.588 m value obtained through a rather crude measurement technique. In this latter method the length was obtained simply by marking points on a string threaded through the timing detectors mounted without the foils and measuring the distance between the marker points using a meter rule. For this reason a more appropriate value of the uncertainty in l would be ±0.005 m or 0.85 %.

3.7.2 Time calibration and timing resolution

To assess the timing properties of the time of flight telescope for a range of recoil masses the TDC had to be calibrated using the calculated time of flight of different recoils from known targets, as opposed to the usual method of using the delay box unit. In effect this alternative method was supposed to show whether or not the TDC linearity is dependent on mass. Two of the target sample types, CaF_2\Si and Al_2O_3\Si were each prepared by electron beam evaporation of calcium fluoride and aluminium oxide, onto plain silicon wafer

pieces. Figure 3.23 shows the result of a Rutherford Backscattering Spectroscopy (RBS) measurement carried out using a 2 MeV He^{2+} beam to check the thickness and possible impurities of one of the CaF_2\Si test samples (**CaF_1**), nominally given as 100 nm by the quartz oscillator thickness monitor used during the evaporation. SIMNRA [22] simulation gives the thickness as 792 x 10^{15} at cm^{-2}, which is about 106 nm, assuming a bulk density of 3.18 g cm^{-3} [23] for the deposited layer. No major impurities were detected. The difference between the two thickness values could be due to uncertainties caused by response time lags in the (manual) operation of the shutter of the electron beam evaporator.

For the ToF detector calibration measurements, to obtain the desired recoils a 27.5 MeV Kr^{15+} beam was used to forward scatter different ion species from known target samples into the detection system. Figure 3.24 shows a typical 2D $ToF - E$ scatter plot obtained from the coincidence detection of recoils from the same CaF_2\Si test sample, **CaF_1**. The scatter plot shows the major ion species from the sample; Ca, F and Si as well as C and O surface impurities†. [The Al signal was later confirmed to be an experimental artefact in a repeat measurement [see Fig. 4.2] after redesigning the aluminium target holder to prevent possible recoils from the target holder]

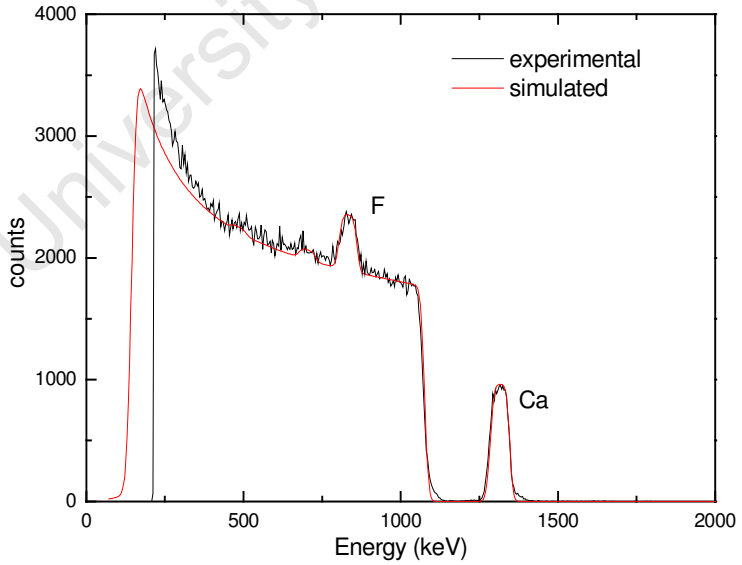

Figure 3.23 RBS spectrum obtained from the measurement of the CaF_2\Si test sample **CaF_1** for thickness measurement.

† The identities of the impurities were confirmed through a procedure described in section 4.2

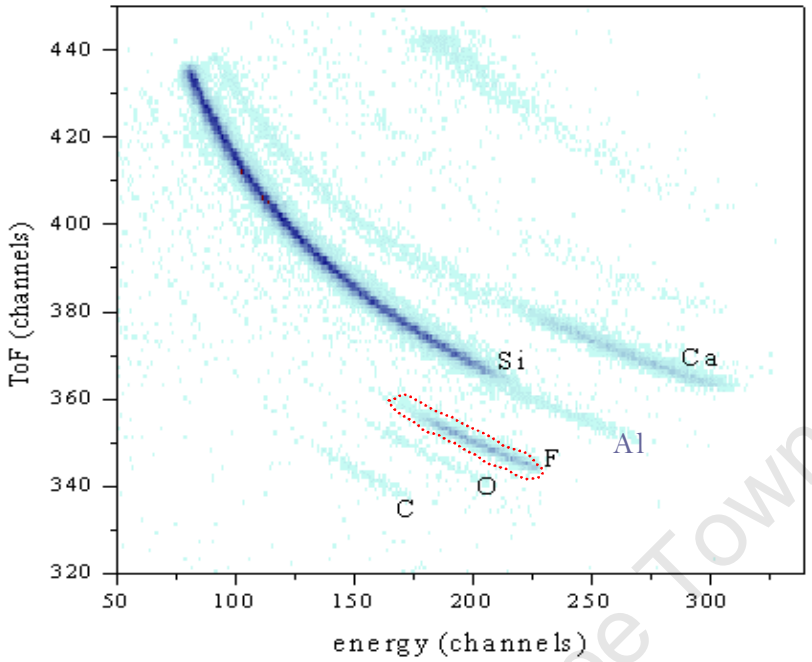

Figure 3.24 2-D ToF – Energy scatter plot of recoils from the CaF_2\Si test sample **CaF_1** bombarded by a 27.5 MeV Kr^{15+} incident beam.

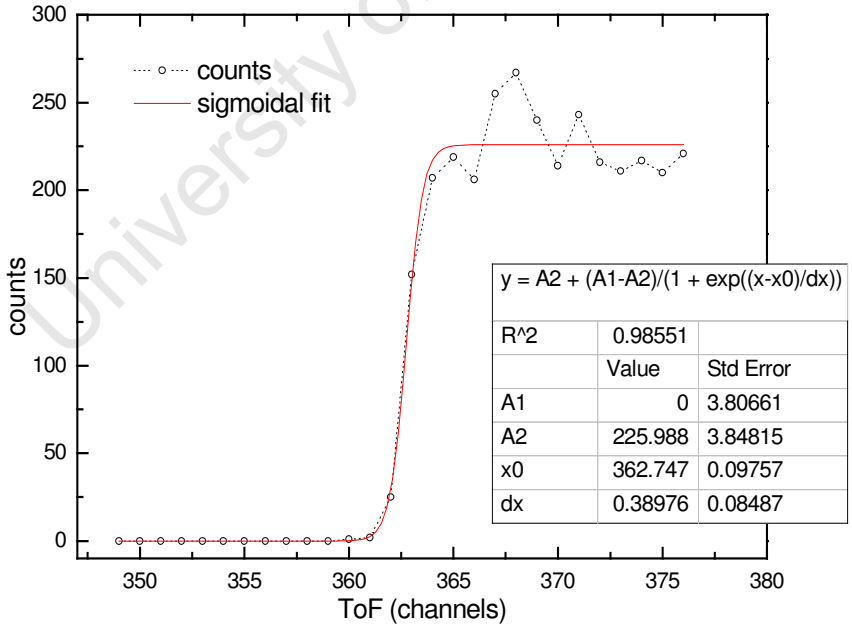

Figure 3.25 An example of a sigmoidal fit to the ToF projection of high energy ^{40}Ca recoils coming from the sample surface.

To calibrate the *ToF* telescope the Ca, F and C mass contours in Fig.3.24 were projected onto the *ToF* axis to get elemental time spectra. Additional calibration points of silicon recoils from a plain silicon target, oxygen from the Al_2O_3\Si target and krypton ions scattered off a thin gold layer on a silicon substrate were also used. Like before, the short time (high energy) edge of the time spectrum of each identified recoil ion was then fitted using a Boltzman sigmoidal fit function using the graphing and analysis software ORIGIN® as illustrated in the example in Fig. 3.25. This gave the channel number corresponding to the shortest time of flight t_i for each recoil ion.

The energy E_F of recoils between the two timing detectors was calculated using Eq. 2.1, again taking into account the energy loss ΔE_{T1} of each ion through the first time detector using Ziegler et al. 's SRIM2008 code. Similarly the energy of the scattered krypton after passing through the T1 carbon foil was calculated using Eq. 3.11, derived from Eq. 2.2. The results of the calculations are displayed in Table 3.1 showing ΔE_{T1} ranging between 0.6 – 1.2% of the initial energy of the recoil ion for the C – Kr mass range. Included in the table is also the theoretical time of flight, calculated using

$$t_i = \sqrt{\frac{m_i}{2E_F}}\, l \qquad [3.13],$$

where l is the flight length of 0.584 m.

The TDC calibration plot is shown in Fig. 3.26. Each data point has an error term of 1.9 % resulting from uncertainties of 3.4 % in the energy E_F and 0.85 % in the length l, both used in the calculation of the time of flight of surface recoils using Equation 3.13. A correlation coefficient of 0.99 obtained between the linear fit and data is a good indicator that the *ToF* calibration was independent of the mass of the detected particles.

recoil ion	E_0 (MeV)	$[S]_C$ (keV/μgcm^{-2})	ΔE_{T1} (MeV)	E_F (MeV)	ToF (ch)	ToF (ns)	Δt (ns)
C	9.037	6.55	0.05895	8.97805	337.5	48.63	1.17
O	11.096	9.71	0.08739	11.00861	341.3	50.71	1.11
F	12.419	11.39	0.10251	12.31649	343.9	52.24	1.08
Si	15.500	19.89	0.17901	15.32099	352.5	56.86	1.23
Ca	18.047	27.02	0.24318	17.80382	362.7	63.04	0.96
Kr	24.500	35.25	0.31725	24.18275	391	78.39	0.97

Table 3.1 Table showing calculated times of flight (in ns) of different recoils against channel number, after taking into account the energy loss ΔE_{T1} of each recoil through the T1 carbon foil. Column $[S]_C$ represents the stopping power of each ion species in carbon and Δt is the timing resolution.

The experimental timing resolution (Δt) for each recoil ion, estimated from the width of the sigmoidal edge fit *dx*;

$$\Delta t = 4.395 dx * slope \qquad [3.14],$$

was however, found to vary only slightly with mass. In absolute terms there is no obvious trend, but expressed as a percentage of the actual time of flight, the timing resolution slightly deteriorates with mass from 1.2 % for krypton ions to 2.4 % for the carbon recoils. This deterioration in resolution with mass could be a result of the decrease in the number of ejected electrons from the timing foils as the mass of the impinging ion species decreases, which in turn leads to lower amplitude MCP timing signals, as seen for alphas in section 3.6.2.

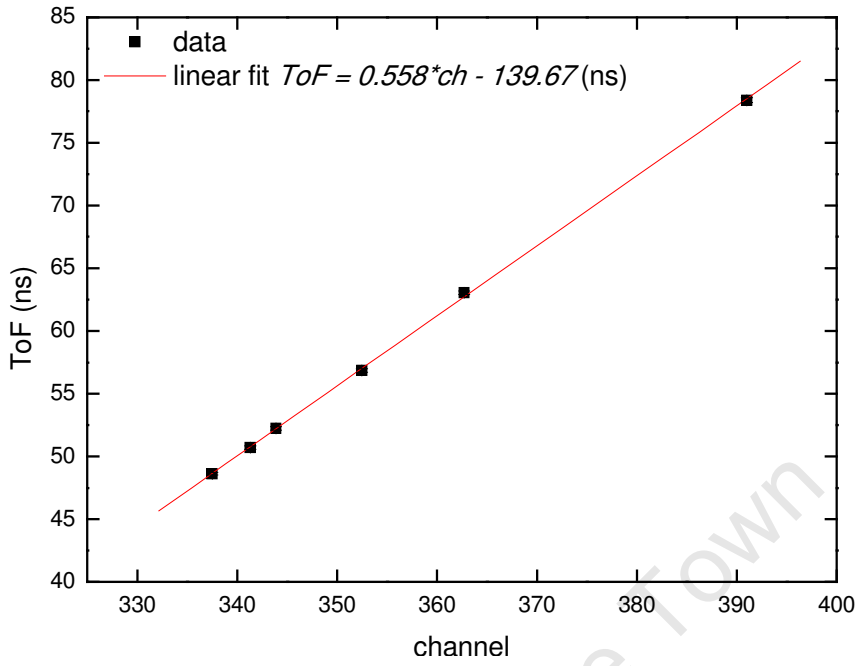

Figure 3.26 TDC calibration plot for heavy ion recoils in the mass range 12 – 84 u.

The calibration equation so obtained could then be used to convert the time axis to an energy axis for each given recoil to give a ToF calculated energy spectrum. Alternatively the energy spectra could be obtained through calibration of the SB detector for each recoil ion species, like was done in this work, since as will be seen in section 3.7.4, the ToF energy resolution was found to be not too different from the SB energy resolution, especially for the light ions.

3.7.3 Energy calibration of the SB detector

The response of charged particle semiconductor detectors is known to be mass (and energy) dependent [13]. The separation of recoil ions according to mass in a ToF-Energy detector set up permits individual recoil energy calibration for elemental analysis. As an example of single element analysis, the dashed line in Fig. 3.24 encloses a region in the 2-D ToF-Energy plane that contains events due to fluorine recoils only. Projecting those events onto the Energy axis gives the energy spectrum. Energy calibration (for each

element) is done by extracting paired entries of ToF and Energy from the 2-D scatter plot and using energy calculated from the ToF (after time calibration) to calibrate the energy detector. Table 3.2 illustrates this method using fluorine recoils as an example.

Energy (ch)	ToF (ch)	ToF (ns)	Energy (MeV)
182	355	58.420	9.7304
189	353	57.304	10.118
197	351	56.188	10.529
200	350	55.630	10.744
209	348	54.514	11.193
217	346	53.398	11.671
223	345	52.840	11.921

Table 3.2 SBD energy calibration for fluorine recoils

The main source of uncertainty in ToF values calculated in Table 3.2 is the accuracy with which centroids of ToF peak channels corresponding to particular energy channels can be identified from the 2-D ToF-Energy scatter plot. As a rule of thumb, half the peak width, or half the timing resolution, determined from values in Table 3.1, was found to be an adequate description of the uncertainty in the calculated ToF values.

This uncertainty is further propagated to the energy calibration (E_{SB}), defined by

$$E_{SB} = \frac{m}{2}\left(\frac{l}{ToF}\right)^2 - \Delta E_{T2} \qquad [3.15],$$

where m and l are, respectively, the mass of the recoil ion and the flight length. ΔE_{T2} represents the energy loss of recoils through the carbon foil of the second timing detector T2. This quantity was estimated using SRIM 2008 and from the calculations made, ranged

between 0.8% and 1.1% of the initial energy for ^{19}F recoils. Figure 3.27 shows linear fits to data presented in Table 3.2 for ^{19}F recoils as well as to a similarly obtained data set for ^{40}Ca recoils. Error bars of 2.6 % for ^{19}F recoils are calculated using Eq. 3.16 from the 0.85 % uncertainty in l and the 1.0 % uncertainty estimate in the ToF values;

$$\frac{\Delta E_{SB}}{E_{SB}} = \sqrt{\left(\frac{2\Delta ToF}{ToF}\right)^2 + \left(\frac{2\Delta l}{l}\right)^2} \qquad [3.16],$$

For ^{40}Ca recoils half the ToF resolution is 0.48 ns, or 0.76 % leading to error bars of 2.3 % in the calculated energy values. The absolute uncertainty in E_{SB} due to the uncertainty in energy straggling through the carbon foil is only a few keV and is much smaller than that due to ToF resolution and so is ignored in the above calculations.

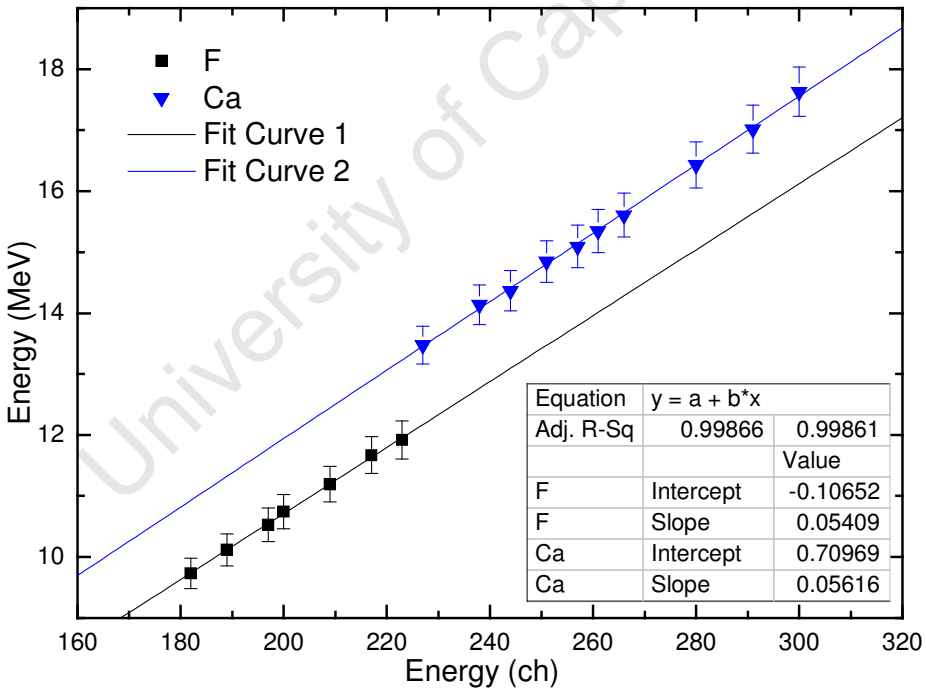

Figure 3.27 Elemental energy calibration of the SB detector for ^{19}F and ^{40}Ca recoil ions from test sample **CaF_1**.

The calibration shows linear response within the energy range used for calibration for each ion species but gives different offsets due to the well known ion dependent pulse height defect effect [13] in the SB detector.

3.7.4 Energy resolution: comparison of SBD and ToF detectors

Factors that contribute to the total energy resolution, briefly discussed in Section 2.3, are either due to experimental conditions or due to the nature of the target itself. The summation of the individual contributions is a non trivial task; a detailed theoretical treatment of the subject can be found in work by Szilágyi [24], already mentioned in section 2.3. Szilágyi and co-workers' work on theoretical approximations for depth resolution calculations in ion beam analysis methods resulted in a depth analysis code DEPTH, available from www.kfki.hu/~ionhp/.

The calculations implemented in DEPTH consider the following contributions to energy spread; energy and angular spread of the incident beam, energy straggling in the target sample, multiple scattering effects in the target sample, geometric energy spread due to the finite size of the beam spot and detector solid angle, energy resolution of the detection system, and for conventional ERDA and NRA, the effect of the absorber foil. While there may be instances where some of the effects are not totally independent (e.g energy straggling and multiple scattering), in practice these fluctuations of experimental and physical origin are treated as independent random variables [24]. Probability distributions of the different contributions are then convoluted together to get an effective value of the energy spread.

An attempt was made in this work to determine the *total* energy resolution from experimental energy profiles of recoils from a thin film layer and use DEPTH calculations to determine the level of energy spread contribution due to each of the aforementioned effects. Energy profiles obtained from both the SB and ToF detectors were analysed to compare the energy resolution of the detectors for light and heavy ion species, using ^{19}F and ^{40}Ca ions as examples from each mass group. The analysis entailed fitting high and low

energy edges of the energy profiles with the Boltzman sigmoidal function and taking the width of each edge as equivalent to the total energy resolution at that energy. In this way it was possible to get a sense of the variation of (energy) depth resolution with *depth* for the same recoil mass, since the high and low energy edges correspond to surface and interface recoils respectively.

Experimental energy resolution was evaluated for ^{40}Ca and ^{19}F recoils from test sample **CaF1**. Figure 3.26 shows the ToF energy spectra of recoils detected from that sample, and Fig. 3.27 illustrates an example of the fitting procedure where the high-energy edge of ^{19}F recoils is fitted. Figures 3.28 and 3.29 show the same results for the SB detector energy spectrum. The rest of the energy resolution calculations for both ^{19}F and ^{40}Ca recoils are summarised in Tables 3.3 and 3.4.

	Surface		Interface	
recoil ion	**E_{ToF} (MeV)**	**ΔE_{ToF} (MeV)**	**E_{ToF} (MeV)**	**ΔE_{ToF} (MeV)**
F	12.29	0.41	9.83	0.79
Ca	17.95	0.62	13.84	1.30

Table 3.3 Total energy resolution (ΔE_{ToF}) calculated from the ToF detector energy spectra of ^{19}F and ^{40}Ca recoils scattered from the surface and the substrate interface of target sample **CaF_1**.

	Surface		Interface	
recoil ion	**E_{SBD} (MeV)**	**ΔE_{SBD} (MeV)**	**E_{SBD} (MeV)**	**ΔE_{SBD} (MeV)**
F	12.19	0.28	9.71	0.82
Ca	17.70	0.94	13.55	1.41

Table 3.4 Total energy resolution (ΔE_{SBD}) calculated from the SB detector energy spectra of ^{19}F and ^{40}Ca recoils scattered from the surface and the substrate interface of target sample **CaF_1**.

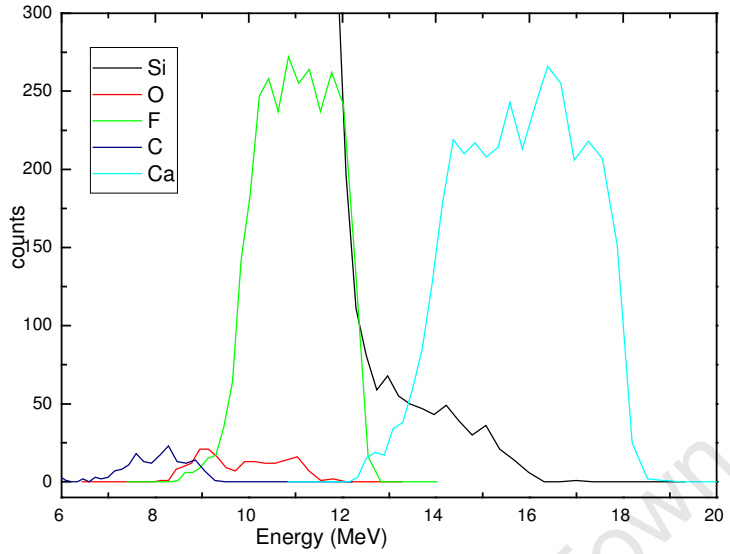

Figure 3.28 ToF calculated energy spectra of recoils scattered from target sample **CaF_1**. Also included are energy profiles of carbon and oxygen impurities detected in the CaF_2 layer.

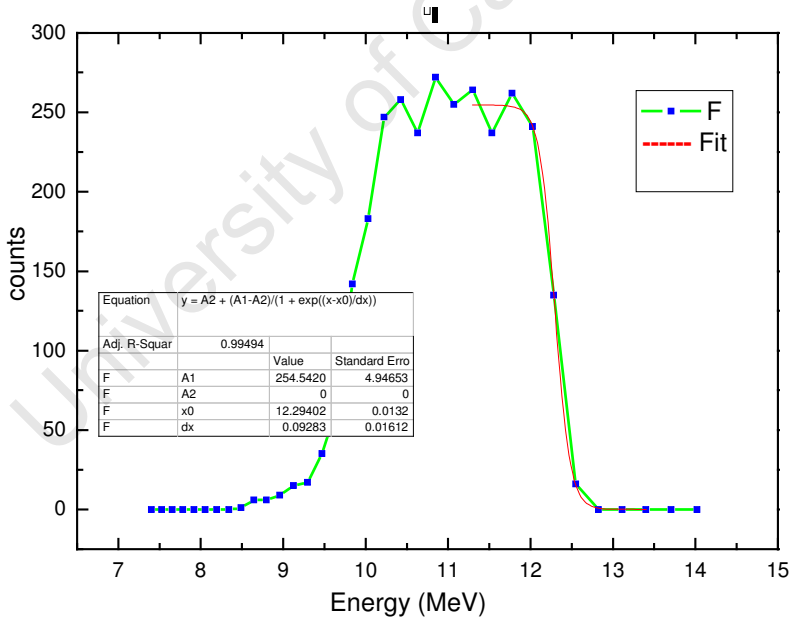

Figure 3.29 High-energy edge fit to the ToF calculated energy spectrum of ^{19}F recoils to determine the ToF experimental energy resolution. The surface energy E_{ToF} is given by x_o and the edge width ΔE_{ToF} is given by $4.395 \cdot dx$.

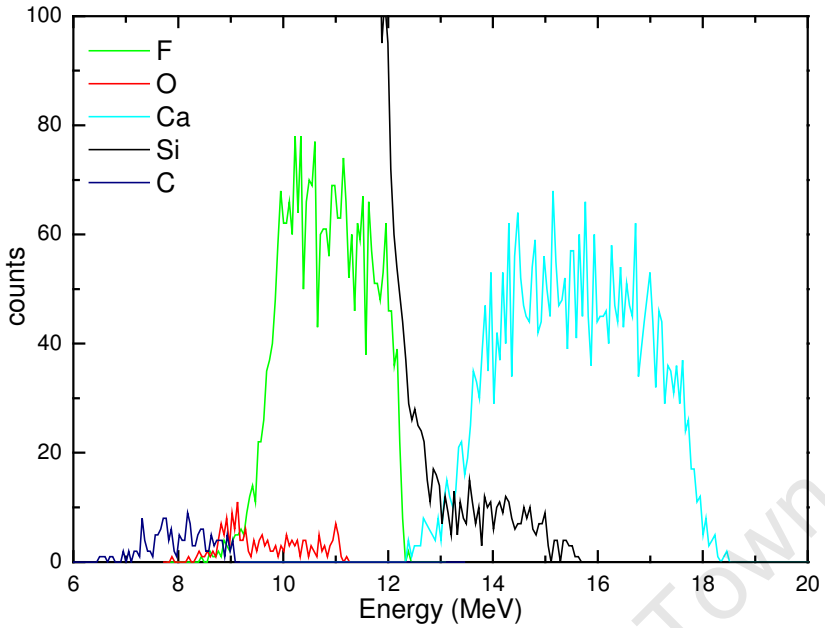

Figure 3.30 SBD energy spectra of recoils scattered from the target sample **CaF_1**. Also included are energy profiles of carbon and oxygen impurities detected in the CaF_2 layer.

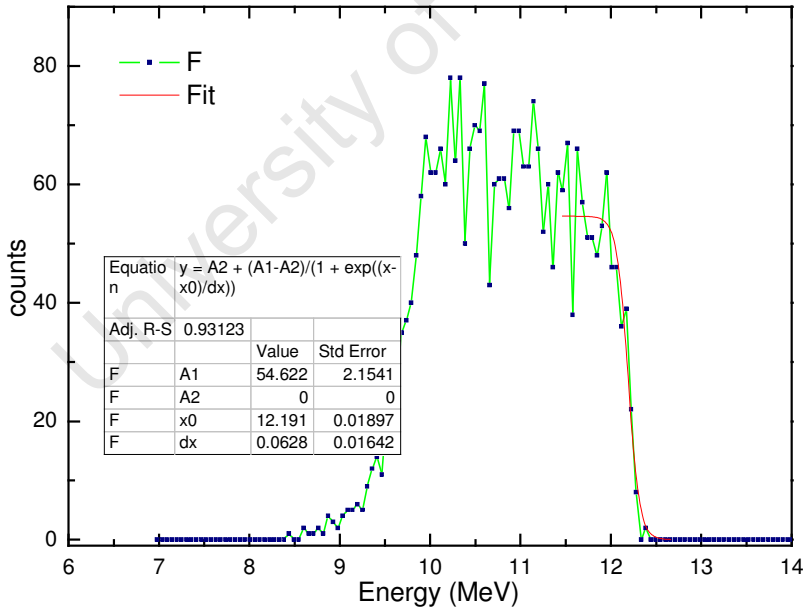

Figure 3.31 High-energy edge fit to the SB detector energy spectrum of ^{19}F recoils to determine the SB detector experimental energy resolution. The surface energy E_{SBD} is given by x_o and the edge width ΔE_{SBD} is given by $4.395 \cdot dx$.

Results recorded in Tables 3.3 and 3.4 indicate that energies measured by the SB detector are systematically lower than those measured by the ToF detector due to energy loss through the carbon foil of the second timing detector between the ToF and the SB detectors. The total energy resolution at the surface is a good indicator of the detector resolution since the surface energy resolution is dominated by the detector contribution [9]. The total energy resolution for ^{19}F surface recoils, appearing at the high energy edge, determined from the SB detector energy spectrum is better than that from the ToF detector energy spectrum. Similar calculations (not shown here) carried out for other light ions (^{12}C and ^{16}O) show that total energy resolution measured from the SB detector energy spectra is generally better than that from ToF energy spectra.

On the contrary, for the heavier ^{40}Ca recoils total energy resolution from the ToF detector energy spectrum is better than that from the SB detector energy spectrum. This situation could be a direct consequence of the fact that timing resolution generally improves with atomic mass of recoil species, leading to better ToF detector energy resolution. Experience in other Ion Beam laboratories shows that in most cases the energy resolution of ToF detectors is generally better than that of solid state detectors for most ion species except for the lightest of ions; H, He and Li [19]. For this particular set up then, the implication is that the ToF energy resolution can still be improved further.

While the main contribution to total energy resolution comes from the intrinsic energy resolution of the detector itself, it is nonetheless important to investigate how each of the effects mentioned earlier contributes to, and compares with, the experimental energy (and depth) resolution. Calculations from a code such as DEPTH become very useful in such an exercise as some of the energy resolution contributors are not so easily determinable experimentally. The main limitation in the code though is that roughness and plural scattering effects are not included.

3.7.4.1 DEPTH calculations

Energy and depth resolution calculations were made for ^{19}F and ^{40}Ca recoils from the **CaF1** test sample to estimate the level of energy spread contribution due to each of the energy

spread causes discussed in section 2.3. The experimental parameters used in the calculation for the two recoil species were as follows;

- Incident beam : 27.5 MeV $^{84}Kr^{15+}$
- Beam energy and angular spread : 30 keV, 0.1°
- Incidence angle : 15° (i.e. 65° to sample normal)
- Beam spot size : 2.0 x 4.0 mm^2
- Scattering angle, solid angle : 30° , 0.15 msr

The solid angle was calculated using the 73.4 cm distance between the target and the SBD collimator of 1.0 cm diameter. The CaF_2 layer determined by RBS measurement to be 106 nm thick, was, for the calculation, divided into about 80 monolayers of about 1 x10^{16} at cm^{-2} thick each, to get an iteration step of just over 1 nm. DEPTH was used to calculate energy spread contributions due to energy spread ($\Delta E_{beam\ energy}$) and angular spread ($\Delta E_{beam\ divergence}$) of the incident beam, energy straggling in the target sample ($\Delta E_{straggling}$), multiple scattering effects into ($\Delta E_{MS\_projectile}$) and out of (ΔE_{MS_recoil}) the target sample and geometric energy spread due to the finite size of the beam spot and detector solid angle ($\Delta E_{geometry}$). The sum of these effects gives the energy spread in recoil ions *before* reaching the detector system. The resultant depth resolution due to these beam and sample effects was also calculated as a function of depth.

Energy and depth resolution of fluorine recoils

Figure 3.30 shows the DEPTH calculated contributions to the total energy spread of ^{19}F ions as a function of depth. The experimental energy resolution (determined from the SB detector energy spectrum) is shown by the two data points corresponding to the surface and interface regions. It is 0.28 MeV at the surface and 0.82 MeV at the interface. The plots suggest that geometric energy spread ($\Delta E_{geometry}$), at ~0.12 MeV, is the dominant cause of energy spread in ^{19}F surface recoil ions before they reach the detector system. Multiple scattering and straggling effects are by definition, zero at the surface. Beam energy and angular divergence account for 0.028 keV of the total energy spread. When these recoils reach the detector, the intrinsic energy resolution of the detector and energy straggling

through the foils of the timing detectors are convoluted with this initial energy spread to give the total energy resolution of 0.28 MeV that is obtained experimentally.

Energy spread calculation due to straggling in the timing foils is not currently implemented in DEPTH and so was estimated through a SIMNRA [22] calculation. The energy straggling model selected was that of Yang which takes into account charge state fluctuations of ions in Chu's modification of Bohr's simplified straggling formula. Straggling was calculated for ^{19}F ions passing through both foils, each 9.0 $\mu g.cm^{-2}$ thick. It was found to be 44 keV at an incident energy of 12.40 MeV and 38 keV at 9.80 MeV. These two energies respectively correspond to recoils originating from the surface and interface regions of the sample. On average then, energy straggling through the timing foils would be about 0.37 % of the incident recoil energy. Given a ± 10% estimate for the foils thickness variation [26], energy spread due to thickness non-uniformity was also estimated to be ± 10 % of the energy loss value, which, for surface recoils turns out to be 10 keV.

Considering just the 120 keV estimate of energy spread due to geometrical effects and the 44 keV accounted for by straggling through the foils, to get the 280 keV obtained experimentally, the intrinsic energy resolution of the SB detector for ^{19}F ions should then be about 250 keV, or 2 % of the measured recoil energy.

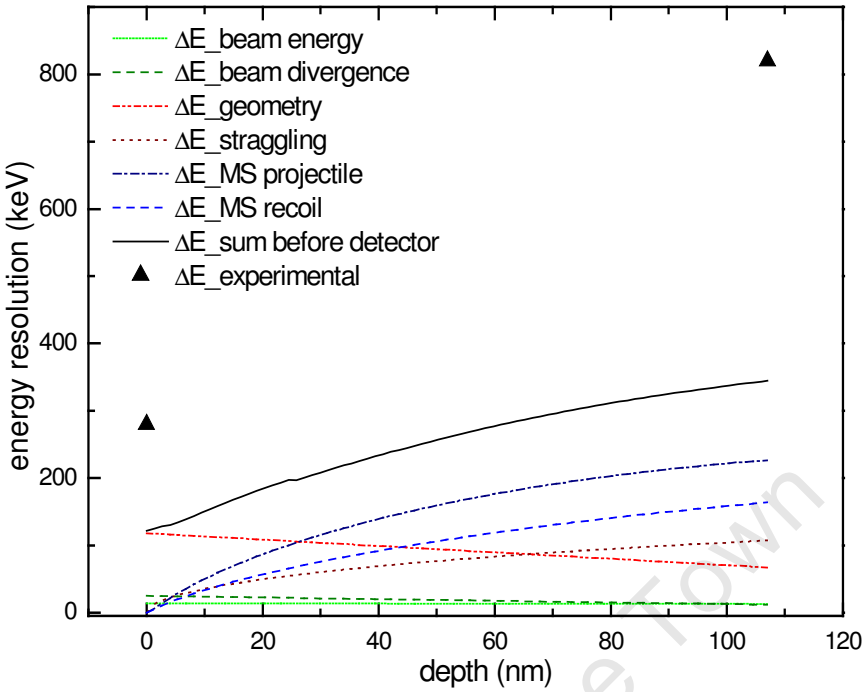

Figure 3.32 A comparison of the experimental energy resolution and the DEPTH calculated contributions to the depth-dependent total energy resolution for ^{19}F ions.

Going into the bulk of the sample $\Delta E_{geometry}$ decreases and multiple scattering effects become more dominant as the number of projectile-recoil interactions increases. It is noted that MS effects are higher for the heavier ^{84}Kr projectile ions because of the Z^2 dependency. Energy loss straggling $\Delta E_{straggling}$ also increases, but to a lesser extent. There is however a dramatic decrease in the total (experimental) energy resolution for recoils emerging from the layer-substrate interface. Assuming a marginal change in the intrinsic resolution of the SB detector over the energy range concerned, the worsening of the total energy resolution could, apart from increased multiple scattering and straggling, be attributed to roughness and (or) plural scattering. The tailing of the ^{19}F energy spectrum at low energies in Fig. 3.29 is an effect that also points to plural scattering and (or) a rough surface [25, 27].

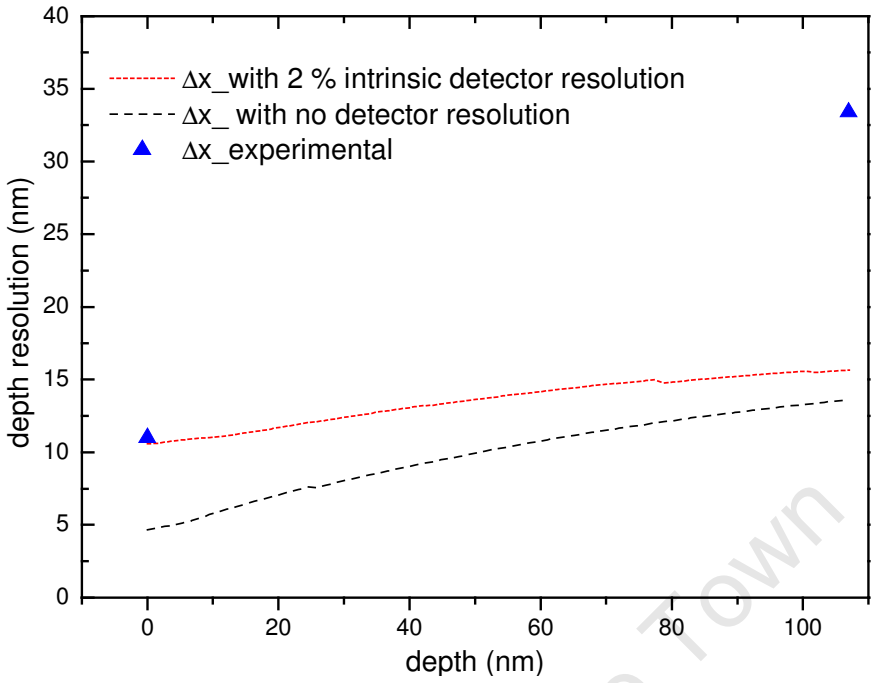

Figure 3.33 Calculated and experimental depth resolution of ^{19}F recoil ions as a function of depth, with and without the effect of the intrinsic energy resolution of the SB detector.

The depth resolution of ^{19}F ions is shown as a function of depth in Fig 3.31. The experimental depth resolution Δx was evaluated using

$$\Delta x = \Delta E / [S]_{eff} \qquad [3.17],$$

where ΔE is the experimental energy resolution corresponding to a certain depth and $[S]_{eff}$ is the effective stopping power of a given matrix for a particular recoil. The effective stopping power is a function of the stopping powers of both the projectile and the recoil ions in that matrix, S_p and S_r, respectively. It is given by

$$[S]_{eff} = K\frac{S_p}{\sin\alpha} + \frac{S_r}{\sin\beta} \qquad [3.18],$$

derived using the surface energy approximation by Chu and co-workers [28]. The angles α and β, both equal to 15°, refer to the beam incidence and exit angles respectively, measured

from the sample surface, and K is the recoil kinematic factor defined by Equation 2.1. The effective stopping power of a calcium fluoride matrix for ^{19}F (and ^{40}Ca) recoils was calculated from Eq. 3.18 making use of SRIM2008 to evaluate S_p and S_r. The effective stopping powers were evaluated at recoil energies corresponding to front and back surface energies using SRIM stopping powers [21], taking into consideration the energy lost by the incident ^{84}Kr beam traversing to the substrate interface.

The calculations give the experimental depth resolution of ^{19}F ions at the surface as 11.0 ± 0.9 nm and at the substrate interface as 33.4 ± 3.0 nm. The quoted (8 %) error term is associated with the level of accuracy of the stopping powers used, and was taken from estimates given by H. Paul [29] in his comparison of stopping power tables for light and medium-heavy ions with experimental data. Theoretical estimation from DEPTH calculation including the added effect of (at most) 2 % energy resolution of the SB detector gives a surface resolution of 10.6 nm, which compares well with the value obtained experimentally. For the interface region the theoretical estimate is 15.7 nm. The discrepancy observed here between the experimental and the predicted depth resolution at the substrate interface could be attributed to roughness and (or) plural scattering.

Energy and depth resolution of calcium recoils

Results of similar calculations of the theoretical and experimental energy resolution of ^{40}Ca recoils are shown below in Fig. 3.32. The experimental energy resolution is that of the ToF detector energy spectrum.

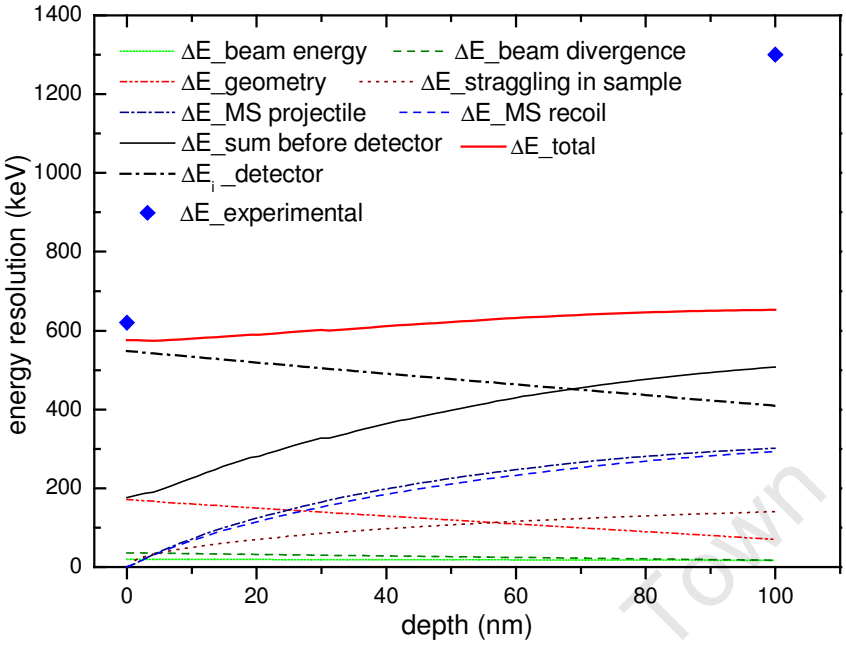

Figure 3.34 A comparison of the experimental energy resolution and the DEPTH calculated contributions to the depth-dependent total energy resolution for ^{40}Ca ions.

As in the case of ^{19}F recoils in Fig. 3.30, barring the detector resolution, the energy spread contribution due to beam spot size and solid angle dominates the energy resolution at the surface, and decreases as the sample is traversed inwards. Multiple scattering effects increase with depth and in this instance, because of a much heavier recoil ion, there is not much difference between the projectile and recoil MS effects. Energy straggling also increases with depth as the number of projectile-recoil interactions increases. The other effects, beam energy and angular spread are initially significant at the surface (higher than both MS and straggling effects), but they remain relatively much smaller with, and largely independent of, depth.

Also included in Fig. 3.32 is a 3 % estimate of the energy spread contribution (ΔE_i) due to the intrinsic energy resolution of the ToF detector. This estimate, is attributed to the detector's intrinsic timing resolution (Δt_i) [2],

$$(\Delta t)^2 = (\Delta t_i)^2 + (36.1\, L\, \Delta E)^2 \frac{M}{E^3} \qquad [3.19],$$

and was obtained by considering the contribution of $\Delta E_i(\Delta t_i)$ to the total energy resolution ΔE_{ToF} according to

$$(\Delta E_{ToF})^2 = \left(\frac{\Delta t_i}{36.1\, L}\right)^2 \frac{E^3}{M} + (\Delta E)^2 \qquad [3.20].$$

In both equations M is the mass of the recoil ion in atomic mass units, E is its energy given in MeV, L is the length of the flight path in metres and Δt_i is the intrinsic resolution of the spectrometer in nano seconds and Δt is the total (experimental) timing resolution. The intrinsic timing resolution is independent of the experimental set up (incident beam, geometry, energy, recoil species, etc), but is determined by the factors like the quality of the output timing signals from the MCPs and delays in the signal processing chain.

The energy spread ΔE is, for surface recoils, a quadratic sum of the angular spread ($\Delta E_{\text{beam divergence}}$) and energy spread ($\Delta E_{\text{beam energy}}$) of the incident beam, the geometric energy straggling ($\Delta E_{\text{geometry}}$), energy straggling ($\Delta E_{\text{foil straggling}}$) in the first timing foil and energy spread due to thickness variation ($\Delta E_{\text{lateral}}$) of the foil. The first three contributions were obtained from DEPTH calculations already done for Fig. 3.32 and were found to be 36 keV, 20 keV and 171 keV respectively. Energy straggling through the timing foil was, like for ^{19}F recoils, estimated using SIMNRA to be 46 keV. Energy spread due to lateral variation in the foil thickness was again limited to ± 10 % of the energy loss value, or 24 keV (see Table 3.1). Substituting the quadratic sum (0.18 MeV) of all these energy spread contributions in Equation 3.19 and using the experimentally determined value of 0.96 ns for Δt, the intrinsic timing resolution of the spectrometer works out to be 0.90 ns.

The total energy resolution evaluated theoretically according to Equation 3.20 becomes 0.55 MeV, determined using Δt_i = 0.90 ns and ΔE = 0.18 MeV. The value of the intrinsic contribution ΔE_i due to the intrinsic timing resolution is calculated to be 0.52 MeV, which is ~3 % of the incident recoil energy, and is expected to be more or less of the same proportion over the energy range corresponding to the thickness of the CaF_2 film. The experimental surface energy resolution, according to an edge fit of the high energy edge in Fig. 3.26, is 0.62 MeV. The ~11 % difference between the experimental and the

theoretically determined values of the surface energy resolution could be due to effects unaccounted for in the theoretical calculation, such as roughness or underestimation of the timing foil thickness uniformity.

The experimental energy resolution for recoils from the substrate interface, at 1.30 MeV, is way above the theoretical estimation, just like in the case of ^{19}F ions. Again this discrepancy is attributed to possible surface roughness and (or) plural scattering. The resultant depth dependant depth resolution for ^{40}Ca recoils is shown in Fig. 3.33, with and without the effect of the detector resolution.

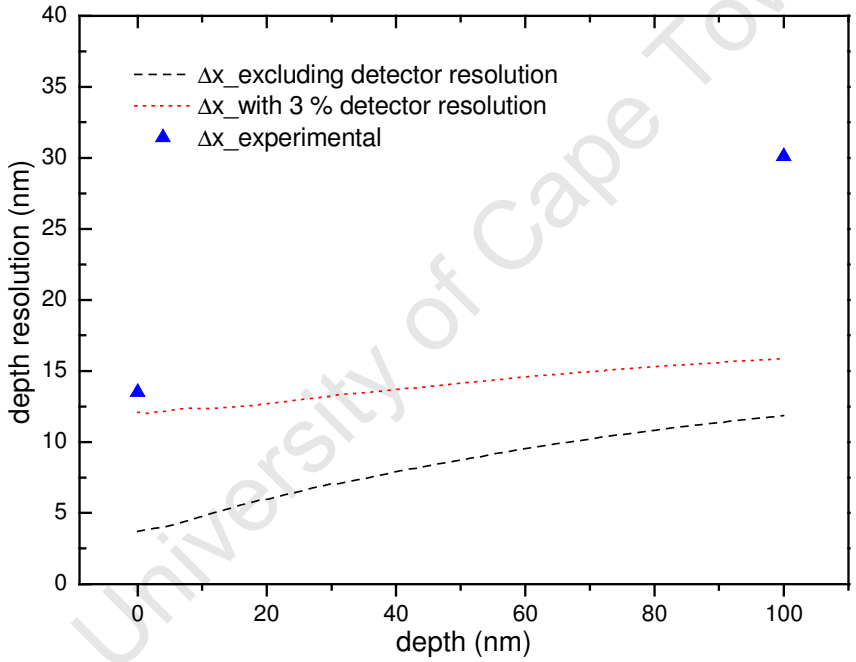

Figure 3.35 Calculated and experimental depth resolution of ^{40}Ca recoil ions as a function of depth, with and without the effect of the intrinsic energy resolution of the ToF detector.

It can be readily seen that the detector resolution indeed has the dominant effect on the surface depth resolution, but deeper in the layer multiple scattering effects and straggling become important as well. DEPTH calculations gave the surface depth resolution as 12.1 nm and that at the interface as 16.0 nm. The experimental depth resolution was

evaluated in the same manner described for ^{19}F recoils. At the surface it was found to be 13 ± 1 nm and at the substrate interface 30 ± 2 nm. The same explanation given for ^{19}F ions, of the probable cause of the huge discrepancy between the theoretical and experimental values of the depth resolution at the interface should also hold true for ^{40}Ca recoils as well; surface roughness and (or) plural scattering, unaccounted for in DEPTH calculations are the most likely causes.

3.7.5 Efficiency considerations

Absolute quantification in ion beam techniques such as RBS, NRA and ERDA generally assumes 100 % detector efficiency for particle detectors. This is particularly true for semiconductor detectors where for each particle that hits the detector volume a count gets registered [13]. The same cannot be said for $ToF-E$ telescopes where the efficiency of the timing detectors is, among other factors, largely dependent on the number of electrons ejected from the carbon foil by each passing recoil. In this instance, the yield (Eq. 2.4) of each detected recoil has to be normalised by the detection efficiency for better accuracy in quantification. A detailed experimental study by Zhang et al [30] to investigate factors that determine the efficiency of ToF detectors showed that in addition to the electron emission coefficient, which is directly proportional to the stopping power, the CFD threshold setting and the MCP bias voltage are also important factors. Their investigation covered a wide range of ions H – Nb at energies 0.05 to 1.0 MeV per nucleon.

In these initial test runs, the detection efficiency for a few ions was extracted from spectra already acquired in the course of timing resolution characterisation measurements and found to increase with atomic mass from 0.75 for 9.0 MeV C ions to 0.96 for Kr ions of 8.4 – 25.0 MeV. Owing to the fact that among other factors, detection efficiency depends on experimental settings like MCP bias voltage and CFD thresholds, which are not necessarily kept the same between experimental runs carried out at different times, a detailed presentation of efficiency characterisation is reserved for Chapter 4, in the context of measurements carried out to perform real sample analyses.

3.8 Chapter Summary

Chapter 3 begins by describing the installation of the HI – ERDA set up at iThemba LABS, and goes on to detail the construction of the ToF – Energy spectrometer; piecing together the different elements that make up the ToF detectors. The signal processing electronics and data acquisition system are then described and thereafter, followed by a series of characterisation measurements.

The electronic timing resolution was found to be 0.1 ns, a rather small contribution to the total timing resolution when compared to that of the detector system. The timing resolution of the whole spectrometer was found to be on average 1.1 ns, and in relative terms was seen to improve with ion mass. Energy calibration measurements and analyses showed that the SBD has a better energy resolution than the ToF detector for light elements $Z \leq 9$ but the ToF detector shows better energy resolution for heavier elements.

Depth resolution capabilities of the spectrometer were investigated experimentally and compared with extensive theoretical calculations performed using DEPTH code. Theoretical prediction was largely in agreement with experiment for depth resolution at the sample surface. The resolution at the surface region of a thin CaF_2 film deposit was shown to depend largely on the detector resolution. Energy spread due to beam spot size was demonstrated to be an additional major contributor to surface depth resolution. Going deeper into the sample though, multiple scattering and straggling effects were seen to become more dominant for recoils just ejected before reaching the detector. Roughness and plural scattering effects were suspected to be the most probable causes of poor resolution at the substrate interface.

3.9 References

1. Giangrandi S. et al, *Nucl. Instr. and Meth.* **B 266** (2008) 5144.
2. Kim J. K. et al, *Nucl. Instr. and Meth.* **B 140** (1998) 380.
3. Razpet A., Pelicon P., Rupnik Z. and Budnar M., *Nucl. Instr. and Meth.* **B 491** (2003) 272.
4. Bohne W., Röhrich J. and Röschert G., *Nucl. Instr. and Meth.* **B 136 – 138** (1998) 633.
5. Siketić Z., Radović I. B. and Jakšić M., *Nucl. Instr. and Meth.* **B 266** (2008) 1328.
6. Thomae R., *iThemba LABS Accelerator Group, private communication* (2007).
7. Dollinger G., *Universität der Bundeswehr München, private communication.*
8. Busch F., Pfeffer W., Kolmeyer B., Schiil D. and Pihlhofer F., *Nucl. Instr. and Meth.* **171** (1980) 71.
9. Dollinger G and Bergmaier A. (2009), in *Handbook of Modern Ion Beam Materials Analysis*, Editors Wang Y and Nastasi M, MRS, Warrendale, Pennsylvania
10. Wiza J. L., *Nucl. Instr. and Meth.* **162** (1979) 587.
11. OrcAD PSPICE Reference Manual (1998) Version 9.0 OrCAD, Inc. USA.
12. Wright A.G., *Nucl. Instr. and Meth.* **A 504** (2003) 245.
13. Knoll G. F, *Radiation Detection and Measurement*, 3rd Edition, Wiley and Sons, New York, 2000.
14. Van Aarle J., Westmier W., Esterlund R. A and Patzelt P., *Nucl. Phys.* **A 578** (1994) 77.
15. ORTEC Constant Fraction Discriminator (CFD) manual (2006) <www.ortec-online.com/electronics/disc/935.htm> accessed June 2006.
16. Ritt S. and Pierre – Andre A., *Maximum Integrated Data Acquisition System* http://midas.triumf.ca accessed 2007.
17. Murray S. *MIDAS Data Acquisition for HI – ERDA at iThemba LABS, private communication*, (2007).
18. Strub E., Bohne W and Röhrich J., *Nucl. Instr. and Meth.* **B 249** (2006) 62.

19. Tirira J, Serruys Y and Trocellier P, *Forward Recoil Spectrometry – Applications to hydrogen determination in solids* (1996) *Plemm Press, New York.*
20. Bergmaier A., Dollinger G., Frey C. M and Faestermann T., *Ferenius J. Anal. Chem.* ***353*** (1995) 582.
21. Ziegler J. F. (2008) SRIM-2008 computer code, available from http://www.srim.org (accessed June 2008).
22. Mayer M., *SIMNRA User's Guide,* Technical Report IPP9/113, Max – Planck Institut für Plasmaphysik, Garching, Germany, (1997).
23. Graper E., *Lebow thin film data book*, Lebow Corporation, 1990.
24. Szilàgyi E., Pàszti F. and Amsel G., *Nucl. Instr. and Meth.* **B100** (1995) 103.
25. Behrisch R., Grigull S., Kreissig U. and Grötzschel R., *Nucl. Instr. and Meth.* **B 136 - 138** (1998) 628.
26. ACF-Metals (2007), Product Descriptions and Technical Information, available from http://www.techexpo.com/WWW/acf-metals
27. Yesil I. M., Assmann W., Huber H. and Löbner K. E. G., *Nucl. Instr. and Meth.* **B 136 - 138** (1998) 623.
28. Chu W. K., Mayer J. W. and Nicloet M. *Backscattering Spectrometry* (1978), *Academic Press, New York.*
29. Paul H., *Nucl. Instr. and Meth.* **B 247** (2006) 166.
30. Zhang Y. et al., *Nucl. Instr. and Meth.* **B 149** (1999) 477.

Chapter 4

Test analyses of thin film and bulk samples

4.1 Introduction

The introductory chapter of this work alludes to the point that multiparameter detector systems like ToF – Energy spectrometers in Heavy Ion – ERDA greatly improve the analytical strength of the technique when compared to the conventional *foil – detector* configuration. For instance, for a ^{84}Kr projectile, a range of light elements (A ≤ 40) can be analysed simultaneously with much better energy resolution using a *ToF – Energy* spectrometer than usually attainable in a *foil – detector* set up [1]. The closing subsections of Chapter 3 deal with characterisation of the physical parameters of the detector system as a whole, such as timing resolution, energy and depth resolution. The bulk of this chapter details results of measurements carried out to assess performance aspects of the *ToF – E* spectrometer specific to the analysis of light elements in thin film and bulk matrices. Key attributes of the set up that are investigated, namely mass resolution, detection efficiency, depth profiling and thickness measurement, and detection limit are demonstrated through analyses of a variety of samples.

The measurements described in section 3.7.2 had as their main objective the determination of the timing resolution of the detector system for different ions. In parallel with that objective, some of those measurement results are analysed again here in section 4.2 to determine the effect of timing resolution on the mass resolution of the spectrometer. Detection efficiency, depth profiling and thickness measurements are demonstrated in section 4.3 through the analysis of a layer of chromium oxide deposit on a silicon substrate [2]. Section 4.4 describes the analysis of amorphous silicon [3] and steel samples [4] to get a measure of the detection limit of the spectrometer for light elements.

4.2 Recoil mass resolution

Key to the optimal performance of a Heavy Ion – ERDA set up is the ability of its detector system to separate recoil ions of adjacent mass. In other words the mass resolution Δm of the detector system determines the range of atomic species that can be analysed unambiguously. In a typical ToF – ERDA set up the mass resolution is a function of the SBD energy resolution ΔE_{SB}, the timing resolution Δt and to a lesser extent the relative variation $\Delta l_F / l$ in the lengths of actual flight paths followed by recoils between the timing foils [5, 6].

$$\frac{\Delta m}{m} = \sqrt{\left(\frac{\Delta E_{SB}}{E}\right)^2 + \left(\frac{2\Delta t}{t}\right)^2 + \left(\frac{2\Delta l_F}{l}\right)^2} \qquad [4.1].$$

[Δl_F is not to be confused with Δl; the uncertainty in the distance between the two time detectors].

In the various test measurements carried out in this work a common observation made was that the timing resolution for all the ions detected changed appreciably from one experimental setting to the next. For a given ion species of a particular energy the variation in ΔE_{SB} between measurements is generally insignificant. The path length variation between recoil particles is also negligible [5,7]. It was then deemed important to investigate and understand how different measurement settings for different kinds of analyses affect the timing resolution and ultimately, the mass resolution of the spectrometer.

4.2.1 Analysis of CaF_2\Si and plain Si samples

An approach that seemed quite logical to follow was to compare experimental data obtained from the same type of standard samples of known composition but analysed under different experimental conditions. This was so as to compare the mass resolution of the same recoil ions under different experimental settings. In the course of measurements described in Chapters 3 and 4, CaF_2\Si and plain Si standards were used to provide three of the time calibration data points from Ca, F and Si recoil ions. Experimental data compared here from

these standards was collected during timing resolution measurements already described in Chapter 3, from hereon denoted **TR** tests, and during experiments to measure carbon content in steel samples; from hereon shortened to **DL** tests (for detection limit).

For measurements targets were positioned at 15° grazing incidence angle to an oncoming 27.5 MeV Kr^{15+} beam [see Fig 3.6]. The beam current, measured upstream at a point 3 m before the target, was set at about 20 nA at that point, and so it can be safely assumed that the current on target was just below 20 nA for all the targets. The beam spot size, measured as described in Section 3.2.1, was about 2.5 x 4.0 mm^2. With the above settings unchanged in both sets of experiments, the SBD energy resolution was not expected to be significantly different between measurements either. The same goes for the flight path difference.

The **TR** tests differed from the **DL** tests in two ways. Firstly, and perhaps more importantly, the timing filter preamplifiers (P1 and P2 in Fig. 3.14) were excluded in the **TR** measurements, but *had* to be used in the **DL** measurements. This was because of the apparent deterioration in the intrinsic gain of the MCP detectors to an extent that the MCP output signals had to be amplified before feeding into the timing units; the CFDs. Secondly, for the **TR** tests only the high-energy (fastest) recoils were of interest and so the TDC was set at the smallest possible time range of 140 ns. For **DL** tests however the analytical depth had to extend beyond the surface region and so the TDC time range was increased to 250 ns to accommodate low energy recoils (down to 0.03 MeV/u). Time calibration for the **DL** measurements yielded the following calibration equation;

$$ToF = 0.773 ns/ch * ch\# - 173.78 \ ns \qquad [4.2].$$

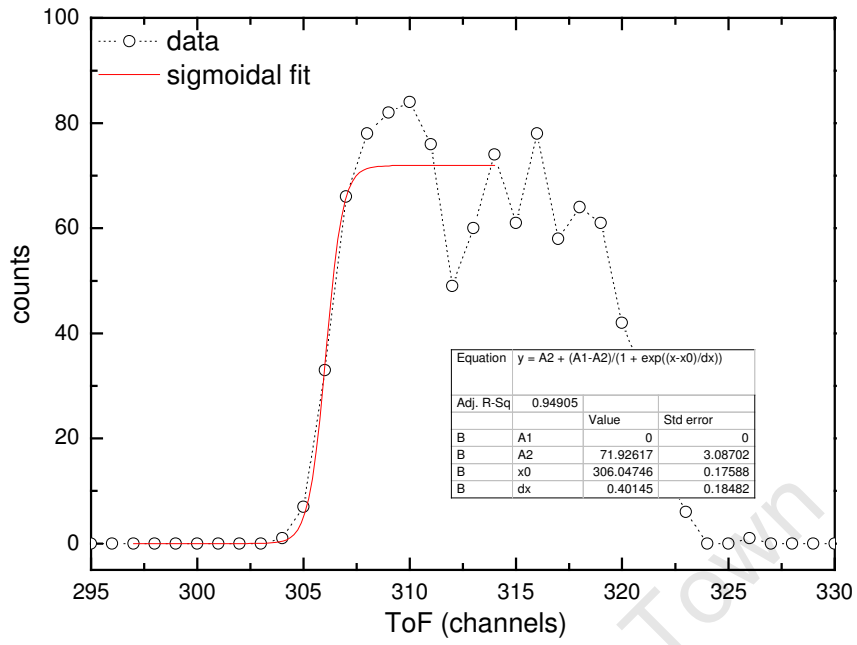

Figure 4.1 ToF projection of the ToF – Energy scatter plot to determine the channel number and width of the short time edge of ^{40}Ca recoils from the sample surface.

Figure 4.1 is an illustrative example showing the ToF spectrum of ^{40}Ca recoils from CaF_2\Si standard **CaF_2** obtained during **DL** tests. The sigmoidal fit to the short time edge gives the channel number x_o corresponding to the ToF of recoils coming from the surface. The width of the short time edge is 0.401 x 4.395 channels (from Equation 3.9), which translates to 1.36 ns timing resolution. For the **TR** measurements discussed in section 3.7.2, the timing resolution for ^{40}Ca recoils of similar energy was found to be 0.96 ns [see Fig. 3.21]. Table 4.1 summarises the comparison of the timing resolution for ^{40}Ca, ^{19}F, and ^{28}Si recoils obtained under the two measurement settings.

As the measurement results show, for these and other ions not included here, the use of timing preamplifiers worsened the timing resolution; increasing it by a factor greater than two in most instances. The qualitative effect of this on the mass resolution, albeit small, can be clearly seen in 2-D Time of Flight – Energy (ToF-E) scatter plots in Fig. 4.2. The individual mass contour lines tend to broaden as the time resolution deteriorates, especially for the lighter ions C, O and F. Not only that, increasing the TDC range setting brings the mass contour lines even closer together, blurring the boundaries between the already

broadened lines. A case in point here is the O and F mass contour lines. The net effect is that elemental analysis is not quite accurate when the mass contour lines are indistinguishable. Another deleterious effect of the preamps is an increase in accidental coincidences due to amplified MCP noise signals, which leads to a significant proportion of background events in the 2-D scatter plot.

Ion	**ToF (ns)**	**Time resolution (ns)**	
		TR Measurement settings: no timing preamps TDC range: 140 ns	**DL** Measurement settings: timing preamps connected TDC range: 250 ns
Ca	63.04	0.960	1.36
Si	56.86	1.23	1.94
F	52.24	1.08	2.65

Table 4.1 Results showing the effect of measurement settings on the timing resolution for three ions.

In an attempt to quantify the mass resolution under the different measurement settings, a procedure suggested by Kottler et. al [8] was adapted to convert the 2D ToF – E scatter plots into mass spectra using ORIGIN®. The conversion of scatter plots like the ones shown in Fig 4.2 into atomic mass spectra, from which the experimental mass resolution Δm is then determined, is the subject of sub-section 4.2.1.1 below. The procedure is exemplified by the analysis of the **CaF_2** sample from the DL runs, with the TDC set at the 250 ns range.

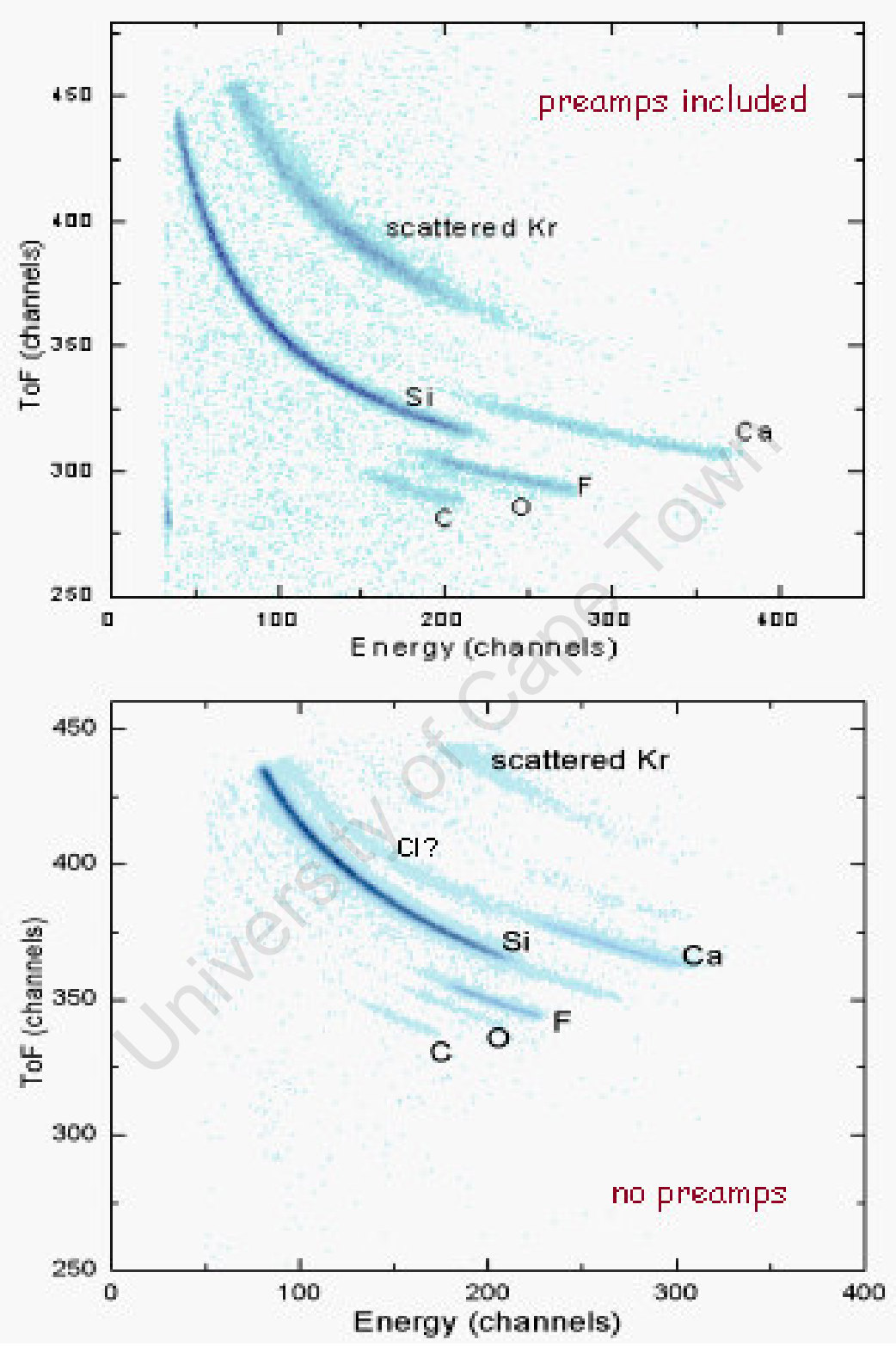

Figure 4.2 2-D ToF – E scatter plots of recoils from CaF_2\Si standards measured with (top) and without (bottom) MCP signal preamplifiers.

4.2.1.1 From 2D ToF – Energy scatter plots to mass spectra

The mass contour lines in Fig. 4.2 each follow a trajectory defined by the relationship between the time of flight and energy. For a given recoil of mass m_k,

$$t_j - t_o = K\sqrt{\frac{m_k}{E_i - E_o}} \qquad [4.3],$$

where t_o, E_o and K are calibration constants [8].

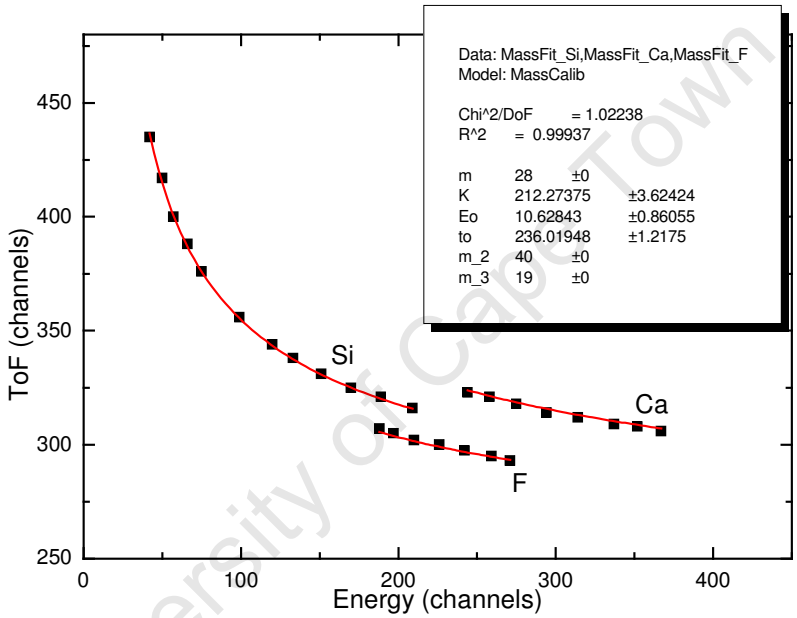

Figure 4.3 A plot of the peak coordinates along the mass contour lines for mass calibration.

Figure 4.3 is a plot of the coordinates of peak points in the ToF – Energy plane along each mass contour line. These coordinates are obtained from the scatter plot by scanning across each line along the ToF axis at several fixed energy intervals. The result is a reproduction of the scatter plot but with only a few data points to show the general trend line. A non-linear least squares fit was carried out on the three major mass contour lines in Fig. 4.2; Si, Ca and F, to determine the values of the calibration constants. In the fit procedure E_o, t_o, and K are variable parameters shared amongst the three mass curves. The three m_k's are fixed parameters, with m_1=28 **u**, m_2=40 **u** and m_3=19 **u**, representing the atomic masses of silicon, calcium and fluorine respectively. The fit results, pasted on Fig 4.3 are;

t_o = 236.0±1.2 *channels*, E_o = 10.63±0.86 *channels* and K = 212.3±3.6 $(channels)^{3/2}\mathbf{u}^{1/2}$. Each pair of coordinates (E_i, t_j) in the ToF – Energy spectrum can be associated with a mass m_k given by

$$m_k = c \cdot (t_j - t_o)^2 \cdot (E_i - E_o) \qquad [4.4],$$

where c = 1/K and i , j = 0, 1, 2…….511.

Raw data of the 2-D ToF – E coincidence scatter plot that is imported into the ORIGIN® analysis program comes in a 3 – column format; Energy (E), ToF (t) and Counts (C). If plotted in 3-D, the counts are represented by the z – coordinate. Equation 4.4 facilitates mapping the ToF – Energy matrix into a 1-D column of atomic mass, effectively converting the 2-D ToF – Energy data representation into a mass - counts domain.

The process of converting the 512 x 512 matrix generates negative m_k values or m_k values greater than the known atomic mass range. Corresponding counts for masses in these ranges, for all the calculations performed for this and all the other samples, should of necessity be all zero. This is one of the conditions that are used to check validity of the conversion procedure. In fact, in the final analysis, the calculated mass spectrum is only valid for the same mass range as that of the atomic species used for the calibration. Mass spectra of CaF_2\Si standards obtained under the two measurement settings are presented below.

4.2.2 Mass resolution with and without timing preamps

Figure 4.4 shows a mass spectrum of sample **CaF_2** resulting from **DL** measurement settings, with the timing preamps included in the signal processing electronics and the TDC set at 250 ns range.

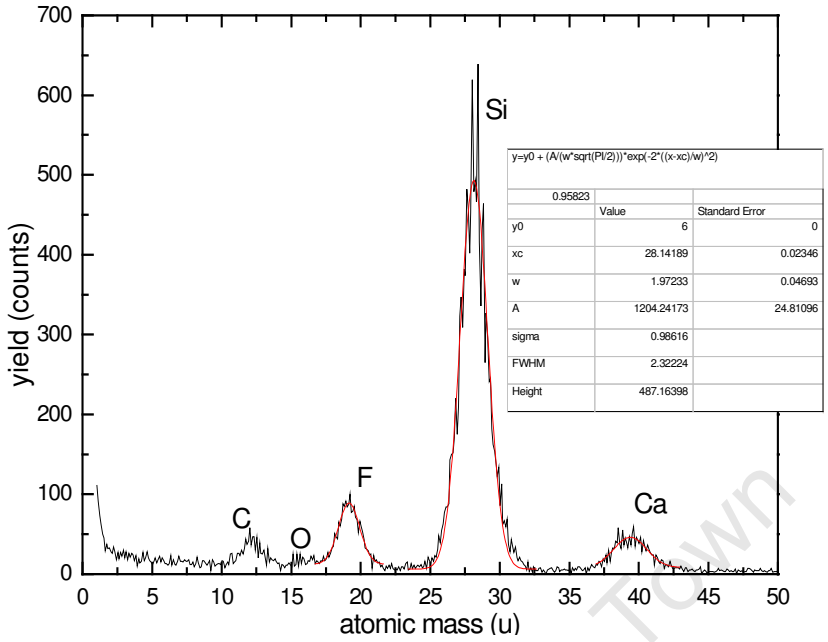

Figure 4.4 Mass spectrum of a CaF_2\Si sample, obtained under DL measurement settings.

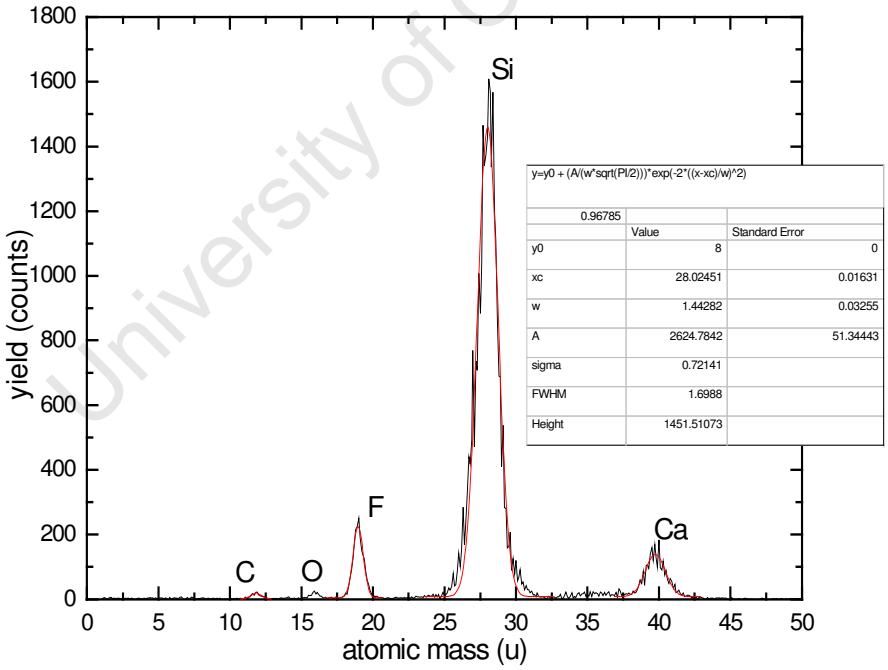

Figure 4.5 Mass spectrum of a CaF_2\Si sample obtained under TR measurement settings.

The identities of the carbon and oxygen impurities mass lines in Figs. 3.20 and 4.2 are now confirmed in the atomic mass spectrum shown. The mass resolution for each of the major ion species in the sample was determined by performing Gaussian fits to each of the elemental peaks. The peak width w was used to calculate the Full Width at Half Maximum (FWHM) used as a measure of the mass resolution Δm;

$$\Delta m = FWHM = 2\sqrt{2\ln 2}\left(\frac{w}{2}\right) \qquad [4.5].$$

The fit result pasted in Fig. 4.4 gives the mass resolution for ^{28}Si ions as 2.3 **u**. Similar fits to the ^{19}F and ^{40}Ca peaks yielded $\Delta m_F = 1.8$ **u** and $\Delta m_{Ca} = 2.8$ **u** respectively.

The mass spectrum of sample **CaF_1** from data acquired without the timing preamplifiers and with the TDC range set at 140 ns (i.e TR measurement settings) is shown in Fig 4.5. Telling features of the spectrum immediately stand out; the major elemental peaks are narrower and the amount of background noise is significantly less than in the other measurement setting. Table 4.1 is now reproduced below with the experimentally determined values of the mass resolution for the three ions included.

Ion	**TR measurement settings: No timing preamps TDC range 0 – 140 ns**			**DL measurement settings: Timing preamps connected TDC range 0 – 250 ns**		
	Δt (ns)	**Δm_{expt} (u)**	**Δm_{theory} (u)**	**Δt (ns)**	**Δm_{expt} (u)**	**Δm_{theory} (u)**
Ca	0.960	1.7	2.4	1.36	2.7	2.7
Si	1.23	1.7	1.8	1.94	2.3	2.2
F	1.08	0.9	0.9	2.65	1.8	2.0

Table 4.2 Results showing the effect of measurement settings on the timing and mass resolution for Ca, F and Si ions.

Included in Table 4.2 are calculated values of the mass resolution; calculated according to Equation 4.1 to compare experiment with theory. The SBD energy resolution ΔE_{SBD} for ^{40}Ca and ^{19}F recoils was taken as the experimental energy resolution values obtained in Section 3.7.4. These were 0.94 MeV for calcium ions and 0.28 MeV for fluorine ions. The energy resolution for ^{28}Si ions, found to be 0.70 MeV, was determined from an edge fit of the energy spectrum of a plain Si wafer as shown in Fig. 4.6. The timing resolution for each ion is given in Table 4.1. The path length variation $\Delta l_F/l$ was estimated to be much smaller than both the energy and timing resolution [7] and so was ignored in the calculation of the mass resolution.

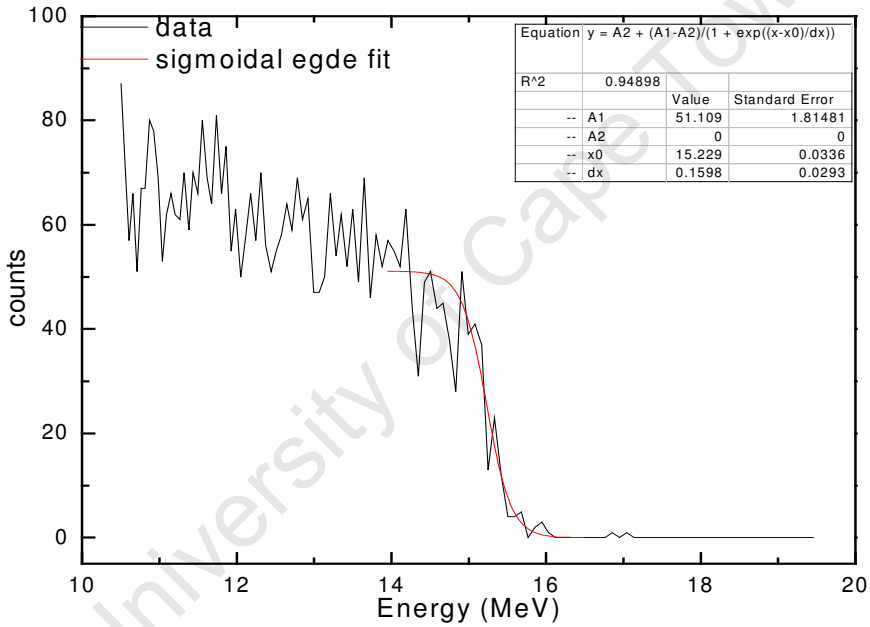

Figure 4.6 High energy edge fit to the Si energy spectrum to determine surface energy resolution

The results in Table 4.2 show that theory and experiment agree quite well (except for the TR results for ^{40}Ca ions). Theory suggests that deterioration in timing resolution would lead to deterioration in mass resolution and this is confirmed by the measurement results. When measurements are done without the preamps recoil ions up to fluorine can be separated quite clearly as Fig. 4.2 shows. The mass resolution for carbon the peak for example is 0.8 **u**. Beyond fluorine the mass resolution gets worse than 1 **u** and mass

separation gets blurred for adjacent masses. In Fig 4.5 peaks of oxygen and carbon impurities show up quite distinctly, but there is another impurity in the mass region of 35 **u** (chlorine?) not clearly identifiable. That this latter element cannot be identified with certainty attests to the limitation in mass resolution for A > 19 elements.

The use of timing preamplifiers, necessitated by ageing MCPs, is seen here to be the main cause of the deterioration in mass resolution. With a mass resolution of 1.8 **u** for fluorine ions the separation between oxygen and fluorine recoils gets rather fuzzy as Fig. 4.2 shows. The mass spectrum in Fig. 4.4 suggests that it would be even difficult to get carbon and nitrogen well separated. Apart from the degradation in mass resolution caused by the timing preamps, in the 2-D ToF- E scatter plot in Fig. 4.2 the larger TDC range also makes it rather difficult to demarcate contour lines of adjacent masses.

The implication of these findings is that timing preamplifiers should be avoided as much as possible unless the key objective of the analysis is not limited by mass resolution, which is only possible if target elements of interest differ widely in terms of mass, as in the case of measuring carbon content in steel described in Section 4.4.

4.3 Depth profiling and thickness measurement of thin layers

Spectral data used to assess the performance of the spectrometer in depth profiling and thickness measurement of thin layers is from the analysis of a target sample made up of a layer of Cr_xO_y on a silicon substrate. The sample was prepared as part of a broader study to investigate photo induced and non-linear optical properties of nano α - Cr_2O_3 coatings [2]. It was prepared by electron beam evaporation of Cr_2O_3 onto a Si substrate. The evaporant was placed in a molybdenum boat and an electron beam from a thermionic filament used to melt and vaporise it towards the substrate. The HI – ERDA measurement was also expected to determine the stoichiometry of the deposited chromium oxide layer and for this the relative detection efficiency of the spectrometer had to be evaluated.

4.3.1 Detection efficiency

The relative detection efficiency η of a $ToF-E$ detector system for any given ion species is generally defined as the ratio

$$\eta = \frac{number\ of\ tripple\ coincidence\ counts}{number\ of\ \ SBD\ \ counts} \qquad [4.6].$$

Triple coincidence here refers to coincident registration of a recoil ion in both time detectors *and* the SBD detector. The number of coincident counts over a given energy range can be obtained from the 2-D ToF *vs* Energy scatter plots and the number of counts registered by the SBD over the *same* energy range are also obtainable from the raw SBD spectra. It should be noted that for a chosen recoil ion, there should be no other ion overlapping in energy in the 2-D scatter plot. This requirement then precludes using recoils from the chromium oxide film under investigation [see Figure 4.11]. Naturally the best measurement would be where the target is a bulk single-element target.

Single element bulk target materials that could be readily sourced for detection efficiency measurement were graphite and silicon. An incidental advantage of these materials is that they span a mass range (12 – 28 u) that covers recoil ions such as ^{16}O not quite available in single element bulk form and so values of η for such ions could be estimated by extrapolation. For the measurements, a 27.5 MeV Kr^{15+} projectile beam was used, at a grazing incidence angle of 15°. Like in prior analyses, the beam spot was measured to be about 2.5 x 4 mm^2 and the beam current adjusted to just less than 20 nA. The MCP signal preamplifiers were *not* used in this instance as the MCP signals (new MCPs mounted) were found to be well above noise level and large enough not to warrant any pre-amplification. The TDC range was set at 400 ns to accommodate low energy recoils and thereby extend the analytical depth.

Acquired raw spectra were converted into ASCII format for further analysis using ORIGIN. Time and energy calibration results are given in Section 4.3.3. Figure 4.7 illustrates the general analysis procedure used to determine the detection efficiency using raw counts of carbon recoils from a plain graphite sample.

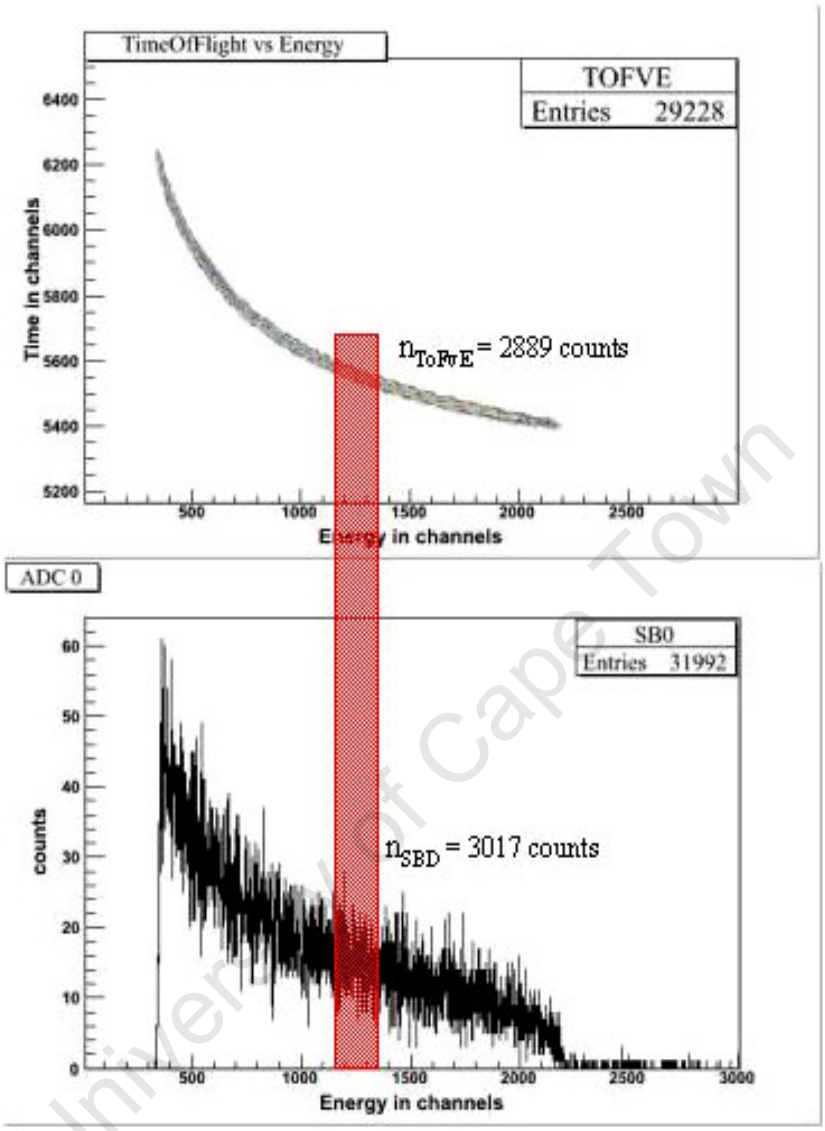

Figure 4.7 Raw ToF vs Energy and SBD energy spectra used in evaluating the efficiency of the ToF spectrometer for carbon recoils. The shaded strip shows a typical energy range over which the efficiency is averaged.

Integrating the number of counts in the 2-D scatter plot in Fig. 4.7 over energy channels 1150 to 1350 gives a total of 2889 triple coincidence counts. The same procedure in the raw SBD energy spectrum gives the total number of carbon recoils stopped in the SBD after passing through the ToF telescope as 3017. The ratio of the two integrals, 0.96, is taken as the average relative detection efficiency of carbon recoils over that energy range, spanning

about 0.70 MeV. This is repeated over the entire energy range to determine the efficiency at different energies.

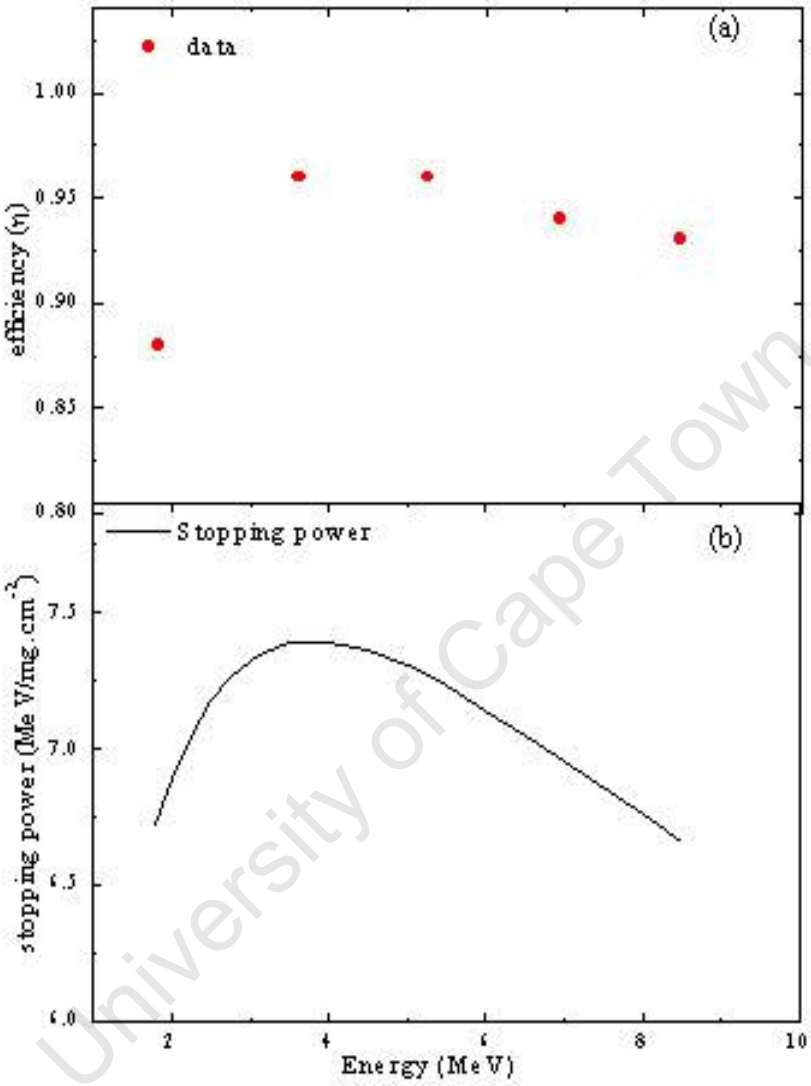

Figure 4.8 Spectrometer detection efficiency for carbon recoils (a), and stopping power (b) of ^{12}C ions in carbon as a function of incident energy.

The detection efficiency for a given ion with a particular energy depends on the number of electrons ejected from the timing foils, as stated earlier. It may well be expected therefore that the efficiency should depend on the electronic stopping power of carbon for the various ion species as demonstrated by Zhang et al [9]. Figure 4.8 **a** gives the detection efficiency

for carbon recoils as a function of energy, where the energy values are the midpoints of the energy ranges used in the calculation. Affixed to it in Figure 4.8**b** is a plot showing the variation of the stopping power of carbon in carbon over an identical energy range. SRIM 2008 code [10] was used to calculate the stopping power. What emerges from the two plots is that the efficiency follows the same pattern as the stopping power; it is lower at low energies and it also peaks at the Bragg peak and starts to decrease at higher energies.

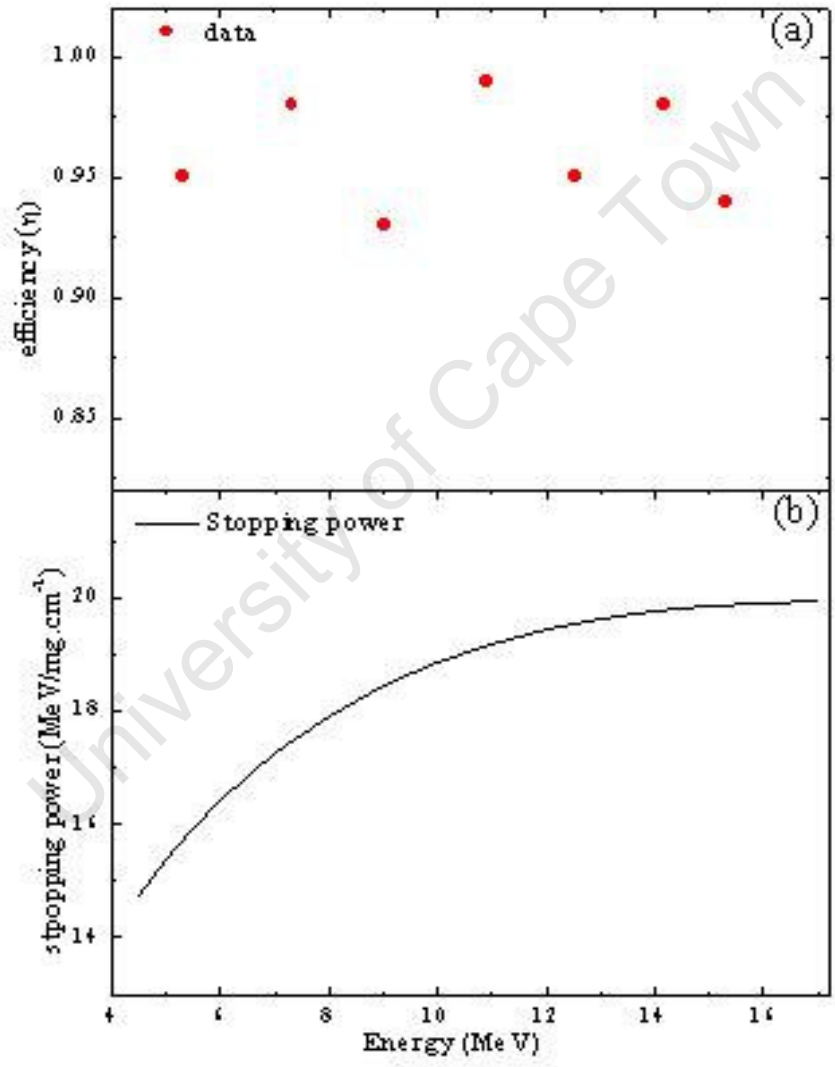

Figure 4.9 Spectrometer detection efficiency for silicon recoils (a), and stopping power (b) of ^{28}Si ions in carbon as a function of incident energy.

Figure 4.9 presents results of a similar calculation for silicon recoils. In this instance there is no clear trend between detection efficiency and energy; instead the detection efficiency appears to be independent of energy and saturated at ~0.95 over the energy range shown. The apparent scatter observed can be attributed to statistical fluctuations. The stopping power on the other hand changes considerably (more than 25 %) over the same energy range.

The two results above suggest that the detection efficiency depends on the stopping power only up to a certain threshold (about 6.0 MeV/mg cm^{-2}), beyond which the efficiency becomes constant at about 0.95. This is further illustrated in Figure 4.10 where the detection efficiency is plotted as a function of stopping power. SRIM calculations show that the stopping power of 0.1 – 1.0 MeV/u ions heavier than carbon lies above 7.0 MeV/mg.cm^{-2}. This energy range is typical of recoil ions encountered in this work. It would not be unreasonable therefore to assume that for the analysis of the chromium oxide sample described in the next section, the detection efficiency for the major recoils (O, Si, Cr) would be about 0.95, which in relative terms, becomes 1.0.

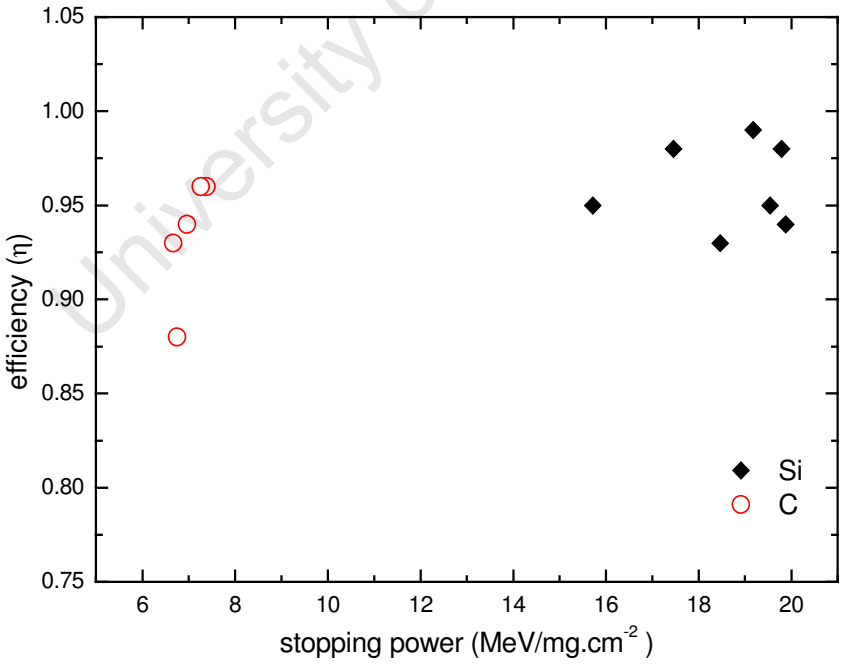

Figure 4.10 Detection efficiency η vs. electronic stopping power in carbon for ^{12}C and ^{28}Si recoils.

4.3.2 Analysis of a Cr_xO_y\Si sample

Figure 4.11 shows a 2-D ToF – Energy scatter plot of recoil ions (and scattered krypton ions) from the Cr_xO_y\Si sample. Mass contour lines of the major atomic species in the sample namely Cr, O and Si, stand out quite clearly. A closer look shows two additional mass lines of trace quantities of light elements; one between Si and O, and the other below oxygen. An inherent limitation of ToF - ERDA though is its poor mass resolution for heavy recoils [1], to an extent that mass lines of any heavy ions (in this case A > 52) present in the sample cannot be resolved from that of the forward scattered incident ^{84}Kr beam. A mass fitting procedure performed on the 2-D spectrum as described in section 4.2.1.1 yields the mass spectrum shown in Fig. 4.12, identifying the two trace impurities as magnesium and carbon.

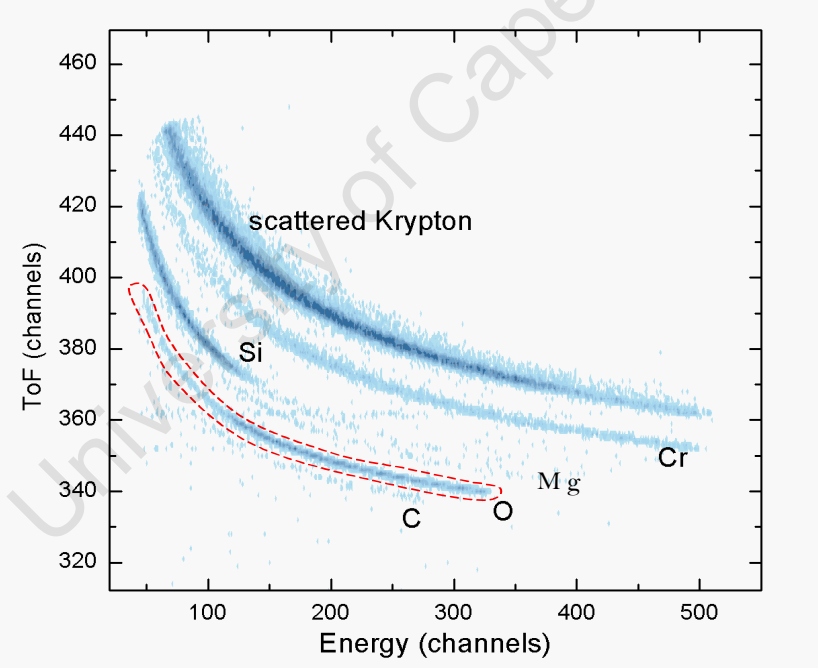

Figure 4.11 2-D ToF – Energy scatter plot from the analysis of a CrO_2\Si sample using a 27.5 MeV Kr^{15+} incident beam. The dashed line encloses an example of a region used for [oxygen] elemental analysis.

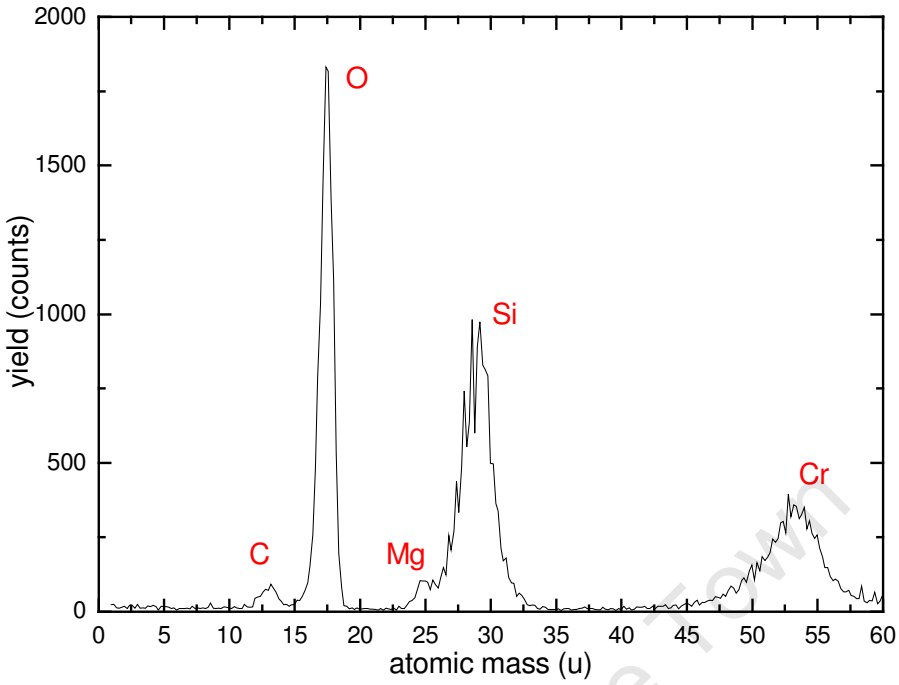

Figure 4.12 Mass spectrum of the CrO_2\Si sample showing the presence of carbon and magnesium trace impurities.

4.3.3 Energy calibration

Energy calibration was performed in the same manner as described in section 3.7.3. Table 4.3 illustrates this method using oxygen recoils as an example. Time calibration was carried out using calculated times of flight of the following high energy (surface) recoils; C from the graphite standard, O from the Cr_xO_y\Si sample, Si from an amorphous silicon sample and Cr from the Cr_xO_y\Si sample. The following calibration equation was obtained,

$$ToF = 1.504\,ns/ch * ch - 460.49\ ns \qquad [4.7].$$

The timing resolution (in ns) for each of the ion species was as follows; C (2.7), O (1.4), Si (1.6) and Cr (1.3). Because of poor statistics for the Mg recoils an upper estimate of 1.6 ns was used for the *ToF* resolution of Mg ions.

Figure 4.13 shows a linear fit to the data presented in Table 4.3 for oxygen recoils. Energy calibration parameters obtained from Fig. 4.13 were *Slope = 33.4* keV/ch, and *Intercept = 155* keV. The same procedure was repeated for the remaining ion species; C, Mg, Si and Cr. In each instance the calibration error (ΔE_{calc}) in the calculated energies due to the uncertainty in *ToF* channel centroids in Table 4.3 was estimated from

$$\frac{\Delta E}{E}=\sqrt{\left(\frac{2\Delta ToF}{ToF}\right)^2+\left(\frac{2\Delta l}{l}\right)^2} \qquad [4.8],$$

where ΔToF is taken as half the *ToF* resolution and the *ToF* value is that of high energy surface recoils, just as in Equation 3.16. Table 4.4 summarises the calibration parameters for all the five ions.

Energy (ch)	ToF (ch)	ToF (ns)	Energy (MeV)
55	388	123.06	1.87
69	379	109.53	2.36
85	370	95.99	3.07
112	362	83.96	4.01
157	354	71.93	5.46
193	349	64.41	6.82
239	346	59.89	7.88
270	343	55.38	9.22
291	342	53.88	9.74
320	340	50.87	10.93

Table 4.3 Energy calibration for oxygen recoils

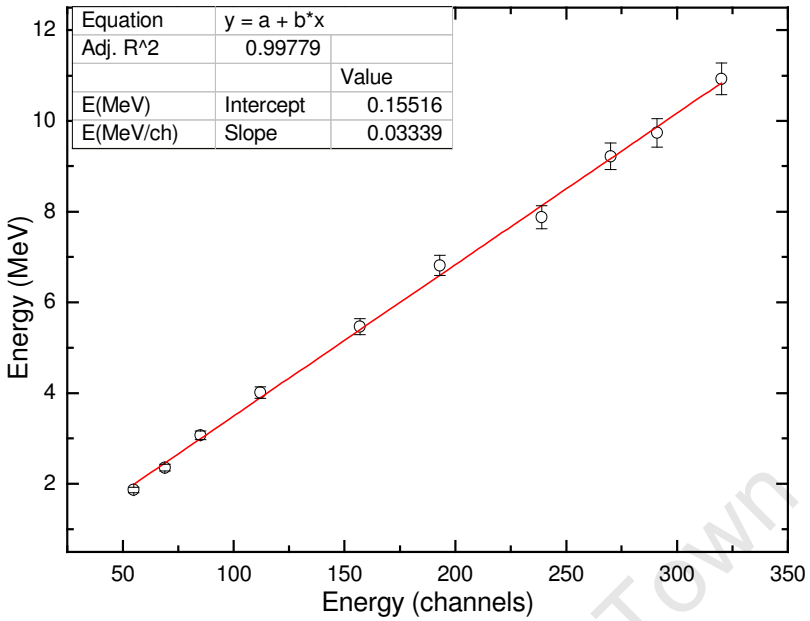

Figure 4.13 Energy calibration plot for oxygen recoils with error estimates of 3.2 % in the energy values calculated from the *ToF*.

Ion	ΔE_{calc} (%)	Slope (keV/ch)	Intercept (keV)
C	5.7	33.9	-14.3
O	3.2	33.4	155
Mg	2.9	34.7	575
Si	2.9	36.4	273
Cr	2.0	37.4	879

Table 4.4 Energy calibration factors for recoil ions detected from the Cr_xO_y\Si sample

Figure 4.14 shows energy spectra in channels of the individual recoil ions, as well as that of the scattered incident beam all plotted on the same axes. A quick kinematics calculation shows that the incident krypton ions, at 27.5 MeV, scatter off chromium atoms with an energy of about 16 MeV. This is less than the ~19.5 MeV of chromium surface recoils. The

forward scattering of krypton ions at more than 20 MeV as indicated in Fig. 4.14 then indicates presence of a heavy element (A≥79) species in the target.

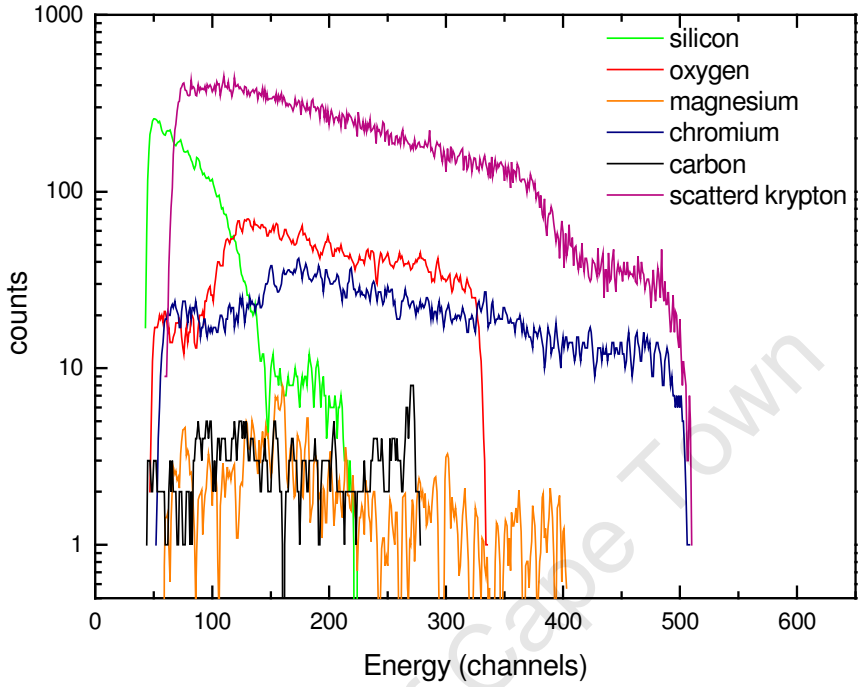

Figure 4.14 Raw energy spectra of recoils and scattered incident beam detected from the Cr_xO_y\Si sample measured in channels.

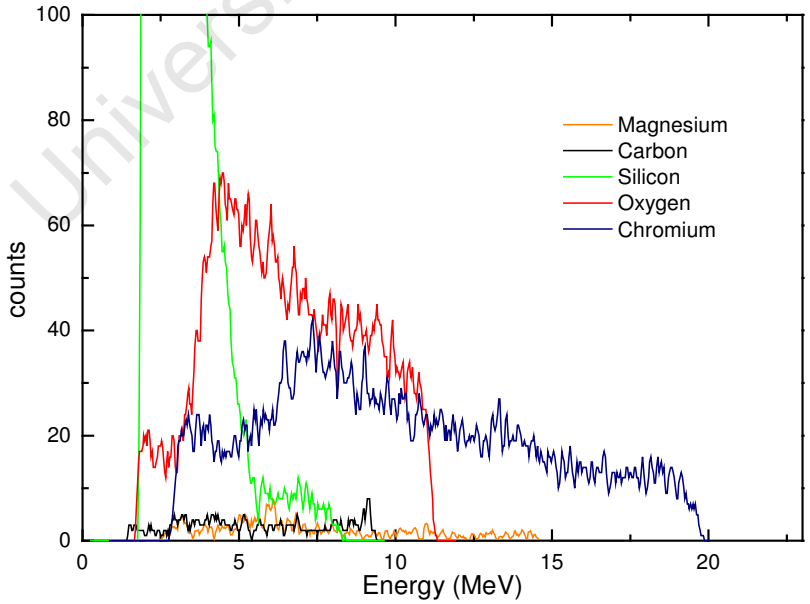

Figure 4.15 Energy spectra of recoils detected from the Cr_xO_y\Si sample.

The same spectra are now redrawn in Fig. 4.15 with the energy axis in MeV. Due to the limited mass resolution for very heavy elements, the heavy impurity present in the sample could not be resolved from the scattered krypton in the 2D scatter plot. Its identity and concentration could only be ascertained through RBS analysis, described in section 4.3.5.

4.3.4 Depth profile extraction

The analyses described in the following subsections are of the separated elemental energy spectra of recoils detected from the target. One of each of the three types of ion beam analysis codes described in section 2.4 is used to extract the sample structure from the energy spectra. The experimental surface depth resolution for oxygen and chromium recoils was calculated in the same manner described in section 3.7.4.1, from the edge widths of the elemental energy spectra using Equations 3.17 and 3.18. For oxygen, the resolution was found to be 11.7 ± 0.9 nm or (123 ± 9) x 10^{15} at.cm^{-2}, and for chromium it was found to be 13 ± 1 nm or (137 ± 10) x 10^{15} at.cm^{-2}. These surface depth resolution values are practically of the same magnitude as those of fluorine and calcium recoils calculated in section 3.7.4.1 for a CaF_2 matrix, which is an indication of consistency in the detector resolution.

4.3.4.1 Direct calculation of depth profiles using KONZERD

As already discussed in section 2.4, KONZERD [11] employs an iterative procedure to transform the energy scale of an energy spectrum into a depth scale using SRIM stopping powers, and from the measured recoil yield calculates atomic concentrations at each energy (depth) using Rutherford recoil cross sections. The code, which runs on a Linux® environment, requires as part of its input, single column energy spectra of detected recoils. Measurement parameters such as scattering angle, incidence angle, incident beam energy, projectile mass and nuclear charge, energy calibration (slope and offset) for each element, and detector resolution all form part of the input variables.

An additional pertinent parameter in KONZERD is the calibration factor for each element, important in cases where the detection efficiency η is different for different ions. Given the

detection efficiency analysis results in section 4.3.1, the calibration factor for all the recoils detected from the current sample can be considered to be one.

After a successful calculation KONZERD produces three output files; OUT1 – OUT3. OUT2 details most of the calculation result as illustrated in the excerpt in Table 4.5. OUT1 and OUT3 are smaller versions of OUT2. Table 4.5 shows entries in the first three and last three rows of OUT2. The first column is the selected depth interval from the surface into the bulk of the sample. The next five columns B – F show the variation of *relative* atomic concentration with depth. It is a *relative* concentration because not all elements in the target sample are necessarily included in the analysis. This is particularly true for heavy constituent elements of comparable mass with (and so not resolvable from) that of the incident beam.

Columns G – K give energy channel numbers corresponding to each depth interval for each atomic species. This is particularly useful for checking the accuracy of the energy calibration, since the calculated energy channel numbers at the surface region (depth ~ 0.0 /at cm^{-2}) must agree with those observed in counts *vs* energy (in channels) spectra in Fig. 4.9. The high energy edge for oxygen recoils in Fig. 4.9 is at channel ~330, and from KONZERD the surface energy in channels is 327.3. For chromium recoils the two channel numbers are 500 and 497.4 respectively.

The last column L gives the product Q of beam dose and detector solid angle at each depth interval. Beam dose and detector solid angle are external variables that are independent of the analytical depth. As such Q should not vary with depth. Should this not be the case then that would be an indication of any of incorrect energy calibration, inaccurate impinging angle and inaccurate stopping powers [12].

The calculated relative atomic concentration profiles for the Cr_xO_y\Si sample are plotted in Fig. 4.16. The average atomic ratio of the major constituents (Cr and O) of the deposited layer can be deduced from the plotted profiles. This ratio†, x/y, is roughly 1/2. The carbon

† The stoichiometric ratio of Cr and O can also be confirmed from the averages of the atomic ratios over the 0 – 2500 at cm^{-2} depth range in Table 4.5.

and magnesium trace impurity content is on average below 5 at% for both elements. The thickness of the CrO_2\Si layer was found to be (2500 ± 220) x 10^{15} at.cm^{-2}, estimated by an edge fit to the depth profile of oxygen recoils as shown in Fig. 4.17. The 9 % error is due to a conservative estimate of 8 % uncertainty in the stopping powers used, taken from H Paul's comparison of stopping power tables for light and medium-heavy ions with experimental data [13], and an upper limit of 3.4 % energy spread due to the detector resolution estimated from the width of the high energy edge of oxygen.

	A(X)	B(Y)	C(Y)	D(Y)	E(Y)	F(Y)	G(Y)	H(Y)	I(Y)	J(Y)	K(Y)	L(Y)
Long Name	depth	C	O	Mg	Si	Cr	C	O	Mg	Si	Cr	Q
Units	10^{15} at.cm^{-2}	atomic fraction					channel number					dose x Ω
1	0	0.12555	0.55452	0.01466	1E-5	0.30526	266.6	327.3	394.4	417.5	497.4	2.06E7
2	20	0.11382	0.63471	0.00934	1E-5	0.24211	265.3	325.5	391.8	414.7	493.8	2.39E7
3	40	0.05463	0.61185	0.05408	1E-5	0.27943	264	323.8	389.4	412.1	490.3	2.84E7
4	--	--	--	--	--	--	--	--	--	--	--	--
5	3300	0.00918	1E-5	1E-5	0.99079	1E-5	47.9	44.5	41.4	50.2	46.9	2.84E7
6	3320	0.01575	1E-5	1E-5	0.98422	1E-5	46.7	43.2	40.1	48.9	45.4	2.53E7
7	3340	0.01957	1E-5	1E-5	0.9804	1E-5	45.6	41.9	38.8	47.6	43.9	2.25E7
8												

Table 4.5 An excerpt of the first three and the last three rows of the main output table from a KONZERD calculation.

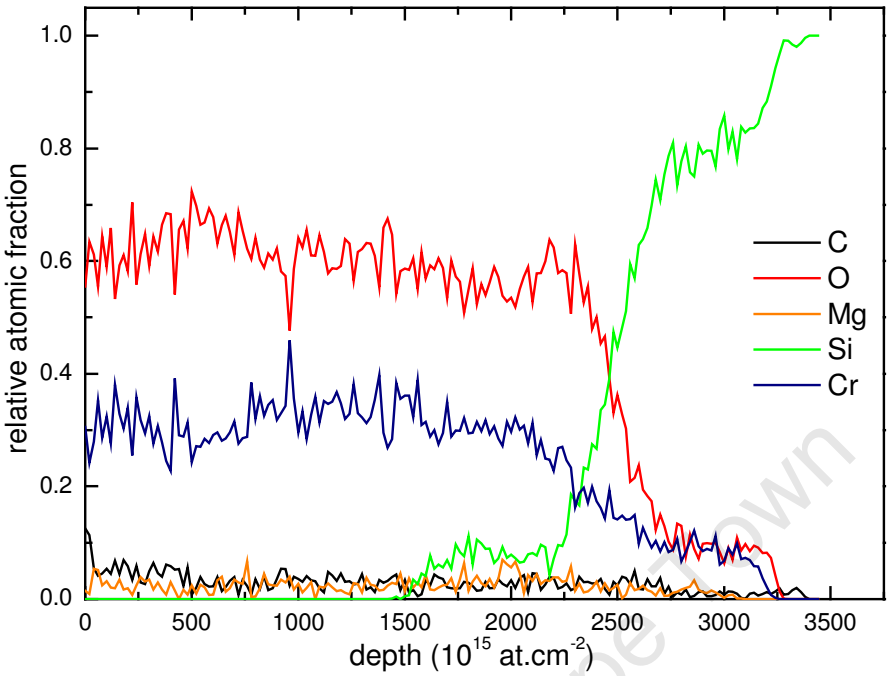

Figure 4.16 Atomic depth profiles of recoils from the CrO2\Si target sample.

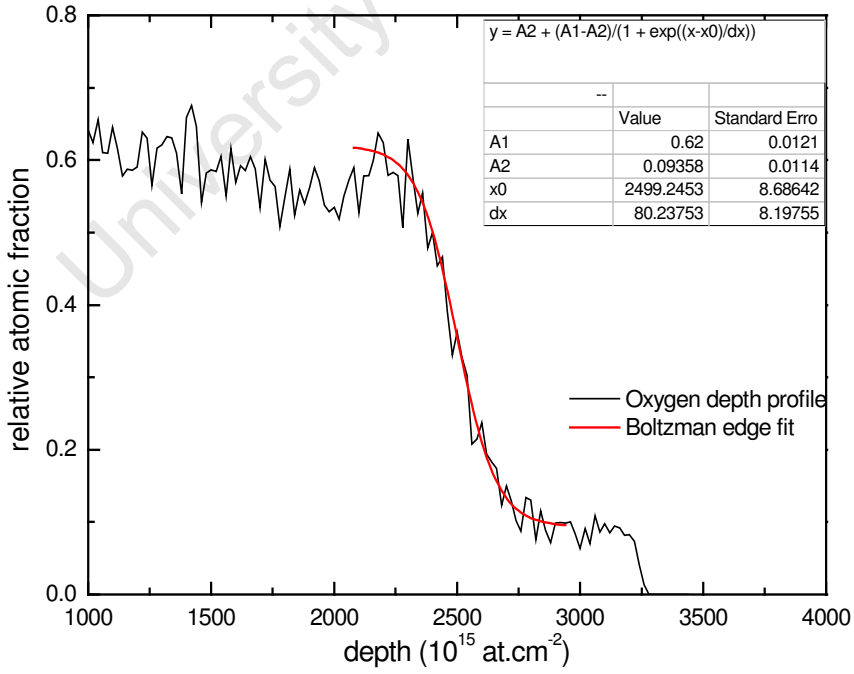

Figure 4.17 Determination of the thickness of the CrO_2\Si layer using the depth profile of oxygen recoils.

The low energy tails in the chromium and oxygen spectra in Fig. 4.15 suggest one or both of two effects; surface roughness and plural scattering. In-diffusion into the substrate is highly unlikely, as the sample was not annealed after deposition and there was no external heating of the substrate during deposition.

4.3.4.2 Iterative analytical simulation using SIMNRA

An inherent limitation of the direct calculation method, as pointed out in section 2.4, is that energy spread effects are not taken into account when extracting depth profiles from the measured energy spectra. Iterative spectrum simulation using SIMNRA [14] includes most of the beam and sample related energy spread effects described earlier.

The main aim of the analysis was to determine the thickness and stoichiometry of the deposited chromium oxide layer. As such only the oxygen and chromium energy spectra are analysed, seeing as, according to KONZERD results, the magnesium and carbon content in the layer are in trace amounts. (RBS results in section 4.3.5 show that the heavy element impurity is ^{96}Mo, but also present in minor quantity (< 1%)). Figure 4.18 compares the experimental and simulated energy spectra of oxygen and chromium recoils. The simulated spectra are from the same sample description.

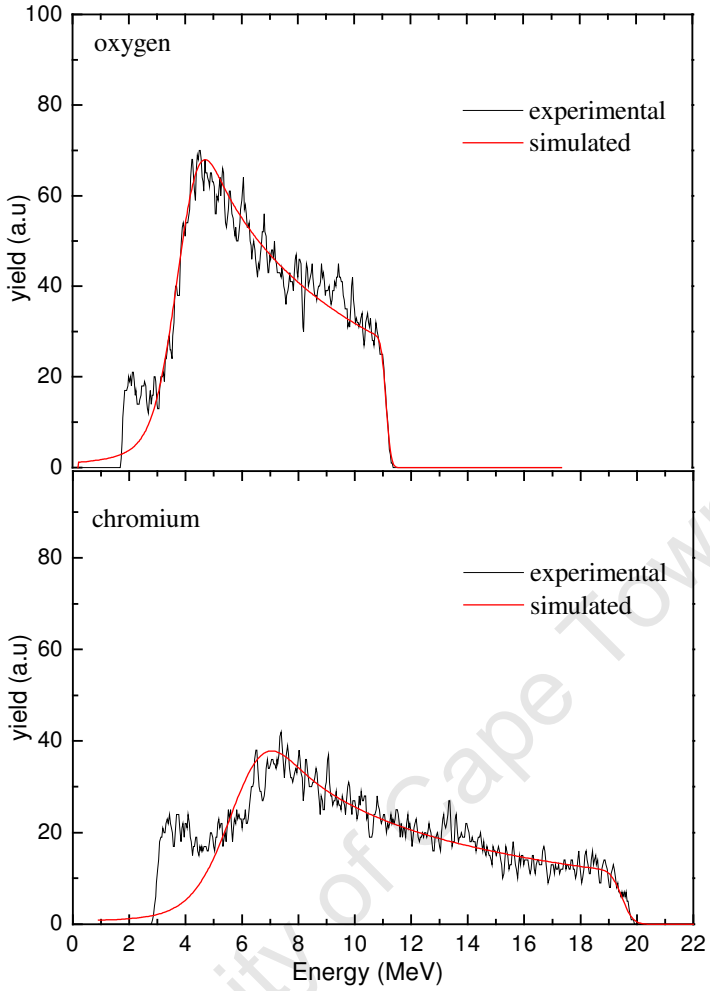

Figure 4.18 Experimental and SIMNRA simulated energy spectra of oxygen and chromium recoils from a chromium oxide deposit on a silicon substrate.

The above simulations are for a three-layer model of the deposited film. The top layer is 1030 x 10^{15} at cm^{-2} thick, with the following stoichiometry: Cr(0.28) O(0.63) Mo(0.04) C(0.02) Mg(0.03). The second layer is 1151 x 10^{15} at cm^{-2} with only a notable decrease in the proportion of the ^{96}Mo impurity; Cr(0.29) O(0.63) Mo(0.02) C(0.03) Mg(0.03), and the third layer is 260 x 10^{15} at cm^{-2} thick and with much less impurity content; Cr(0.30) O(0.68) C(0.01) Mg(0.01).

Energy spread effects included in the simulation were energy loss straggling (Chu + Yang model), geometrical straggling, multiple scattering as well as 300keV and 800 keV detector

energy resolution estimates for oxygen and chromium recoils, respectively. Dual scattering effects calculations were impractically slow and so were neglected. As for surface roughness effects, since there was no prior measurement of roughness done, a ballpark figure was obtained by gradually increasing the simulation value from zero up to a point where the slopes of the low energy edges of the oxygen and chromium spectra were optimally fitted. This was done with the optimal atomic concentrations kept fixed.

In the end the best fit was obtained using a roughness estimate of about 500 x 10^{15} at cm^{-2} (or ~20 %). The actual value is likely to be much less though since plural scattering (which has the same effect on the shape of the low energy edge) was not included in the simulation. Finally, the total layer thickness was simulated to be (2440 ± 200) x 10^{15} at cm^{-2}, with, this time the 8 % error estimate stemming from just the uncertainty in the heavy ion stopping powers. The average stoichiometry worked out to be Cr(1) O(2).

4.3.4.3 Iterative Monte Carlo simulation using CORTEO

CORTEO [15] simulations were again carried out for oxygen and chromium energy spectra from identical models of the film layer structure. Like for SIMNRA simulations, a three layer model was used with the first layer 987 å thick, consisting Cr(0.30) O(0.61) C(0.02) Mg(0.03) Mo(0.04). The second layer was 1125 å thick with the following atomic proportions Cr(0.31) O(0.60) C(0.03) Mg(0.03) Mo(0.03) and the third layer 244 å thick, consisting Cr(0.32) O(0.66) C(0.01) Mg(0.01). The best fits were obtained for 5 x 10^5 incident projectiles, a cone angle of 90^o and an ERD virtual detector 20 times larger than the real one positioned a distance of 734 mm from the target.

Monte Carlo (MC) methods have the advantage that by calculating individual ion trajectories through the sample and the detector system energy spread effects are intrinsically included in the simulations. When it comes to scattering effects there is no longer a distinction between multiple and plural scattering. What is required though is a roughness input, which unfortunately in this case was not available. A comparison of the

experimental and MC simulated energy spectra for oxygen and chromium recoils is again shown in Figure 4.19.

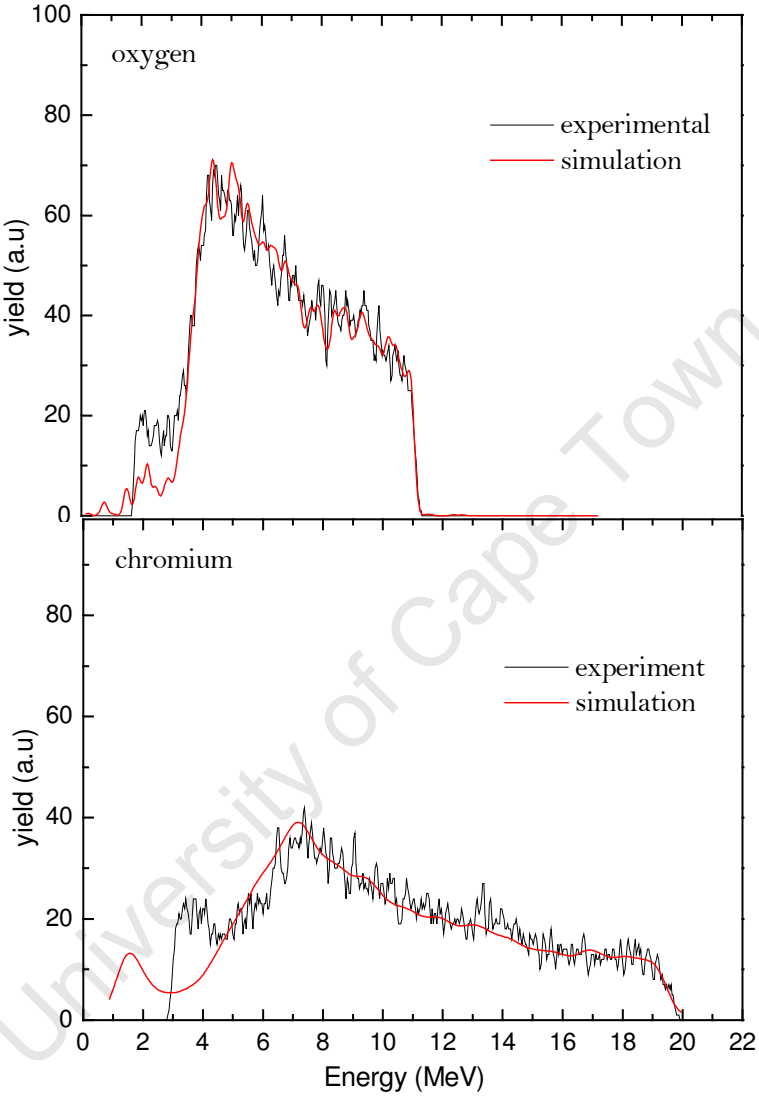

Figure 4.19 Experimental and CORTEO simulated energy spectra of oxygen and chromium recoils from a chromium oxide deposit on a silicon substrate.

What stands out in the above spectra is that the MC simulation describes the low energy tails much better than the analytical approach, presumably because of better treatment of multiple/plural scattering effects. Keeping the layer compositions fixed, the roughness of the surface layer was increased from zero in small steps until best fits were obtained at

about 290 å, or 305 x 10^{15} at cm^{-2}, assuming a bulk density of 4.89 g cm^{-3}[16]. This is much less than the estimate obtained by SIMNRA, which is understandably higher because plural scattering effects were not considered in the SIMNRA simulation. The total layer thickness according to CORTEO analysis was 2360 ± 230 å or (2480 ± 200) x 10^{15} at cm^{-2}. The average stoichiometry of the chromium oxide layer was, like in the first two analyses, found to be Cr(1) O(2).

4.3.5 Comparative RBS analysis

Rutherford Backscattering Spectrometry (RBS) was performed using an incident beam of 2.0 MeV He^{2+} ions. The sample normal was tilted 10° to the beam axis and a surface barrier detector positioned 165° to the incidence direction. Results of this analysis are included here not only to complement the HI – ERD results but also as an independent check of the latter's integrity.

The results of RBS measurement are presented in Fig. 4.20. Spectrum analysis was carried out using SIMNRA. The experimental spectrum is overlaid with a theoretical spectrum of a simulated sample structure that best matches the real sample. The simulation, on the one hand, points to a presence of a heavy element in the deposited film, ^{96}Mo, whose signal could not be resolved from that of scattered incident beam in the ToF – ERDA measurement. On the other hand, the RBS measurement cannot convincingly detect the light impurity elements Mg and C, so clearly identified by ToF–ERDA. A priori knowledge of their presence, obtained from the ToF – ERDA measurement, led to their inclusion in the RBS simulation.

The origin of the ^{96}Mo impurity can be traced back to the molybdenum boat in which the chromium oxide evaporant was placed during the electron beam deposition process. Simulation of the RBS spectrum however confirms that ^{96}Mo is not distributed throughout the whole of the deposited film; it accounts for less than 3 % of the top 2030 x 10^{15} at cm^{-2} of the simulated layer structure.

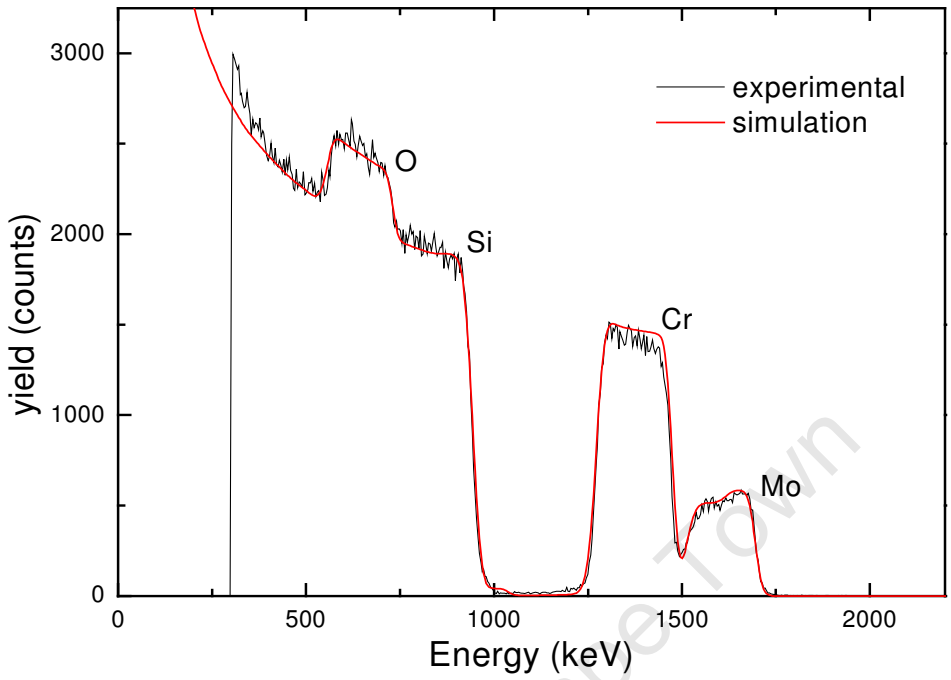

Figure 4.20 Experimental and simulated RBS spectra of the CrO_2\Si target sample. The labels indicate high-energy edges of incident beam scattered from Cr, O and Mo atoms found in the surface layers of the deposited film, as well as from the Si substrate atoms.

Using a layer model similar to that described for the ToF – ERDA simulations the thickness of the whole film was found to be (2290 ± 90) x 10^{15} at cm^{-2}, with again an average stoichiometry of Cr(1) O(2). In this case the error term is considerably smaller (~4 %) due to the fact that stopping powers of helium ions are known to a better degree of accuracy than those of heavier ions [17].

Energy spread effects included in the simulation were energy loss straggling, geometrical straggling and multiple scattering. Plural scattering was not included. Like before, an estimate of the surface roughness was arrived at by gradual increments of the simulated roughness to fit the slope of the low energy edges of the O, Cr and Mo peaks. The eventual best fit value was 290 x 10^{15} at cm^{-2}, which is of the same order of magnitude as that

estimated through MC simulation of the ToF – ERDA spectra, which accounts for plural scattering effects in a natural way.

The roughness estimate according to SIMNRA simulation of the ToF – ERDA energy spectra was 500 x 10^{15} at cm^{-2}. MC simulation of the same spectra gave an estimate of 305 x 10^{15} at cm^{-2} and now SIMNRA simulation of the RBS result gives 290 x 10^{15} at cm^{-2}. If the last two roughness values are considered close estimates of the true roughness then the large difference between the two SIMNRA estimates (ERDA and RBS) indicates that plural scattering effects are much more pronounced in a heavy ion glancing incidence configuration than in a near normal incidence helium ion RBS set up. It is advisable then that for Heavy Ion – ERDA analysis programs used particularly include multiple/plural scattering effects.

The inherent poor mass resolution of ToF – ERDA for heavy ions precludes its use in (very) heavy element analysis. An exception to that would be in instances where the *difference* between the mass of the incident beam and that of any heavy element in the target sample (and between the masses of any two such elements in the target sample) is several times the mass resolution. ^{84}Kr and ^{52}Cr provided a good example of such a scenario since the mass resolution for ^{52}Cr ions was 4.2 **u**, whereas the same could not be said of ^{84}Kr and ^{96}Mo, where the mass resolution for ^{84}Kr ions was about 10 **u**, hence the inseparable mass lines in Fig. 4.6. While RBS may also exhibit poor mass resolution for heavy elements compared to lighter ones [18, 19], the extent of this problem is certainly much less than in ToF – ERDA. The issue with using RBS for light element analysis is that peaks due to light elements are often buried within the substrate background particularly when such elements are present only in trace quantities.

In conclusion, the ToF – ERDA and RBS results were within experimental limits, found to be in agreement. The slight difference in the actual thickness values is most probably linked to inaccuracies in the stopping powers the relevant heavy ions and helium ions in the chromium oxide matrix. Multiple/plural scattering in a grazing incidence configuration, by distorting the width of the low energy edge could also be responsible. What both results affirm though is that the two techniques can be used in a complementary mode to each

other; ToF – ERDA providing information on the light element content of a sample and RBS shedding light on the heavy elements present in the sample.

4.4 Trace element analysis in bulk samples

Simultaneous detection *and* quantification of light elements in heavy element matrices has been known to be a chink in the armoury of the more established nuclear analytical techniques such as RBS, PIXE and NRA [19]. It is when these techniques are used in conjunction and the analysis results combined that more accurate conclusions may be made. The relative advantage of Heavy Ion ToF – ERDA over these other techniques is that depth profiles of several atomic species present in a sample can be obtained in a single experiment. Sections 4.2 and 4.3 aptly display this unique feature of HI – ERDA. This section seeks to quantify oxygen content in amorphous silicon samples, and to determine the amount of carbon in an unknown steel sample using a known standard. The broader aim of these analyses being the evaluation of the detection sensitivity of the ToF spectrometer for light elements in heavier matrices.

4.4.1 Determination of oxygen content in amorphous silicon

Measurements were performed to quantify the amount of oxygen impurity in intrinsic silicon layers on silicon substrates. The thin film structures were prepared as part of a broader study to investigate material properties of intrinsic silicon for applications in photovoltaic devices [3]. Oxygen is an unwanted impurity as it introduces defect states in the band gap of the intrinsic material leading to degradation in the efficiency of devices.

Three samples were prepared by Hot Wire Chemical Vapour Deposition (HW – CVD) of the intrinsic layer onto a silicon substrate. In HWCD precursor gases are decomposed at the surface of a hot filament and the resulting species deposited on a heated substrate positioned near the filament [20]. Table 4.6 below summarises the deposition conditions for the three samples that were analysed. The filament material was Tantalum.

Sample	Precursors	Gas pressure (μbar)	Filament Temperature (°C)	Substrate Temperature (°C)
S160	0.95 H_2 & 0.05 SiH_4	60	1600	410
S161		40		
S162		20		

Table 4.6 Deposition conditions for the three a-Si/Si thin film samples.

4.4.1.1 Fourier Transform Infrared Spectroscopy (FTIR) analysis

Prior to ToF – ERD analysis a host of structural, optical and electrical characterisation measurements were performed on the samples [3]. Amongst these, Fourier Transform Infrared Spectroscopy (FTIR) analyses were performed to determine the bonded hydrogen content in the samples, with the results obtained ranging between 1.3 and 1.9 at %. Of interest in the current study though is that FTIR spectra showed features that were ascribed to trace amounts of oxygen in the sample that could not be quantified. E. San Andrés and co-workers [21] have also reported on attempts to quantify oxygen in Electron Cyclotron Resonance (ECR) deposited silicon layers from FTIR measurements, but with inconclusive results. At best the results can only be qualitative, hence the need for ToF – ERDA in the case of ref [3]'s samples.

4.4.1.2 ToF – ERD analysis

The analyses described here were performed under the same experimental conditions as listed in section 4.3; 27.5 MeV Kr^{15+} incident beam, 2.5 x 4 mm^2 beam spot, 15° grazing incidence angle, < 20 nA beam current and 400 ns TDC range setting. No MCP signal preamplifiers were used either. Figures 4.21 – 4.23 show the 2D ToF – Energy scatter plots of recoils (and scattered incident beam) generated from the three samples. The recoil

mass lines were identified using the already known line trajectories of the CrO_2\Si sample recoils (see section 4.3.2).

The three plots exhibit similar features; from each sample there is the expected dominant silicon substrate mass line as well as the faint oxygen line. An unexpected carbon impurity is also observed in all three, pointing out to a possible contamination of the deposition chamber. Hydrogen is again not observed because of the ToF spectrometer's poor detection efficiency for hydrogen. Depth profiles were calculated in a similar manner as for the CrO_2\Si sample using KONZERD. Results of the calculations are shown in Figs. 4.24 – 4.26.

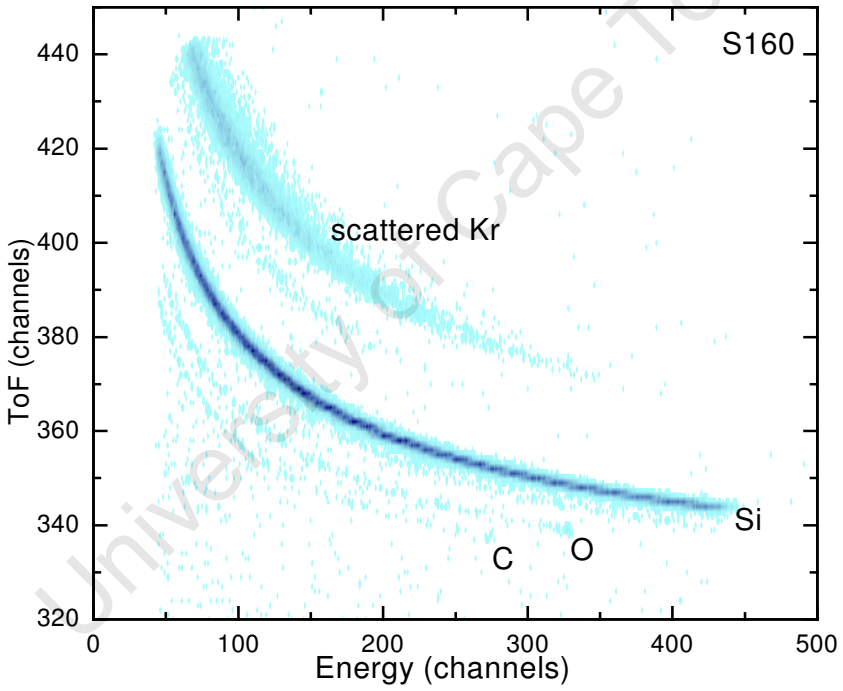

Figure 4.21 2D ToF – Energy scatter plot showing recoils detected from target sample S160.

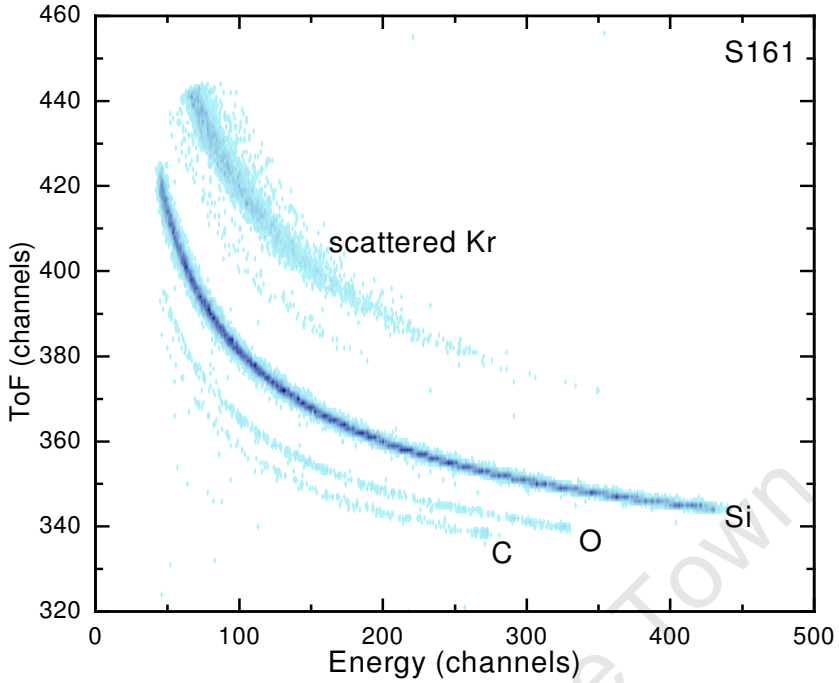

Figure 4.22 2D ToF – Energy scatter plot showing recoils detected from target sample S161.

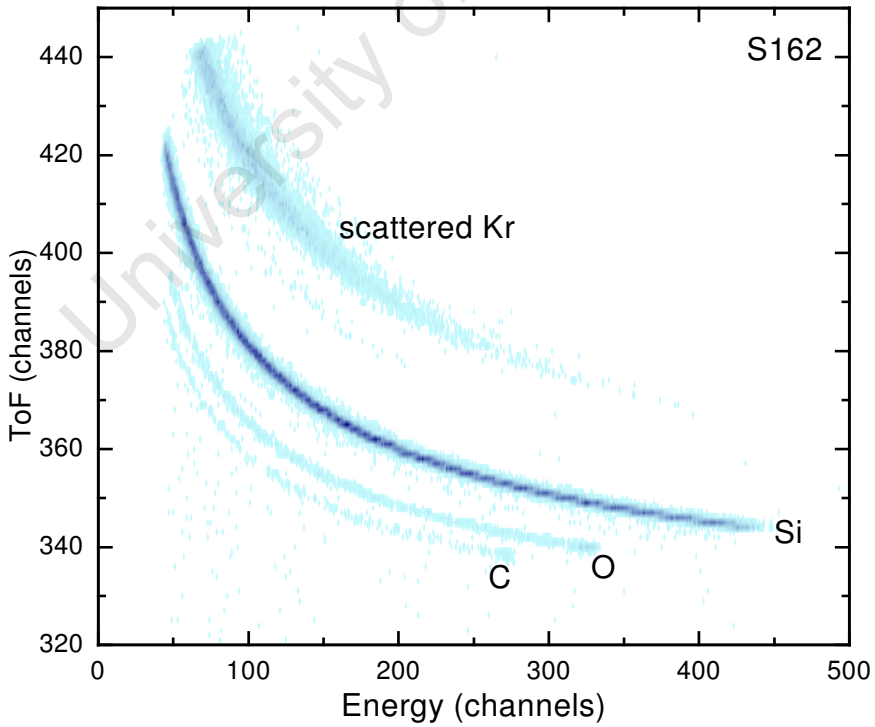

Figure 4.23 2D ToF – Energy scatter plot showing recoils detected from target sample S162.

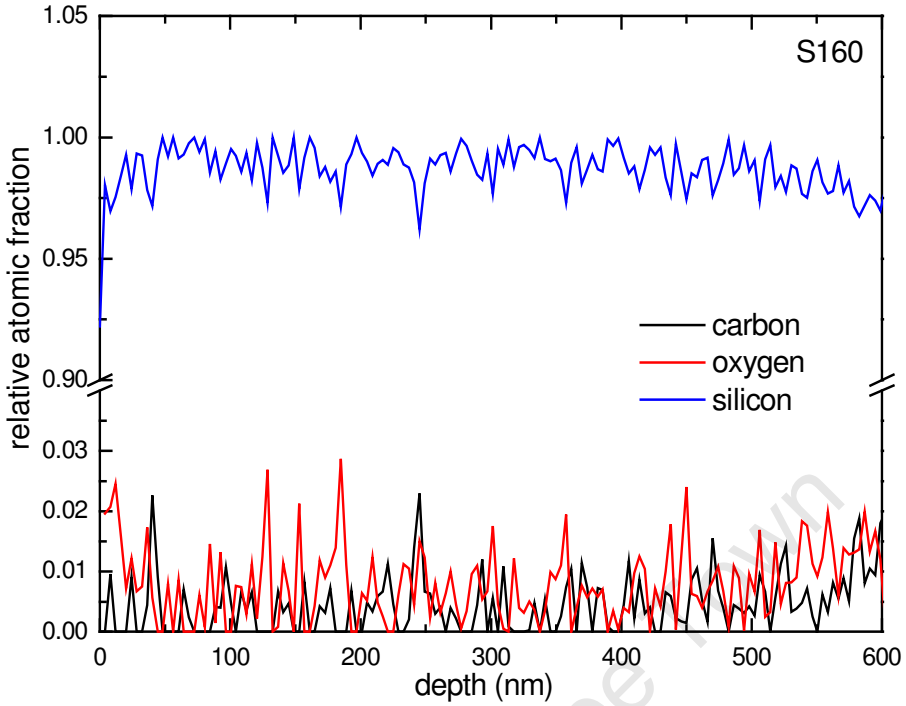

Figure 4.24 Relative atomic depth profiles of recoils from target sample S160.

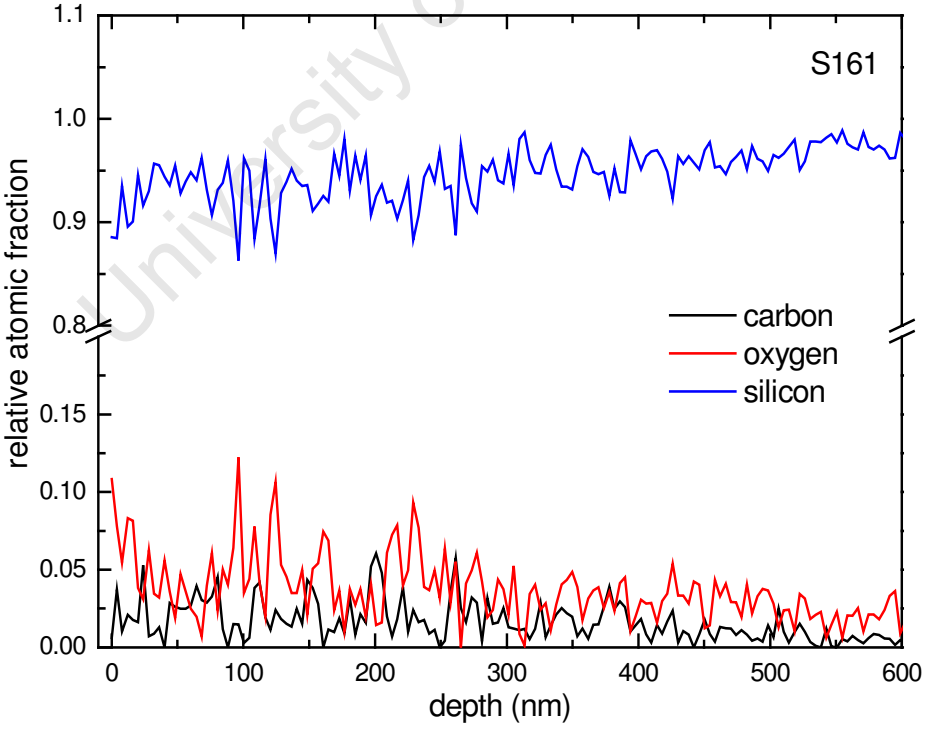

Figure 4.25 Relative atomic depth profiles of recoils from target sample S161.

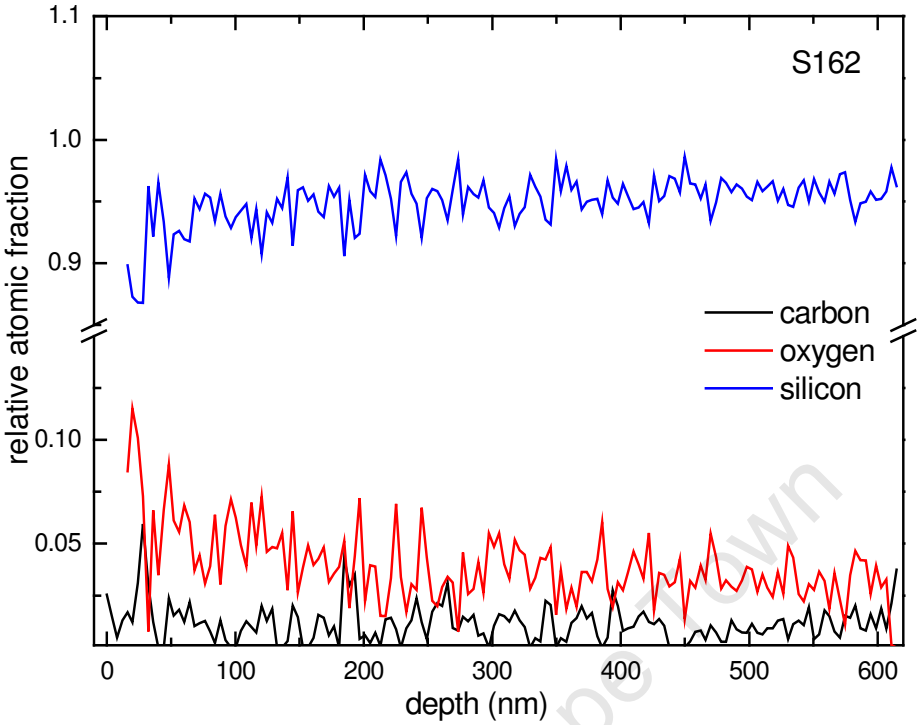

Figure 4.26 Relative atomic depth profiles of recoils from target sample S162.

To convert the unit of depth from that of areal density (10^{15} at.cm^{-2}) to nm the atomic density of silicon (4.98 x 10^{22} at.cm^{-3}) was assumed for the whole film, seeing as silicon makes up over 95% of the deposited layer in each of the samples. The depth profiles show considerable fluctuation with depth in the relative concentrations of the detected recoil species.

To check if the fluctuations could be attributed to low counting statistics Monte Carlo simulation of the energy profile of silicon recoils from one of the samples (S161) was performed using CORTEO. The same experimental setting used for the CrO2\Si sample was also used, the main difference being the target. In this instance the target was described as a thick (> 1μm) silicon slab with 5 at % oxygen content. Two theoretical spectra were generated and compared with the experimental one. The only difference in the simulation inputs was a ten-fold difference in the number of incident beam ions. The result, in Figure 4.27, shows a higher degree of fluctuation in the recoil energy profile where the number of incident particles is smaller. As the number of incident projectiles increases so

does the number of recoils detected and the energy profile tends to smoothen out, which suggests that the observed jitter in the experimental spectrum could also be statistical in nature rather than actual physical variations in the atomic concentration.

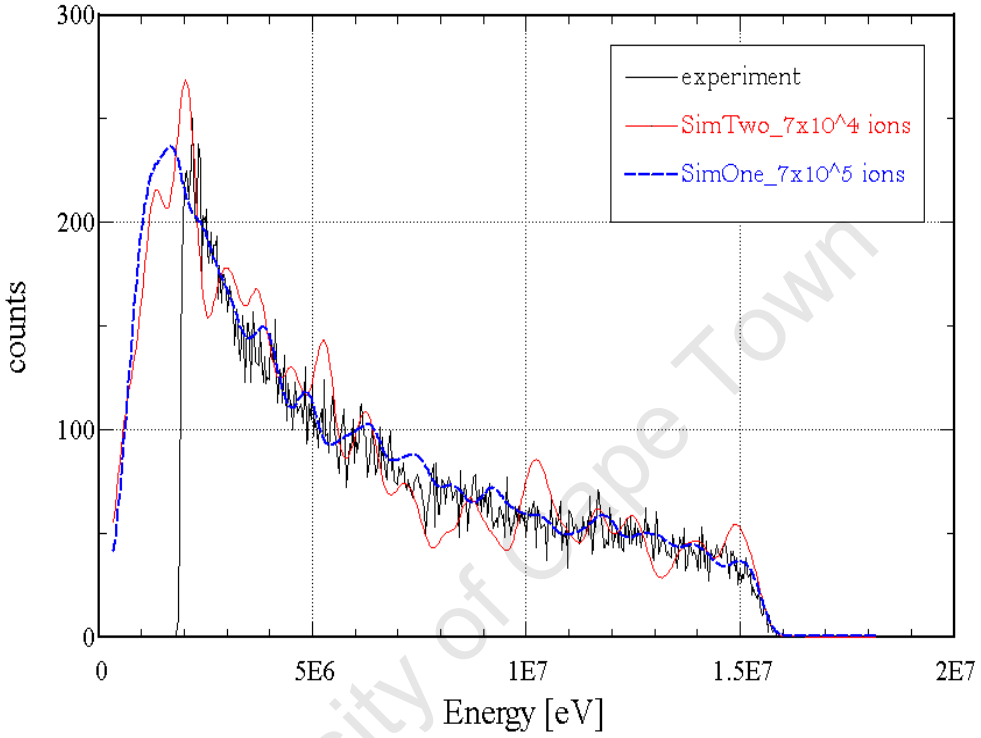

Figure 4.27 Comparison of experimental and simulated energy spectra of Si recoils from sample S161 demonstrating the effect of the number of incident ions on the statistical fluctuations in the number of detected recoils.

The average relative concentration of each recoil species, taken over the whole layer thickness, was then obtained by averaging the data points as listed in the KONZERD output calculations. Table 4.7 summarises the calculation results. The deposition pressure, the only variable between the samples during sample preparation is also included in the table for comparison purposes.

Sample	Deposition pressure (μbar)	Atomic fraction (%)		
		Si	O	C
S160	60	98.7	0.84	0.46
S161	40	94.3	3.54	2.16
S162	20	94.5	4.31	1.16

Table 4.7 Relative atomic fractions of Si, O and C in Hot Wire – CVD films deposited on Si substrates.

The results in Table 4.7 show that the amount of oxygen impurity content decreases as the deposition pressure increases. This is to be expected since increasing the pressure of the precursor gases (for the same deposition temperature) implies an increase in their volume concentrations in the deposition chamber, which should increase their relative concentration in the deposited film.

4.4.2 Measurement of carbon content in steel

The amount of carbon content in steel alloys has a direct effect on the mechanical, thermal and electrical properties of these alloys, and the different types of steel are classified according to their carbon content. The Centre for Materials Engineering at the University of Cape Town has as part of its research program, research projects in Metal Processing and Alloy Development. A sample piece of stainless steel was obtained from the centre to quantify its carbon content using the newly set up ToF – ERDA facility. This was after initial Scanning Electron Microscopy (SEM) measurements performed at the centre gave inconclusive results [4].

The method of analysis adopted was to determine the relative proportion of measured carbon and iron contents in a reference steel sample and in the unknown sample. Then, using reference values quoted for the standard sample [in Appendix A], a scaling factor **κ** for the experimentally determined carbon content could be calculated. This factor would then be used to evaluate the true carbon content in the sample under investigation.

4.4.2.1 Analysis of a NBS standard reference sample

The NBS reference sample [19] was in the form of a disc of 50.0 mm that was cut in half to mount it onto the target ladder. As in all the other measurements, a 27.5 MeV $^{84}Kr^{15+}$ beam was used as the probe beam at an angle of 15° to the sample surface. Up to 10^6 events were recorded to enhance statistics of light trace elements in the steel. Figure 4.28 shows the ToF – Energy scatter plot of recoils from the target sample. Collision kinematics between ^{84}Kr and ^{56}Fe nuclides at 30° scattering angle allow the incident beam to be scattered into the detector system hence the high intensity of scattered beam.

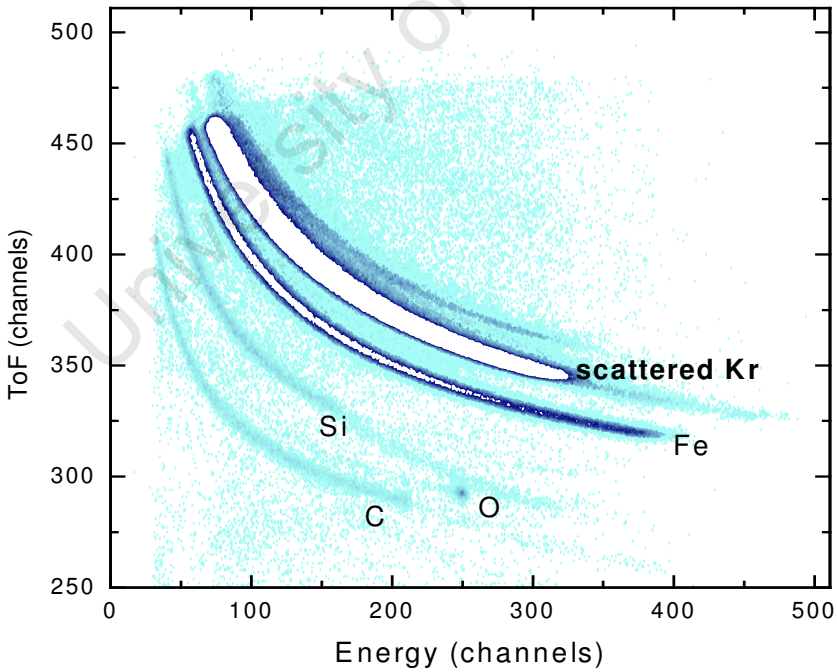

Figure 4.28 2D ToF – Energy scatter plot of recoils (and scattered beam) from the NBS 1264 standard sample.

The elemental content of the reference standard consists of a few light elements and a host of medium to heavy metallic elements in the following weight proportions (in %); H (<0.0005), B(0.011), **C(0.870)**, N(0.003), O(0.0017), Mg(0.0001), Al(0.008), **Si(0.067)**, S(0.028), P(0.018), Mn(0.255), Cu(0.249), Ni(0.142), Cr(0.065), V(0.105), Mo(0.49), W(0.10), Co(0.15), Ti(0.24), As(0.052), Sn(0.005), Nb(0.157), Ta(0.11), Pb(0.024), Zr(0.068), Sb(0.035), Bi(0.0009), Ca(<0.0001), Se(0.0003), Te(0.0003), In(0.0002), Ce(0.00025), La(0.00007), Nd(0.00012), Pr(0.00003), Hf(0.005), Ge(0.003) and **Fe(96.7)**. In the analysis carried out, however, only C and Fe are of interest.

The limitation in mass resolution for heavy elements ruled out any meaningful separation of their mass contour lines in Fig. 4.28. Iron stands out mainly because of its relative abundance in steel and because of the relatively large difference in mass between ^{56}Fe and the incident ^{84}Kr. The ^{56}Fe mass line still contains trace amounts of adjacent elements nonetheless. On the other hand the situation is quite different for the lighter elements. In particular, carbon stands out without any interference from adjacent elements. Figure 4.29 shows a mass spectrum of the standard sample obtained through the same procedure that is outlined in section 4.2.1.1; using ^{56}Fe and ^{12}C mass lines for mass calibration.

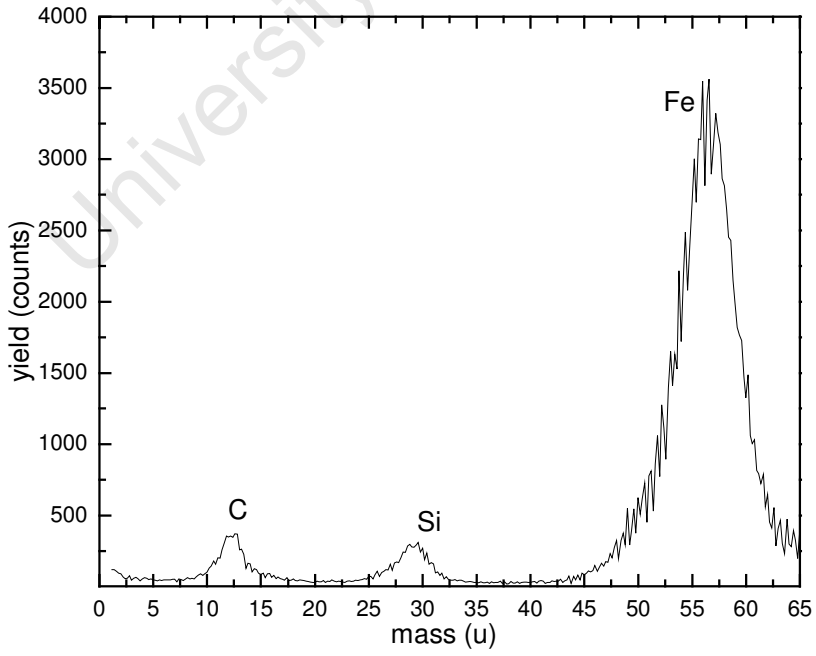

Figure 4.29 Partial mass spectrum of the NBS 1264 steel standard sample.

The mass spectrum also confirms presence of ^{28}Si in the sample. The Si 'peak' however, is in effect an aggregate peak of ^{28}Si and the adjacent elements ^{27}Al and ^{31}P. This is largely because of poor mass resolution; a consequence of the settings used during the measurement. These settings are described in detail in section 4.2.1. In the same vein, the broad 'Fe' peak includes nearby elements such as ^{52}Cr, ^{55}Mn and ^{59}Co, all in relatively small amounts though. Figure 4.30 shows a *partial* depth profile of the sample; *partial* in the sense that it shows only the two main constituent elements, ^{56}Fe and ^{12}C. This however, should only introduce a negligible uncertainty in the energy – depth conversion calculation, principally because the two elements make up ~98% by weight of the sample.

The depth profile shows an abrupt change in atomic concentration from the surface into the bulk of the steel. On the surface the concentration of iron is virtually 100 %, whereas that of carbon is close to 0 %. In practice though, the concentration of iron is below 100 % because of oxygen [in the oxide layer] present on the surface as indicated by the ToF – E scatter plot in Fig. 4.28. The exclusion of the surface oxygen in the depth profile calculation renders the surface layer composition ~100 % iron, even though that is not the case.

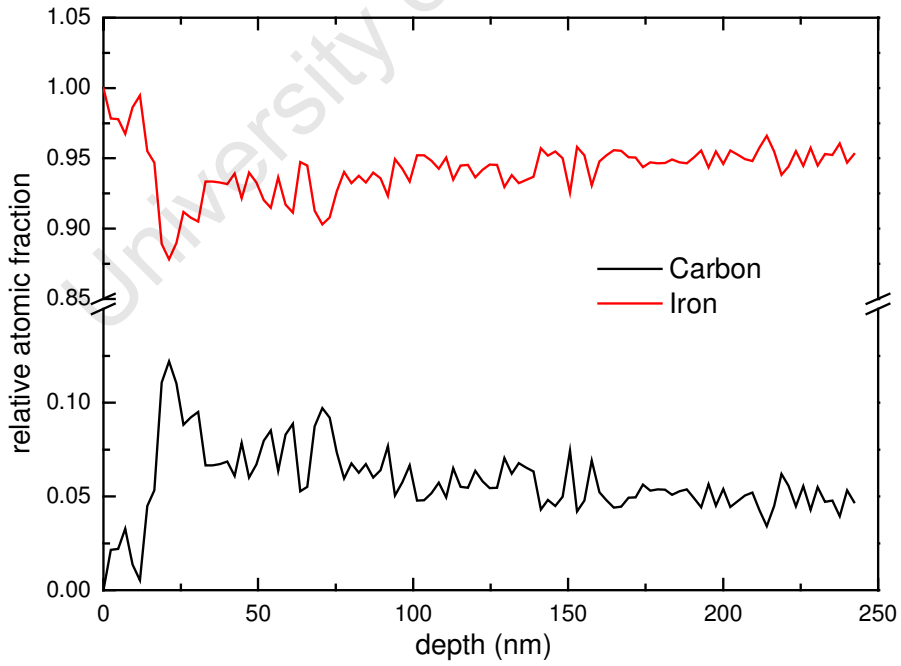

Figure 4.30 Partial depth profile of the NBS 1264 steel standard sample.

The average relative atomic concentration of carbon in the standard reference sample was evaluated over the 50 – 250 nm depth range to avoid the artificial variation in the surface region. From statistical analysis of the tabulated data the relative concentration was found to be 5.97 at %. A similar procedure for the iron content gave an average relative atomic concentration of 94.03 at %, with the standard deviation in each of these values equal to ± 0.013 %. The values in the reference table are quoted in weight %. For an effective comparison these have to be converted to at %.

The molecular mass of steel M_s is given by the sum of the products of the number of atoms n_i and the atomic mass A_i of each element present;

$$M_s = \sum_{i=0}^{i=N} n_i A_i \qquad [4.9],$$

and the weight percentage w_i of each element is given by

$$w_i M_s = n_i A_i \qquad [4.10].$$

The total number of atoms n_T is then given by

$$n_T = \sum_{i=0}^{i=N} n_i = M_s \sum_{i=0}^{i=N} \frac{w_i}{A_i} \qquad [4.11].$$

Combining equations [4.10] and [4.11], the atomic fraction of each element can be calculated from

$$\frac{n_i}{n_T} = \frac{w_i / A_i}{\sum_{i=0}^{i=N} w_i / A_i} \qquad [4.12].$$

In the summation in Eq. [4.11], the contribution of atoms whose percentage by weight is less than 0.01 % was ignored because of the relative insignificance of such amounts. For example for ^{115}In at w_i = 0.002 %, the number of ^{115}In atoms in the reference sample would be 1.7 x 10^{-7} M_s, whereas for ^{11}B at w_i = 0.011 % the same calculation gives 1.0 x 10^{-5} M_s. The total number of atoms, expressed in terms of the molecular weight of the sample, was found to be 0.0184 M_s. The atomic fraction of ^{12}C at w_i = 0.87 % then becomes

$$n_c = \frac{0.0087/12}{0.0184} = 0.0394 \qquad [4.13].$$

The relative atomic fraction of ^{12}C determined experimentally was 0.0597. Equation 4.13 gives the true value according to the NBS [19] reference table. The scaling factor κ for the experimental value would then be 0.0394/0.0597 = 0.66. This factor is meant to account for two effects. Firstly the fact that in the analysis the ^{56}Fe mass line is in reality that of iron and trace quantities of adjacent heavy elements, which are inseparable because of the limitation in the mass resolution of heavy elements. Secondly and more importantly, the excessive count rate (> 10^6 s^{-1}) on the first timing detector due to scattered incident beam led to 'ghost' mass lines of the scattered beam and the equally intense iron recoil beam. These Kr and Fe ghost lines, most probably due to double triggering in T1, are seen as overlays on the Si and C mass lines respectively, which incorrectly increases the number of counts for each of these ion species., hence the need for a correction factor to account for this noise effect.

4.4.2.2 Carbon content of an unknown steel sample

Figure 4.31 shows the 2D ToF – E scatter plot of recoils (and incident beam) scattered off the unknown steel sample. On comparison with Fig. 4.28, indications are that the major trace elements present in this sample are the same as those in the reference sample. Again the ghost line effect observed in the standard sample due to a similarly high count rate in timing detector T1 is also seen in this sample. The resultant partial depth profile in Fig. 4.32 shows relative distributions of ^{56}Fe and ^{12}C in the sample.

Like in the preceding subsection the relative atomic concentrations were found through statistical analysis of the tabulated KONZERD output, giving 6.5 at. % for ^{12}C and 93.5 at. % for ^{56}Fe, each quoted with a standard deviation of ± 1.8%.

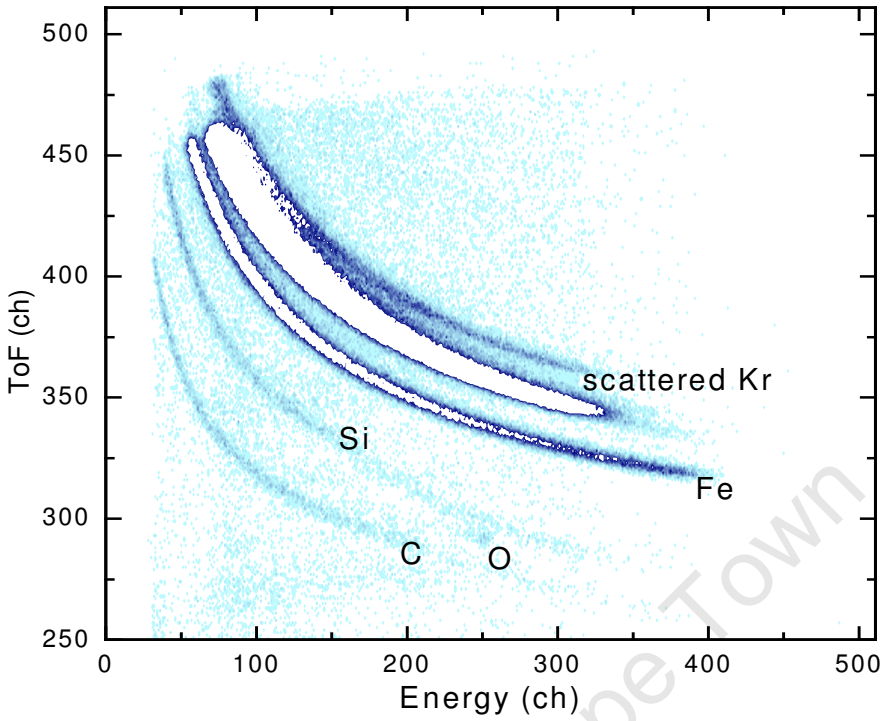

Figure 4.31 2D ToF – Energy scatter plot of recoils (and scattered beam) from an unidentified steel sample.

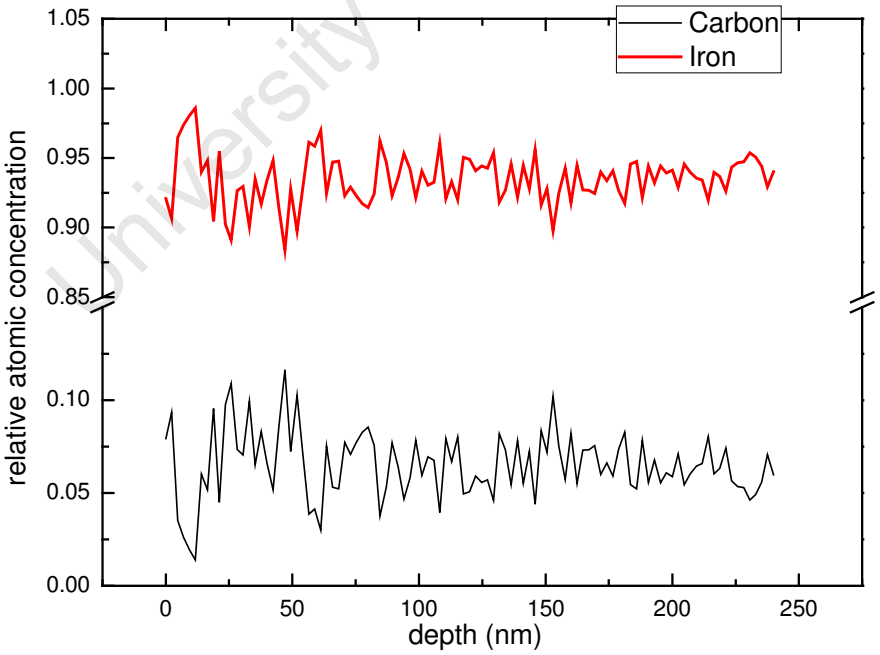

Figure 4.32 Partial depth profile of the unidentified steel sample.

Using the scaling factor κ (= 0.66) obtained for carbon from the analysis of the reference sample, the atomic concentration of carbon in the unknown steel was found to be 0.66 x 0.065 = 0.0429, or 4.3 at. %.

4.5 Chapter Summary

The aim of the test analyses described in this chapter was to evaluate performance characteristics of the ToF – ERDA system and, at the same time, demonstrate potential application areas of the set up in thin film materials analysis.

The mass resolution investigations performed were in the context of observed variations in the timing resolution under two different sets of experimental conditions. It should be understood however, that this is not to imply that other factors, like the surface barrier detector energy resolution, are unimportant. The best mass resolution for some of the recoils measured was found to be 0.9 **u** for ^{19}F and 1.7 **u** for both ^{28}Si and ^{40}Ca recoils, obtained under conditions where no timing preamplifiers were used in the signal processing chain. The procedure devised to convert the raw 2D ToF – Energy scatter plots into mass spectra made it possible to identify light element impurities in thin layers by their atomic mass. This was demonstrated for ^{12}C and ^{16}O impurities in a CaF_2\Si layer and for ^{12}C and ^{24}Mg impurities in a layer of CrO_2 deposited on silicon.

Measurements were performed to demonstrate depth profiling and thickness measurement capabilities of the spectrometer. As Fig.4.11 showed, good elemental separation could be achieved for elements in the ^{12}C – ^{52}Cr **u** mass range. The separated elemental energy spectra were analysed using both direct profile calculation and iterative simulation ion beam analysis programs, which yielded similar stoichiometric ratios and similar sample structure models. Of these though, the Monte Carlo based method gave a more realistic sample structure, concurring with the result obtained from the more established RBS analysis technique. The measured layer thickness was confirmed by the RBS measurement to be relatively accurate.

Trace element analysis measurements performed shed light on the range of detection limit achievable. It was observed that a light element matrix, of HW – CVD silicon, could be analysed without need for a standard for quantification because of distinct separation of individual elements mass lines. The lowest detectable impurity concentration was that of 0.46 at % of carbon in silicon. For a heavier matrix like steel though, it was seen that a reference sample could be very useful for quantitative analysis of light element impurity content. In the unknown steel sample that was analysed the amount of carbon content was found to be 4.3 at % by using a scaling factor obtained from the analysis of the reference sample.

4.6 References

1. Tirira J, Serruys Y and Trocellier P, *Forward Recoil Spectrometry – Applications to hydrogen determination in solids* (1996) *Plemm Press, New York.*
2. Saleh K. (2009), *MSc Project, NanoSciences Laboratory, iThemba LABS.*
3. Halindintwali S. (2009), *Hot Wire – CVD a-Si for photovoltaic devices, University of the Western Cape*, private communication.
4. Topic M. (2008), *Materials Research Department, iThemba LABS*, private communication.
5. Kim J. K. et al., *Nucl. Instr. and Meth.* **B 140** (1998) 380.
6. Razpet A., Pelicon P., Rupnik Z. and Budnar M., *Nucl. Instr. and Meth.* **B 201** (2003) 535.
7. Hong W. et al., *Nucl. Instr. and Meth.* **B 124** (1997) 95.
8. Kottler C., Döbelli M., Glaus F. and Suter M., *Nucl. Instr. and Meth.* **B 248** (2006) 155.
9. Zhang Y. et al., *Nucl. Instr. and Meth.* **B 149** (1999) 477.
10. J. F. Ziegler, SRIM-2008, http://www.srim.org
11. Bergmaier A., Dollinger G. and Frey C. M., *Nucl. Instr. and Meth.* **B 99** (1995) 488.
12. Bergmaier A. (2009) *private communication.*
13. Paul H., *Nucl. Instr. and Meth.* **B 247** (2006) 166.
14. Mayer M., *SIMNRA User's Guide*, Technical Report IPP9/113, Max – Planck Institut für Plasmaphysik, Garching, Germany, (1997).
15. Schiettekatte F (2008), *Nucl. Instr. and Meth.* **B266** 1880.
16. Graper E., *Lebow thin film data book*, Lebow Corporation, 1990.
17. Paul H. and Schiner A., *Nucl. Instr. and Meth.* **B 249** (2006) 1.
18. Chu W. K., Mayer J. W. and Nicloet M. *Backscattering Spectrometry* (1978), *Academic Press, New York.*
19. INTERNATIONAL ATOMIC ENERGY AGENCY, *Ion beam techniques for the analysis of light elements in thin films, including depth profiling*, IAEA-TECDOC-1409, IAEA, Vienna, (2004).

20. Street R. A., *Hydrogenated Amorphous Silicon*, Cambridge University Press, Cambridge (1991).
21. San Andrés E. et al., Thin Solid Films **492** (2005) 232.
22. Michaelis P. E., *NBS Standard Reference Materials, 1200 Series Iron and Steel Standards, Summary Report,* (1972).

Chapter 5

Measurement of heavy ion stopping powers in thin foils

5.1 Introduction

For over a hundred years now the stopping of energetic ions in matter has been a subject of extensive and ongoing theoretical and experimental research interests [1,2]. The study of the energy loss and range of ions in matter lends its advancement to the need to understand the fundamentals of the interaction between energetic ions and matter, and equally important to the widespread technological and medical applications of the passage of ion beams through matter. This chapter details measurements carried out to add on to the global database new experimental stopping power data of heavy ions in the oxide ceramic Zirconium Oxide (ZrO_2) and the polymeric plastic Mylar®.

Zirconium Oxide has interesting properties for micro/nano device applications. For example it has been shown to have superior properties to SiO_2 in prospective applications in metal-oxide-semiconductor (MOS) devices because of its much higher dielectric constant [3]. Mylar finds applications in many established and emerging technologies based on flexible thin films. Metallised mylar films for instance, are now used in solar engineering for solar concentrators because of several advantages over traditional glass mirrors: higher reflectivity, ease of manufacture, low cost and weight [4]. Surface modification of mylar films by irradiation with high energy heavy ion beams has facilitated tailoring of the material properties of the polymer for a range of applications in electronic device fabrication [5].

The important role played by (heavy) ion beam techniques in the characterisation and modification of materials for new devices on the micro/nanometer scale need not be over emphasised. Not much experimental data on stopping powers of heavy ions in compound materials (like ZrO_2 and Mylar for instance) is available in the literature, hence the need for

accurate data of heavy ion stopping. In instances, for some ions, as will be shown later, the stopping power data presented here is completely new.

Section 5.2 starts off with a look into the development of stopping power theory in general and eventually highlights the need for experimental data particularly in heavy ion beam analysis. A brief discussion of methods commonly used to provide experimental stopping power data is given in section 5.3, followed by a description of the local experimental set up in section 5.4 together with a detailed account of the procedure followed to extract stopping power values from raw data. The target foils used to measure the stopping powers are described and characterised in section 5.5. Measurement results, and the discussion thereof, given in section 5.6 conclude the chapter.

5.2 Stopping power theory: a historical insight

Ziegler J. F and co-authors in the introductory chapter of their seminal book *The Stopping and Range of Ions in Solids* [6], sum up the following as the essential problems of stopping theory; the mechanism of inelastic energy loss of projectiles to quantised target electrons, treatment of the effective charge state of traversing ions, screening effects and relativistic corrections. They further note that following Bohr's initial works [7] advances in theoretical studies tackling these problem areas have been driven by external developments.

For example, theoretical investigations into quantal scattering by Bethe and Bloch in the 1920's provided fundamental equations for the stopping of very fast (10 MeV/u – 2 GeV/u) particles in a quantised electron plasma [6]. The Bethe - Bloch formula, on which several subsequent theoretical advances are based [8] predicts the stopping cross section S of a projectile of atomic number Z_1 in a target of atomic number Z_2. In its simplest form it is given by

$$S = \frac{4\pi Z_1^2 Z_2 e^4}{mv^2} \ln \frac{2mv^2}{I} \qquad [5.1],$$

where m and v are, respectively, the mass and velocity of the projectile and I is the mean

ionisation potential of the target. The underlying theory assumes that the projectile is completely stripped of its electrons hence the high velocity restriction.

Subsequent to the work of Bethe and Bloch, the discovery of nuclear fission in the late 1930's required an approach that would take into account the possibility that fission fragments traversing matter may not be fully stripped of their orbital electrons [9]. The concept of effective charge then arose out of the need to address the problem of stopping of partially stripped ions in the low velocity regime. In Bohr's classical stopping theory for low energy ions [10] the stopping cross section becomes

$$S = \frac{4\pi Z_1^2 Z_2 e^4}{mv^2} \ln \frac{Cmv^3}{Z_1 e^2 \omega} \qquad [5.2],$$

where $\omega = 2\pi I/h$ and C = 1.1229. In his scheme Bohr showed that the effective charge Z_1^* of an ion with a velocity v could be defined as $Z_1^* = Z_1^{1/3} \frac{v}{v_o}$, where $v_o \sim 2.2 \times 10^6$ ms^{-1} is the electron Bohr velocity. In the process he estimated a screening distance between two colliding atoms that limits the energy transfer between nuclei. Further work by Lindhard, Scharff and Schiott on the stopping of low energy ions culminated in 1963 in what is commonly called the LSS theory, later reviewed in detail by Peter Sigmund in 1983 [11].

Another push factor in the development of stopping theory came from advances in experimental nuclear and particle physics in the middle of the last century, where the energies of particles studied were now in the relativistic regime. In his extensive review, Ahlen [12] details modifications to relativistic formulations that have evolved over the years based on the initial Bethe – Bloch theory.

Figure 5.1 shows typical variation of stopping power with projectile energy for charged particles [13]. On the low energy side LSS theory describes stopping relatively well and on the high energy end the modified Bethe-Bloch formula is adequate. At very low energies nuclear stopping dominates the energy loss processes. For the intermediate region, where the stopping power maximum lies, a satisfactory theory remains to be devised [14, 15].

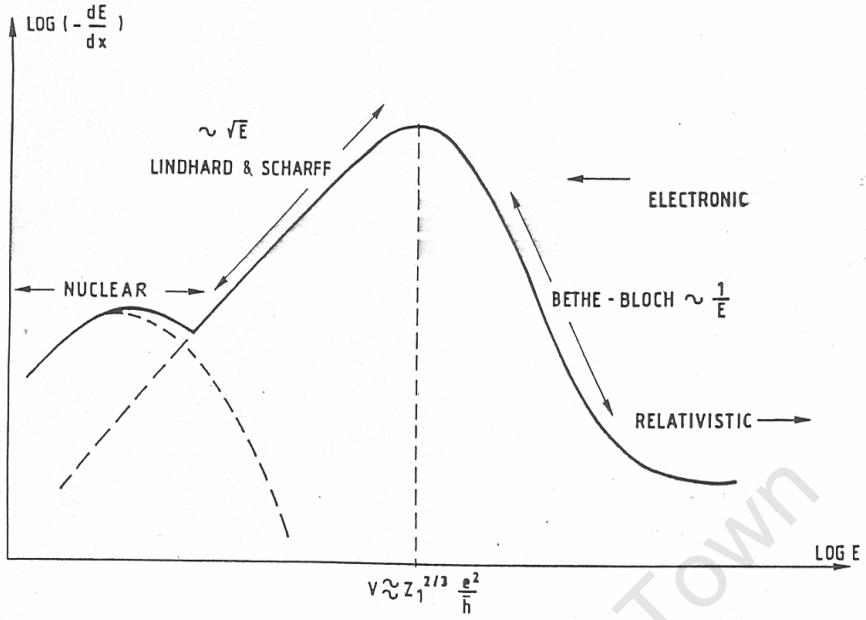

Figure 5.1 Typical variation of stopping power as a function of projectile energy from ref [13].

Major theoretical advances, building on the LSS and Bethe-Bloch theories, bolstered not in the least by the advent of widespread computing power, include the works referenced in the Handbook of Ion Beam Analysis [16]; Sigmund (1982), Oddershede and Sabin (1983), Brandt and Kitagawa (1982), and Ziegler et al. (1985). A number of computer codes based on these developments have been developed for the calculation of stopping powers of ions in matter. The most common, listed in ref [17] are CasP (Convolution approximation for swift Particles), CKLT (Convergent Kinetic Lindhard Theory), PASS (Binary theory), TCS (Transport cross section) and calculations by Heredia-Avalos et al. [18]. On the whole the accuracy of different theoretical formulations is restricted to specific energy ranges [14].

The need for accurate estimates of stopping power values of ions in matter to validate theory as well as for various practical applications has led to the development of semi-empirical formulations based on experiment, in tandem with theoretical developments. The latest semi-empirical codes include SRIM 2010 [19] and MSTAR [20], and stopping power tables from the ICRU 73 [21].

SRIM 2010 (and its earlier versions) is the prime source of stopping power data in popular ion beam analysis programs like SIMNRA, IBA, RUMP and WiNDF [22]. As mentioned in Chapter 2, while largely accurate for hydrogen and helium ions, for [†]heavy ions (Z > 3) the deviation from experimental values can sometimes go up to 20% [23, 24]. The maximum deviation in compound targets has been observed to occur in the energy region of the stopping power maximum where deviation from Bragg's rule of stopping power additivity for compound is greatest [8]. This is particularly the case because of sparse and varied experimental stopping power data for compounds compared to single element targets. Difficulties associated with preparing suitable compound targets for measurement have contributed to this higher level of predictive inaccuracies because a lot less measurements have been made for targets in this category.

Typical ion energies in ion beam analysis techniques lie within the 0.1 – 1.0 MeV/u energy range, and the stopping power maximum, or the Bragg peak as it is commonly known, lies within this range. The availability of accurate heavy ion stopping power data is becoming increasingly important for precision work in ion beam analysis and materials modification [25], where the dimensions of sample materials investigated continue to shrink. The work presented in this chapter aims to contribute to the global database of stopping power data of technologically important materials to test and improve the predictive accuracy of widely used codes like SRIM and MSTAR.

5.3 Methods for experimental stopping powers in ion beam analysis

An overview of methods used for experimental determination of stopping powers in all phases of matter is given in ref [21]. In ion beam analysis the interest is mainly in solid thin films. Within this area different techniques used to measure stopping power fall into one of the following categories [13]; transmission, backscattering and gamma resonance shift.

[†] 'Heavy ions' in stopping power literature generally refers to ions of Z > 3, whereas in HI-ERDA elements in the hydrogen – neon mass range are considered 'light' elements

In traditional transmission techniques energy loss is measured directly through self-supporting foils. The difference in the energy of a projectile ion measured with and without a target foil placed in front of a detector gives the amount of energy lost in traversing the foil. To get several data points the incident projectile energy is varied by adjusting the accelerator voltage. The target foil thickness is measured either by measuring the mass of the foil and dividing by the area or by measuring the energy loss of particles (usually alphas) whose stopping cross section is accurately known.

In backscattering measurements a thin layer is deposited onto a thick substrate. The difference between the energy of a projectile scattered from the front surface of the thin film and that scattered from the film-substrate interface gives the energy loss in the incident and outgoing paths. The range of projectile ions that can be studied using this method is limited by the target composition, since the backscattering cross section decreases as the projectile becomes heavier than the target atoms. N. P. Barradas and C. Pascual-Izarra and co-authors have produced a series of articles [26] describing two methods used to extract continuous stopping power curves from raw RBS spectra. The two independent analysis methods are based on Simulated Annealing and Bayesian Inference techniques as implemented in the Hotstop® and Data Furnace® analysis codes [26].

The gamma resonance (or X-ray) energy shift method entails bombarding a known backing material (e.g Au, Al) with protons (or any other selected ions) and measuring the gamma resonance yield [27]. The same measurement is repeated for a sample made up of the backing substrate now covered with a thin layer of a target material of interest. The shift in the photon yield energy is then used to calculate the stopping power of the target layer for the incident projectile ions. Though relatively accurate, the fact that this method is energy specific limits its application to those cases where there is a sharp resonance in the projectile-target interactions.

By far the most common experimental methods involve transmission measurements since any projectile mass can be used over a wide and continuous energy range. Backscattering techniques are most suitable for light projectiles on heavy targets and gamma resonance

shift methods are restricted in applicability by the energy specific nuclear reactions that are involved. The technique used in this work is fully described in the following section.

5.4 The ToF – E *s*topping power measurement set up at iThemba LABS

A ToF-E stopping power measurement is in essence a transmission technique. It requires a slight adaptation [28, 29] of the ToF – E spectrometer described in Chapter 3.2 that entails insertion of the stopper foil between the ToF telescope and the Energy detector as illustrated in Figure 5.10.

The ions whose energy loss is measured could either be incident projectile ions from the accelerator scattered off a suitable (heavy) target element or recoil ions ejected from the target by the incident beam. In either case the beam of ions incident on the stopper foil is of a continuous range of energies. Therein lies the uniqueness of this kind of set up; the possibility to measure stopping powers over a range of energies in a single run.

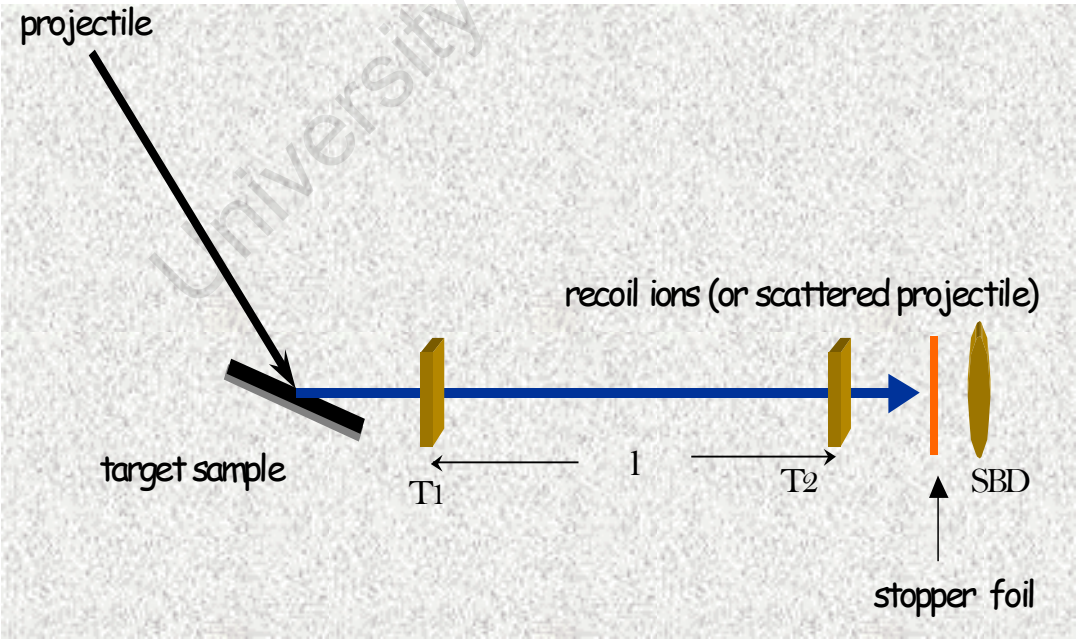

Figure 5.2 A simple shematic showing the ToF - E spectrometer-foil configuration for stopping power measurements.

The schematic arrangement shown in Figure 5.2 is such that the inserted stopper foil is perpendicular to the path of the incoming beam. In practice the set up looks as shown in Figure 5.3, where the top image shows the stopper foil holder viewed from the end of the flight flange and the bottom image is a bird's eye view illustration of how the holder is fitted into the flight flange. The SBD is mounted on the end flange and the second timing detector is affixed to a metal plate that extends from that flange, leaving a gap between the SBD and T2 as previously shown in Figure 3.4. The foil holder can be moved in and out of the beam path between T2 and the SBD without having to break vacuum.

5.4.1 Measurement of energy loss ΔE

The energy of the incident ion before hitting the stopper foil is determined from the measured ToF and the exit energy is, in principle, measured by the SBD. In practice though, to avoid uncertainties associated with the non-linear response of semiconductor detectors for heavy ions, the exit energy is determined from a ToF – E coincidence measurement *without any stopper foil* between T2 and the SBD [30]. The energy signal from the SBD is used to tag events of a similar energy on two ToF – E curves with and without the stopper foil. The ToF curve without the stopper foil effectively calibrates the SBD for each recoil ion species. The scatter plots in Figure 5.4 are typical examples of 2D ToF – E coincidence plots showing in this instance two recoil ion species (Al and O from a thick layer of Al_2O_3 on a Si substrate) obtained in runs with and without a stopper foil.

Figure 5.3 Experimental set up of the apparatus for stopping power measurements showing the mounting of the stopper foil holder as seen from the end of the flight path (top picture) and from above (bottom picture).

5.4.2 Data manipulation for determination of stopping power

The same calibration procedure described in section 3.7.2 in Chapter 3 is followed in performing time calibration for stopping power measurements. The time of flight measured in coincidence with and tagged by a particular SBD energy response is extracted from the 2D ToF – E scatter plot by projecting onto the ToF axis the section (or slice) of the scatter plot corresponding to that energy. This is illustrated in the example in Figure 5.4 for Al recoils incident on a ZrO_2 foil, where t_1 and t_2 are the measured flight times with and without the stopper foil respectively.

The raw t_1 and t_2 spectra so obtained are converted into ASCII format for further analysis in ORIGIN®. The mean peak values are obtained by fitting the ASCII time spectra with a Gauss function. The conversion from ToF in channels to ToF in (nano)seconds is performed using the calibration fit function. The energy loss ΔE of a recoil (or scattered) ion of mass m (in SI units) after passing through the stopper foil is then given by

$$\Delta E = E_1 - E_2 = \frac{m}{2}\left(\left(\frac{L}{t_1}\right)^2 - \left(\frac{L}{t_2}\right)^2\right) \qquad [5.3],$$

where L is the flight distance as before, E_1 and E_2 being the incident and exit energies respectively.

The effective energy E_{av} at which the energy loss is measured is calculated from

$$E_{av} = \frac{E_1 + E_2}{2} \qquad [5.4].$$

Normalising the energy loss by the foil thickness yields the stopping power. This procedure is repeated for a number of channels (bins) along the energy axis to determine the stopping power over a range of energies.

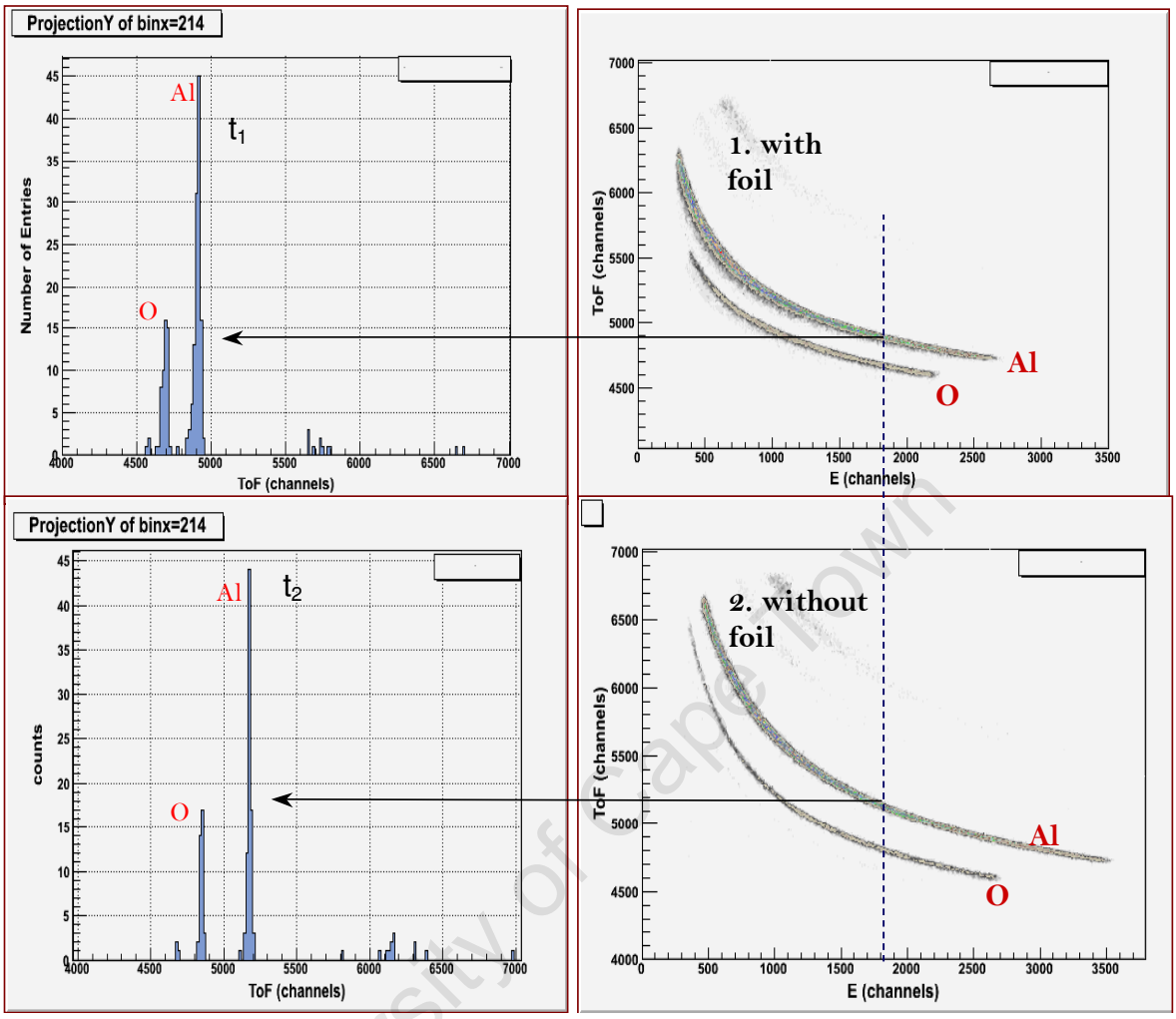

Figure 5.4 An example of raw data from measurements carried out with and without a ZrO_2 stopper foil. The projections show ToF slices used to calculate energy before and after the Al ion passes through the foil.

5.4.2.1 Propagation of uncertainties

The quantities in Equation 5.3 used to calculate the energy loss are themselves derived quantities and so the error propagation analysis should start from the raw variables. The theoretical time of flight t_i used for the time calibration is calculated as described in section 3.7.1 from the recoil (or scattered) ion energy E_F and the flight length L;

$$t_i = \sqrt{\frac{m_i}{2}\frac{1}{[(K_m \cos^2\Phi)E_o - \Delta E_{T1}]}}\ L \qquad [5.5]$$

where $K_m \cos^2\Phi E_o - \Delta E_{T1} = E_F$ with K_m in this case being the ratio $4m_1m_2/(m_1+m_2)^2$.

The uncertainty ΔE_F of the energy of the incident recoil/scattered ions is largely determined by the ± 0.5° uncertainty in the angle of recoil/scattering, which translates to a 2.3% error in the $\cos^2\Phi$ term. The spread ΔE_o in the incident beam energy is of the order of 10^{-3} [31] and the energy loss ΔE_{T1} in the carbon foil of the first timing detector is 1.1%. When combined in quadrature,

$$\frac{\Delta E_F}{E_F} = \sqrt{\left(\frac{\Delta \cos^2\Phi}{\cos^2\Phi}\right)^2 + \left(\frac{\Delta E_o}{E_o}\right)^2} + \frac{\Delta(\Delta E_{T1})}{\Delta E_{T1}} \qquad [5.6],$$

the error terms give an uncertainty of 3.4 % in the energy E_F. The error in the calculated t_i values used for time calibration then becomes 1.7 % since $t_i \propto E^{1/2}$. The uncertainty in L becomes redundant as this variable cancels out when the calibration equivalent of Equation 5.5 is substituted in Equation 5.3. The end result is that the energy loss, which is calculated from two different *ToF* values, has an uncertainty of about 4.8%.

5.4.3 Validating the measurement technique

To build confidence in the integrity of the data generated here, it was deemed important to do a measurement on a relatively well-studied ion – target combination that would validate (or discount) the measurement technique developed. H.Paul, in his popular web based database [32], lists over twenty-one references providing experimental data for the stopping of oxygen ions in carbon. The oxygen – carbon system was therefore found to be an appropriate test *ion – target* combination.

Figure 5.5 shows experimental the data from Paul's website including predictions from numerous theoretical and semi-empirical codes. The letters A – V in the plot represent data

taken from each of the references A – V listed on the right. The percentage values next to each reference entry indicate the degree of uncertainty in the measured values. Except for a few outliers, there is in general good agreement between experiment and theory over energy ranges before and after the stopping power maximum. Maximum deviation occurs within the Bragg peak and on average should be within 20%.

5.4.3.1 Determination of the stopping power of oxygen ions in carbon

For the test measurement 4.0 MeV $^{18}O^{3+}$ ions were accelerated from the SPC2 ECR ion source towards a target of a thick layer of gold on a silicon substrate. The incident beam was scattered into the ToF – E detector telescope and two 2D ToF – E coincidence spectra acquired with and without a 50.0 µg cm^{-2} carbon stopper foil. The foil thickness was determined by dividing the measured energy loss of ^{228}Th alpha particles through the foil by the stopping power of helium ions in carbon calculated from SRIM2008.

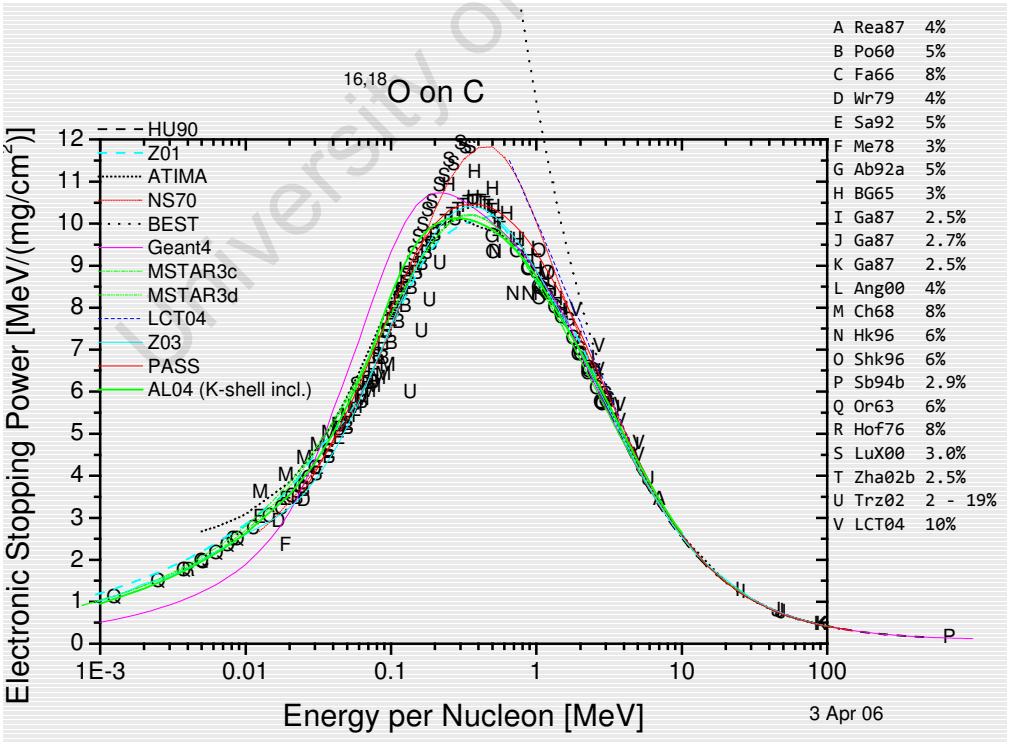

Figure 5.5 Experimental, theoretical and semi-empirical stopping power values of oxygen ions in carbon from H.Paul's database [32].

A 'fortunate accident' that occurred during beam production and acceleration was heavy carbon contamination in the ion source due to an unexpected shut down of some of the vacuum pumps. As a result 2.66 MeV C^{2+} ions also came through the SPC2 together with the $^{18}O^{3+}$ ions and these came in handy for time calibration. Additional target samples, plain Si and carbon graphite, pre-loaded together with the Au/Si target were also used for time calibration. The energy loss ΔE_{T1} through the first (carbon foil based) time detector, though small (~1.0%) was calculated using SRIM2008 and accounted for in the calculation of the energy E_1 of the scattered (or recoil) ions between the two time detectors.

In the absence of the carbon beam, time calibration using the oxygen beam would have meant using SRIM stopping powers of oxygen in carbon to calculate ΔE_{T1}. Yet the object of the experiment was to measure the stopping power of oxygen in carbon and compare with SRIM prediction. Though using SRIM stopping power values of ^{18}O ions in carbon would have introduced a minor 'cyclic' error, availability of the unintentional carbon beam meant that this could be avoided by using the kinematics of the *carbon – target* interaction for time calibration, leaving out the $^{18}O^{3+}$ ions under study. Table 5.1 summarises the time calibration calculations.

Ion	Scattered by	E_o (MeV)	$[S]_C$ (MeV/mgcm^{-2})	ΔE_{T1} (MeV)	E_1 (MeV)	ToF (ns)	ToF (channels)
C	Au on Si	2.610	7.210	0.06489	2.5451	91.55	367.81
C	Plain Si	2.363	7.105	0.06395	2.2991	96.32	370.59
C	graphite	1.990	6.880	0.06192	1.9281	105.18	376.39
Si	Incident oxygen	2.842	12.105	0.10895	2.7331	134.94	395.89

Table 5.1 Table showing calculated times of flight (in ns) of scattered carbon projectiles (and Si recoils) against channel number, after taking into account the energy loss ΔE_{T1} of each ion through the T1 carbon foil. Entries in column $[S]_C$ are the SRIM2008 stopping power of each ion in carbon.

The following calibration equation was obtained from a linear fit of the ToF(ns) vs ToF(channels) scatter plot;

$$ToF = 1.538\,ns/ch * ch - 473.68\ (ns) \qquad [5.7].$$

Using this equation and Equation 5.3 for the calculation of energy loss, the stopping power of oxygen ions in carbon was determined over the energy range 0.05 to 0.20 MeV/u. The upper limit of the energy range of the ^{18}O ions scattered into the ToF – E telescope was set by the energy of the incident beam from the accelerator. Table 5.2 displays the results of the whole calculation procedure; from raw t_1 and t_2 peak values to the stopping power. The results are further presented in Figure 5.6 together with experimental data, taken from three of the latest references in Figure 5.5. Also included are predictions from SRIM2008 and the other popular semi-empirical formulation MSTAR [20]. The choice of experimental data for comparison was based on those data sets overlapping in the energy range with the results from this work.

A quick glance at Figure 5.6 shows that within experimental error, the stopping power values obtained using the ToF – E spectrometer developed in this work agree with literature data obtained through other measurement procedures. This is particularly true over the energy range from low energy up to just below the Bragg peak. For energies at the Bragg peak the performance of the ToF - E spectrometer is not so easy to judge in this measurement because of the limited energy range predetermined by the energy of the incident beam used. This however, should not be an issue for the present work because, as will be seen in the results presented later, most of the stopping power measurements were performed at energies up to just below the Bragg peak. And it has now been shown that the measurement method used here works quite reliably in this energy range.

Energy ch	T1raw ch	T2raw ch	T1 ns	T2 ns	E1 MeV	E2 MeV	ΔE MeV	E_{av} MeV/u	S MeV/mgcm^{-2}
79	417.94	435.24	169.11	195.72	1.112	0.830	0.282	0.054	5.637
93	410.69	425.67	157.96	181.00	1.275	0.971	0.304	0.062	6.077
114	402.04	414.84	144.66	164.34	1.520	1.178	0.342	0.075	6.847
127	398.26	409.46	138.84	156.07	1.650	1.306	0.344	0.082	6.882
138	395.05	405.66	133.91	150.23	1.774	1.409	0.364	0.088	7.289
149	392.22	402.17	129.55	144.86	1.895	1.516	0.379	0.095	7.585
158	390.19	399.71	126.43	141.07	1.990	1.598	0.392	0.100	7.832
169	387.94	396.66	122.97	136.38	2.103	1.710	0.393	0.106	7.866
189	384.41	392.26	117.54	129.62	2.302	1.893	0.409	0.117	8.178
202	382.37	389.74	114.41	125.74	2.430	2.012	0.418	0.123	8.368
214	380.60	387.72	111.68	122.63	2.550	2.115	0.435	0.130	8.701
226	378.93	385.68	109.11	119.50	2.671	2.227	0.444	0.136	8.880
237	377.63	383.92	107.11	116.79	2.772	2.332	0.440	0.142	8.804
250	376.11	382.15	104.78	114.07	2.897	2.445	0.453	0.148	9.053
263	374.71	380.58	102.62	111.65	3.020	2.551	0.469	0.155	9.373
277	373.42	378.86	100.64	109.01	3.140	2.677	0.464	0.162	9.271
288	372.20	377.55	98.76	106.99	3.261	2.778	0.482	0.168	9.645
289	372.10	377.55	98.61	106.99	3.271	2.778	0.492	0.168	9.849
302	371.00	376.12	96.92	104.79	3.386	2.896	0.490	0.175	9.795
314	369.98	374.95	95.35	102.99	3.498	2.998	0.500	0.180	10.000
326	369.14	373.85	94.06	101.30	3.595	3.099	0.496	0.186	9.916

Table 5.2 A compilation of stopping power values (**S**) of oxygen in carbon at different energies ($\mathbf{E}_{av}$) calculated from experimental data.

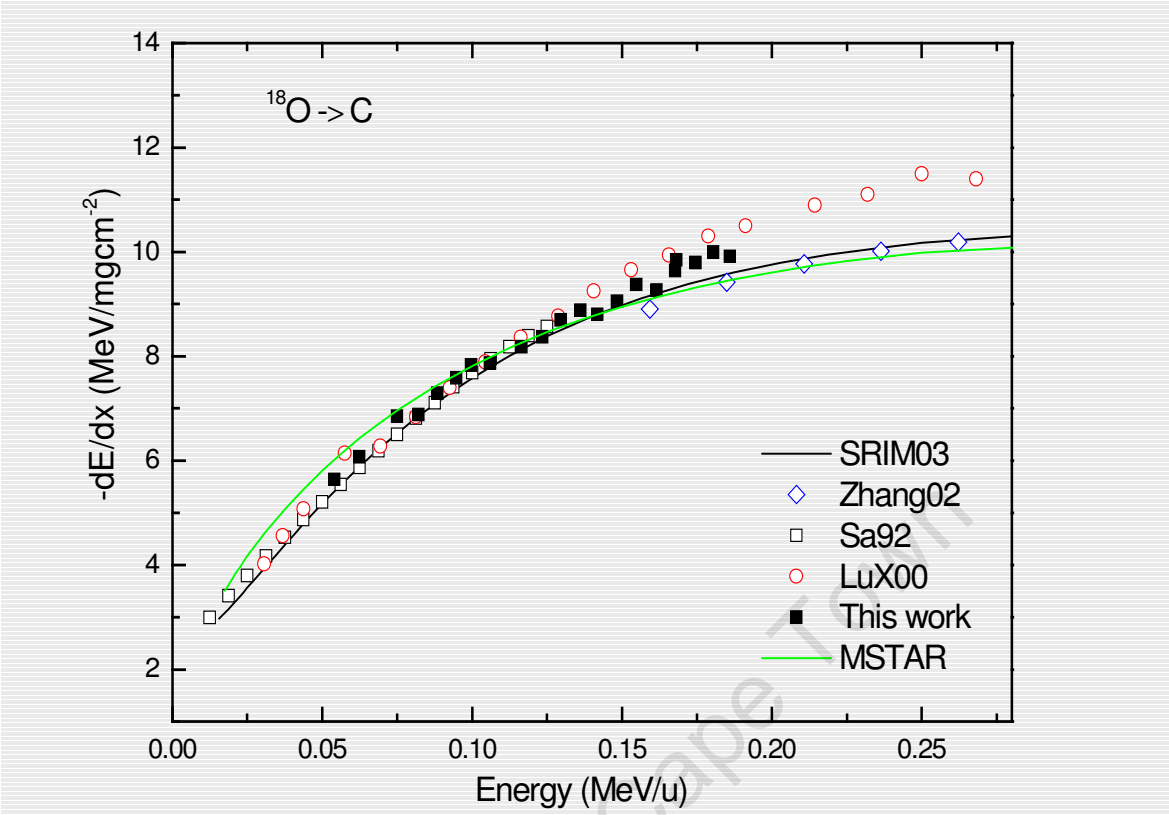

Figure 5.6 A graphical comparison of the measured stopping power of oxygen in carbon with some of the data in literature taken from Figure 5.5 and predictions from the codes SRIM2003 and MSTAR.

5.5 Characterisation of the target foils

The Zirconium Oxide (also known as zirconia) and Mylar target stopper foils used in this work were in the form of freestanding self – supporting foils. The [†]ZrO_2 foils, purchased from ACF-Metals (Arizona, USA), were produced by physical vapour deposition. To improve the mechanical stability of the deposited foils trace quantities of either yttrium oxide or cerium oxide are sometimes incorporated during the deposition process to stabilize the foils on cooling [33]. The foils were delivered mounted on steel frames each with a circular aperture of 0.8 cm in diameter. Mylar foils were mounted in-house by pulling a large strip of the polymer over the 0.8 cm aperture frame and cutting off half the material

[†] The stoichiometry of the zirconium oxide foil is later ascertained in Section 5.4.3 to be practically Zr_1O_2.

covering the aperture. This was so that stopping measurements could be performed in one run [34], thereby eliminating any likely errors due to drift in beam energy and detector response. Unfortunately this configuration was not possible for the zirconia foils because of their brittleness.

5.5.1 Topography

The topography of the foils was mapped using an Atomic Force Microscope (AFM), scanning over areas of up to 20 x 20 μm^2 at a time. Several regions on each foil were scanned. Figures 5.7 and 5.8 show typical AFM images of the two foils, from which the roughness of each foil surface was estimated. A measure of the surface roughness helps in determining the significance of the topographic variations in the measurement of the foil thickness. The roughness determined from each of the images was 3.83 nm for the Zirconia foil and 1.58 nm for the Mylar foil.

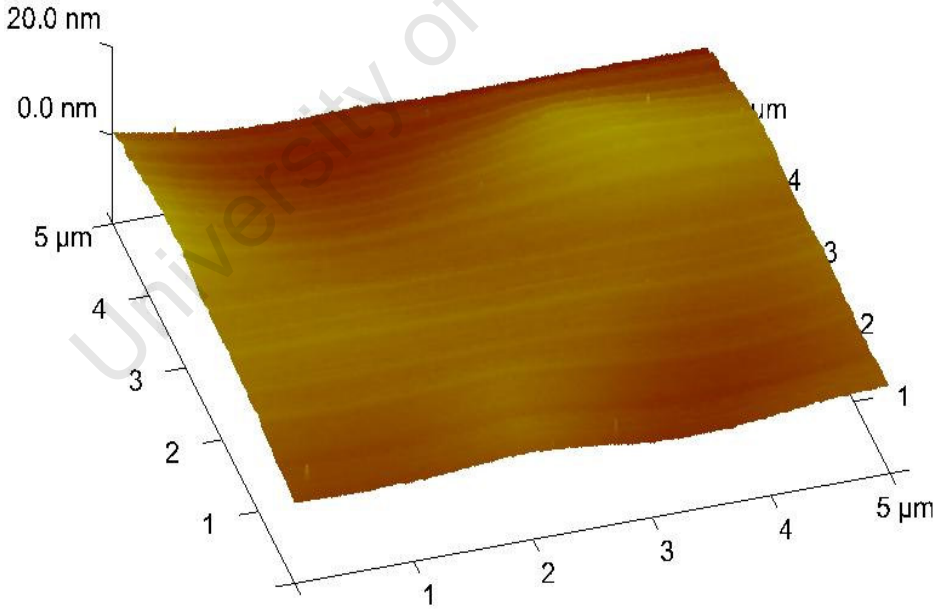

Figure 5.7 An AFM image of a 5 x 5 μm^2 region of the Mylar foil

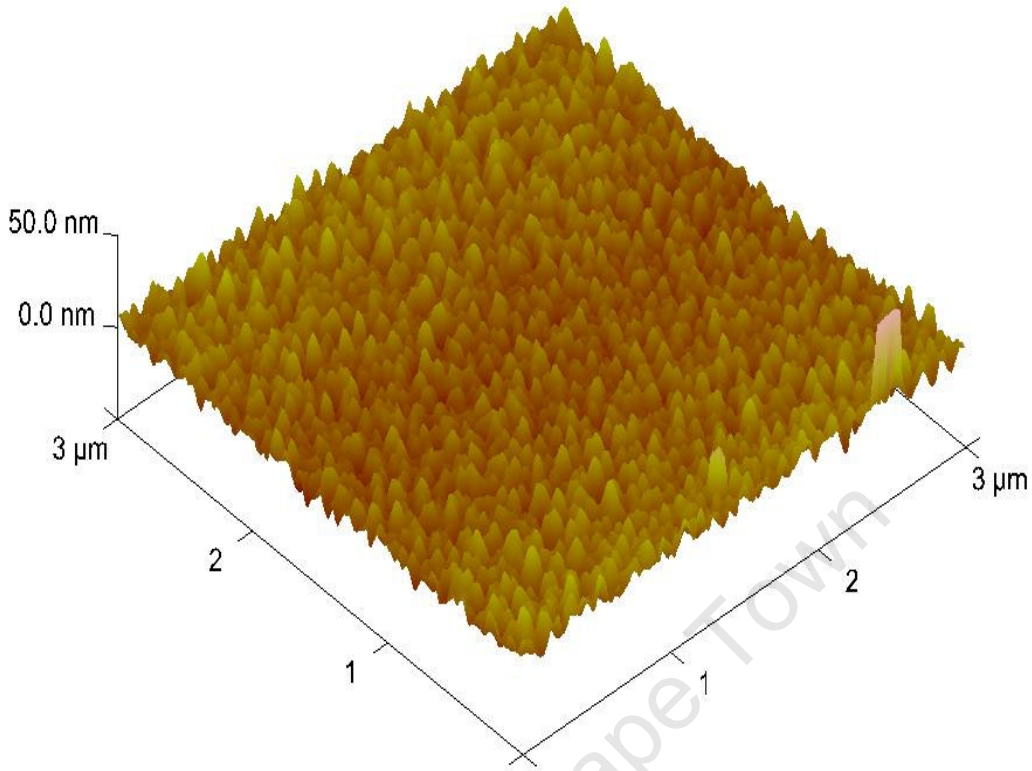

Figure 5.8 An AFM image of a 3 x 3 µm^2 region of the zirconia foil.

5.5.2 Foil thickness measurement

The thickness of the target foils was measured using the energy loss of 5.48 MeV ^{241}Am alphas through each foil. For the zirconia foil the thickness (and impurity content) was further measured by RBS analysis as an independent check. In the first method the SBD energy detector was calibrated using a ^{228}Th radioactive source. Figure 5.9 shows the ^{228}Th alpha particle energy spectrum together with an insert of the SBD energy calibration plot.

For the thickness measurements, the method adopted was to acquire an energy spectrum of the ^{241}Am alpha source with and without the target foil inserted between the source and the SBD. The ^{241}Am source was temporarily attached to the mounting of the second time detector T2 using vacuum compatible Plasticine®. The positioning of the source was such that it was a perpendicular distance of 6 cm from the SBD. The first run, with the Mylar foil between the source and the SBD, yielded two peaks simultaneously with the higher energy

peak due to alphas incident directly on the detector and the lower energy peak due to alphas passing through the foil before reaching the detector.

Results are displayed in Figure 5.10 with the energy axis already converted to MeV. The peak values shown in the plot were determined by Gauss fits. The SBD resolution, measured at 5.50 MeV, was found from the Gauss fit to be 0.019 MeV.

An apparent deterioration of the resolution (to 0.036 MeV) can be observed for those alphas passing through the foil. This can be attributed to energy straggling of the incident alphas as they traverse the foil. The thickness Δx of the foil is calculated using a simplified version of Equation 2.8;

$$\Delta x = \frac{\Delta E}{S} = \frac{E_1 - E_2}{S} \qquad [5.8],$$

where E_1 is the incidence energy (5.505 MeV) measured without the target foil and E_2 is the energy (5.316 MeV) measured after the target foil.

The stopping power S, quoted at an average energy $E_{av} = (E_1 + E_2)/2$ was obtained from SRIM2008 calculations as 0.8023 MeV/mg cm^{-2}. This gave a thickness of 235.5 μg cm^{-2} (1.69 μm) for the Mylar foil. A discussion of the uncertainties associated with the foil thickness measurements is given in sub section 5.5.2.1.

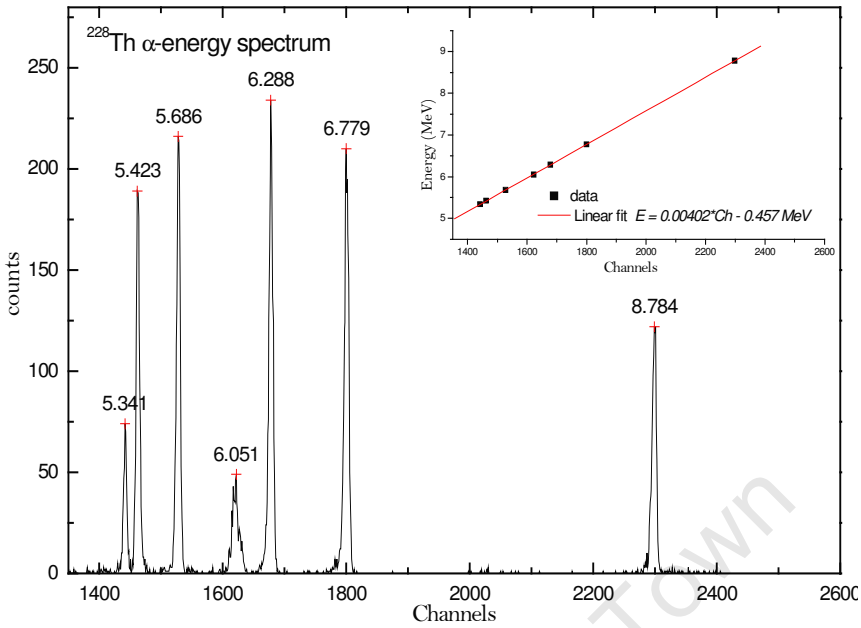

Figure 5.9 Energy spectrum of alpha particles from a Thorium-228 source with an insert showing the energy calibration plot for the SBD.

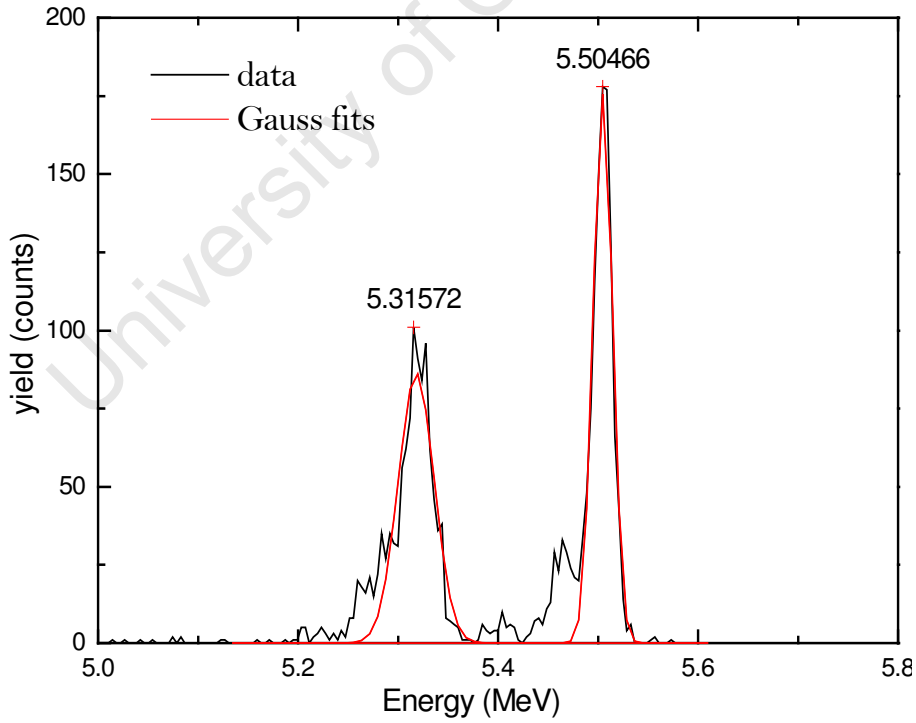

Figure 5.10 Energy spectrum of Am-241 alphas showing the energy loss shift through Mylar for determination of the foil thickness.

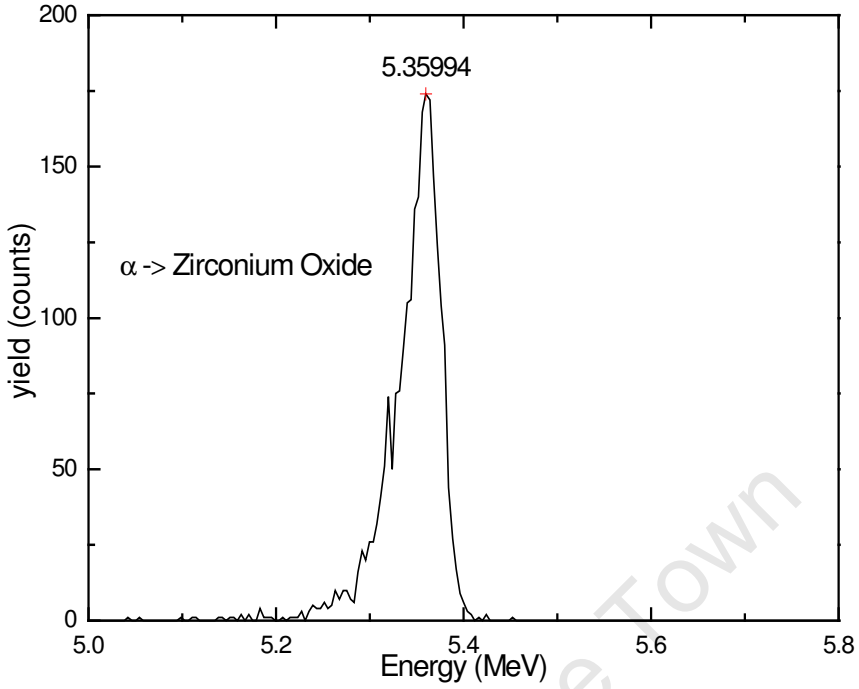

Figure 5.11 Energy spectra of Am-241 alphas through the Zirconium Oxide foil for determination of foil thickness.

Subsequent measurement of the zirconia foil performed under the same experimental conditions as the for the Mylar foil, yielded one major alpha energy peak since this foil fully covered the frame aperture. The same reference peak (E_1) from the measurement of the Mylar foil was used for thickness calculations. Results of the measurements are shown in Figure 5.11. A similar calculation gave 0.1447 MeV for the alpha energy loss through the zirconia foil and the stopping power at an average energy of 5.43 MeV worked out to be 0.437 MeV/mg cm^{-2}, giving a foil thickness of 331.2 μg cm^{-2}.

5.5.2.1 Uncertainties in the measurement of foil thickness

Sources of uncertainty that can be identified in the measurements just described are the energy resolution of the detector, energy straggling through the foil, accuracy of stopping powers used, surface roughness of the foils and lateral variation in the thickness of the foils.

The detector resolution ΔE_{det}, calculated from the reference peak is

$$\Delta E_{\text{det}} = \frac{FWHM}{E_1} = \frac{0.019}{5.505} = 0.3\% \qquad [5.9].$$

Energy straggling Ω in the foil manifests itself in the broadening of the energy peak of alpha particles that have passed through the foil, which results in an increase in the uncertainty of the centroid peak values determined through Gaussian fitting. Given that the energy loss of alpha particles through each foil is given by $\Delta E = E_1 - E_2$ (equation 5.8), an appropriate estimate of the energy-spread Ω due to straggling would be given by

$$\Omega = \Delta E_1 + \Delta E_2 \qquad [5.10].$$

where ΔE_1 and ΔE_2 are, respectively, the uncertainties of the energy peak centroids *without* and *with* the foil between the alpha source and the detector. For the Mylar foil, where ΔE_1 = 0.0002 MeV and ΔE_2 = 0.0009 MeV, Equation 5.10 yields Ω = 0.0011 MeV. This works out to be 0.58 % energy loss straggling for an energy loss ΔE of 0.189 MeV. Using the same calculation procedure one gets 0.59 % for energy loss straggling through the ZrO_2 foil.

The accuracy of the stopping powers of He^{2+} ions in ZrO_2 and Mylar from SRIM calculations is taken from the analysis by H. Paul and A. Schinner [35]. In the energy range 0.3 – 30 MeV/u the mean relative difference between experimental data and calculation, averaged over 150 compounds, is –0.8 %, with a standard deviation of 4.1 %. A negative average relative difference implies that on average SRIM overestimates stopping by 0.8 %. The standard deviation is related to the mean experimental accuracy of all data surveyed [35], and this is the quantity that was taken to be a reasonable estimate of the uncertainty in the stopping powers used for the thickness measurements.

Surface roughness (∂x) can be considered to affect the thickness measurement by having an effect on the total path length traversed by the transmitted particles. This effect is illustrated in the simplified schematic in Figure 5.12. The distance traversed by a particle that enters the sample surface at point **A** will most certainly be greater than that traversed by a particle entering the sample at point **B**, assuming that both particles follow straight

line trajectories through to the exit surface. Whether or not this difference becomes significant depends on the size of the humps and troughs (the roughness) on the surface relative to the total thickness. The measured roughness for each foil, expressed as a percentage of the nominal foil thickness, was 0.09 % and 0.36 % for the Mylar and ZrO_2 foils respectively.

Lateral variation (∂w) in foil thickness is generally considered a major source of error in thickness measurements [36]. The transmission method employed here to measure foil thickness in effect gives an average thickness because the source-detector solid angle is such that the alpha beam reaching the energy detector passes through an area more than half the size of the frame aperture. A hindsight realisation that came in handy was that to get an estimate of the order of magnitude of the lateral variation of the foils a second value of the thickness of the ZrO_2 foil could be extracted from RBS measurements for comparison. RBS analysis was carried out mainly to ascertain the stoichiometry and impurity content of the vacuum deposited foil and is described in section 5.5.3.

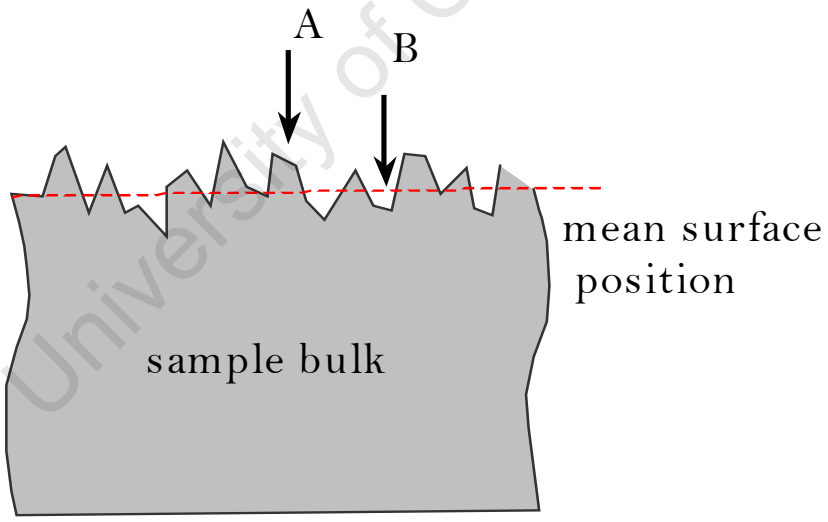

Figure 5.12 A simple schematic to illustrate the concept of roughness in thickness measurement

For the measurement, a piece of foil measuring roughly 5 x 5 mm^2 was fixed onto a silicon wafer piece for support using silver glue. Care was taken to apply the glue only at two edges of the sample to avoid contamination. A 2 MeV He^{2+} ion beam with a spot size of about 2.0 mm diameter was used, which meant that the thickness measurement was

relatively much more localised. Figure 5.13 shows the RBS spectrum obtained from the measurement together with a theoretical fit to the data using the program RUMP [37]. The thickness of the ZrO_2 foil at the spot of measurement was found to be 4790 x 10^{15} at cm^{-2}. In units of areal density this is 326.7 µg cm^{-2}.

The transmission method using the ^{241}Am alpha source gave an average thickness of 331.2 µg cm^{-2}. If the difference (4.5 µg cm^{-2}) between the two results can be regarded as the average thickness deviation between adjacent regions of the foil, it translates to 1.4 % in percentage terms. Given that the RBS measurement was done on just one spot of the whole foil it is possible that measurements on several different spots could give quite varied results. A conservative estimate of the average value of the lateral variation would therefore be of the order of 1 %.

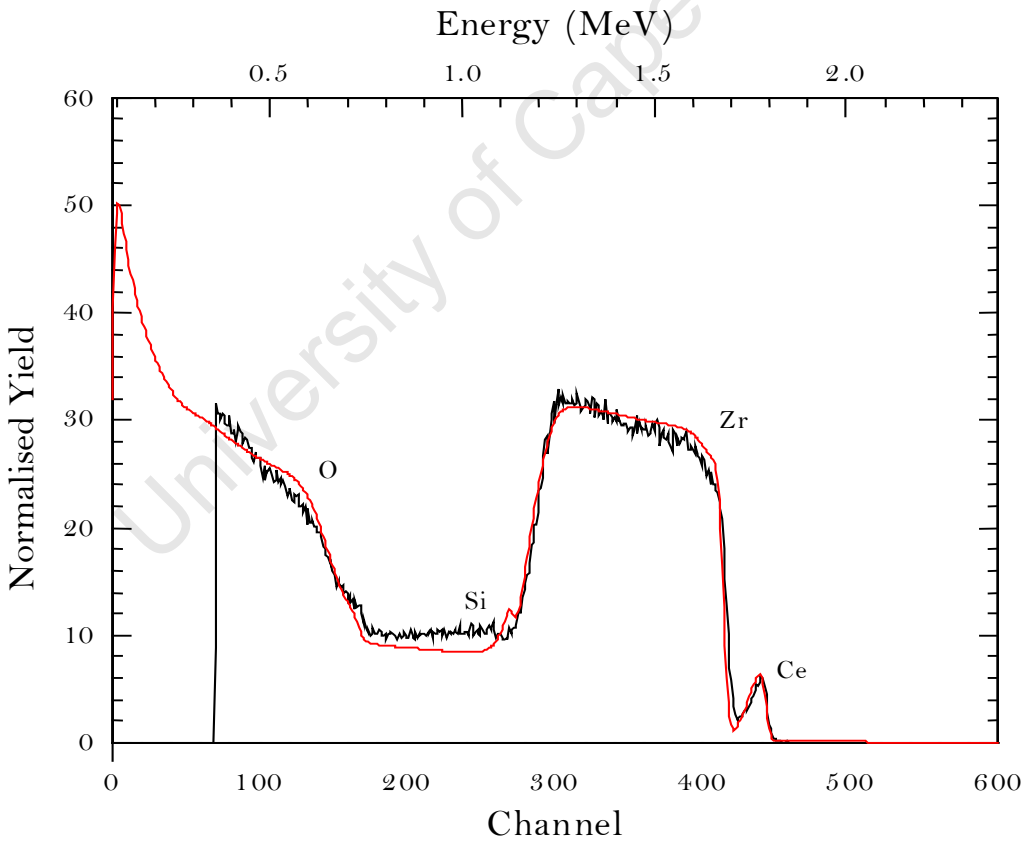

Figure 5.13 Experimental (black) and simulated (red) RBS spectra of the Zirconium Oxide target foil for determination of the foil thickness and stoichiometry.

One of the causes of energy straggling through each foil is the difference in the path lengths traversed by monoenergetic particles due to lateral variation. The ratio of the calculated straggling constants between any two foils should then be indicative of the proportionate difference in the lateral variation of the two foils, e.g.

$$\frac{\Omega_{ZrO_2}}{\Omega_{Mylar}} = \frac{\partial w_{ZrO_2}}{\partial w_{Mylar}} \qquad [5.11].$$

Substituting the straggling constants calculated for the two foils and the estimated maximum lateral variation of 1% in the ZrO_2 foil in Equation 5.10, one also gets $\partial w_{Mylar} = 1.0$ % for the estimate value of the lateral variation in the Mylar foil.

All these factors described in the preceding discussion that contribute to the uncertainty in the measurement of foil thickness can be added up in quadrature to get an effective value of the fractional uncertainty δx (in %). Table 5.3 sums up these factors for the two foils.

Foil	ΔE_{det}	ΔS_{He}	Ω	∂x	∂w	δx
ZrO_2	0.3	4.1	0.59	0.36	1.0	4.3
Mylar	0.3	4.1	0.58	0.09	1.0	4.2

Table 5.3 A summation of the various factors contributing to the overall uncertainty δx in the measurement of foil thickness for the two foils. [ΔE_{det} – SB detector resolution, ΔS_{He} – uncertainty in the stopping power of Helium ions in the foil, Ω-straggling, ∂x – roughness and ∂w – lateral variation].

5.5.3 Zirconium Oxide foil stoichiometry

The essential features of the spectrum shown in Figure 5.13 are the oxygen (O) and zirconium (Zr) peaks. The simulation indicates presence of an element heavier than Zr in the foil. From the information provided by the foil manufacturer the high-energy end peak suggests that the stabilizing material used during the deposition process was cerium oxide. The best-fit simulation of the experimental spectrum indicates that the Ce impurity is in the uppermost layers of the foil. It most probably aggregated on the surface layers after the deposition since it does not appear to extend into the bulk of the foil. The simulated thickness of the whole Zr peak was found to be 4790 at cm^{-2} and that of the Ce-containing layer 350 x 10^{15} at cm^{-2}, implying that the cerium oxide is found in 7.2 % (i.e 350/4790) of the total foil thickness. In that layer the simulated atomic fraction of Ce is 4.6 % and when considering the total foil thickness the relative concentration of Ce falls to 0.33 %.

SRIM calculations of stopping powers in Zirconium Oxide with and without the 0.33 % Ce impurity showed that maximum deviation between stopping power values with and without the impurity was at the Bragg peak and, below 1 %. At such a low concentration the effect of Ce was neglected in subsequent stopping power calculations. The simulated Si content in Fig. 5.13 is not a real concentration since the Si signal was due to the wafer piece that was used as a support for the foil piece during measurement. This was thought to be a result of either, a bigger beam spot than initially thought, or beam instability. Nonetheless, the stoichiometric ratio of zirconium to oxygen in the (350 x 10^{15} at cm^{-2} thick) surface layers was simulated to be 1: 2.4. In the bulk (> 90 %) of the foil the simulation gave a ratio of 1: 2 and so for practical purposes, the stoichiometric ratio used for SRIM calculations was 1 to 2[†], ignoring the slight deviation of 1: 2.4 in the surface layers.

[†] Near perfect agreement among oxygen stopping powers measured in this work (see section 5.6.1.4), those predicted by SRIM and experimental data from Zhang and Weber [38] also points out to a stoichiometric ratio of Zr (1) : O (2).

5.6 Results and discussion of stopping power measurements

Stopping power measurements were carried out using an incident beam of 27.5 MeV Kr^{15+} ions. Various targets were used to produce a variety of recoils; a thick (>1 μm) layer of aluminium oxide on a silicon substrate to get aluminium and oxygen recoils, a lithium fluoride crystal for fluorine recoils, a magnesium oxide layer on silicon for magnesium (and oxygen) recoils, carbon graphite for carbon recoils, and a plain silicon wafer piece for silicon recoils. The following is a series of results obtained using the data analysis procedure described in 5.4.2 for each *ion - target foil* combination. Raw ToF – E scatter plots obtained with and without the stopper foils are included in Appendix B, with the ToF axes already converted from channels to (nano) seconds using the time calibration fit;

$$ToF = 0.696 * Ch - 149.8 \ (ns) \qquad [5.12].$$

Whereas measurements give *total* stopping power, SRIM calculates the electronic and nuclear contributions to stopping separately. Although the nuclear stopping contribution in the energy ranges concerned here is relatively small, it was nonetheless added to the electronic component to get a more complete representation of total stopping according to SRIM. Comparisons between experiment and SRIM prediction are presented separately for each ion species in following discussion. Comparisons with pure theory using calculations from the PASS code [38], also included in the data plots for ZrO_2, are discussed at a later stage.

5.6.1 Heavy ion stopping powers in ZrO_2

The first set of results presents stopping powers of Al, Mg, F, O and C ions through the (331.2 μg cm^{-2}) ZrO_2 foil. Given uncertainties of 4.8% in the energy loss measurements and 4.3 % in the foil thickness measurement, the stopping power values presented each have a 6.4 % spread, indicated by the error bars. At the time of writing, the only other available experimental stopping power data is for C, O and F ions from Zhang and co-workers [39, 40]. No experimental data for Al and Mg ions is available in the literature for comparison.

MSTAR stopping power compilations do not include ZrO_2 as a target hence the comparison with just SRIM (2008 version), the only other semi-empirical code covering a wide range of ions and targets. Some of the results presented here have been published in the journal of *Nuclear Instruments and Methods in Physics Research* ***B*** [41].

5.6.1.1 Aluminium

The experimental stopping power of ^{27}Al ions through ZrO_2 and predictions from SRIM and PASS are plotted together in Figure 5.14. At first glance it can be seen that, within experimental error, the experimental and SRIM values generally agree with each other. However to get a more quantitative description of the apparent difference between experiment (S_{EXPT}) and SRIM (S_{SRIM}) calculations the ratio S_{EXPT}/S_{SRIM} was calculated for each pair of values at each particular energy.

The results of the calculations are summed up in Figure 5.15 revealing a systematic trend in the deviation between S_{EXP} and $S_{SRIM2008}$ values. At low energies SRIM2008 calculations underestimate experiment by up to 5% and at higher energies SRIM2008 overestimates experimental values by up to 5% as well. The shift from under - to overestimation can be modelled by a linear fit function as illustrated in the data plot. The fit function may be regarded as a correlation factor (f_c) function for SRIM, valid over the 0.1 – 0.5 MeV/u energy range. That is, for ^{27}Al ions through ZrO_2, stopping power values in that energy range that were obtained in this work can be approximated by $S = f_c S_{SRIM2008}$, where $f_c = 1.0814 - 0.2513E$, with the energy E given in MeV/u.

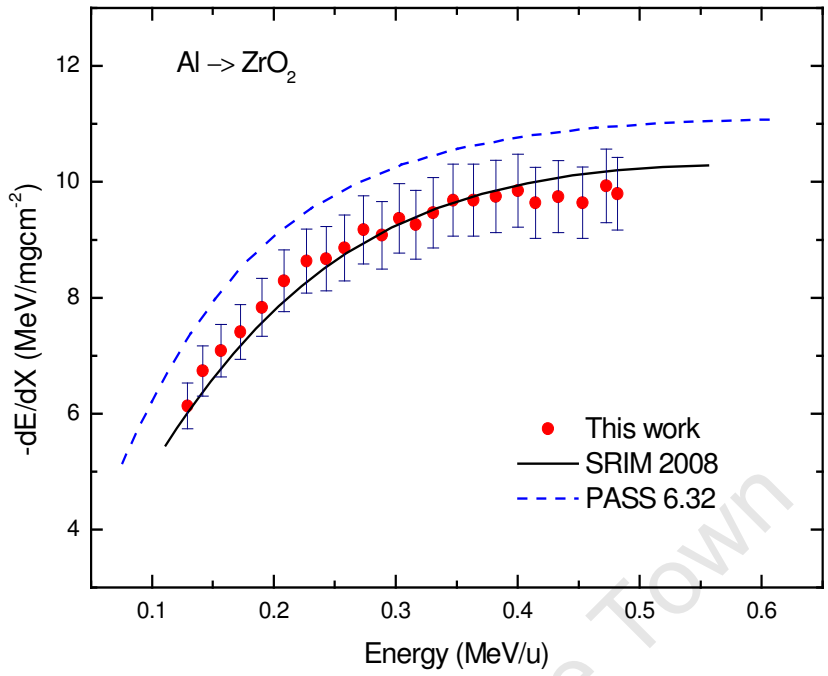

Figure 5.14 Experimental stopping powers of ^{27}Al ions in ZrO_2 in the 0.10 – 0.50 MeV/u energy range compared to SRIM2008 and PASS 6.32 predictions.

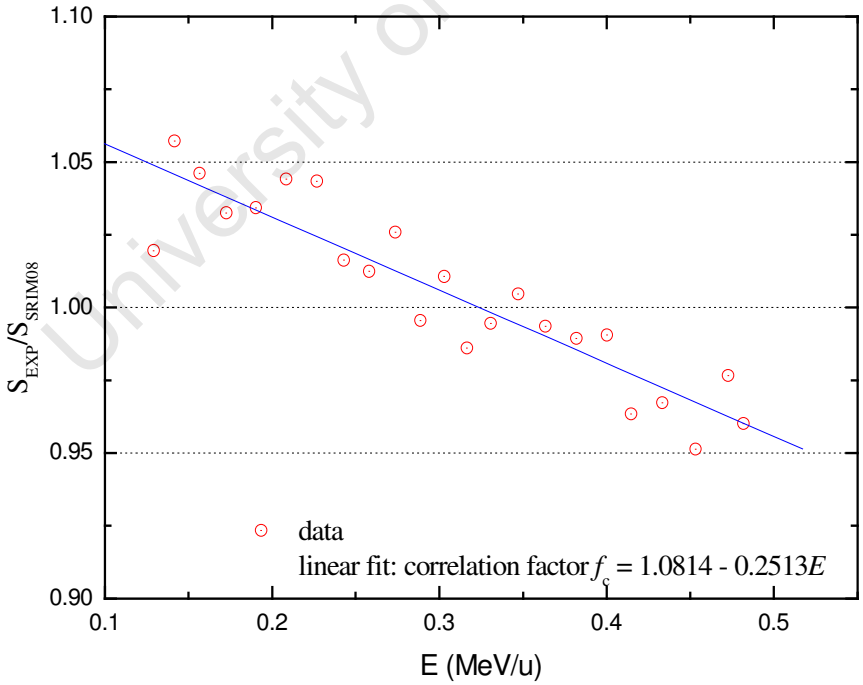

Figure 5.15 Plot showing the energy dependency of the ratio of experimental to SRIM2008 stopping power values of ^{27}Al ions in ZrO_2.

5.6.1.2 Magnesium

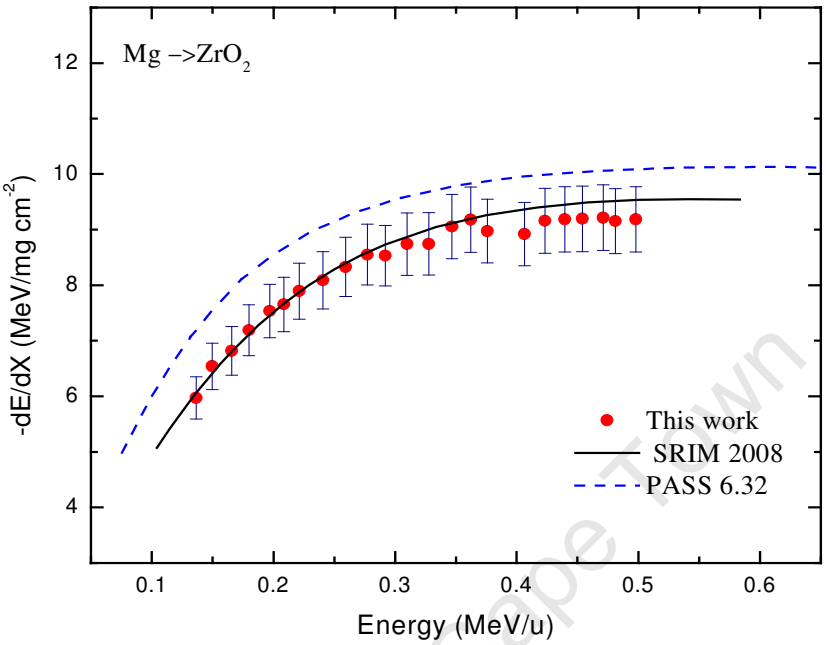

Figure 5.16 Experimental stopping powers of ^{24}Mg ions in ZrO_2 in the 0.10 - 0.50 MeV/u range compared to SRIM2008 and PASS 6.32 predictions.

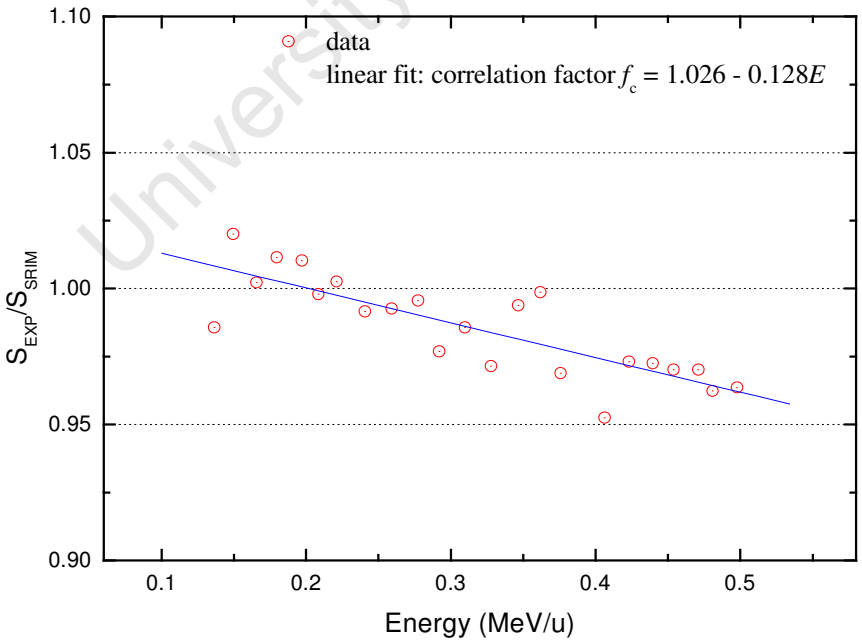

Figure 5.17 Plot showing the energy dependency of the ratio of experimental to SRIM2008 stopping power values of ^{24}Mg ions in ZrO_2.

The stopping power values of ^{24}Mg ions in ZrO_2 are compared in Figure 5.16. Indications are that there is good agreement between experiment and SRIM from 0.10 to 0.35 MeV/u. Thereafter SRIM overestimates the experimental stopping power, but to a lesser extent than in the Al – ZrO_2 system. Again a plot of the S_{EXPT}/S_{SRIM} ratio against energy in Figure 5.17 gives a more quantitative perspective of the observed deviations. Like for the ^{27}Al ions, the (slight) deviation between experimental and SRIM stopping powers over the 0.10 – 0.50 MeV/u energy range can be approximated by a linear function: $f_c = 1.026 - 0.128E$.

5.6.1.3 Fluorine

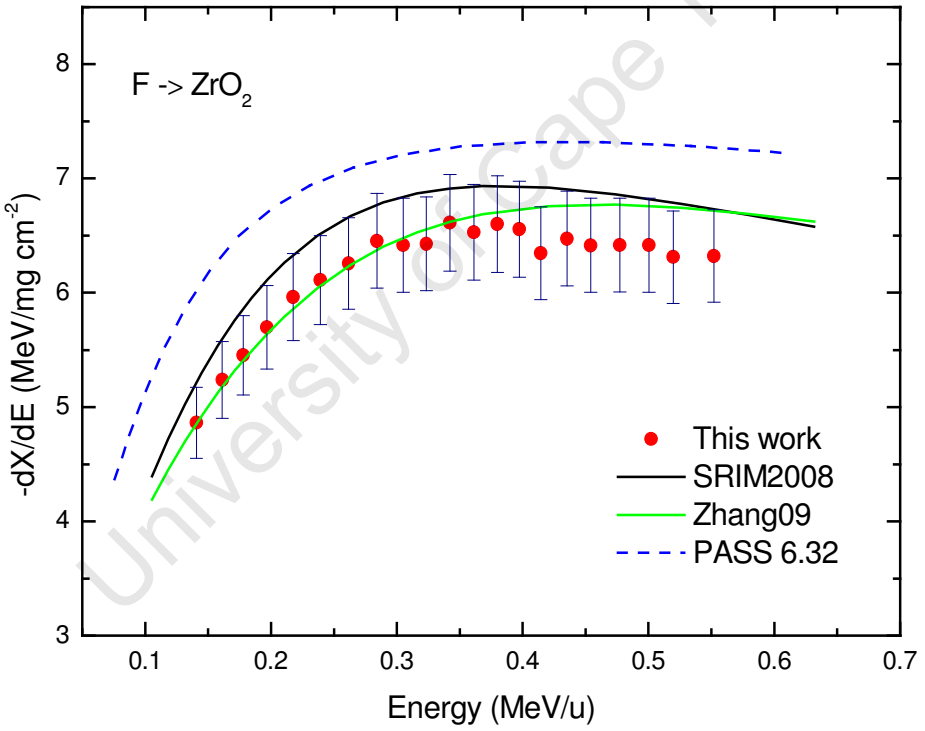

Figure 5.18 Experimental stopping powers of ^{19}F ions in ZrO_2 in the 0.1 - 0.6 MeV/u energy range compared to SRIM2008 and PASS 6.32 predictions, and data from ref [39].

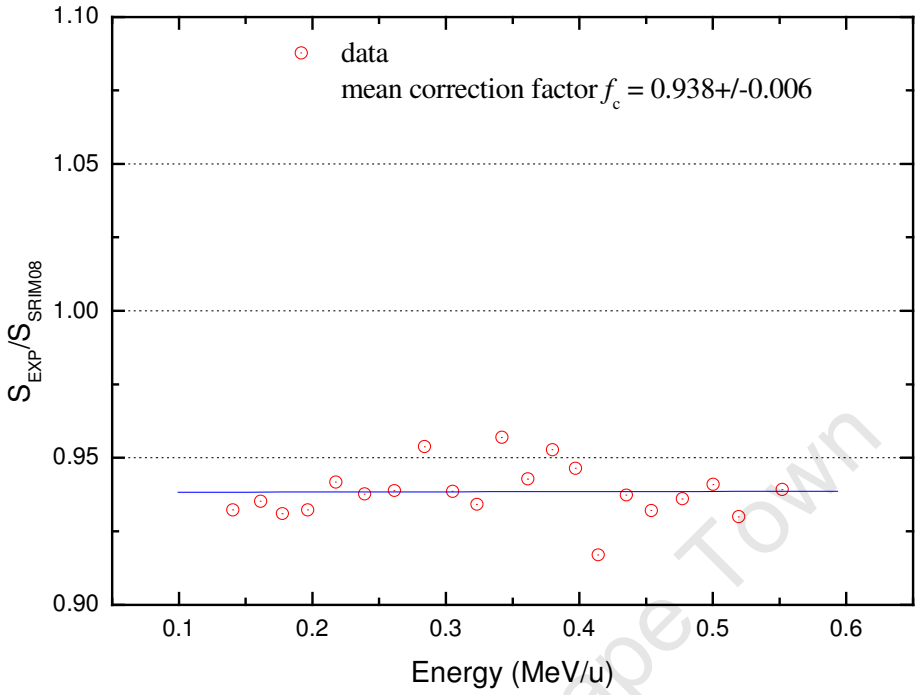

Figure 5.19 Plot showing the energy dependency of the ratio of experimental to SRIM2008 stopping power values of ^{19}F ions in ZrO_2.

Results of the measurements and calculations of the stopping power of ^{19}F ions in ZrO_2 are plotted in Figure 5.18. Also plotted in the same figure are experimental results by Zhang and Weber [39], whose data was reproduced here using the following fit equation to their experimental data plots;

$$-\left\langle \frac{dE}{dX} \right\rangle = \left\{ \frac{1}{A_1 E^{A_2}} + \frac{1}{\left[\frac{1000 \text{ x } A_3}{E} \text{ x ln}\left(1 + \frac{1000 \text{ x } A_4}{E} + \frac{A_5 E}{1000} \right) \right]} \right\}^{-1} \qquad [5.13],$$

where E is the energy in keV/u and A1-A5 are the fitting coefficients, given in ref [39].

The two experimental data sets are in near perfect agreement between 0.1 and 0.4 MeV/u, after which deviations in the order of the experimental uncertainty occur. In the region of agreement SRIM consistently overestimates the experimental data by more than 6%. A plot of the ratio S_{EXPT}/S_{SRIM} against energy in Figure 5.19 shows that the deviation is

independent of energy. A mean correlation factor between S_{EXP} and $S_{SRIM2003}$ given by f_c = 0.938±0.006 describes the average disagreement between experiment and SRIM prediction.

5.6.1.4 Oxygen

Figure 5.20 displays the comparison between experimental and calculated stopping power values of ^{16}O ions in ZrO_2. Current data and that from ref [39] agree quite well within the energy range 0.10 – 0.50 MeV/u. In that range SRIM prediction is slightly (< 3 %) above experimental data. From above 0.5 MeV/u the deviation between current data and ref [39]'s data and that between present data and SRIM prediction approaches 5 – 7 %.

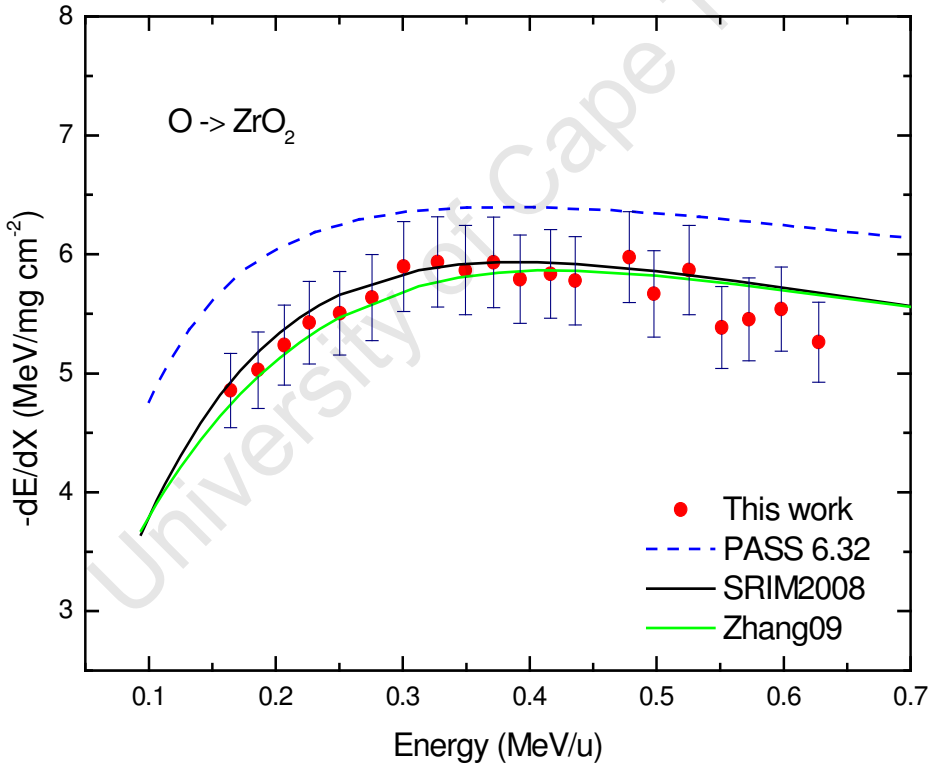

Figure 5.20 Experimental stopping powers of ^{16}O ions in ZrO_2 in the energy range 0.1 - 0.6 MeV/u compared to SRIM2008 and PASS 6.32 predictions, and data from ref [39].

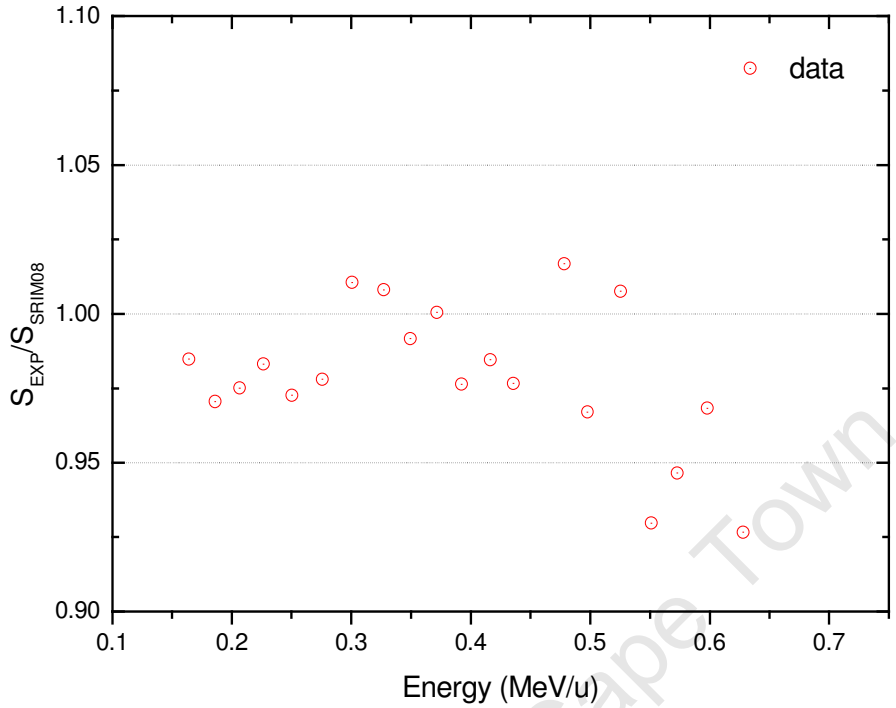

Figure 5.21 Plot showing the energy dependency of the ratio of experimental to SRIM2008 stopping powers of ^{16}O ions in ZrO_2.

Figure 5.21 shows the comparison in greater detail and reveals that the deviation between the experimental and the SRIM predicted values in the 0.1 – 0.5 MeV/u energy range is well within 3%. This is much less than the measurement uncertainty. Unlike in the previous cases the deviation here varies randomly with ion energy.

The oxygen ions in Figure 5.20 above were obtained as recoils ejected from a thick layer of Al_2O_3 on a Si substrate. In a separate earlier run aimed at determining the stopping power of ^{24}Mg ions in ZrO_2, ^{24}Mg ions were obtained as recoils ejected from a layer of MgO on Si. In the process, ^{16}O ions were also ejected as recoils. Measuring the stopping power of these ^{16}O ions provided a means of checking the consistency of the measurement procedure. Data from this measurement is shown in Figure 5.22 as solid squares, overlaid on data from Figure 5.20. The two experimental data sets agree quite well at low energies. At higher energies there is a gradual increase in scatter seen in earlier data plots, but in general the results agree to within the experimental uncertainty of the measurement.

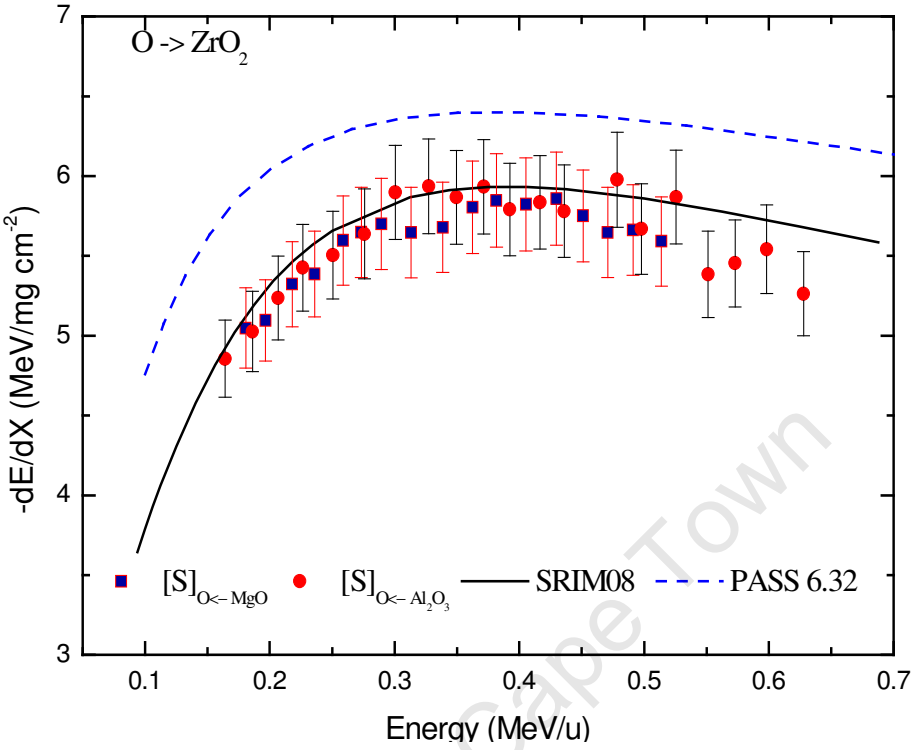

Figure 5.22 Experimental stopping powers of ^{16}O ions in ZrO_2 in the energy range 0.1 - 0.6 MeV/u compared to SRIM2008 and PASS 6.32 predictions. The ^{16}O ions were obtained as recoils from two different targets; Al_2O_3\Si (red dots) and MgO\Si (navy squares, to check the consistency of the measurement procedure.

5.6.1.5 Carbon

Results of the measurements and calculations of the stopping power of ^{12}C ions in ZrO_2 are plotted in Figure 5.23. Also included in the plot is experimental data by Zhang *et al.* [40], also reproduced here using Equation 5.11.

The measurement uncertainty in the data from ref [40] is less than 4%. The data plots show that, save for the initially good match between current data and SRIM 2008 in the range 0.2 to 0.3 MeV/u, the latter tends to overestimate the experimental stopping power in the region of energies beyond 0.3 MeV/u. Overestimation by SRIM 2008 is also observed when comparing with data from Zhang *et al.*, occurring from below 0.2 MeV/u.

Figure 5.24 gives a more quantitative picture of the relative differences between the current experimental data and each of SRIM 2008 and Zhang *et al*'s data. Discarding the data point just below 0.6 MeV/u, observation is that on the whole, the deviation between data from either source and present data is within 10% over the energy range shown. With such a relatively wide degree of scatter in this instance the idea of a possible SRIM correlation factor might not be quite useful. On average the spread between this data and that from Zhang and co-workers is less than that between the current data and SRIM2008 calculations.

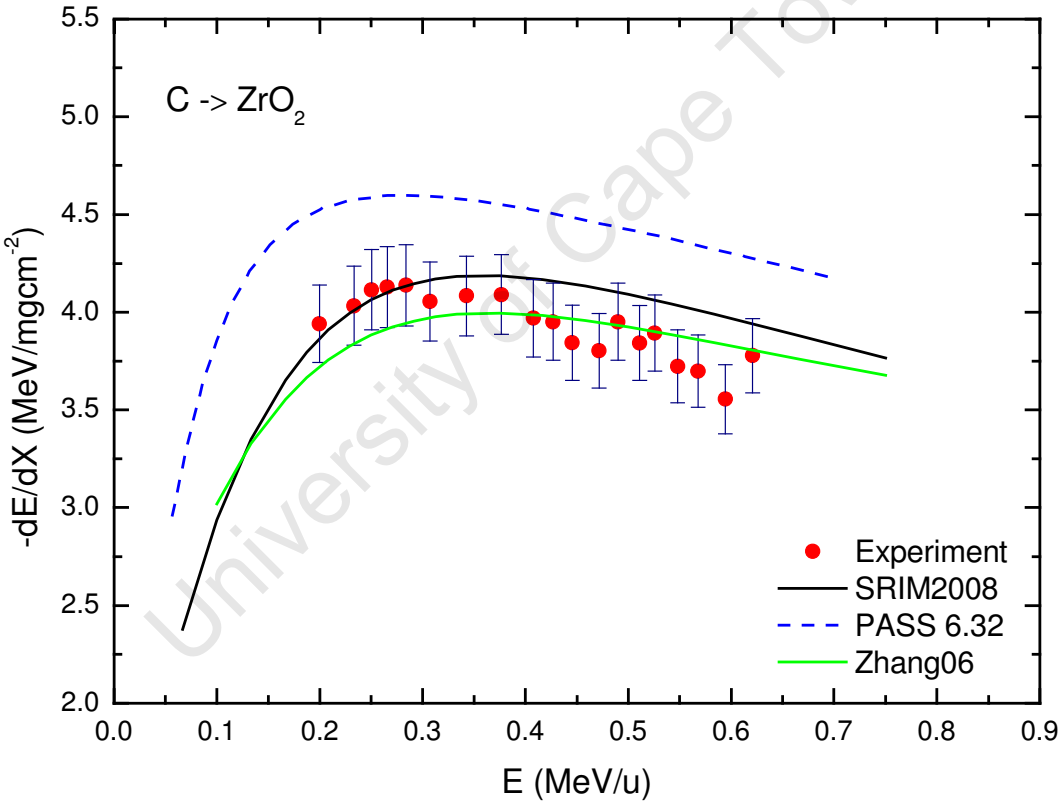

Figure 5.23 Experimental stopping powers of ^{12}C ions in ZrO_2 in the energy range 0.1 - 0.7 MeV/u compared to data from ref [40], SRIM2008 and PASS 6.32 predictions.

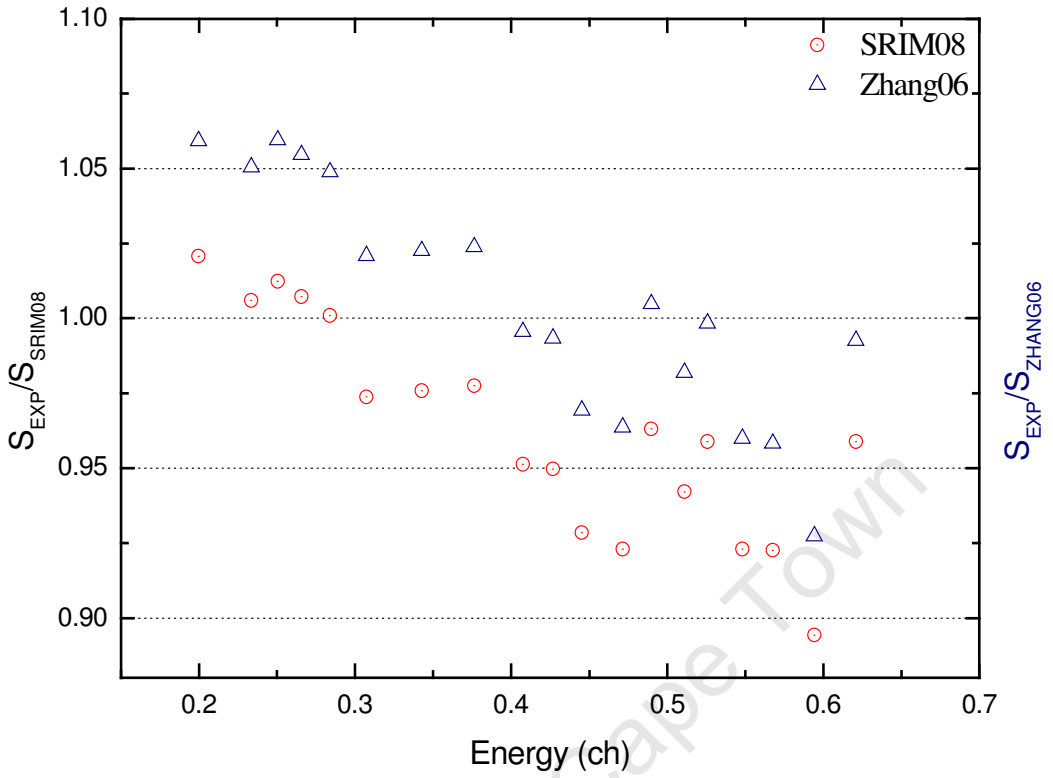

Figure 5.24 Plot showing the energy dependency of the ratio of experimental stopping power data of ^{12}C ions in ZrO_2 to SRIM2008 prediction and the ratio of current data to experimental data from Zhang et al [40].

5.6.1.6 Comparison with PASS 6.32

Calculation results from PASS were sourced from the author of the code [38] to compare experiment with predictions of the binary encounter theory [42]. Like in SRIM, the output of the calculation of the stopping power lists the electronic and nuclear contributions to total stopping separately. For purposes of comparison the two components were added together to get the total stopping power at each given ion energy.

From the results displayed in Figures 5.14, 5.16, 5.18, 5.20 and 5.23, indications are that PASS overestimates the stopping power of ZrO_2 over the respective energy ranges for all the ions studied here. Unlike for SRIM, a direct comparison of each experimental data point against theory at each given ion energy is not quite possible as the PASS code is not readily available to users. As an alternative approach, PASS stopping power values (S_{PASS}), quoted

at the same energy values as the experimental ones (S_{EXP}), were estimated by extrapolation from the PASS stopping power curve for each ion species. The degree of overestimation, quantified by the ratio S_{EXP}/S_{PASS} like before, is plotted as a function of ion energy in Figure 5.25.

The general impression from Figure 5.25 is that minimum deviation between experiment and theory, for all the ions, occurs in the 0.3 – 0.4 MeV/u energy region, i.e within the stopping power maximum energy region. At lower energies, on closer inspection, an interesting trend that can be observed is that the discrepancy between experimental data and PASS lessens as the mass of the projectile ion increases. A case in point to confirm this observation is a comparison of the experimental stopping power data of ^{84}Kr ions in ZrO_2, measured in this work and published elsewhere [43], with PASS calculation. The comparison is shown in Figure 5.26 where it can be seen that PASS describes stopping quite well, better than SRIM even.

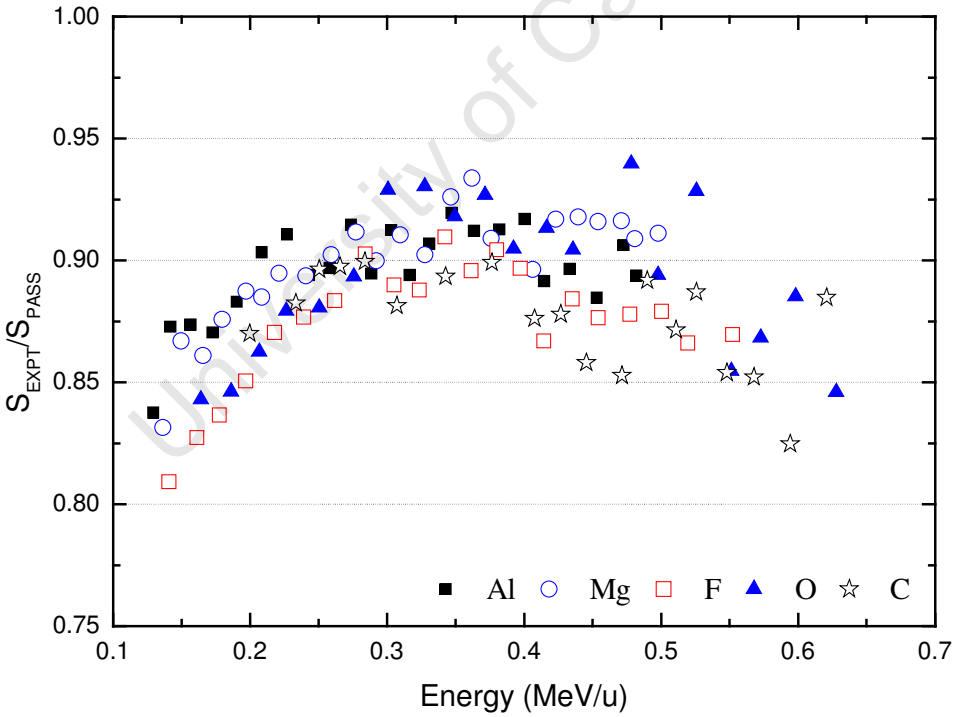

Figure 5.25 Plot showing the energy dependency of the ratio of experimental stopping powers to theoretical values predicted by the PASS code for ^{27}Al, ^{24}Mg, ^{19}F, ^{16}O and ^{12}C ions in ZrO_2.

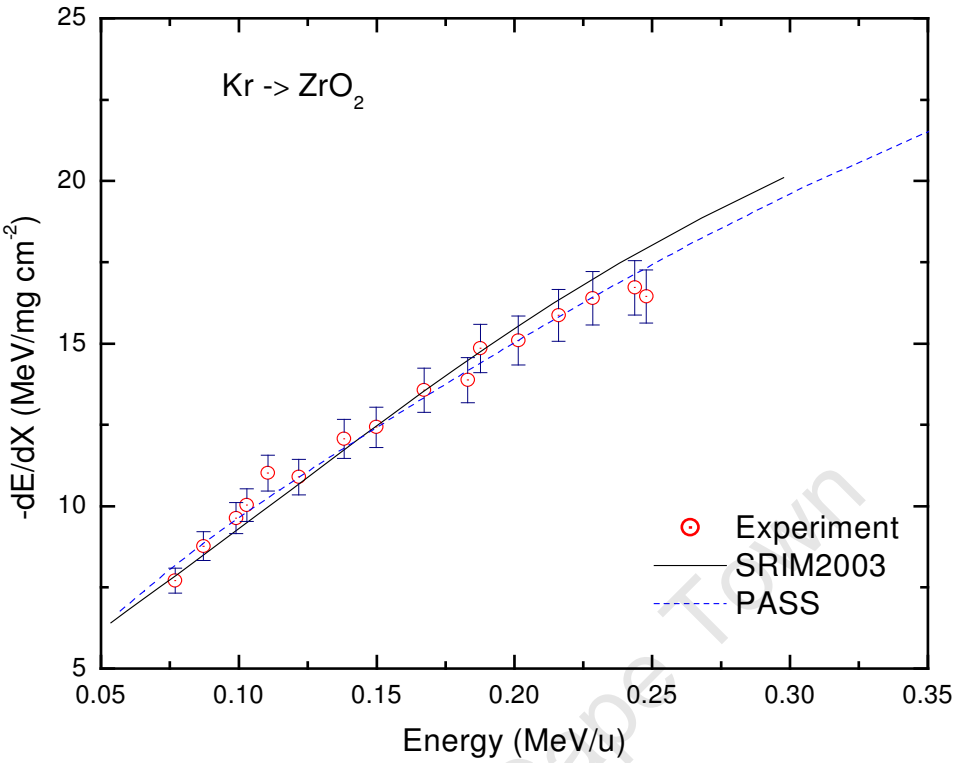

Figure 5.26 Experimental stopping powers of ^{84}Kr ions in ZrO_2 in the energy range 0.05 - 0.30 MeV/u compared to SRIM2008 and PASS 6.32 predictions [from ref 43].

5.6.2 Heavy ion stopping powers in Mylar®

Stopping powers of Mylar for ^{28}Si, ^{27}Al, ^{24}Mg, ^{19}F, ^{16}O and ^{12}C ions measured in this work are presented in this section and compared with predictions from SRIM and MSTAR [20]. Experimental data from the literature, where available, is also included.

5.6.2.1 CAB corrections

In calculating stopping powers in compounds, SRIM uses what is known as Bragg's additivity rule, whereby the stopping power of a compound for a given projectile ion is estimated by the linear summation of the stopping powers of its constituent elements for that ion [23]. Deviation from Bragg's rule however does occur in compounds because of the changes that take place in the orbital electronic structure of elemental atoms when they

form bonds in compounds. This effect has been observed to be more pronounced in compounds of light elements (particularly hydrocarbons) than in compounds containing heavy elements, presumably because the proportion of orbital electrons that take part in bonding decreases as the atomic number increases.

Based on experimental work done from the 1960s by the Baylor University and the Köln University groups on the stopping of H, He and Li ions in hydrocarbons [44], Ziegler and Manoyan [2] devised a method of predicting stopping powers in compounds using the superposition of contributions from atom "cores" with that from "bonds". Their method is now generally known as the cores-and-bonds (CAB) approach. CAB calculations enable one to compute correction factors for Bragg's rule calculated stopping powers for many *ion – compound* combinations (where the compound is a light element compound), by using the ratio of the CAB approach calculation to Bragg's rule value of the stopping power of 125 keV protons in that compound. This ratio is scaled by the effective charge of that projectile ion at any given velocity (energy) to get the correction factor. The choice of energy of 125 keV for the proton has its origins from the experimental observation that the maximum deviation from Bragg's rule occurs at the stopping peak and for protons 125 keV is near the stopping peak in most of the studied compounds [2].

The following data plots of heavy ion stopping in Mylar then include both types of SRIM calculations; with and without CAB corrections. The degree of error in the measured stopping powers, resulting from the 4.2% and 4.8% uncertainties in foil thickness and energy loss measurements respectively, is about 6.4%.

5.6.2.2 Silicon

Figure 5.27 shows the measured stopping power of ^{28}Si ions in Mylar over the energy range 0.15 – 0.45 MeV/u compared with SRIM and MSTAR predictions. As it happens only one other set of experimental data with only a slight overlap in the energy range is available in the literature [45]. The default CAB correction for the stopping power of heavy ions in Mylar is –6.57 %. Current data agrees quite well with data from ref [45] over the energy range of overlap, 0.36 – 0.45 MeV/u, and from 0.36 MeV/u onwards, CAB

corrected SRIM calculations describe data quite well. At lower energies however, from 0.15 – 0.35 MeV/u, Bragg's rule seems to predict the stopping power reasonably well without need for correction. In fact CAB corrections underestimate stopping by more than 5% in the energy range up to about 0.30MeV/u. MSTAR predictions are accurate to within 5% of the present data over whole energy range studied as shown. An interesting observation to note is the kink in the experimental data between 0.36 and 0.40 MeV/u as agreement with calculation shifts from uncorrected to CAB corrected predictions.

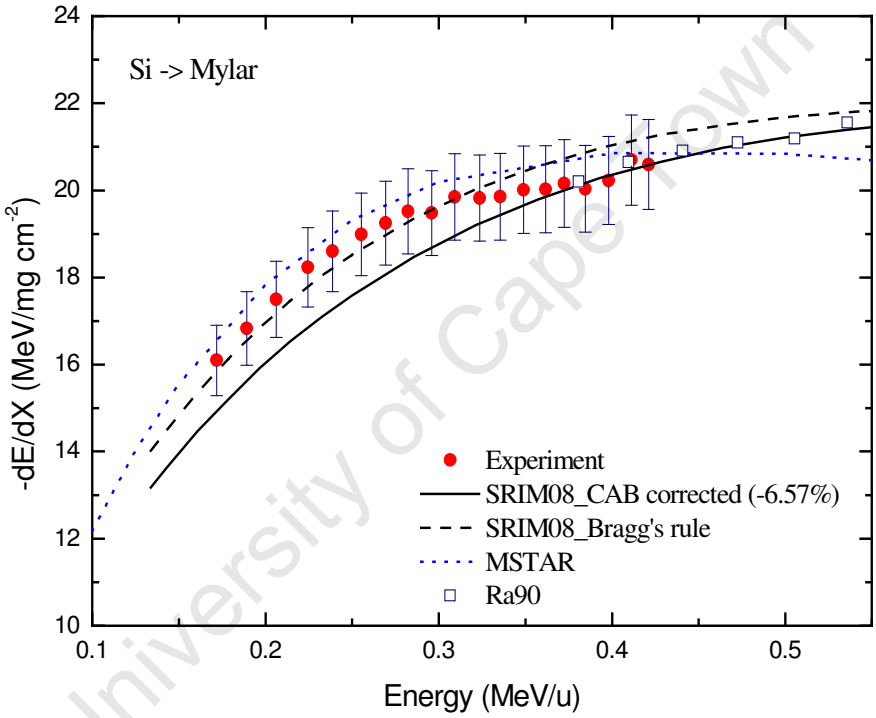

Figure 5.27 Experimental stopping powers of ^{28}Si ions in Mylar in the energy range 0.15 - 0.50 MeV/u compared to SRIM2008 and MSTAR predictions and data from ref[45].

5.6.2.3 Aluminium

Results from the measurement of ^{27}Al stopping powers in the Mylar foil are displayed in Figure 5.28, together with SRIM and MSTAR predictions. Data from experiments found in the literature is again from ref [45] like for ^{28}Si ions.

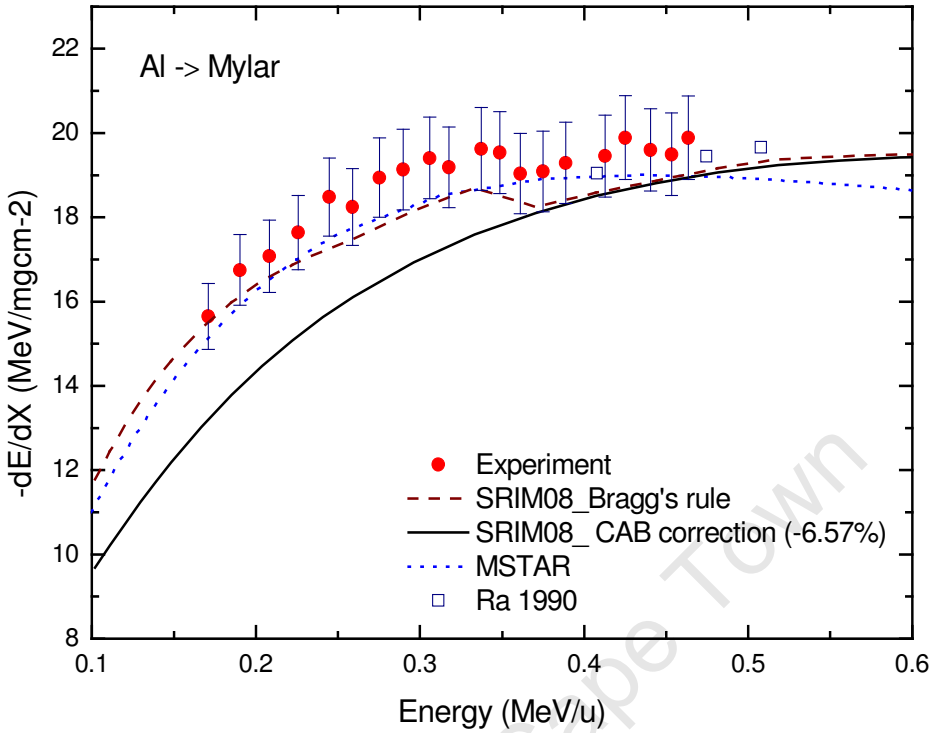

Figure 5.28 Experimental stopping powers of ^{27}Al ions in Mylar in the energy range 0.15 - 0.55 MeV/u compared to SRIM2008 and MSTAR predictions and data rom ref [44].

It is again noted here like in the Si – Mylar® system that within experimental error limits current data agrees with data from Räisänen and Rauhala [45] albeit over the small 0.4 – 0.55 MeV/u energy range covered by the reference data set. In that same energy range the CAB corrected and uncorrected Bragg's rule calculations strangely enough, coincide, and both slightly underestimate the two data sets. At lower energies, from just under 0.20 MeV/u to 0.34 MeV/u, the CAB corrected calculation grossly underestimates experimental data by up to 12%. Predictions from Bragg's rule are just within 5% of data. MSTAR predictions lie within the 6 % experimental error limit but in this case underestimating the data. The kink seen in the Si – Mylar system shows up again here between 0.35 and 0.40 MeV/u. Interestingly, the Bragg's rule trend line has a similar step in the same energy region.

5.6.2.4 Magnesium

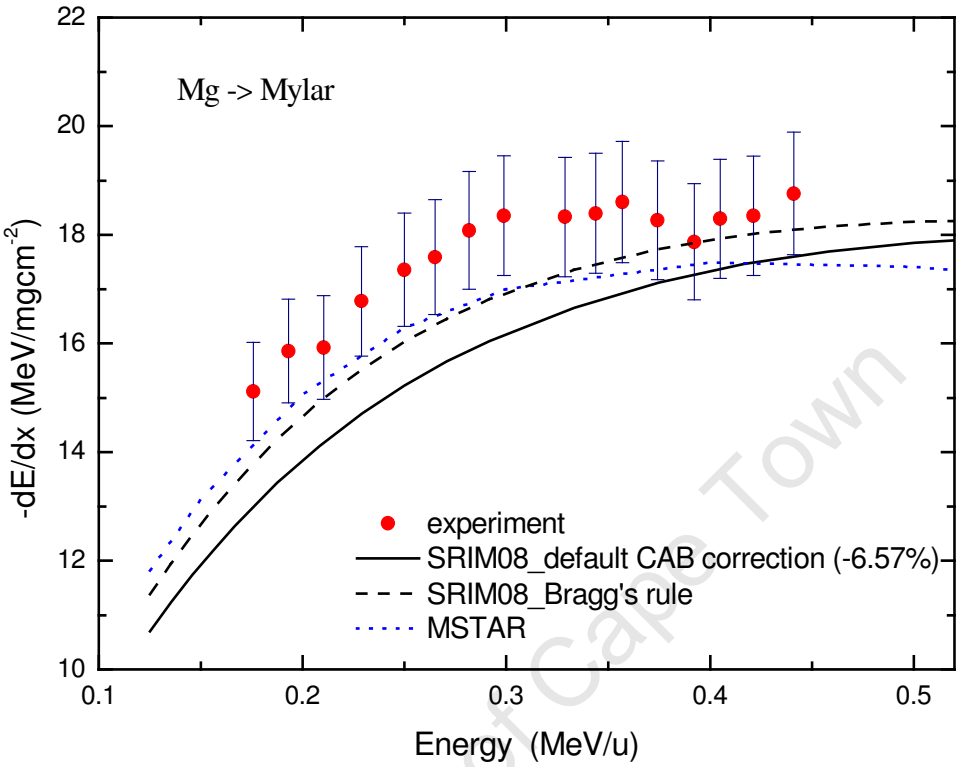

Figure 5.29 Experimental stopping powers of ^{24}Mg ions in Mylar in the energy range 0.15 - 0.50 MeV/u compared to SRIM2008 and MSTAR predictions.

Figure 5.29 displays results from measurements of the stopping of ^{24}Mg ions in Mylar. Unfortunately for this system no experimental data from the literature could be found for reference. Included in the data plot are SRIM and MSTAR calculations for comparison.

Bragg's rule underestimates experimental data by slightly more than 6%, from low energies up to about 0.35 MeV/u. Just after that point a dip in data, much like in the Si – Mylar and Al – Mylar systems, is also observed. From ~0.38 MeV/u onwards Bragg's rule prediction is within 6% of data. On the other hand the CAB corrected values fall below experimental data by up to 12% in the low energy region. After the dip the level of agreement with experiment averages 5%. MSTAR calculations also on average deviate from data by slightly over 6% over the whole energy range.

5.6.2.5 Fluorine

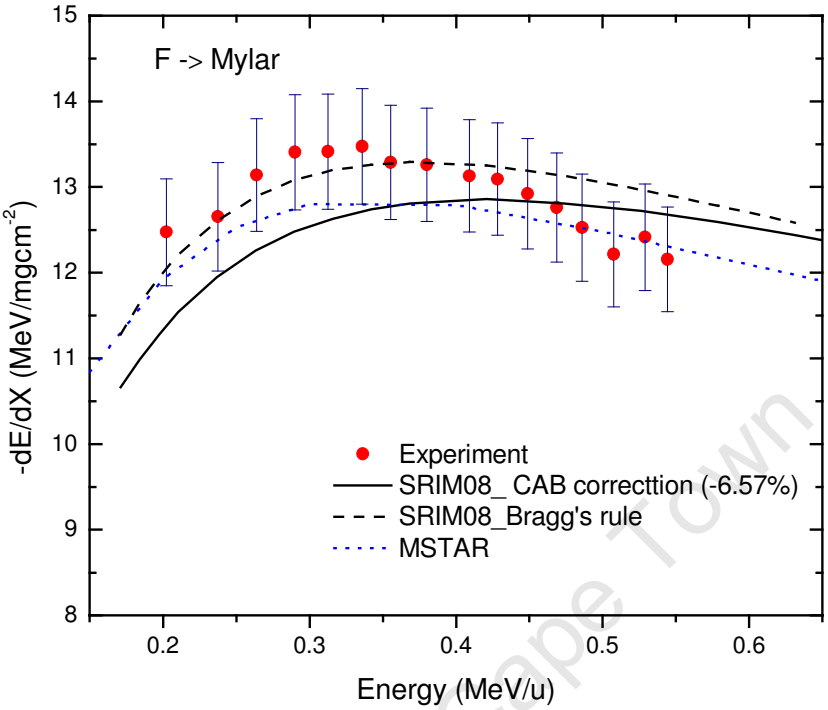

Figure 5.30 Experimental stopping powers of ^{19}F ions in Mylar in the energy range 0.15 - 0.60 MeV/u compared to SRIM2008 and MSTAR predictions.

Figure 5.30 shows experimental and calculated stopping powers of ^{19}F ions in Mylar. Calculations using Bragg's rule appear to predict experimental values better than the CAB based approach. At low energies the CAB corrected stopping power calculations are lower than experimental data by up to 8%. The tendency though at higher energies (> 0.50 MeV/u) is that calculations overestimate experimental values by about 6% and 4% for Bragg's rule and the CAB approach, respectively. MSTAR calculations describe stopping relatively better than both SRIM calculations when averaged over the whole energy range. Deviation from experiment is at a maximum at about 6% at 0.30 – 0.35 MeV/u, getting less on either side of that range.

5.6.2.6 Oxygen

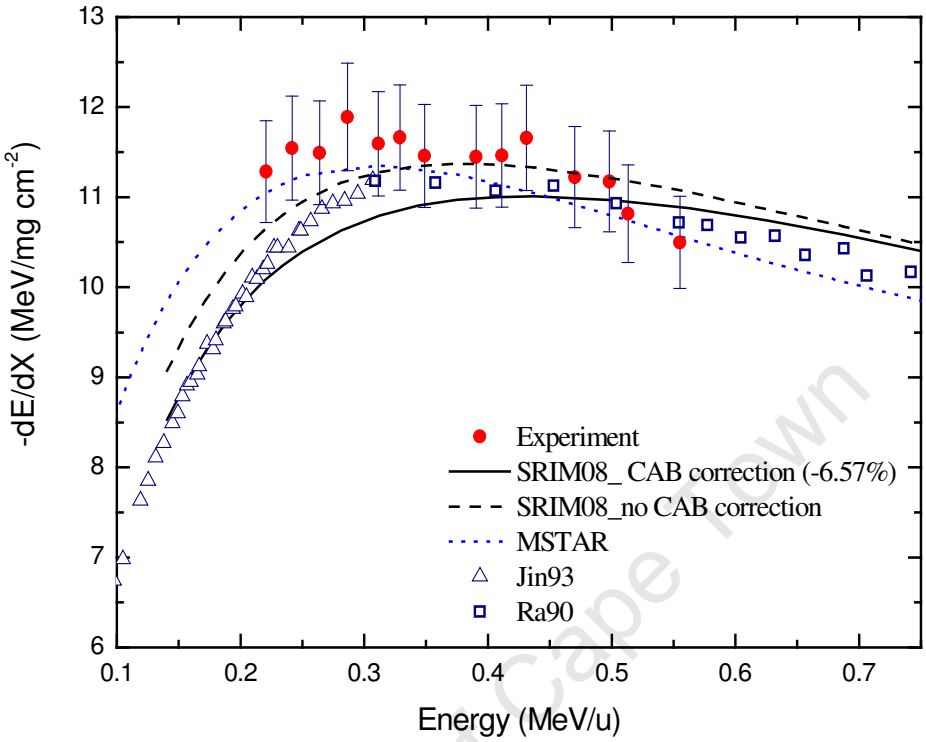

Figure 5.31 Experimental stopping powers of ^{16}O ions in Mylar in the energy range 0.15 - 0.60 MeV/u compared to SRIM2008 and MSTAR predictions and data from refs [45] (□) and [46] (Δ).

Results from measurement of the stopping power of oxygen ions in Mylar are reported in the data plot in Figure 5.31. Included in the data plot are results of measurements by J. Räisäsen with E. Rauhala [45] and Jin *et al* [46]. Both data sets each quote ±4% uncertainty in the reported stopping power values. Calculations by SRIM and MSTAR are also overlaid for comparison.

On comparison of the experimental data sets it is observed that at low energies, 0.20 – 0.30 MeV/u there is up to 9% deviation between current data and that from Jin et al. However, if the experimental uncertainties are taken into consideration, the stopping powers from the two data sets, in that energy range, are within the error limits of each other. At higher energies, above 0.30 MeV/u, current data is in slight agreement with data from ref [45].

When comparing current data with SRIM calculations, the CAB approach underestimates stopping at the stopping power maximum by up to 10 %, and about 5% when compared to data from refs [45] and [46]. At that point Bragg's rule prediction is well within the error limit of each of the three data sets. At higher energies (>0.50 MeV/u), the CAB approach overestimates data to a lesser degree than Brag's rule. Looking at MSTAR prediction, it is interesting to note that MSTAR describes current data better than it does data from the two references. Add to that, stopping power values predicted by MSTAR are well within the 6% error limit of the current data set over the entire energy range; 0.20 – 0.60 MeV/u.

5.6.2.7 Carbon

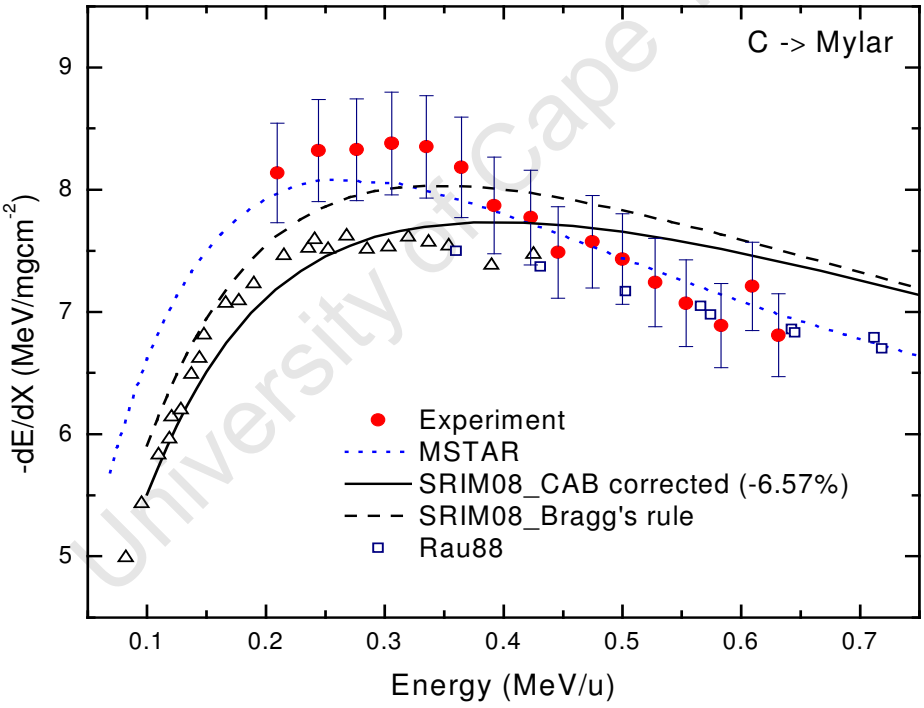

Figure 5.32 Experimental stopping powers of ^{12}C ions in Mylar in the energy range 0.15 - 0.65 MeV/u compared to SRIM2008 and MSTAR predictions, and data from refs [46] (Δ) and [47](□).

Experimental and calculated stopping powers of carbon in Mylar are presented in Figure 5.32. Literature data is from Jin et al [46] and E. Rauhala and J. Räisäsen [47]. Data trends here are almost similar to those of the *oxygen – mylar* system. There is substantial deviation

in stopping powers between current data and literature data at the stopping power maximum. Beyond that (>0.35 MeV/u) data sets tend to converge. The CAB approach predicts data from ref [46] relatively well up to the stopping power maximum and then beyond that, overestimates current data and that from ref [46] by up to 9%. Bragg's rule prediction is within 5% of current data at the stopping power maximum, after which calculations at higher energies overestimate all the data sets plotted in Figure 5.32. As it turns out again in this case, MSTAR predicts the stopping power better than SRIM, up to within 1% - 3% of the present data set, over the entire energy range measured.

5.6.3 Discussion

5.6.3.1 Heavy ion stopping in ZrO_2

The stopping powers of ^{27}Al and ^{24}Mg ions in ZrO_2 measured here are the first experimental data of the stopping of these ions in this refractory ceramic. Results show that within experimental limits, SRIM predictions adequately describe the stopping of both ions. The correlation factors between SRIM predictions and measured values that were introduced in sections 5.6.1.1 and 5.6.1.2 can be used to reproduce the experimental data using SRIM data for comparisons with any future experimental (or theoretical) stopping power data sets.

Measurement results for ^{19}F ions warrant a deeper analysis. The main region of interest is the 0.1 – 0.4 MeV/u energy region where the stopping power variation with energy follows a definite trend. Above 0.4 MeV/u experimental scatter in the stopping power values precludes that energy region in further analyses. That there is near perfect agreement at that energy range between present data and the only other experimental data from the literature [39] makes it difficult to attribute the relatively huge discrepancy between both data sets and SRIM prediction to experimental scatter.

The CAB approach described in section 5.6.2.1 is used to provide SRIM correction factors for quite a number of compounds in the SRIM database, mostly hydrocarbons. Compounds like metallic oxides, have not been included because a lot of previous measurements

concluded that for such compounds, which contain heavy elements, deviations from Bragg's rule disappear [2]. For most of these measurements however, tests of deviation from Bragg's rule were limited to protons and helium ions [48, 49]. The level of disagreement between experiment and SRIM could be a strong indicator of violation of Bragg's rule due to chemical bonding effects in the target foil, which have been suggested to be maximum at the Bragg peak [40]. The effective charge concept, used in the scaling of proton stopping powers to calculate heavy ion stopping in SRIM calculations, might also be the cause of the observed discrepancy because it does not include ionic charge and excitation state distribution within the target itself [50].

It is proposed here that a correction factor of 0.938 calculated from the experimental result of stopping of ^{19}F ions in ZrO_2, be considered a first attempt at obtaining an experimental correction factor for ^{19}F ions in ZrO_2. Figure 5.33 is a reproduction of Fig. 5.18 but with the proposed –6.2 % (i.e 0.938 – 1.000) correction now implemented. The improvement in the predictive accuracy of the corrected SRIM stopping powers is quite evident, even more so for data from ref [39].

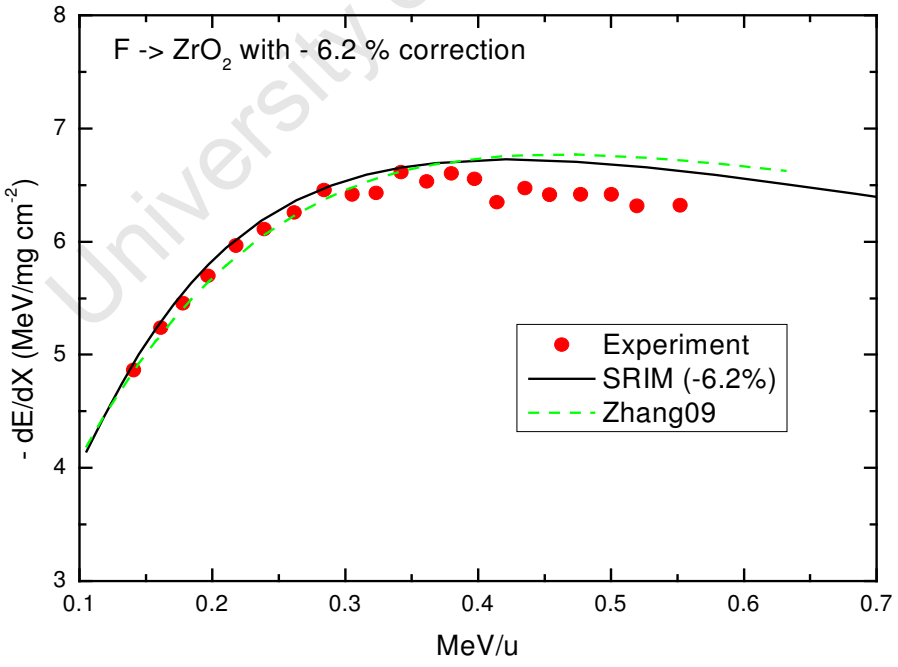

Figure 5.33 Experimental stopping powers of ^{19}F ions in ZrO_2 in the 0.1 - 0.6 MeV/u energy range and data from ref [39] compared to -6.2 %corrected SRIM2008 prediction.

Measurement results of the stopping of ^{16}O ions in ZrO_2, both from the current data set and ref [39]'s measurements suggest that SRIM adequately predicts ZrO_2 stopping powers for oxygen ions, over the 0.10 – 0.45 MeV/u energy range. For ref [39]'s data the energy range of agreement with SRIM prediction extends to over 0.70 MeV/u. For ^{12}C ions in ZrO_2, the general scatter in stopping power data makes it difficult to proffer any meaningful comments on the current results. Repeat measurements should shed more light on this ion – target combination, ref [40]'s results notwithstanding.

5.6.3.2 Heavy ion stopping in Mylar

A survey of the literature on stopping powers of Mylar for ^{28}Si, ^{27}Al, ^{24}Mg and ^{19}F ions reveals that except for data from Räisänen and Rauhala [45], and only for ^{28}Si and ^{27}Al ions at that, there are no other published results on the stopping of these ions in Mylar. Whilst current measurements for ^{28}Si and ^{27}Al cover the 0.1 – 0.5 MeV/u energy range, data from ref [45] begins from 0.4 MeV/u onwards, making any meaningful comparisons of experimental results rather difficult.

What stands out though when looking at experimental data for ^{28}Si, ^{27}Al and ^{24}Mg ions is the step or kink at about 0.38 MeV/u for all the three ions. For ^{27}Al ions this step shows up even in the stopping powers predicted by SRIM using Bragg's rule. Whether the kink is real or an artefact should become clear if and when more experimental data become available. Another observation made is that at low energies, 0.1 – 0.3 MeV/u, the default CAB correction of the stopping powers of Mylar for these ions leads to a greater deviation between experiment and the CAB corrected prediction than between experiment and Bragg's rule calculation. A most probable cause of the observed discrepancies between the CAB corrections and experimental data for heavy ion stopping could be that the proton scaling factors used are mostly from He^{2+} and Li^{+} stopping powers [2] and might not describe heavy ions effective charge adequately. On the other hand MSTAR calculations appear to predict the stopping powers better than SRIM even though they might be off the mark by 2 – 5 % for ^{28}Si, ^{27}Al and ^{19}F ions. Experimental stopping powers for ^{24}Mg ions are the most underestimated by all three calculations.

For ^{16}O and ^{12}C ions there is a considerable disagreement between current data and that from the literature [44-46], especially at the stopping power maximum. Current data is better described by MSTAR than by SRIM for both ions, and the converse is true for data from ref [44]. Once again CAB corrections of SRIM stopping powers at the stopping power maximum do not seem to be working well for these ions either, for any of the experimental data sets.

5.7 References

1. P. Sigmund, *Particle Penetration and Radiation Effects. General Aspects and Stopping of Swift Point Particles*, Springer Series in Solid State Sciences, Springer-Verlag, Berlin, 2006.
2. J. F. Ziegler and J. M. Manoyan, *Nucl. Instr. and Meth.* B **35** (1988) p 215.
3. Kukli et al., *Thin Solid Films* **410** (2002) 53.
4. T.B. Voliak, I.K. Krasyuk and P.P. Pashinin, *Adaptive optical elements based on metallised polymer films*, in Proceedings of the Institute of General Physics Academy of Sciences of the USSR. Editor A.M. Prokhov. **Vol 7** 1987.
5. D. Fink et al., *Nucl. Instr. and Meth* **B 236** (2005) 11.
6. J. F. Ziegler, J. P. Biersack, U. Littmark, *The Stopping and Range of Ions in Solids*, Vol 1, The Stopping and Ranges of Ions in Matter, Pergamon, New York, 1985.
7. N. Bohr, Philos. Mag. **25** (1913) p10; **30** (1915) p581.
8. A. Sharma et al., *Nucl. Instr. and Meth* **B 218** (2004) 19.
9. N. Bohr, *Phys. Rev.* **B 58** (1940) 654.
10. P. Sigmund, *Nucl. Instr. and Meth* B 135 (1998) 1.
11. P. Sigmund, *Phys. Scripta* **28** (1983) 257.
12. S. P. Ahlen, *Rev. Mod. Phys.* **52** (1980) 121.
13. J. Tirira, Y. Serruys, P. Trocellier, Forward Recoil Spectrometry *Applications to hydrogen determination in solids*, 1995 Plemm Press, New York.
14. W. M. Yao et al., *Journal of Physics* **G 33** (2006) p1.
15. H. Giesel., *Nucl. Instr. and Meth* **B195** (2002) p3.
16. J. R. Tesmer, M. A. Nastasi *Handbook of Modern Ion Beam Analysis*, 1995 Materials Research Society.
17. H. Paul, *Nucl. Instr. and Meth.* **B 261**(2007) 1176.
18. S. Heredia-Avalos, J. C. Moreno- Marin, I Abril, R. Garci-Molina, *Nucl. Instr. and Meth.* **B 230** (2005) 118.
19. J. F. Ziegler, SRIM-2010, http://www.srim.org
20. H. Paul, A. Schiner, *Nucl. Instr. and Meth.* **B 179** (2001) 299.

21. International Commission on Radiation Units and Measurements (ICRU) Report 73, Oxford, 2005.
22. E. Rauhala, N. P. Barradas, S. Fazinic, M. Mayer, E. Szilágyi, M. Thompson, *Nucl. Instr. and Meth.* **B 244** (2005) 458.
23. J. F. Ziegler, *Nucl. Instr. and Meth.* **B 219-220** (2004) 1027.
24. H. Paul, A. Schinner, Atomic Data and Nuclear Data Tables **85** (2003) 377.
25. N. Dytlewski, *Improvement of the reliability and accuracy of heavy ion beam nuclear analytical techniques*, IAEA Coordinated Research Project CRP F11013 (2007).
26. C. Pascual-Izarra, N. P. Barradas, G. Garcia, A. Climent-Font, *Nucl. Instr. and Meth.* **B 239** (2005) 135
27. W. K. Chu, *in Material Characterisation Using Ion Beams*, Editors J. P. Thomas and A. Cachard 1978 Plenum Press, New York
28. Y. Zhang, W. J. Weber, *Appl. Phys. Lett.* **83** (2003) 1665.
29. W. H. Trzaska et al., *Nucl. Instr. and Meth.* **B 195** (2002) 147.
30. Y. Zhang, G. Possnert, *Nucl. Instr. and Meth.* **B 190** (2002) 69.
31. R. Thomae, Accelerator Division, iThemba LABS, *private communication.*
32. H. Paul, Stopping Power for Light Ions; Graphs, Data, Comments and Programs. http://www.exphys.uni-linz.ac.at/stopping/.
33. J. Stoner, ACF Metals, Tucson, Arizona, USA, *private communication 2008.*
34. H. Ammi, S. Mammeri, M. Allab, *Nucl. Instr. and Meth.* **B 213** (2004) 60.
35. H. Paul, A. Schiner, *Nucl. Instr. and Meth.* **B 249** (2006) 1.
36. H. Giesel et al, *Nucl. Instr. and Meth* **B 195** (2002) 3.
37. Doolittle L. R. (1985), *Nucl. Instr. and Meth.* **B 9** 344.
38. P. Sigmund, *private correspondence 2008 – 2009.*
39. Y. Zhang and W. J. Weber, *Nucl. Instr. and Meth.* **B 267** (2009) 1705.
40. Y. Zhang et al., *Nucl. Instr. and Meth.* **B 249** (2006) 18.
41. M. Msimanga, C.M. Comrie, C. A. Pineda-Vargas and S. Murray, *Nucl. Instr. and Meth.* **B 268** (2010) 1772.
42. P. Sigmund, *Nucl. Instr. and Meth.* **B 195** (2002) 64.
43. M. Msimanga, C. M. Comrie, C. A. Pineda-Vargas, S. Murray, R. Bark, G. Dollinger, *Nucl. Instr. and Meth.* **B 267** (2009) 2671.
44. D.I. Thwaites, *Nucl. Instr. and Meth.* **B 27** (1987) 293.

45. J. Räisänen and E. Rauhala, *Phys. Rev.* **B 41 (7)** (1990) 3951.

46. C.W.Jin et.al *Phys. Rev.* **B 48**, (1993) 6858.

47. E.Rauhala and J.Räisänen *Phys. Rev.* **B 37** (1988) 9249.

48. G. Blondiaux, M. Valladon, K, Ishii and J.L. Debrun, *Nucl. Instr. and Meth.* **168** (1980) 29.

49. J. S. Feng, W. K. Chu and M. A. Nicolet, *Thin Solid Films* **19** (1973) 227.

50. A. Bauricher, P. Sigmund and A. H. Sørensen, *Nucl. Instr. and Meth.* **B195** (2002) 224.

Chapter 6

Summary and Conclusion

The introductory chapter of this thesis discusses the relative advantages of a ToF – E detector system in HI – ERD thin film analysis. Unfortunately such detector systems are not ordinarily off – shelf commercial detectors, unlike most silicon based solid-state detectors prevalent in the other ion beam analysis techniques. The principal aim of this work therefore was to set up and characterise a ToF – E spectrometer and demonstrate its usability in HI – ERD analysis of thin solid films. This was the major part of a broader project to establish HI – ERD as a complementary technique for the analysis of light elements in thin film materials at iThemba LABS. Equally important was the aim to measure stopping powers of heavy ions in thin foil compound materials using the newly built spectrometer to add more experimental data to the scant global database of heavy ion stopping in technologically important compounds.

The ToF – E spectrometer that was set up consists of two microchannel plate – based time detectors, a flight distance of 0.584 m apart, and a surface barrier energy detector mounted about 6 cm from the second time detector. The ToF – E telescope mounted at an angle of 30^{o} to the incident beam direction, was tested using a ^{252}Cf source while being assembled. System characterisation measurements were performed on the fully assembled spectrometer using recoil ions ejected from known target samples. The best timing resolution obtained was 0.96 ns for 18 MeV ^{40}Ca ions from a Calcium Fluoride layer on a Silicon substrate. The resultant depth resolution was found to be 13.0 ± 1.0 nm.

Test measurements were also carried out to assess performance aspects of the spectrometer specific to the analysis of light elements in thin film and bulk matrices. The mass resolution was found to range between 0.8 **u** and 1.7 **u** in the atomic mass range 12 **u** to 40 **u**. At this level of resolution, it was thus possible to calculate elemental depth profiles in most of the samples analysed. Thin film depth profiling from elemental energy spectra was implemented using both direct calculation and iterative simulation software codes. Of the

latter group, Monte Carlo based simulation using the analysis code CORTEO proved most appropriate for analysis of Heavy Ion – ERDA data, exemplified by the analysis of a Chromium Oxide deposit on a Silicon substrate. At the experimental configuration used analytical depths of up to 0.6 μm were achieved. The lowest atomic concentrations that were measured were 0.46 at% for carbon and 0.84 at% for oxygen, both detected in a layer of intrinsic silicon deposited by HW – CVD onto a silicon substrate.

On comparison with the more established RBS technique it was found that the newly assembled spectrometer performs within expectations in terms of thickness measurement, but surpasses the RBS technique in the detection of light elements like ^{12}C and ^{24}Mg. For heavier elements better results were obtained from RBS analysis than when using ToF – ERDA because of poor mass resolution for heavy elements in the latter technique. What the comparison affirmed though was that the two techniques can be used in a complementary mode to each other; ToF – ERDA providing information on the light element content of a sample and RBS shedding light on the heavy elements present in the sample.

On the measurement of heavy ion stopping powers, new experimental data has been produced in this work. The stopping powers of ^{27}Al and ^{24}Mg in ZrO_2 are the first experimental data for these *ion – target* combinations. For Mylar, new data on the stopping of ^{24}Mg and ^{19}F ions has been made available. While there is already a single data set for the stopping of each of ^{28}Si and ^{27}Al in Mylar, current data extends the energy range to energies below the stopping power maximum, for both ion species,.

The new stopping powers of ^{27}Al, ^{24}Mg and ^{19}F in ZrO_2 were compared with predictions from the widely used semi-empirical code SRIM (2008 version), as well as theoretical calculations from Peter Sigmund's PASS code. Indications are that SRIM describes the stopping of ^{27}Al and ^{24}Mg relatively well. The experimental data for these ions can be reproduced from SRIM stopping powers using the correlation factors calculated for each ion species. The correlation factors are aimed at facilitating easy comparison of present data against any other future measurement results. For ^{19}F stopping power in ZrO_2 around the Bragg peak, the huge discrepancy between experimental data and SRIM prediction was attributed to chemical bonding effects and or a possible inadequacy of the effective charge

concept used for scaling proton stopping powers. It was found that it might be necessary to introduce a correction factor to Bragg's rule SRIM prediction. A correction factor of –6.2% was found to reduce the discrepancy between SRIM values and current data, as well as between SRIM and the one data set found in the literature, to less than 1%.

Theoretical stopping powers predicted by the PASS code were all found to exceed experimental data by more than 6% for the ions studied. An interesting observation though was that for all ions the theoretical values were closest to experimental data in the region of the stopping power maximum. This is in stark contrast to SRIM predictions where deviations between experiment and calculation have been known to be greatest at the stopping power maximum. Another important observation was that at low energies, 0.1 – 0.3 MeV/u, the predictive accuracy of PASS calculations improves with projectile ion mass, surpassing SRIM even, for 0.07 – 0.25 MeV/u ^{84}Kr projectiles.

Experimental stopping powers of ^{27}Al, ^{24}Mg, ^{19}F, ^{16}O and ^{12}C in Mylar were compared against both CAB corrected and uncorrected SRIM predictions. The general conclusion drawn for all ions was that the default CAB corrections in SRIM led to even wider disagreement between experiment and calculation than between experiment and Bragg's rule due to possible deficiencies of the effective charge concept. MSTAR, another semi-empirical code, was found to perform better than SRIM at predicting stopping powers of all the above ions. Another interesting observation worth mentioning is the kink (or step) observed at about 0.38 MeV/u in the stopping powers of ^{28}Si, ^{27}Al and ^{24}Mg ions in Mylar, which warrants further investigation to confirm if it is a real experimental observation or an artefact. That the same kink shows up in SRIM predicted values for ^{27}Al ions makes the observation all the more intriguing.

In conclusion, an assessment of the contribution that the work contained in this thesis makes to the Ion Beam and Materials Research fields suffices. The problem of quantitative and sensitive analysis of light elements in thin film technologies has been found to be best addressable by nuclear analytical techniques using ion beams from particle accelerators. Pioneers of the Heavy Ion – ERDA technique have demonstrated over the last two decades that it is the technique of choice when it comes to light element analysis in thin solid films.

While now considered a mature technique in principle, its realisation in most accelerator labs is not trivial.

The work presented here provides a solid foundation for the full implementation of the technique at iThemba LABS, to support existing and new research programmes in thin film and nano technologies, ranging from solar energy research to sensor technology. A ToF – Energy spectrometer was set up and characterised for HI – ERD analyses. The analysis of CaF_2\Si, CrO_2\Si, HW – CVD amorphous Si and Steel samples all demonstrate the usability of the spectrometer in thin film and bulk materials analyses. The spectrometer was further adapted for stopping power measurements in self – supporting foils, providing much needed new experimental stopping powers of heavy ions in technologically important compound materials. .

Appendix A Some IBA simulation programs

Table A1 Data Analysis Software for Ion Beam Analysis

Fundamental physics handled in the simulations.

Analysis program	Isotope calculation	Screening calculation	Straggling models	Plural scattering	Multiple scattering	Geometric straggling	Channeling
DEPTH	Single isotope	Yes	Bohr, Chu, Yang, Tschalär	None	Yes, Pearson VII distribution	Yes	No
GISA	Natural abundance and/or specific isotopes	Energy/angle; external tables by users	Bohr + Lindhard/Scharff	None	None	No	No
MCERD	Natural abundance and/or specific isotopes	No	Bohr, Chu, Yang	Full MC calculation	Full MC calculation	Yes	No
NDF (DataFurnace)	Natural abundance and/or specific isotopes	Energy/angle; Andersen and L'Ecuyer	Bohr, Chu, Yang, Tschalär	Dual scattering approx. (run-time option)	Yes, Gaussian approximation from DEPTH calculation	Yes, from DEPTH calculation	No
RBX	Natural abundance and/or specific isotopes	Yes	Bohr, Chu, Yang, Tschalär	None	Yes (same model as DEPTH)	Yes	Defect calculation; simulation of channeled spectr
RUMP	Natural abundance and/or specific isotopes	Energy only; L'Ecuyer	Bohr	None	None	No	No
SIMNRA	Natural abundance and/or specific isotopes	Energy/angle; Andersen and L'Ecuyer	Bohr, Chu, Yang, Tschalär	Dual scattering approx. (run-time option)	Yes (DEPTH model approximated as Gaussian)	Yes	No

Taken from ref [37] in Chapter 2

Appendix B NBS Standard Reference

NBS STANDARD REFERENCE MATERIALS

February 24, 1972

1200 SERIES IRON AND STEEL STANDARDS

Summary Report

Revised Information on Compositions

The following table gives the proposed values for the 1200 Series revised certificates. In general, the values shown for the elements C through Mo are the results of chemical determinations made at NBS and at four cooperating laboratories; for all other elements the values are the results of determinations largely made at NBS by two or more independent methods of analyses. Individual Revised Provisional Certificates are in preparation for the steels 1261-1264. A Final Certificate is available for 1265 Electrolytic Iron (see note x below). Plans are to complete work on this series by the end of 1973 and to issue Final Revised Certificates.

No.	1261	1262	1263	1264	1265
Element	Percent, by weight				
C	0.38_2	0.16_0	0.62	0.87_0	0.0067
Mn	.66	1.04	1.50	$.25_5$	.0057
P	.015	0.042	$.02_9$	$.01_8$	$.002_5$
S	.017	.038	.008	.028	.0059
Si	.223	.39	.74	.067	$.008_0$
Cu	.042	.50	$.09_8$	$.24_9$	.0058
Ni	1.99	.59	.32	$.14_2$	.041
Cr	0.69	.30	1.31	$.06_5$	$.007_2$
V	.011	$.04_1$	0.31	$.10_5$	.0006
Mo	.19	$.06_8$	.030	.49	.0050
W	$.01_5$	.21	$.04_5$	.10	(∿.00004) a/
Co	.030	.30	.048	.15	$.007_0$
Ti	.020	.084	.050	.24	.0006
As	.017	$.09_2$	.010	$.05_2$	(.0002)
Sn	$.01_1$	.016	(.095)	[.005] b/	(∿.0002)
Al (Total)	$.02_1$	$.09_5$	.24	(.008)	(.0007)
Nb	.022	.29	.049	$.15_7$	(<.00001)
Ta	.020	.20	(.053)	.11	-(<.00005) c/
B	.0005	.0025+	$.0009_1$	.011	.00013
Pb	$.00002_5$	$.0004_3$	.0022	.024	$.00001_5$ x
Zr	.009	.19	.049	.068	-(<.00001)
Sb	$.004_2$	.012	$.001_6$	(.035)	-(<.00005)
Bi	.0004	(.002)	(.0008)	(.0009)	-(<.00001)
Ag	.0004	(.0010)	(.0038)	(.00002)	(∿.000002)
Cd	(<.00005)	(<.00005)	.0005	.0001	-(<.000002)
Ca	(<.0001)	(.0002)	(<.0001)	(<.0001)	-(<.00001)
Mg	(.0001)	(.0006)	(.0005)	(.0001)	-(<.00002)
Se	.004	[.001]	[.0001]	[.0003]	-(<.00001)
Te	.0006	(.0005)	(.0022)	[.0002]	-(<.00001)
Zn	(.0001)	(.0005)	(.0004)	.002	(<.0001) x
Ce	$.001_3$	(.0011)	(.0016)	(.00025)	-(<.000005)
La	.0004	.0004	.0006	.00007	-(<.000005)
Nd	.0003	(.0005)	(.0007)	(.00012)	-(<.000005)
Pr	(.00014)	(.00012)	(.00018)	(.00003)	-(<.000005)
Hf	[.0002]	[.006]	[.0015]	[.005]	-(<.00002)
N	(.0037)*	(.0041)*	(.0041)*	[.003]*	(∿.0011)*
O	(.0009)*	(.0011)*	(.0007)*	[.0017]*	(∿.0063)*
H	[<.0005]*	[<.0005]*	[<.0005]*	[<.0005]*	(∿.0001)*
Ge	[.006]	[.002]	[.010]	[.003]	(∿.0014)
Fe (by diff.)	(95.6)	(95.3)	(94.4)	(96.7)	(99.9)

* From gasometric certificates, SRM's 1095 through 1099

\+ Isotopic dilution mass spectrometry - 0.00265; nuclear track - 0.00234

x Revised final value

a/ Values in parentheses are not proposed for certification. These values usually were obtained by a single analytical method of analysis.

b/ Values in brackets also are not proposed for certification. They are nominal or approximate values from the heat analyses.

c/ Dash indicates "not detected." Values in parentheses following the dash are conservative "upper limits" of detection by specific methods of analysis.

The value listed for an element is the present best estimate of the "true" value based on the results of the analytical program. The value listed is not expected to deviate from the "true" value by more than ± 1 in the last significant figure reported; for a subscript figure, the deviation is not expected to be more than ± 5. Based on the results of homogeneity testing, maximum variations within and among samples are estimated to be less than the uncertainty figures given above.

P. E. Michaelis, Chief
Metal Standards
Office of Standard Reference Materials

Appendix C ToF – Energy scatter plots for stopping power measurements

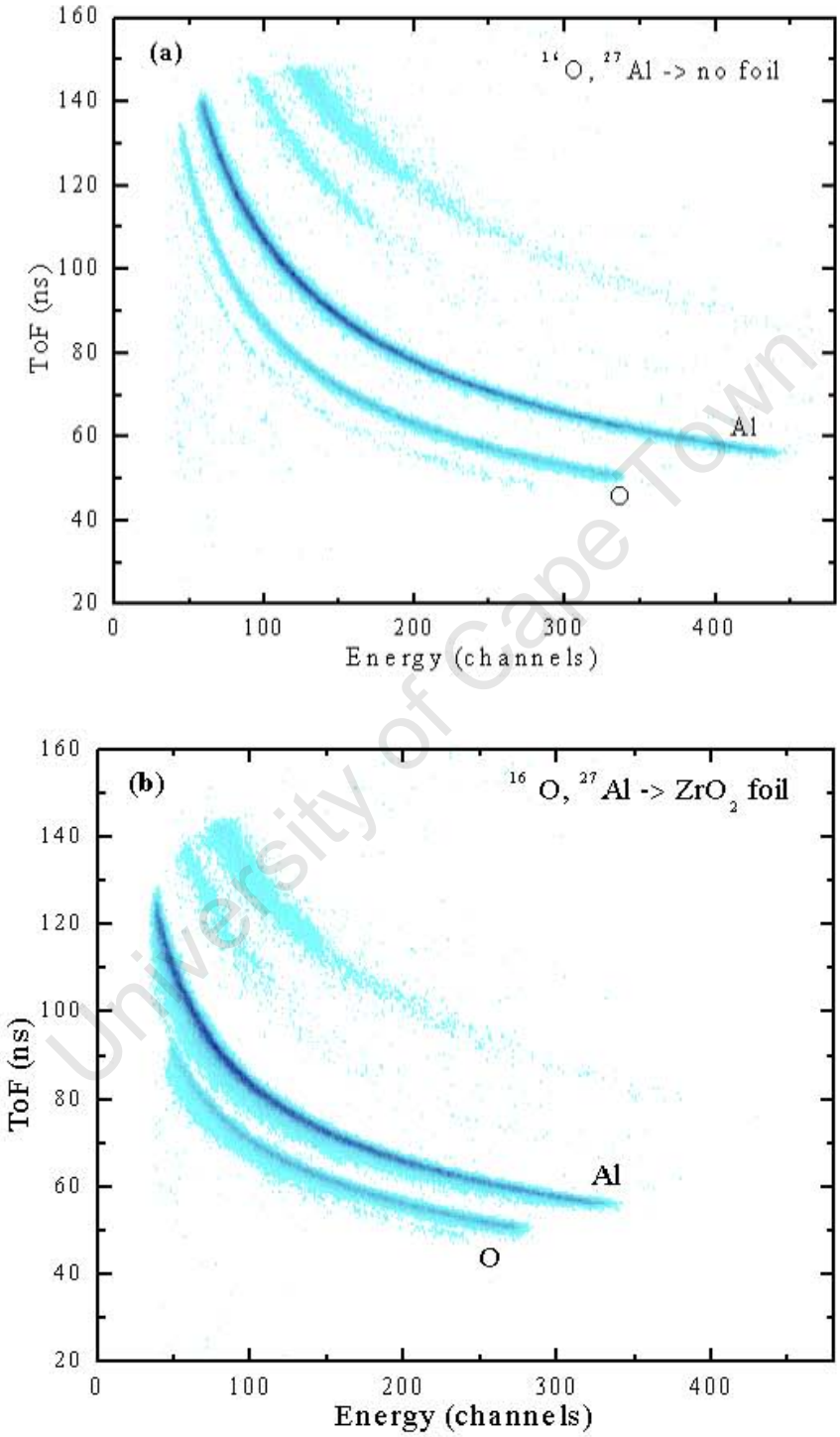

Figure I ToF – Energy scatter plots of ^{16}O and ^{27}Al recoils before (a) and after insertion of the ZrO_2 stopper foil (b).

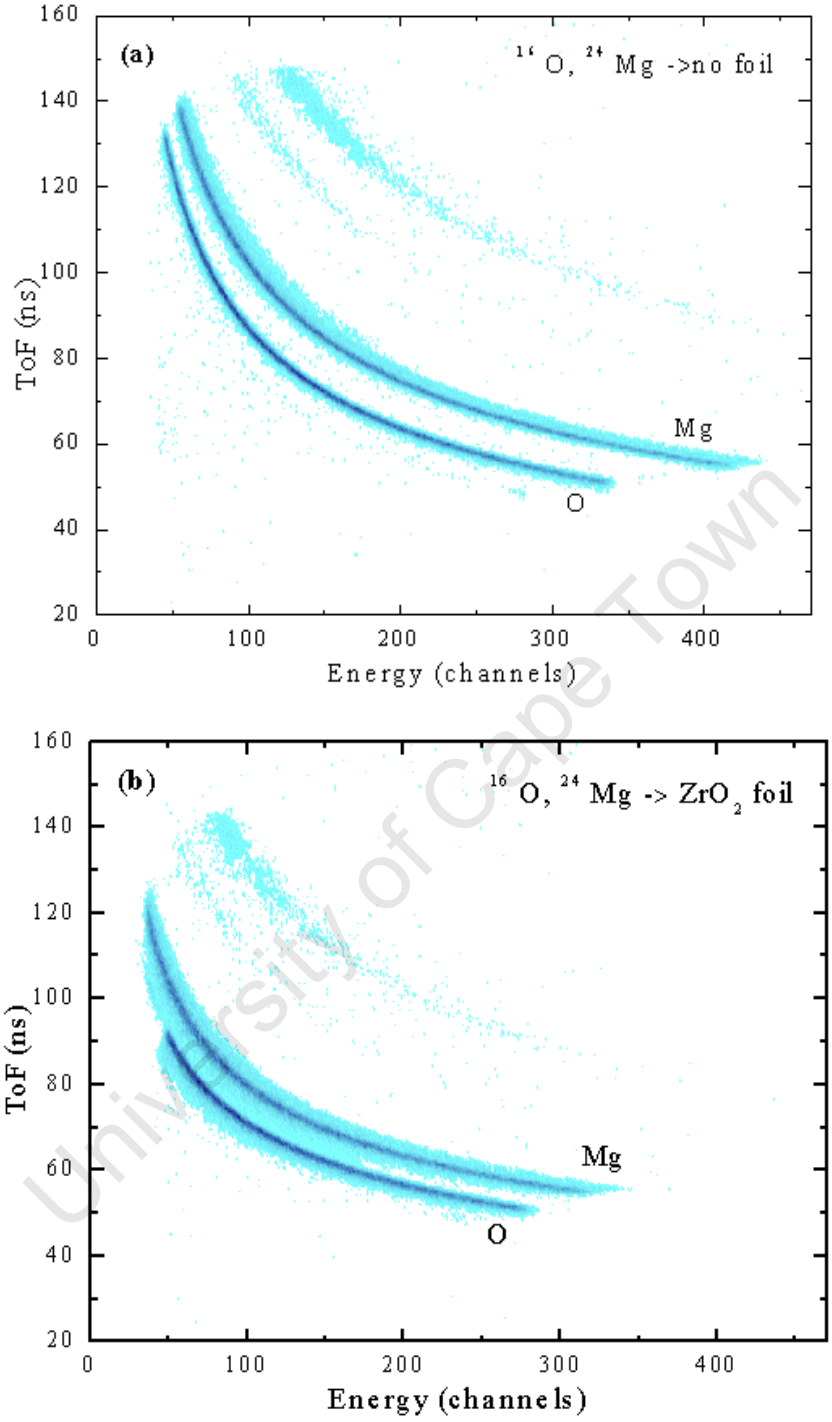

Figure II ToF – Energy scatter plots of ^{16}O and ^{24}Mg recoils before (a) and after insertion of the ZrO_2 stopper foil (b).

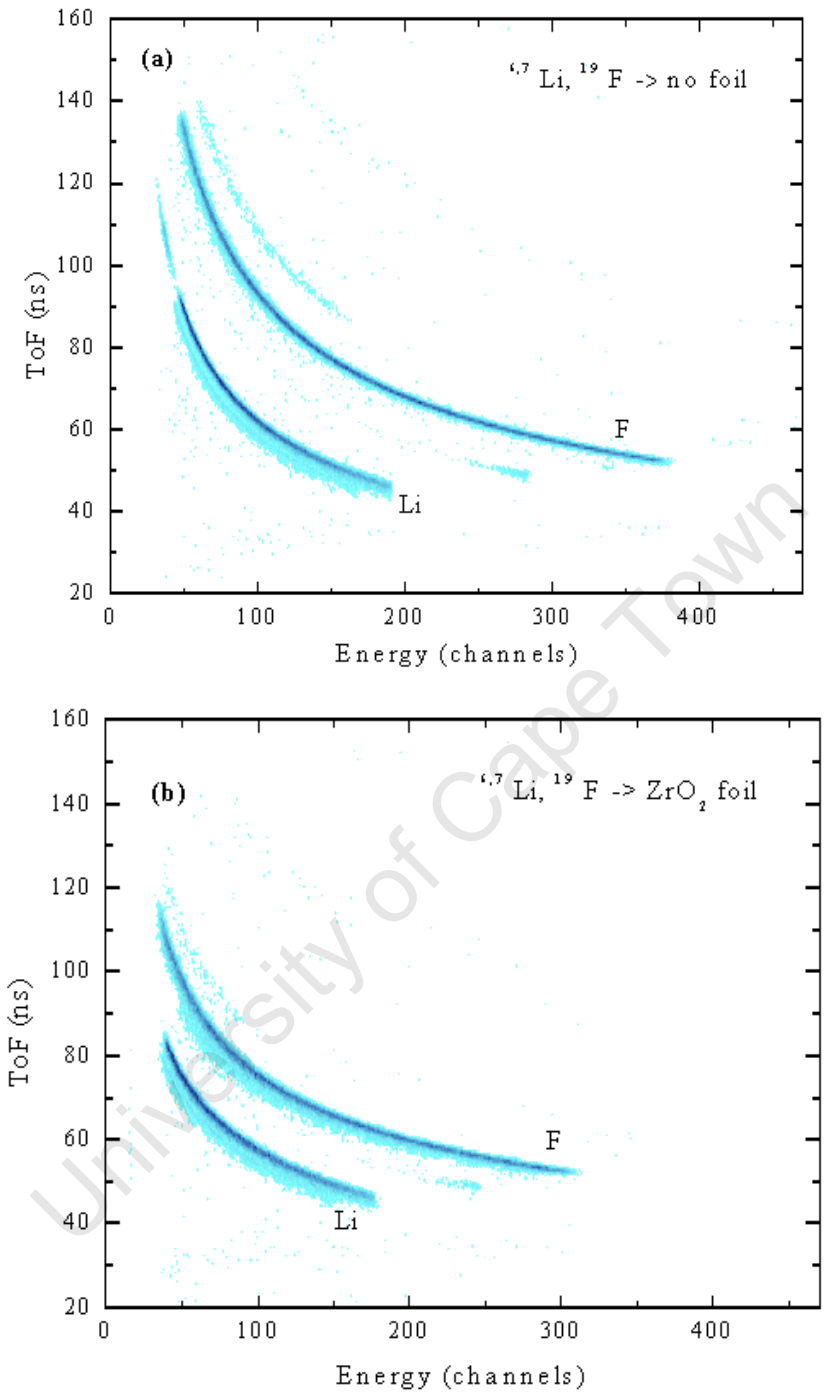

Figure III ToF – Energy scatter plots of ^{6,7}Li and ^{19}F recoils before (a) and after insertion of the ZrO_2 stopper foil (b).

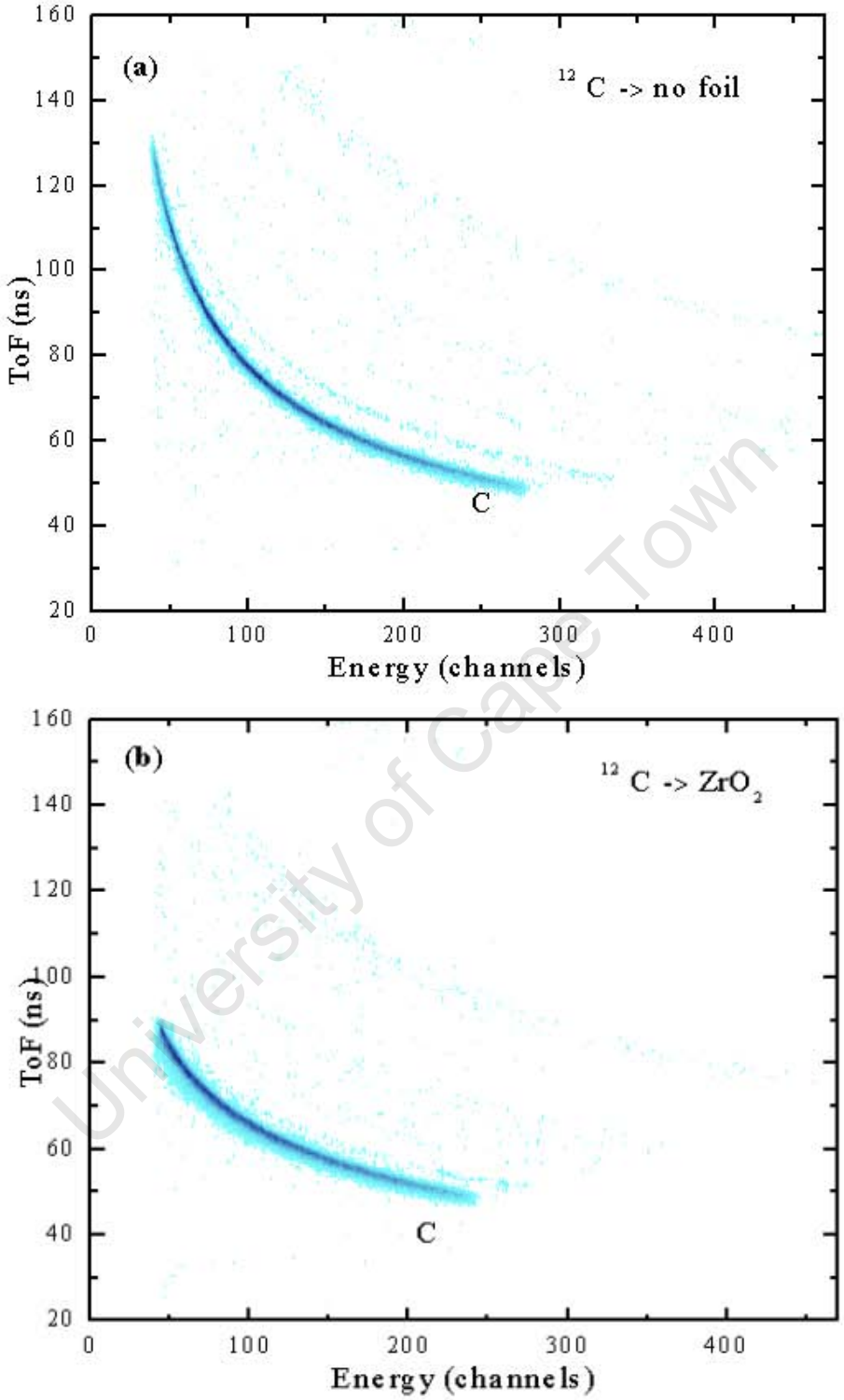

Figure IV ToF – Energy scatter plots of ^{12}C recoils before (a) and after insertion of the ZrO_2 stopper foil (b).

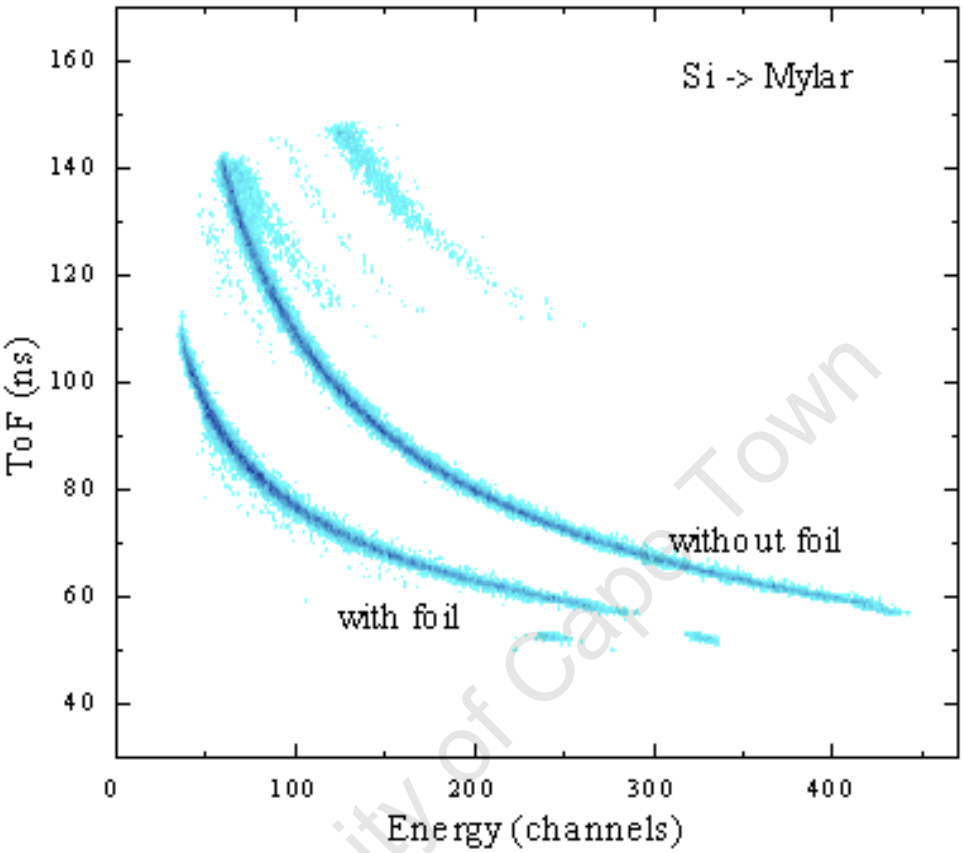

Figure V ToF – Energy scatter plot of ^{28}Si recoils with and without the Mylar stopper foil.

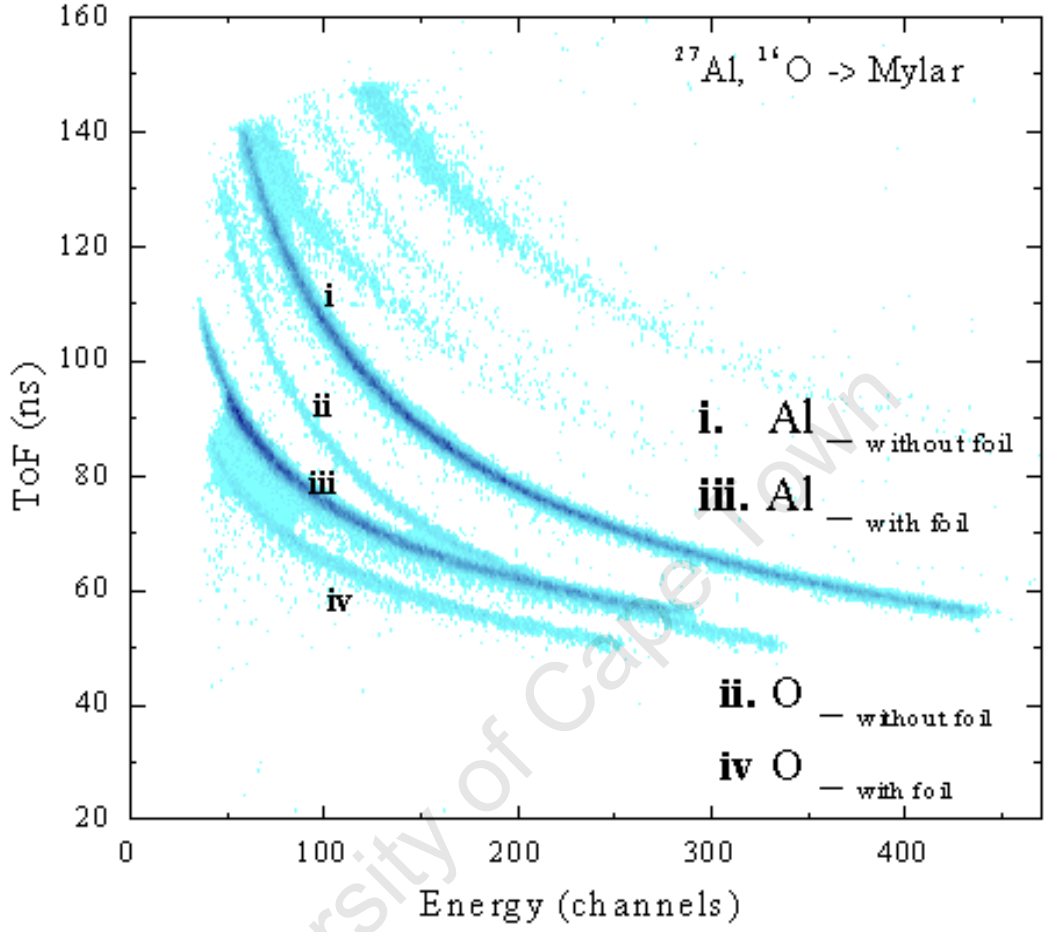

Figure VI ToF – Energy scatter plot of ^{27}Al and ^{16}O recoils with and without the Mylar stopper foil.

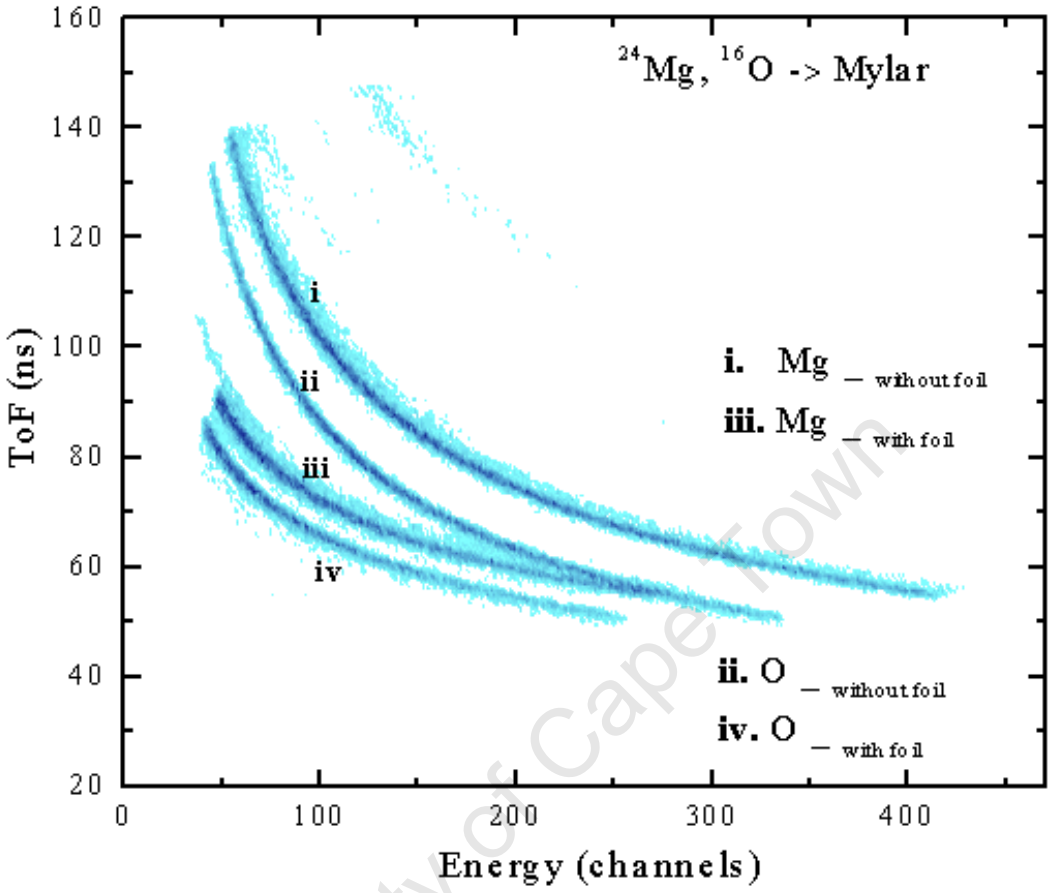

Figure VII ToF – Energy scatter plot of ^{24}Mg and ^{16}O recoils with and without the Mylar stopper foil.

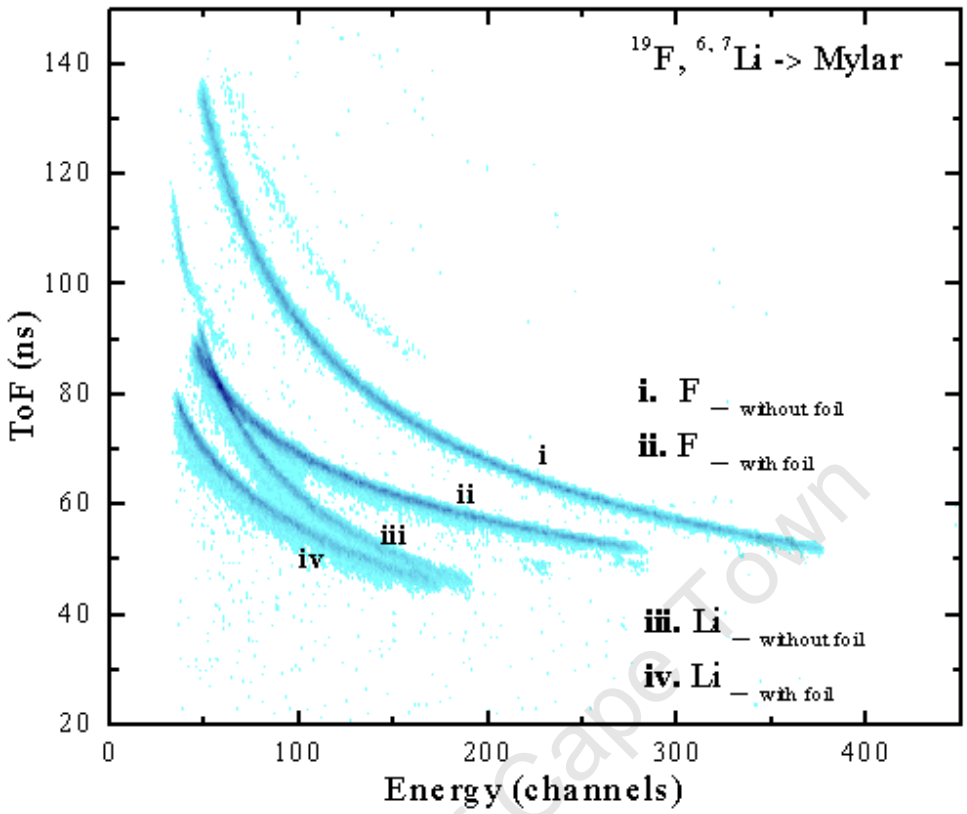

Figure VIII ToF – Energy scatter plot of ^{19}F and ^{6,7} Li recoils with and without the Mylar stopper foil.

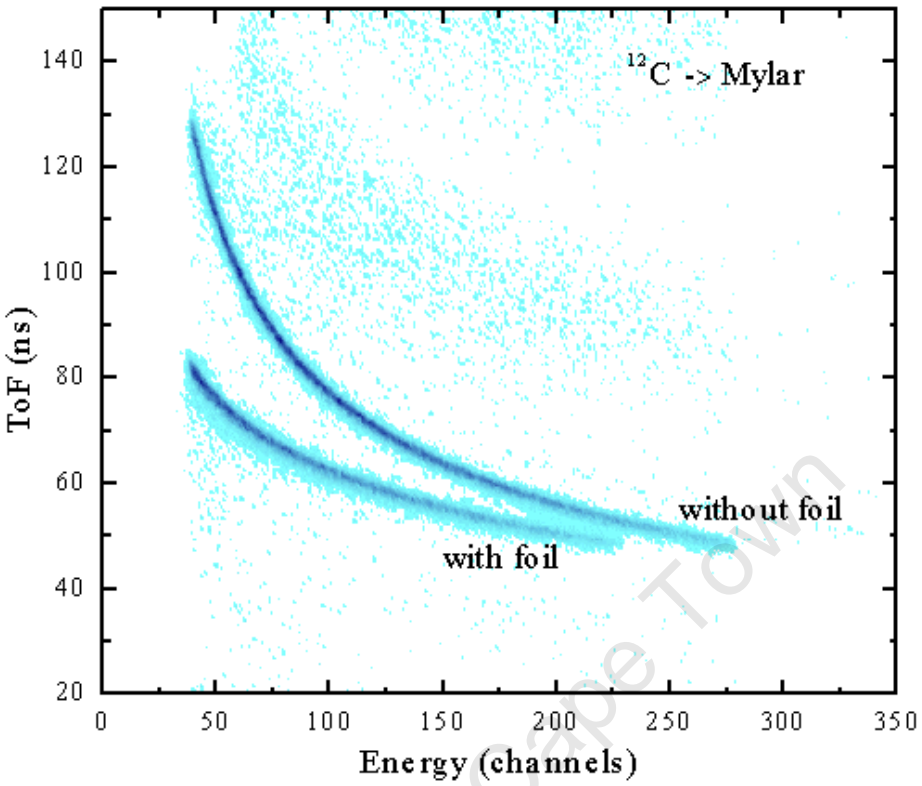

Figure IX ToF – Energy scatter plot of ^{12}C recoils with and without the Mylar stopper foil.